Second-harmonic generation for characterization of interface electric fields in dielectric-semiconductor stacks

Baydaa Obeid

THÈSE

Pour obtenir le grade de

DOCTEUR DE L'UNIVERSITÉ GRENOBLE ALPES

École doctorale : EEATS - Electronique, Electrotechnique, Automatique, Traitement du Signal (EEATS)
Spécialité : Nano électronique et Nano technologies
Unité de recherche : Institut de Microélectronique, Electromagnétisme et Photonique - Laboratoire d'hyperfréquences et de caractérisation

Génération de seconde harmonique pour la caractérisation des champs électriques d'interface dans les empilements diélectriques-semiconducteurs

Second-harmonic generation for characterization of interface electric fields in dielectric-semiconductor stacks

Présentée par :

Baydaa OBEID

Direction de thèse :

Irina IONICA MCF, G-INP	Directrice de thèse
Lionel BASTARD MAITRE DE CONFERENCES, Université Grenoble Alpes	Co-encadrant de thèse

Rapporteurs :

Georges BREMOND
PROFESSEUR DES UNIVERSITES, UNIVERSITE DE LYON
Yannick DUMEIGE
PROFESSEUR DES UNIVERSITES, UNIVERSITE DE RENNES

Thèse soutenue publiquement le **9 juin 2023**, devant le jury composé de :

Georges BREMOND PROFESSEUR DES UNIVERSITES, UNIVERSITE DE LYON	Rapporteur
Yannick DUMEIGE PROFESSEUR DES UNIVERSITES, UNIVERSITE DE RENNES	Rapporteur
Anne KAMINSKI-CACHOPO PROFESSEUR DES UNIVERSITES, GRENOBLE INP	Présidente
Sébastien DUBOIS INGENIEUR HDR, CEA CENTRE DE GRENOBLE	Examinateur

Invités :

Delphine Le Cunff
INGENIEUR DOCTEUR, STMicroelectronics
Guy Vitrant
DIRECTEUR DE RECHERCHE EMERITE, Grenoble INP

In memory of my precious father…

"The important thing in science is not so much to obtain new facts as to discover new ways of thinking about them"

William Lawrence Bragg

Acknowledgments

I would like to thank all the members of the jury: Prof. Georges Bremond, Prof. Yannick Dumeige, Prof. Anne Kaminski, Dr. Sébastien Dubois, Dr. Delphine Le Cnuff, for accepting to judge this work and for giving me of their time.

My sincere gratitude goes to my supervisors, Irina Ionica and Lionel Bastard, for having allowed me to carry out this work during these 3 years and for their scientific knowledge, precious advice, encouragement and trust they have placed in me since my arrival in the laboratory. Their technical and scientific guidance helped me acclimate to this field.

I am really happy with the presence of Guy Vitrant at my defence. I am indebted to him for his intensive help with the modeling and simulation part during the first 7 months of my thesis before his retirement.

A enormous thanks to all the members of IMEP-LAHC laboratory, in particular Aude Bouchard, Martine Gri, Xavier Mescot, Serge Bas for all their valuable technical support.

My heartfelt thanks go to my friends in France and Lebanon for being there when I needed and to all those who have always supported me.

To my family: thank you for encouraging me in all of my pursuits and inspiring me to follow my dreams. I am especially grateful from the bottom of my heart to my beloved mom Khadije, my sisters Hadia, Safaa, Asmaa, my brothers Wissam, Adnan, Houssam, My brothers-in-law Ahmad, Abdel Hamid, Mostafa, my adorable nieces Afaf, Cyrine, Jamila, Joudi and my handsome nephews Abdel Kader, Amine, Zein, who gave me their love and provided me with the motivation that allowed me to be here. I hope you will always be proud of me.

Abstract

The performance of devices such as MOSFETs, image sensors, photovoltaic cells is dramatically influenced by the quality of interfaces, in particular between dielectrics and silicon. Passivation of Si using high-k dielectrics is known to improve the electrical properties of these interfaces. Among the methods used to characterize passivation, the second harmonic generation (SHG) is a promising sensitive and non-destructive technique based on the nonlinear optics. In the dipole approximation, the bulk SHG response is zero in centrosymmetric materials (e.g. Si, Al_2O_3, SiO_2, etc.), therefore the SHG response mainly contains interface-related information, where the symmetry is broken. Additionally, when an electric field (E_{DC}) exists at the interface, the signal is reinforced by the so-called EFISH (electric field induced SHG). Since the interface electric field is related to fixed oxide charges (Q_{ox}) and/or interface states (D_{it}), the SHG technique is sensitive to these electrical parameters. The aim of this thesis is to calibrate the SHG response for E_{DC} measurement, particularly associated with Q_{ox} in the dielectrics. Extracting electrical-related information from SHG experimental data necessitates taking into account the influence of optical phenomena (absorption, interferences, etc.), which was achieved thanks to modeling/simulation of the nonlinear second harmonic response. Our simulation program is based on theoretical models from the literature that we adapted for multilayers. The experiments were performed on several Al_2O_3 layers on Si (100), deposited in different conditions and that exhibit very different interface quality. Complementary electrical techniques, such as corona oxide characterization of semiconductor (COCOS) and capacitance-voltage measurements (C-V), gave access to the electrical field of the samples and complete the SHG results for the calibration. Both experiments and simulations prove the possibility of calibration for monolayers of dielectric on Si. Some challenges related to the characterization of multilayers such as silicon on insulator (SOI) are also discussed, in particular the influence of the layer thicknesses and of the electric fields of various nonlinear interfaces on the SHG response.

Keywords: Second harmonic generation (SHG), passivation, interface electric field, fixed oxide charges, interface traps, capacitance-voltage (C-V).

Résumé

Les performances des dispositifs tels que les MOSFET, les photodétecteurs, les cellules photovoltaïques sont fortement influencée par la qualité des interfaces, en particulier entre les diélectriques et le silicium. La passivation de Si par des diélectriques à forte permittivité (high-k) est connue pour améliorer les propriétés électriques de ces interfaces. Parmi les méthodes utilisées pour caractériser la qualité des interfaces, la génération de seconde harmonique (SHG) est une technique sensible et non destructive prometteuse basée sur l'optique non linéaire. Dans l'approximation dipolaire, la réponse SHG dans les matériaux centrosymétriques (par exemple Si, Al_2O_3, SiO_2, etc.) est nulle. Par conséquent, la réponse SHG contient principalement des informations liées aux interfaces, où la symétrie est brisée. De plus, le signal est renforcé en présence d'un champ électrique (E_{DC}) à l'interface ; ce phénomène est appelé EFISH (Electric Field Induced SHG). Comme le champ électrique d'interface est associé aux charges fixes dans l'oxyde (Q_{ox}) et/ou aux états d'interface (D_{it}) entre oxyde et semiconducteur, la technique SHG est donc sensible à ces paramètres électriques. L'objectif de cette thèse est de calibrer la réponse SHG pour la mesure du champ électrique lié aux charges fixes dans les diélectriques. L'extraction d'informations électriques à partir de données expérimentales SHG nécessite la prise en compte de l'influence des phénomènes optiques (absorption, interférences, etc.), ce qui a été réalisé grâce à la modélisation/simulation de la réponse à la seconde harmonique des structures étudiées. Notre programme de simulation est basé sur des modèles théoriques de la littérature que nous avons adaptés pour les multicouches. Les expériences ont été réalisées sur plusieurs couches d'Al_2O_3 sur Si (100), déposées dans des conditions variables et qui présentent des qualités d'interface très différentes. Des techniques électriques complémentaires, telles que la caractérisation par charge corona (COCOS) et les mesures capacité-tension (C-V), ont permis d'accéder au champ électrique des échantillons et de compléter les résultats SHG pour la calibration. Les expériences et les simulations prouvent la possibilité de calibration pour des monocouches de diélectriques sur Si. Quelques éléments d'étude liés à la caractérisation des multicouches tels que la structure SOI (Silicon On Insulator) sont également discutés, en particulier l'influence sur la réponse SHG de l'épaisseur des couches ou encore des champs électriques présents aux diverses interfaces.

Mots clés : Génération de seconde harmonique (SHG), passivation, champ électrique d'interface, charges fixes d'oxyde, pièges d'interface, capacité-tension (C-V).

Table of contents

General introduction

The silicon surface passivation with high permittivity (high-k) dielectrics is essential to guarantee good performance for devices such as image sensors or solar cells. The first challenge in ensuring stable and reliable operation of these devices is to control the fabrication processes, specifically by introducing and activating the fixed oxide charges (Q_{ox}) for field-effect passivation and/or by reducing the interface states (D_{it}) for chemical passivation.

The second challenge is the characterization of the passivation obtained with dielectric materials on Si, using sensitive, fast and non-destructive techniques, which do not require fabrication of specific test structures. To assess the electrical parameters (Q_{ox} and D_{it}) that quantify the electrical quality, conventional electrical methods such as capacitance-voltage (C-V) or corona oxide characterization of semiconductors (COCOS) can be employed, each has its advantages and inconveniences. Second harmonic generation (SHG), an alternative nonlinear optical method, has demonstrated its ability to meet all of the criteria required for oxide-Si interface characterization. In the dipolar approximation, there is no SHG response in the bulk of centrosymmetric materials such as silicon, alumina, silicon dioxide, etc. Therefore, the nonlinear response comes mainly from the surface/interface of these materials, where the inversion symmetry is broken. In addition, the second harmonic is enhanced by the electric field presented at the interface, which is known as EFISH phenomenon. This phenomenon has been utilized in the literature to study the interface of many oxide-semiconductor materials. For an extensive use of the technique, a calibration is needed, that will allow passing from specific studies on particular structures to a more general approach. The aim of this thesis is to produce such a calibration. During the thesis, we used SHG characterization to probe various passivation layers (in particular Al_2O_3) on silicon in order to calibrate the SHG with respect to the Q_{ox} in the materials.

The thesis chapters will address the context, state of the art, theoretical phenomenology and simulation, experimental methodology and results.

The first chapter "**Dielectric materials on silicon: characterization challenges & SHG**" shows the interest of high-k dielectrics on silicon for microelectronic and optoelectronic devices. In particular, we explain the two passivation mechanisms that improve the interface quality of these materials and thus the device performance. Then, we present two typical characterization techniques that will be used later for calibration: the capacitance-voltage (C-V) and the corona oxide characterization of semiconductor (COCOS) measurements. The chapter ends with a fast explanation of the second harmonic generation

(SHG), which is at the heart of this thesis, and its use in order to characterize the electrical properties of oxide-Si interfaces.

The second chapter shows a **state of art on the SHG use for the characterization of dielectric-semiconductor interfaces**. Based on some examples from the literature, we'll explain the influence of modified electrical properties on the SHG response. The examples cover both single oxide/Si and also multilayer structures and the aim is to give the challenges in each case.

The third chapter explains the **SHG theory and simulation model in multilayer structures.** For an accurate study of SHG from multilayer structures, simulation and modeling are necessary to understand the optical part of the response (absorption, interferences). The development of our theoretical model, the optical and electrical phenomena arising due to the interaction of the laser with the samples, and the simulation progress will be described. The validation of the simulation results will be obtained thanks to experimental tests on single silicon substrates and multilayer structures.

In chapter 4, we show the **experimental methodology**. This chapter covers the deposition processes of high-k dielectric layers on silicon and the characterization techniques employed during the thesis. The SHG experimental setup will be presented, starting with the installation of a new laser in the tool, data treatment to extract the second harmonic response against time and experimental parameters. The electrical C-V measurements will be also described, including the fabrication of metal-oxide-semiconductor (MOS) capacitor structures and the extraction of fixed oxide charges (Q_{ox}) and of interface states densities (D_{it}).

The goal of the thesis is to establish **SHG calibration to characterize dielectric/Si(100) interfaces** and the main results of calibration will be given in chapter 5. The samples under study are various Al_2O_3 layers on silicon, with different electrical properties. SHG measurements and simulations were performed on the samples in order to plot the calibration curve of SHG intensity versus interface electric field E_{DC}. The E_{DC} values corresponding to experiments were first calculated from total oxide charges, extracted using COCOS. The mismatch between total charge (extracted from COCOS) and the fixed charges (needed for the SHG calibration) forced us to use another electrical characterization technique: the C-V. Thus, a second calibration curve was obtained based on the Q_{ox} extracted from C-V. This second calibration gives a better agreement between simulation and experiment. A few SHG results from other structures (different dielectrics, multilayers) will also be shown.

Finally, we summarize the results and draw perspectives in the **general conclusion** chapter.

Chapter 1: Dielectric materials on silicon: characterization challenges & SHG

Abstract

This chapter gives a quick overview on the main topics concerning the context of this PhD. The aim is not to be exhaustive but to give some elements necessary for each part. The first part shows the passivation mechanisms that enhance the interface quality of materials and guarantee proper device operation. The challenge is not only at the fabrication level, but also in the tools and methods for characterization of interfaces. Besides structural information, we need to have access also to the electrical properties of the interfaces. The chapter will show some of these methods, with a focus on the mostly used ones: capacitance-voltage and corona charges measurements. The second harmonic generation (SHG) tool, that is the heart of the thesis, will be quickly introduced. The last section of the chapter explains the aim of the thesis.

Contents of chapter 1

1.1 Dielectric materials on silicon

Dielectrics are one of the critical layers in microelectronic devices such as metal-oxide-semiconductor field-effect transistors (MOSFET), thanks to their excellent insulating and capacitive properties. They are also used for passivation in solar cells and image sensors thanks to improvements that they can bring to the physical structure of the interface and thus to the device itself.

Since the mid-1960s, silicon is the predominant semiconductor material. One of the reasons lies in the possibility to fabricate very good quality silicon dioxide (SiO_2) on the top of Si, which enables fabrication of high performance devices. Its large band gap (~9 eV) provides a large conduction and valence band offset with Si. In addition, SiO_2 has low level of electronic defects because of its amorphous structure, which can offer a good interface with Si. These exceptional electrical properties of SiO_2 obviously pose a significant challenge to any other alternative gate oxide.

Referring to the last 40 years, MOSFET technology has been able to keep pace with Moore's law of scaling of devices associated with lowering power consumption and performance improvements. Moore's law predicts an exponential increase in the number of devices in an integrated circuit [1]. Each year, the size of these devices was decreased in order to integrate the greatest possible number of transistors on a chip, allowing for higher integrated circuits speed, while reducing the cost and the power consumption. However, this scaling is limited because the extreme reduction of the gate oxide thickness (SiO_2) in MOSFETs results in large leakage current because of direct tunneling of electrons through the SiO_2 layer. As a result, the power dissipation increases to an unacceptable values and limits device performance and reliability [2], [3]. This problem can be solved by replacing the SiO_2 with an alternative gate oxide.

The field effect transistors are capacitance-operated devices, i.e. the source drain current depends on the gate oxide capacitance C_{ox} (in F/m^2), which in turn is proportional to the dielectric constant k and inversely proportional to the oxide thickness t_{ox} [4]:

$$C_{ox} = \frac{\varepsilon_0 k}{t_{ox}} \tag{1.1}$$

With ε_0 is the vacuum permittivity.

Hence, a thicker dielectric layer with a higher k can replace SiO_2, while maintaining the same capacitance and reducing the leakage current, as shown in Figure 1.1.

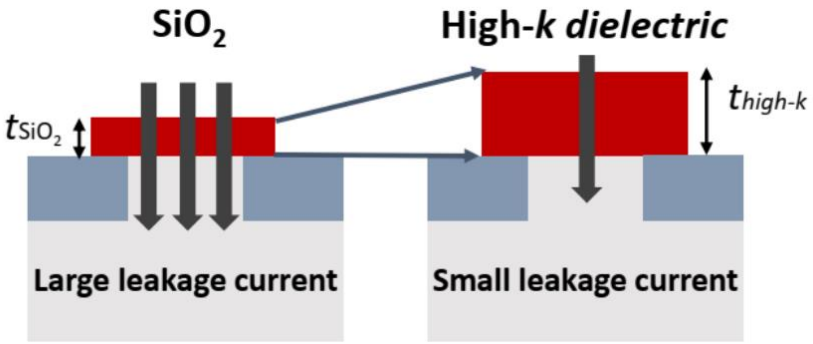

Figure 1.1: *Schematic showing that the use of high-k dielectric reduces the tunnel leakage current in devices while keeping the same C_{ox}. Figure taken from [5].*

High-k dielectrics have also proven useful in passivation for photovoltaic and image sensor applications, as they improve their efficiency. Figure 1.2 shows the structure of conventional (a) and innovative (b) solar cells. The rear of the conventional back surface field solar cell can be replaced with the passivated rear of p-type c-Si with dielectric layer. This process improves the surface quality due to the reduction of recombination losses. As a result, the dielectric passivation can improve the solar cells efficiency [6]. Our research work addresses the characterization of interfaces between dielectric layers and Si substrates. So, in the following section, we will discuss surface defects that cause surface recombination and the passivation mechanisms that reduce this recombination. We also give the most commonly materials used for passivation.

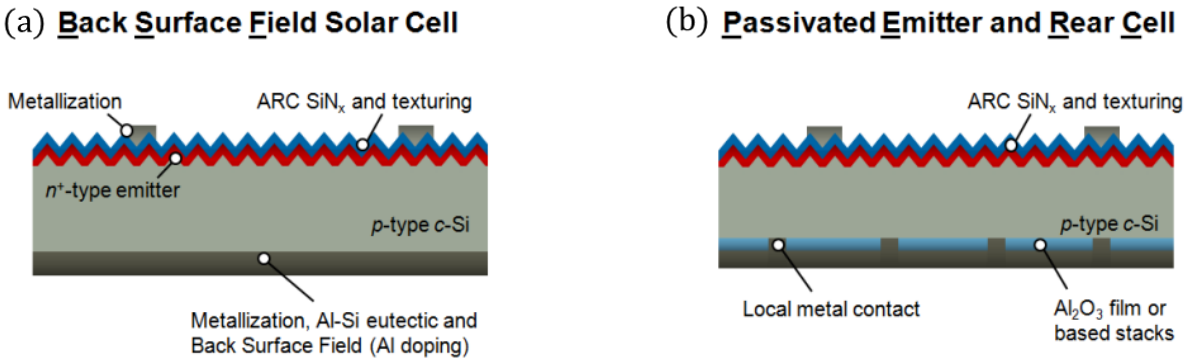

Figure 1.2: *Schematic of* ***(a)*** *conventional p-type c-Si solar cells and* ***(b)*** *innovative solar cell design with a passivation layer. A dielectric passivation layer is also located at the rear of the solar cell. Figure taken from [7].*

1.2 Silicon surface passivation

The silicon surface contains a large number of defects that can cause recombination losses in materials and affect the performance of silicon-based devices. In this section, we describe the interface defects and their origin (section 1.2.1), the recombination mechanisms resulting from the presence of these defects (section 1.2.2), the two passivation mechanisms (section 1.2.3 and 1.2.4) that allow to reduce these defects and some of the materials used for surface passivation (section 1.2.5).

1.2.1 Surface and interface defects

After the deposition of a passivation layer, the silicon surface becomes an interface and may exhibit new types of defects. Among these defects, dangling bonds can appear at silicon surface with or without passivation and are caused by crystal lattice interruption. For the Si(100) oriented material, on which we focused during this thesis, there are two centers of dangling bonds depending on their configuration, as shown in Figure 1.3 [8]:

- P_{b0} which is attributed to trivalent silicon atoms ($Si_3{\equiv}Si\bullet$).
- P_{b1} which is partially oxidized and corresponds to $Si_2O{\equiv}Si\bullet$.

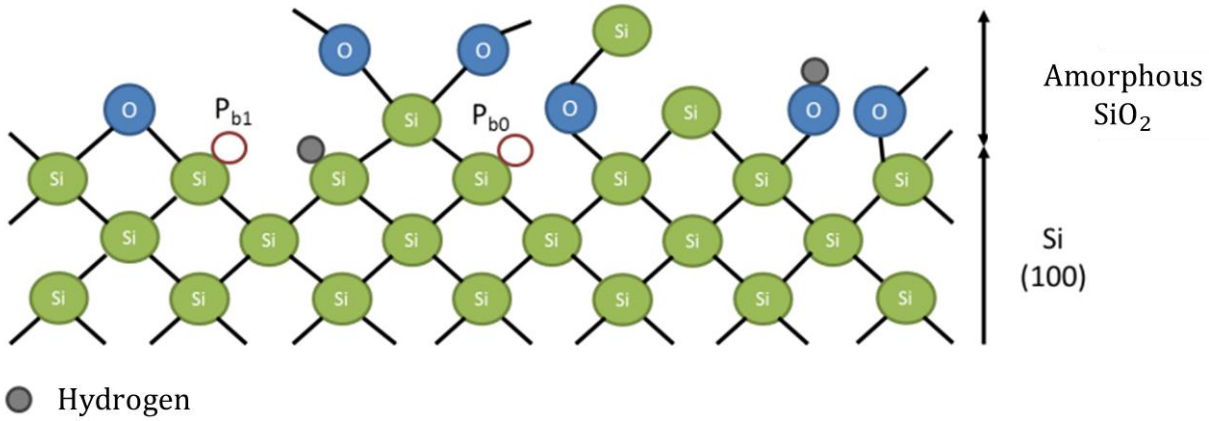

Figure 1.3: *Types of dangling bonds in silicon (100). Figure taken from [9].*

These centers are considered to be amphoteric, which means that their charges can be positive, negative, or neutral depending on the occupancy rate of the dangling orbital [10]. Figure 1.4 shows the energy distribution of the dangling bonds and the interface traps D_{it} for a SiO_2/Si structure determined by electron paramagnetic resonance (EPR) and

capacitance-voltage measurements, respectively. In this figure, the nonbonded orbitals of the two P_b centers have two energy levels in the silicon gap, one located at E_v+0.2 eV and behaving like acceptors, and other at E_c-0.2 eV, acting as donors. The correlation between dangling bonds density and interface states density indicates that the dangling bonds are the main source of interface states. The existence of these defects increases the recombination rate of minority carriers, as we will show the relationship between them in the next section.

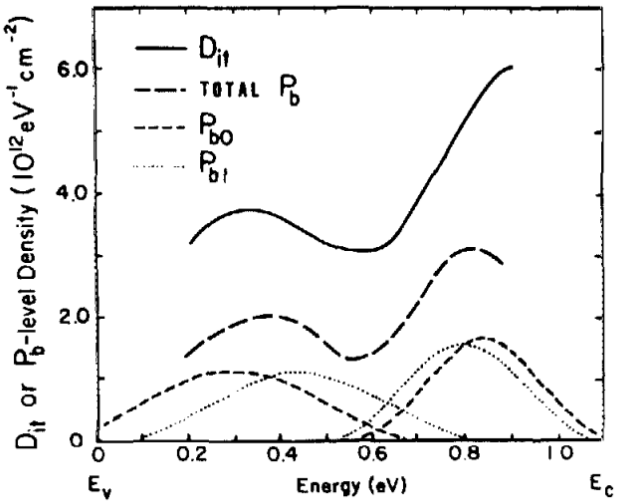

Figure 1.4: *Interface state density and P_{b0}, P_{b1} defect centers distribution in silicon (100). Figure taken from [8].*

1.2.2 Surface recombination mechanism

Generally, there are several bulk recombination processes (radiative, Auger and Schockley-Read-Hall) in semiconductor materials [11]. In our study, we are interested in the recombination occurring at the surface of material. As described above, the silicon surface has a strong discontinuity in its crystal lattice, increasing the probability of charge carrier recombination at the surface. According to Shockley, Read and Hall, the recombination rate U_s is described as [12]:

$$U_s = v_{th} N_{it} \frac{n_s p_s}{\frac{n_s}{\sigma_p} + \frac{p_s}{\sigma_n}} \tag{1.2}$$

Where n_s and p_s (cm^{-2}) are the density of electrons and holes at silicon surface respectively. v_{th} is the thermal velocity of charge carriers and $\sigma_{n/p}$ is the electrons/holes capture cross-section. N_{it} is the surface/interface traps density (cm^{-2}). N_{it} is assumed to be

energy independent, considering that the defect is located in the middle of the silicon gap. Indeed, the interface defects are distributed in the whole gap at different energy levels, so, N_{it} can be replaced by D_{it} ($eV^{-1}cm^{-2}$).

Given this equation, carrier recombination can be decreased in two ways: either by reducing defect density D_{it}, which can be done by a so-called chemical passivation, or by minimizing the carrier concentration (n_s or p_s) at the surface, which can be accomplished through a field effect passivation. These two mechanisms will be explained in the next sections.

1.2.3 Chemical passivation

In chemical passivation, the dangling bonds are filled with external elements. A native chemical passivation of silicon can be obtained through SiO_2 that forms in the ambient air. However, a very high density of interface defects remains after this native oxidation. Instead of the native oxide, growing thermal SiO_2, followed by an annealing step in the presence of hydrogen can reduce the density of interface states, thanks to the reactions between the surface dangling bonds and the hydrogen which fills the majority of them (Figure 1.5). This kind of passivation is excellent but in addition to being expensive, it modifies the layers already existing in the wafers because of the high temperature used. Thus, SiO_2 has been replaced by high-k dielectrics which can be deposited at relatively low temperature (<400°C). These materials provide good surface and volume passivation by reducing the interface traps and, consequently, the probability of surface carrier recombination.

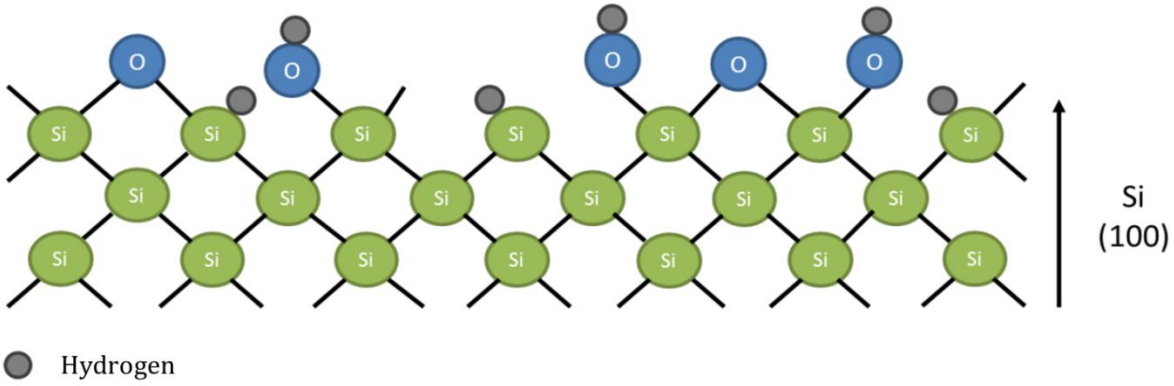

Figure 1.5: *The process of chemical passivation involves filling dangling bonds with external elements such as hydrogen atoms. Figure taken from [9].*

1.2.4 Field-effect passivation

For this passivation mechanism (complementary with the previous one), the electrical activity of the remaining interface defects is reduced. More specifically, the deposition of a high-k dielectric layer that contains a large number of fixed charges (Q_f or Q_{ox}) induces a "static" electric field in the semiconductor at the interface. Due to the influence of this field, the electrons are repelled from the silicon surface, reducing recombination between them and the remaining defects, shown in Figure 1.7.

In general, the oxide charges are distributed between its volume, its interfaces with the metallic contact and the semiconductor as illustrated in Figure 1.6 [13]. The quantity and nature of these charges depend on the oxide type, the interface elements and the deposition technique.

- Q_{sc} are the charges at the semiconductor surface.
- Q_{it} and Q_{ox} charges are mentioned above as the interface trapped charges and the fixed oxide charges, respectively.
- Q_{ot} are the oxide trapped charges and are produced by trapped holes or electrons in the oxide.
- Q_m are localized in the oxide volume, correspond to the oxide mobile charges, which come from ionized impurities such as metallic contamination or from elements present in the precursors, such as sodium or hydrogen.

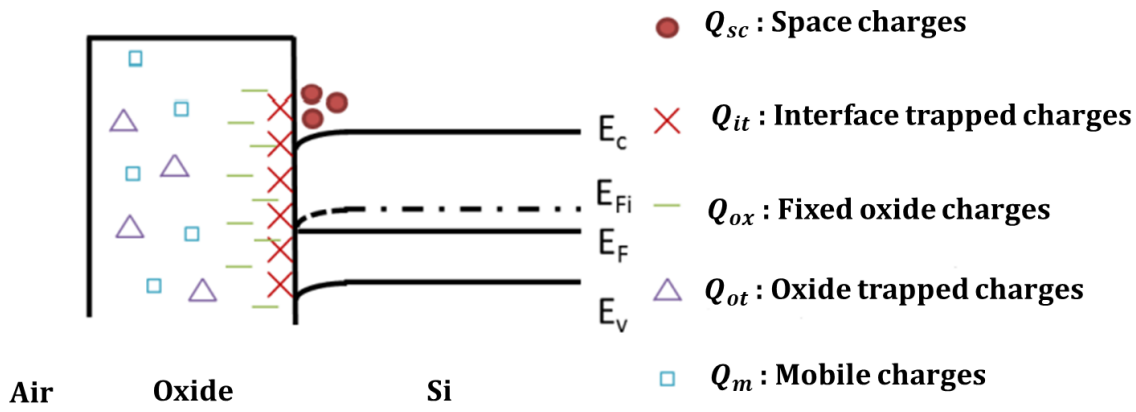

Figure 1.6: *Charges distribution in oxide on p-type silicon system. Figure taken from [9].*

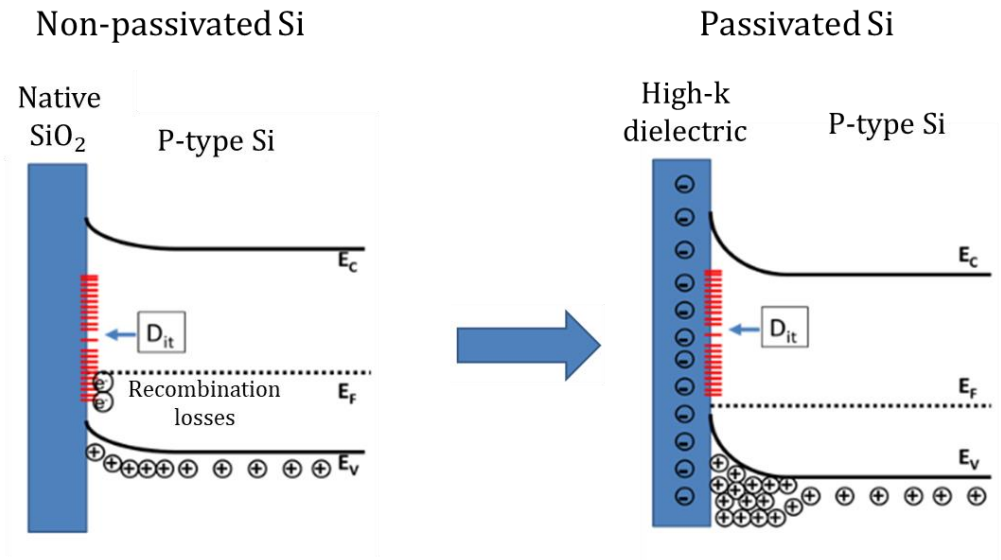

Figure 1.7: *Field effect passivation of p-type Si surface. Figure taken from [14].*

1.2.5 Passivation materials

The material used for surface passivation must meet several criteria. Most importantly, it should reduce the trapping by surface defects, either by reducing their number or by repelling carriers away from the surface. For image sensors or solar cells applications, the surface is exposed to illumination, so the passivation material used must be transparent with the lowest possible absorption coefficient. It must not be modified during the next fabrication steps of the devices. The dielectrics with a relative permittivity greater than 9, such as Al_2O_3, HfO_2, ZrO_2, Y_2O_3, and various lanthanides, satisfy these requirements [15]. However, there is a trade-off between the dielectric constant and the band gap, since higher *k* values are accompanied by lower band gaps. Thus, the choice of dielectric materials depends on the substrate type and the desired application. In this thesis, we focused on the passivation with Al_2O_3 and we studied briefly HfO_2, so we will give more details on these two materials in the next subsections.

A. Passivation with Al_2O_3

Alumina (Al_2O_3) has shown interesting properties for the silicon passivation, in particular for applications in image sensors [16]. It allows both chemical and field effect passivation. Alumina is generally deposited by thermal atomic layer deposition (ALD) from the precursor TriMethylAluminium ($Al(CH_3)_3$), abbreviated TMA, using various reactants such as water (H_2O), ozone (O_3), and so on [17], [18]. The chemical passivation is attributed to the diffusion of hydrogen atoms from towards the interface with the silicon [19]. Additionally, the presence of high fixed negative charge density close to the Al_2O_3/Si

interface induces field effect passivation [20]. Regardless of the surface preparation, the presence of a thin SiO_x interfacial layer has been demonstrated in the literature as shown in Figure 1.8 [21]. An annealing step enables the organization of the interface between Al_2O_3 and Si as illustrated in Figure 1.8a and induces an increase in the SiO_2 layer thickness. This step is critical to reduce the difficulty of measuring the fixed charge density, since the lower thickness of SiO_2 allows electrons tunneling into defect states at the SiO_2/Al_2O_3 interface during measurements [22]. Annealing can also vary the effective charge density, either increasing [23] or decreasing it [24].

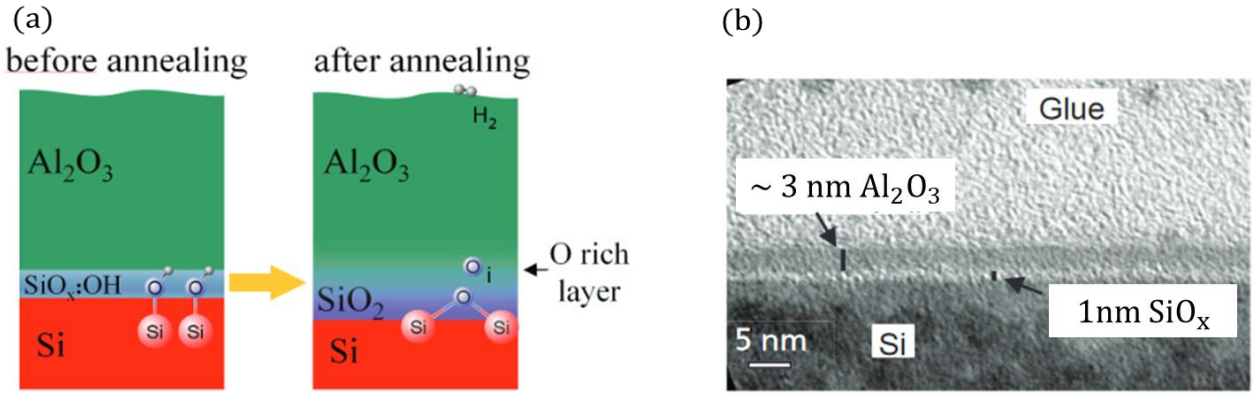

Figure 1.8: (a) *Reorganization of Al_2O_3/Si interface by annealing.* ***(b)*** *Transmission electron microscopy (TEM) image of the interface. Figure taken from [21].*

B. Passivation with HfO_2

Although hafnium oxide (HfO_2) has not been used as frequently as alumina as a passivation layer, its higher optical refractive index makes it ideal as anti-reflective coating [14]. HfO_2 is generally deposited by ALD from $HfCl_4$ or TEMAH (TriEthylMethylAmide Hafnium) precursors [25]. As in the case of alumina, the reactants used for deposition are H_2O, O_3, etc. For passivation, HfO_2 contains hydrogen which enhances chemical passivation. It can contain also fixed negative [26] or positive [27] charges, depending on the deposition conditions. First, it was shown by Dingemans et al. [28] that the passivation properties of HfO_2 are lower than those of Al_2O_3, giving a much higher recombination rate but an annealing step can improve the passivation. Then, several studies have shown that passivation with HfO_2 presents similar levels of passivation as Al_2O_3 [26], [27]. More recently, Cheng et al. [29] underlined the importance of surface preparation before deposition for better passivation. Therefore, HfO_2 can provide good passivation quality, with low D_{it} and high Q_{ox}. Regardless of the choice of the passivation material, electrical characterization methods are needed in order to quantify and compare various passivation schemes. The next section will give a quick overview of the main characterization methods.

1.3 Characterization techniques for passivation

Generally, the characterization of passivation quality consists in measuring the interface defect density (D_{it}), which must be as low as possible, the fixed charge density (Q_{ox}) or the effective minority carrier lifetime, which must be as high as possible. In this thesis, we focus on the D_{it} and Q_{ox} study using the second harmonic generation [30]. However, several conventional techniques (i.e. C-V, surface photovoltage (SPV) such as COCOS and KPFM) have been successful in this type of characterization. In the following sections, we explain the principle of these techniques.

1.3.1 Capacitance-voltage (C-V)

Capacitance-Voltage (C-V) method is widely used to determine parameters such as oxide thickness, oxide charges, mobile ions (contamination) and interface trap density in MOS capacitors [13]. It consists in creating Metal-Oxide-Semiconductor (MOS) capacitor structures and subjecting them to C-V measurements. C-V measurement involves the application of DC and small ac voltages on the gate while making measurements (Figure 1.9). In general, the ac frequencies used for measurements are between 10 kHz and 1 MHz. The DC part (bias voltage) allows driving the device into different regimes. For example, for a p-type Si substrate, the bias sweep from negative to positive DC voltage induces successively accumulation, depletion and inversion regimes for the MOS capacitor structure.

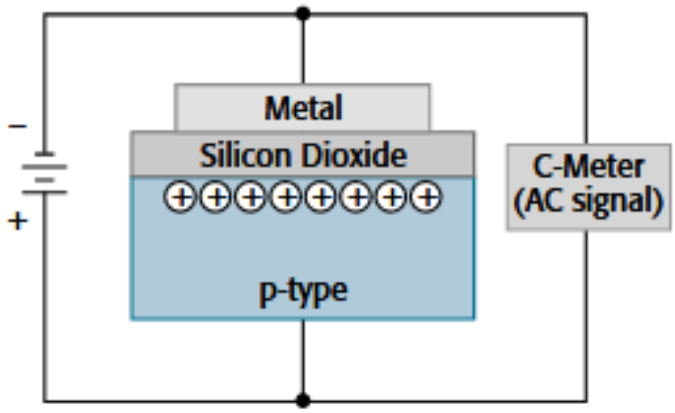

Figure 1.9: *C-V measurement circuit for MOS capacitors on a p-type substrate. Figure taken from [31].*

The total impedance measured during C-V is complex and the separation between real and imaginary parts leads to the extraction of conductive and capacitive terms, respectively. This is done mainly using a parallel model, as shown in Figure 1.10.

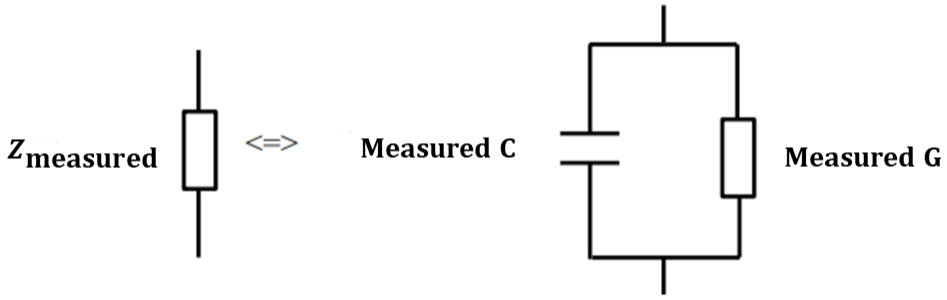

Figure 1.10: *Equivalent circuit of MOS structure for capacitance and conductance measurements. Figure taken from [9].*

The Figure 1.11 shows an example of total capacitance of the MOS capacitance (C) versus gate voltage V_g curves at high and low frequency for p-type semiconductor [9]. Both curves exhibit three regimes: accumulation, depletion and inversion. The names of these regimes are derived from the type of charge carriers present at the semiconductor surface. Figure 1.12 shows the equivalent electrical scheme for each regime with a p-type semiconductor.

In a simplified model, the C consists of the oxide capacitance, C_{ox}, in series with the semiconductor capacitance, C_{sc}:

$$\frac{1}{C} = \frac{1}{C_{ox}} + \frac{1}{C_{sc}} \tag{1.3}$$

More specifically this expression should be adapted for each regime as explained next (assuming a p-type semiconductor).

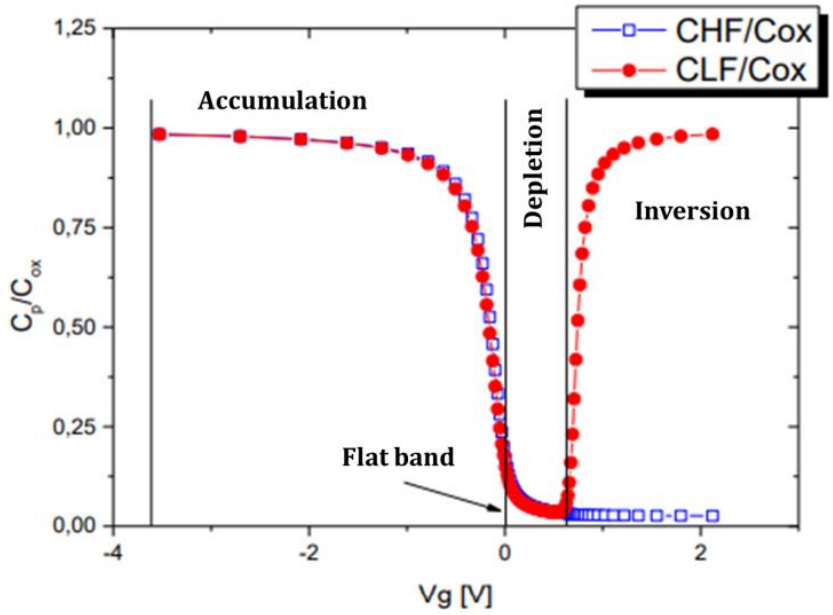

Figure 1.11: *Normalized C-V curve at high (C_{HF}) and low (C_{LF}) frequency for p-type semiconductor. Figure taken from [9].*

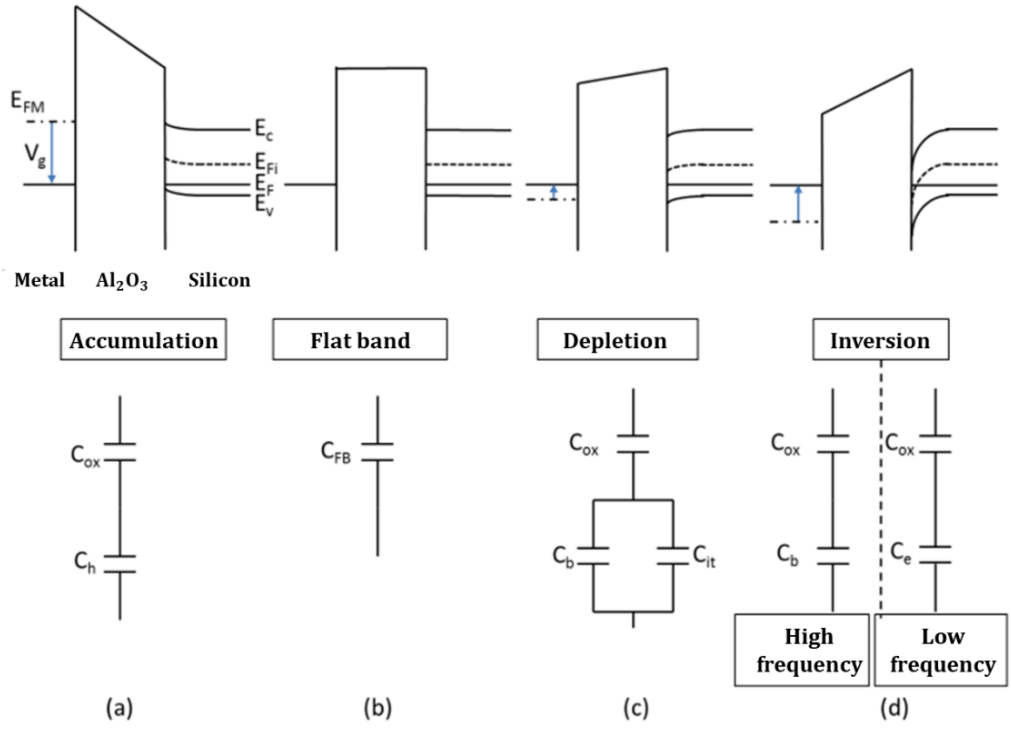

Figure 1.12: *Different capacitance regimes. Figure taken from [9].*

- **Accumulation regime**

The bias voltage is negative in this instance (Figure 1.12a), i.e. the negative charges are present on the metal "plate". The positive charges induced in the semiconductor plate are the holes, which are the majority carriers in this case. The regime corresponds to an accumulation of the majority carriers. A band bending appears to bring the valence band level closer to the Fermi level. Consequently, the hole capacitance (C_h) is very high and the structure can be modeled as a plane capacitor associated to C_{ox} only according to eq. (1.3).

- **Flat band regime**

By increasing the bias voltage, the band bending attenuates until it vanishes at V_{FB} (flat band voltage)(Figure 1.12b). At this point, the carrier concentrations at the surface are the same as in the volume. For an ideal MOS capacitor, $V_{FB}=0$. In a MOS where the work functions are different and the oxide contains fixed charges or defects at the interfaces, V_{FB} will not be equal to zero anymore.

- **Depletion regime**

For a positive applied bias voltage, the majority carriers (holes) are repelled from the semiconductor-oxide interface and the band bending is inverted. In this case, ionized acceptor impurities form a depleted space charge region (SCR) in which free carriers are absent (or at least negligible). The equivalent capacitance here includes the capacitance of the oxide, as well as of the interface defects (C_{it}) and of the space charge zone (C_b) as shown in Figure 1.12c.

- **Inversion regime**

When the bias voltage applied is more positive, the hole density at the interface decreases while the minority carriers density increases. At a certain point, the band bending gives a surface potential equal to the Fermi potential; in this case, the number of electrons at the surface is the same as the number of holes in the volume. Beyond this voltage, the surface of the semiconductor is in inversion regime (Figure 1.12d), in which the minority carriers from the volume become the majority at the surface of the semiconductor.

As shown in Figure 1.12d, the equivalent model depends on the ac probe frequency. At low frequencies, the electrons (inversion charges) are able to follow the ac applied voltage. Thus, the electron capacitance (C_e) is very large (inversion charge has an exponential dependence of potential) and the equivalent circuit becomes the oxide capacitance again (C_{ox}). Additionally, the electrons could be trapped by the interface states responding at these frequencies. Therefore, the C-V curve could give information on interface traps. This will be used in chapter 4.

At high frequencies, the electrons (forming the inversion layer) are unable to follow the ac signal and the equivalent circuit is the oxide capacitance (C_{ox}) in series with the SCR capacitance C_b. Note that in general, the interface traps are assumed not to respond at these frequencies.

C-V is one of the measurements used during this thesis, because it provides direct access to the fixed charge density Q_{ox} and interface trapped charges D_{it}. Q_{ox} can be simply determined from the shift of the C-V curve with respect to a "theoretical" one. Various methods exist for the extraction of D_{it} starting from C-V measurements. The simplest one consists in comparing curves at HF and LF. The methodology details for extracting these electrical parameters using the C-V curves will be explained in detail and used in chapter 4.

1.3.2 Surface photovoltage (SPV) measurements

Surface photovoltage (SPV) is the light-induced change in the contact potential difference (V_{CPD}) at the surface of a photoactive material. In general, V_{CPD} parameter corresponds to the difference between the vacuum level of the measuring electrode and the sample surface. SPV signal can be produced by the separation of photo-generated charge carriers in the space charge region of a semiconductor, or the injection of charge carriers into an insulator. It is affected by processes such as light absorption, photogeneration, charge separation, charge transport, recombination, trapping, and charge carrier emission.

SPV signal corresponds to the difference between the surface potential measured under illumination (V_s^{ill}) and in the dark (V_s^{dark}). Figure 1.13a and b show the effect of light on the energy band diagrams for a surface in depletion and in accumulation, respectively. The electric field present in the SCR induces the migration of electrons (holes) towards the surface in the case of depletion (accumulation). The energy E is directed upwards, thus, the potential is oriented downwards. Therefore, the difference between V_s^{ill} and V_s^{dark} in depletion gives a negative SPV signal, while in accumulation it is positive. As a result, the sign of SPV signal gives the direction of charge separation. In flat band condition ($V_s^{dark} = V_{FB}$), the SPV signal is zero since there is no charge separation.

There is a wide variety of methods that use SPV measurement [32]. The choice of the method depends on the desired application. In the following subsections, we will focus on two of these methods used for characterization of passivation layers: Corona oxide characterization of semiconductors and Kelvin Probe Force Microscopy.

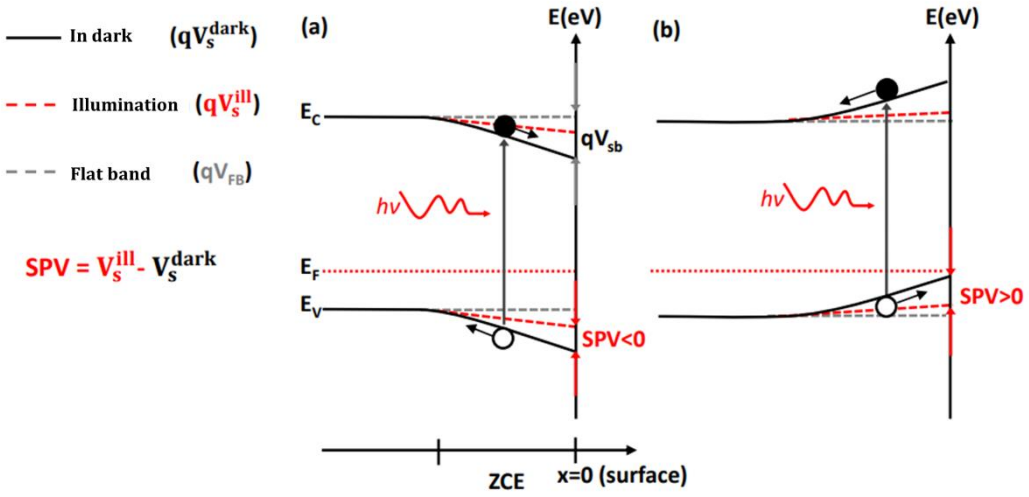

Figure 1.13: *Band diagram for a surface in* ***(a)*** *depletion and* ***(b)*** *accumulation. Figures taken from [33].*

1.3.3 Corona oxide characterization of semiconductor (COCOS)

Corona charge deposition measurement is a non-contact technique [34], used to evaluate defect and charge density in oxide/semiconductor structures. Corona charges are usually negative (CO^{-3}) or positive (H_3O^+) ions deposited onto the sample surface after applying a high DC voltage (in the order of 5 to 10 kV) across a corona wire, at atmospheric pressure. These ions do not pose any danger because their low mobility limits the oxide breakdown. The presence of these corona ions on the oxide in addition to the already existing charges in the structure modifies the surface potential at the semiconductor interface. The contact potential difference (V_{CPD}) is measured using a Kelvin probe, as illustrated in Figure 1.14a. This potential is measured in dark and also under illumination to eliminate the space charge region contribution. It gives the potential drop across the surface barrier ΔV_{SB} and across the oxide ΔV_{ox} as a function of the corona charge dose Q_c [34]:

$$\Delta V_{CPD}^{Dark} = \Delta V_{ox} + \Delta V_{SB}$$
$$\Delta V_{CPD}^{illumination} = \Delta V_{ox} \qquad (1.4)$$

Consequently, these two measurements can be used to calculate the initial potential barrier ΔV_{SB}.

$$\Delta V_{SB} = \Delta V_{CPD}^{Dark} - \Delta V_{CPD}^{illumination} \quad (1.5)$$

When this difference equals to zero, i.e $\Delta V_{SB} = 0$, the corresponding point represents the flat band voltage V_{FB}. Figure 1.14b shows the measured V_{CPD} in the dark and under illumination versus the quantity of deposited corona charges (Q_c). The value of Q_c necessary to reach the flat band condition corresponds to the total charges (Q_{tot}) in the oxide/semiconductor structure and that is "balanced" by Q_c:

$$Q_{tot} = Q_{surf} + Q_{it} + Q_{ox} + Q_m + Q_{ot} \quad (1.6)$$

Q_{surf} corresponds to any initial charges at the air-dielectric surface. Q_{it}, Q_{ox}, Q_m and Q_{ot} were defined in section 1.2.4.

ΔQ_c is the corona charge deposited between two consecutive measurement cycles. In order to respect the principle of charge neutrality, the incremental corona charge, ΔQ_c, is imaged by the space charge region charge (ΔQ_{sc}) and also by the interface traps charge (ΔQ_{it}).

$$\Delta Q_c = -(\Delta Q_{sc} + \Delta Q_{it}) \quad (1.7)$$

The interface state density, D_{it}, is calculated from the ratio:

$$D_{it} = \frac{\Delta Q_{it}}{\Delta V_{SB}} \quad (1.8)$$

Since the COCOS method is able to measure Q_{tot}, it is a powerful diagnostic tool to identify any sort of charge change that occurs in the dielectric layer during device fabrication. However, it does not give access to the exact value of Q_{ox} only, which is the main parameter associated to the field effect passivation. It also requires a surface cleaning step after the measurements to remove the deposited corona charges. This technique will appear later in this thesis, since it was used by our collaborators from STMicroelectronics to pre-characterize the samples analyzed during the thesis.

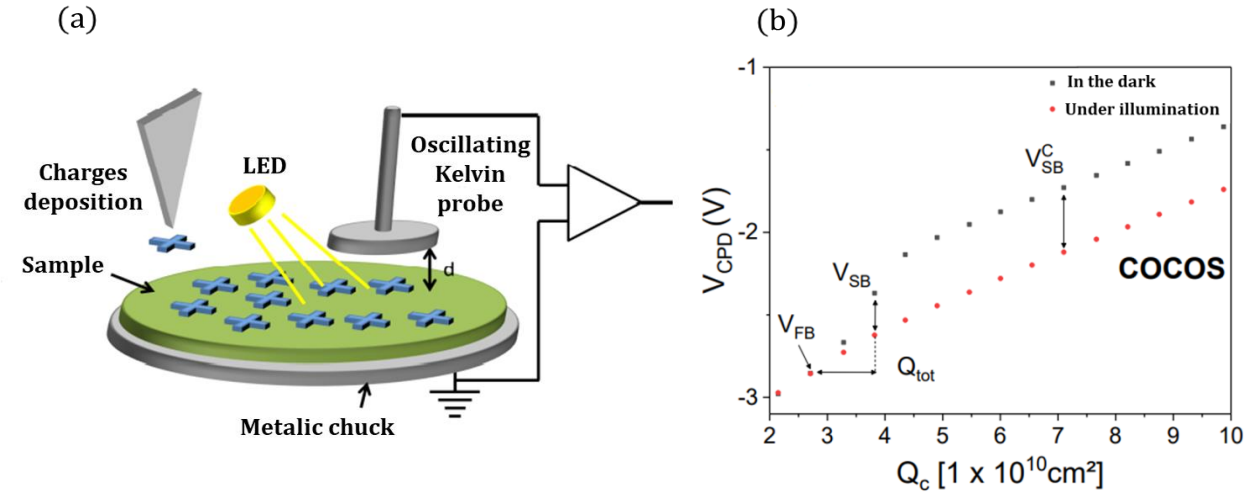

Figure 1.14: (a) *Corona charging principle* [9]. ***(b)*** *Measurement curve of V_{CPD} versus corona charge deposition in the dark and under illumination. Figure taken from [33].*

1.3.4 Kelvin Probe Force Microscopy (KPFM)

KPFM is another characterization technique for the passivation that uses the SPV signal; the V_{CPD} in this case is measured between an Atomic Force Microscopy (AFM) tip and the sample (Figure 1.15a). When conductive AFM tip is brought close enough to the sample surface to allow electron tunneling, an electrical force is generated between the tip and sample surface, due to the differences in their Fermi energy levels. This force gives access to the V_{CPD} between the tip and the sample. There are several methods to perform KPFM measurements such as Pump-probe KPFM (pp-KPFM), heterodyne KPFM, etc. For example, pp-KPFM is a time-resolved measure of surface potential; this technique works by exciting (pumping) the sample by illumination and measuring (probing) the excitation response over a reasonable time range, as shown in Figure 1.15b. Photoexcitation provokes charge generation in the semiconductor, which modifies the SPV measured by the KPFM probe. The time resolution is determined by the pump-probe time delay, which allows measuring the SPV response to the excitation at specific instants. This technique allows identifying the quality of chemical passivation by monitoring the trapping and detrapping mechanisms. It also allows determining the polarity of the interface traps. However, it is a very local measurement because the AFM tip size is only a few tens of nanometers. Therefore, characterizing an entire wafer with pp-KPFM measurements would be very time consuming. This disadvantage is resolved by Aubriet et al. [33] who propose replacing the surface potential measurement by KPFM with a Kelvin probe (KP) approach.

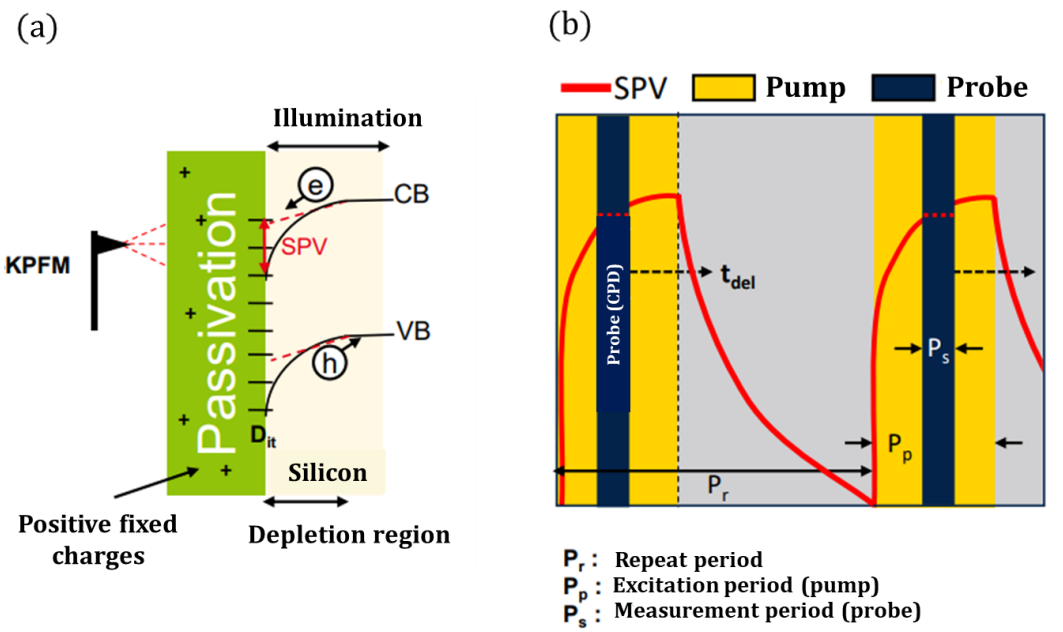

Figure 1.15: (a) *KPFM measurement principle.* ***(b)*** *pp-KPFM approach. Figures taken from [33].*

1.4 Second harmonic generation characterization

Apart from the techniques described above, Second Harmonic Generation (SHG) has gained significant recognition for its ability to probe properties of the surfaces and interfaces [35], [36]. This technique offers several advantages over conventional methods in the study of buried interfaces:

- It avoids material damage and supplementary steps for the fabrication of a particular measurement structure (such as MOS capacitors) or by "contamination" associated with charged particle deposited (as in COCOS).

- It is fast and can be performed on the entire wafer.

- Buried interfaces could be accessible thanks to a quite large penetration depth of the optical radiation. For example, for $\lambda_{SH} = 390$ nm in Si, the penetration depth is of 133 nm.

This method is the heart of the thesis, so we will give more details in the next sections in order to better explain the aim of our work.

1.4.1 SHG principle

From a material point of view, the valence electrons are linked to their ionic nuclei and their "heart" electrons. When an external electric field is applied on the material, the electrons are slightly displaced from their initial positions, while the ions remain fixed. This creates a dipole and induces polarization in the material. If the excitation electric field is oscillating, the dipole is also oscillating and it emits an electromagnetic wave. Light can play this excitation role.

In conventional optics, when the material is subjected to a luminous electric field E of low amplitude, the resulting electric dipole oscillates and emits radiation at the same incidence oscillation. The polarization induced is linearly proportional to the external excitation electric field. The proportionality constant is the electrical susceptibility of the material $\chi^{(1)}$. The relation between the linear polarization P and the electric field E is given by:

$$P = \epsilon_0 \chi^{(1)} E \tag{1.9}$$

Where ϵ_0 is the vacuum permittivity. The polarization of the material in turn gives rise to a radiated electric field. In the linear case described by equation (1.9), the interplay between the electric field caused by the polarization P and the exciting electric field E modifies the propagation of light, which is described by the refractive index and absorption coefficient of the material. These quantities do not depend on the amplitude of the applied electric field.

The nonlinear optics is now a wide research field, which emerged following the demonstration of second harmonic generation by Peter Franken et al. in 1961. This demonstration took place a year after the discovery of the laser [37], which is practically the only light source able to trigger observable optical non-linear effects. The first experiment was carried out on a quartz crystal that interacted with a ruby laser ($\lambda = 694.3$ nm) to generate light at doubled incident frequency. High intensity light leads to dipoles oscillating with large excursions, which changes the optical properties of the material and introduces nonlinear phenomena. The polarization vector can then be described by a power series expansion of the excitation field strength [36]:

$$\begin{aligned} P &= \epsilon_0 \chi^{(1)} E(\omega) + \epsilon_0 \chi^{(2)} E^2(\omega) + \epsilon_0 \chi^{(3)} E^3(\omega) + \cdots \\ &= P^{(1)} + P^{(2)} + P^{(3)} + \cdots \end{aligned} \tag{1.10}$$

Where $\chi^{(n)}$ is the nonlinear susceptibility of order "n" of the material. $\chi^{(n)}$ is a tensor of rank n+1 [38]. The second harmonic generation (SHG) is induced by the second order

nonlinear polarization $P^{(2)}$. The SHG response is measured by its intensity, which is proportional to the square of the second-order polarization [39].

$$I_{2\omega} \sim \left| P^{(2)}(2\omega) \right|^2 = \left| \epsilon_0 \chi^{(2)} \right|^2 \left| E(\omega) \right|^4 \tag{1.11}$$

SHG principle is illustrated schematically in Figure 1.16a, where a laser beam of frequency ω interacts with a nonlinear material and generates the second harmonic beam at a frequency 2ω. From a quantum mechanical point of view (Figure 1.16b), two photons of the same frequency ω are combined to create a photon with frequency 2ω. The atomic ground state is represented by the solid horizontal line and the virtual states by the dashed lines.

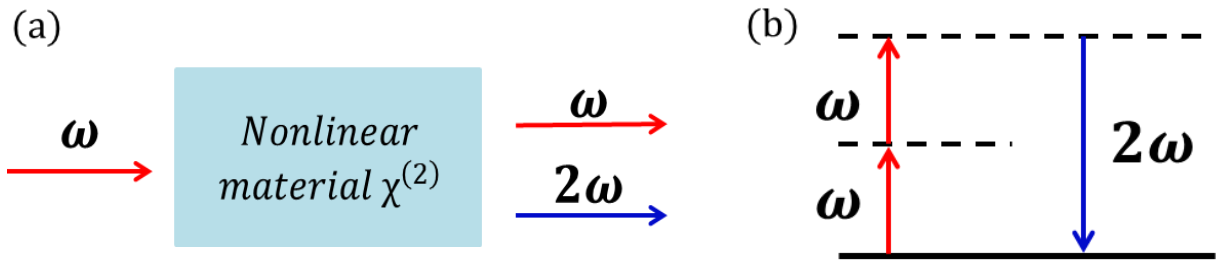

Figure 1.16: (a) *Second harmonic generation principle.* ***(b)*** *Energy levels of electron involved in the creation of second harmonic generation [39].*

1.4.2 SHG for centrosymmetric materials

One of the main issues in surface nonlinear optics is the question about nonlinear polarization components in a restricted environment. For example, in non-centrosymmetric media that have no inversion symmetry center, the main nonlinear response is generated by the nonlinear polarization of the bulk dipole and is only little sensitive to the presence of the surface/interface.

However, the situation is fundamentally different with centrosymmetric media, where the electric field and polarization vectors are invariant under the inversion of the coordinate system. This means that by inverting $r \rightarrow -r$, the electric vector and polarization vector will also be inverted as $E \rightarrow -E$ and $P^{(2)} \rightarrow -P^{(2)}$. Due to the inversion symmetry, the properties do not change with the change in sign:

$$\begin{aligned} -P^{(2)} &= P^{(2)} \\ \Rightarrow -\epsilon_0\,\chi^{(2)}(-E)(-E) &= \epsilon_0\,\chi^{(2)}EE \end{aligned} \tag{1.12}$$

Obviously, this equality is only possible if the second order susceptibility is equal to zero:

$$\chi^{(2)}_{Bulk} = 0 \tag{1.13}$$

Thus, for the centrosymmetric materials, the SHG from the bulk material is forbidden within electric dipole approximation. Many materials as silicon dioxide (SiO_2), high-k dielectrics (alumina Al_2O_3, hafnium dioxide HfO_2, etc.), and crystalline silicon, of interest for applications are centrosymmetric. However at the surfaces of the materials, the symmetry is broken, so the surface susceptibility $\chi^{(2)}_{surf}$ is present and can give a dominant dipole contribution:

$$P^S(2\omega) = \epsilon_0\chi^{(2)}_{surf}\,E^2(\omega) \tag{1.14}$$

1.4.3 Electric field induced second harmonic (EFISH) phenomenon

Another factor that breaks the inversion symmetry and allows an electric dipole contribution is the existence of a DC electric field (E_{DC}) at interfaces. E_{DC} can be created by an external bias signal, by fixed charges in dielectrics and by the charged surface states [40]. This phenomenon, known as electric field-induced second harmonic (EFISH), induces the dependence of the SHG on the third-order susceptibility ($\chi^{(3)}$) of the material. EFISH was firstly-observed by C. H. Lee et al. in 1967 [41], who evidenced a quadratic dependence of the SHG on the applied voltage in both p- and n-type of silicon. This quadratic response is related to the EFISH, as described in [40]:

$$P^{EFISH}(2\omega) = \epsilon_0\chi^{(3)}\,E_{DC}\,E^2(\omega) \tag{1.15}$$

In silicon, E_{DC} is present in the space charge region (SCR) and is oriented perpendicular to the interface.

The full SHG intensity for dielectric on semiconductor structures containing only centrosymmetric materials can be expressed as [42]:

$$I_{2\omega} = \left|\epsilon_0[\chi^{(2)}_{surf} + \chi^{(3)}\, E_{DC}(t)]\right|^2 (I_\omega)^2 \quad (1.16)$$

With E_{DC} being the interface "static" electric field, created by the fixed oxide charges presented near the oxide/semicondutor interface, by the interface traps, etc. Therefore, SHG can provide access to the interface parameters. The aim of the thesis is to exploit this phenomenon simply described by eq. (1.16) in order to characterize electrical properties of interfaces. One of our focuses will be to discriminate the $\chi^{(2)}$ term from the $\chi^{(3)}\, E_{DC}$ term in equation (1.16) in order to extract information about the fixed oxide charge Q_{ox} and trap density D_{it} of a given interface in a possibly complex semiconductor/dielectric stack.

1.5 Thesis aim and methodology

This chapter covered some techniques used to characterize the quality of passivation: C-V and SPV measurements such as COCOS and KPFM. In theory, these techniques should comply to the requirements specified in the first column of Table 1.1, but in practice, each of them has advantages and difficulties. Although C-V is used to determine interface properties, it can only be applied on MOS capacitors, thus it necessitates fabrication of specific test structures and does not work at full wafer level. COCOS measurement is nondestructive and works at wafer level, but it provides the total charge values and not the fixed oxide charges. Additionally, it charges the surface. KPFM mainly quantifies the chemical passivation (D_{it}). Since none of these techniques responds to all criteria, there is room to propose and develop other measurement methods. In this context, during the thesis, we focused on another technique based on the SHG. Its feasibility in probing surfaces and interfaces has been proven by a large number of results for many years [35] on various materials, geometries and conditions. However, it is not obvious to generalize the approach. The new aspect in this thesis is that we take a step forward to the calibration of this technique in order to characterize the field effect passivation. We also investigate the effect of chemical passivation.

Table 1.1: *Passivation characterization techniques: advantages (+) and difficulties (-).*

	C-V	COCOS	pp-KPFM	SHG
Specific test structure	-	+	+	+
Non-destructive	-	+	+	+
Full wafer measurement	-	+	-	+
Q_{ox} extraction	Direct	Indirect	-	To be calibrated
D_{it} extraction	Direct	Direct	Qualitative	To be calibrated

The thesis was done in the frame of the Nano2022 project, supported by STMicroelectronics. As part of our collaboration, we received several samples of silicon passivated by various dielectric layers, such as Al_2O_3/Si(100) and HfO_2/Si(100) [33]. The interface quality of these samples was investigated by several techniques in order to calibrate SHG for the extraction of Q_{ox} and the estimation of D_{it} values.

Figure 1.17 explains the methodology followed in the thesis. The SHG calibration combines both experimental and numerical studies. The numerical approach is carried out by a simulation code developed in our group, which was improved during this thesis.

Secondly, in order to explain the SHG response and to validate the SHG calibration curves, we used results from other complementary methods, such as:

- COCOS characterization on the same samples at STMicroelectronics [33].
- Capacitance-voltage (C-V), which we carried out at IMEP-LAHC.

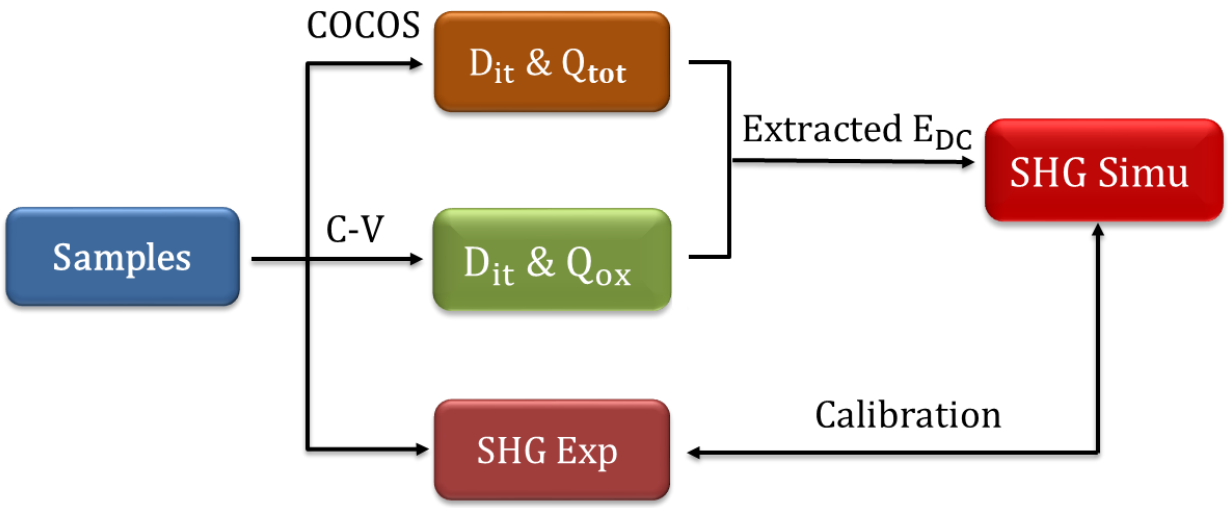

Figure 1.17: *Thesis methodology/approach.*

To better present the relationship between the electrical parameters (D_{it} and Q_{ox}) and the SHG response, the following chapter presents some literature results on this topic with a focus on the identification of interface quality for single and multilayer dielectric/semiconductor structures.

1.6 Chapter references

[1] G. E. Moore, 'Cramming more components onto integrated circuits', Proc. IEEE, vol. 86, no. 1, pp. 82–85, 1998.
[2] J. Robertson, 'High dielectric constant gate oxides for metal oxide Si transistors', Rep. Prog. Phys., vol. 69, no. 2, p. 327, 2005.
[3] S.-H. Lo, D. A. Buchanan, and Y. Taur, 'Modeling and characterization of quantization, polysilicon depletion, and direct tunneling effects in MOSFETs with ultrathin oxides', IBM J. Res. Dev., vol. 43, no. 3, pp. 327–337, 1999.
[4] R. M. Wallace and G. D. Wilk, 'High-κ dielectric materials for microelectronics', Crit. Rev. Solid State Mater. Sci., vol. 28, no. 4, pp. 231–285, 2003.
[5] S. N. Supardan, Study of High-k Dielectrics and their Interfaces on Semiconductors for Device Applications. The University of Liverpool (United Kingdom), 2019.
[6] J. Schmidt et al., 'Surface passivation of silicon solar cells using industrially relevant Al2O3 deposition techniques', Photovolt. Int., vol. 10, pp. 52–57, 2010.
[7] S. Bordihn, 'Surface passivation by Al2O3-based film stacks for Si solar cells', PhD Thesis, Doctoral dissertation, Technische Universiteit Eindhoven, 2014.
[8] G. J. Gerardi, E. H. Poindexter, P. J. Caplan, and N. M. Johnson, 'Interface traps and Pb centers in oxidized (100) silicon wafers', Appl. Phys. Lett., vol. 49, no. 6, pp. 348–350, 1986.
[9] M. Pawlik, 'Etude de la passivation de surface du silicium cristallin type P par dépôt de couches atomiques d'alumine pour application aux cellules solaires à haut rendement', PhD Thesis, Ecole centrale de Lille, 2015.
[10] N. M. Johnson, D. K. Biegelsen, M. D. Moyer, S. T. Chang, E. H. Poindexter, and P. J. Caplan, 'Characteristic electronic defects at the Si-SiO_2 interface', Appl. Phys. Lett., vol. 43, no. 6, pp. 563–565, 1983.
[11] G. P. Agrawal, N. K. Dutta, G. P. Agrawal, and N. K. Dutta, 'Recombination mechanisms in semiconductors', Semicond. Lasers, pp. 74–146, 1993.
[12] D. Blanc-Pelissier and N. Schneider, 'ALD pour les cellules photovoltaïques', Tech. Ing., 2016.
[13] D. K. Schroder, Semiconductor material and device characterization. John Wiley & Sons, 2015.
[14] E. Oudot, 'Oxydes métalliques pour la passivation de l'interface Si/SiO_2 des capteurs d'images CMOS', PhD Thesis, Université Grenoble Alpes (ComUE), 2018.
[15] J. Robertson, 'Band offsets of wide-band-gap oxides and implications for future electronic devices', J. Vac. Sci. Technol. B Microelectron. Nanometer Struct. Process. Meas. Phenom., vol. 18, no. 3, pp. 1785–1791, 2000.
[16] G. Dingemans and W. M. M. Kessels, 'Status and prospects of Al2O3-based surface passivation schemes for silicon solar cells', J. Vac. Sci. Technol. Vac. Surf. Films, vol. 30, no. 4, p. 040802, 2012.
[17] R. L. Puurunen, 'Surface chemistry of atomic layer deposition: A case study for the trimethylaluminum/water process', J. Appl. Phys., vol. 97, no. 12, p. 9, 2005.
[18] M. B. M. Mousa, C. J. Oldham, and G. N. Parsons, 'Atmospheric Pressure Atomic Layer Deposition of Al_2O_3 Using Trimethyl Aluminum and Ozone', Langmuir, vol. 30, no. 13, pp. 3741–3748, Apr. 2014, doi: 10.1021/la500796r.

[19] R. Kotipalli, R. Delamare, O. Poncelet, X. Tang, L. A. Francis, and D. Flandre, 'Passivation effects of atomic-layer-deposited aluminum oxide', EPJ Photovolt., vol. 4, p. 45107, 2013.
[20] B. Hoex, J. Schmidt, R. Bock, P. P. Altermatt, M. C. M. Van De Sanden, and W. M. M. Kessels, 'Excellent passivation of highly doped p-type Si surfaces by the negative-charge-dielectric Al_2O_3', Appl. Phys. Lett., vol. 91, no. 11, p. 112107, 2007.
[21] V. Naumann, M. Otto, R. B. Wehrspohn, M. Werner, and C. Hagendorf, 'Interface and material characterization of thin ALD-Al_2O_3 layers on crystalline silicon', Energy Procedia, vol. 27, pp. 312–318, 2012.
[22] N. M. Terlinden, G. Dingemans, V. Vandalon, R. Bosch, and W. M. M. Kessels, 'Influence of the SiO_2 interlayer thickness on the density and polarity of charges in Si/SiO_2/Al_2O_3 stacks as studied by optical second-harmonic generation', J. Appl. Phys., vol. 115, no. 3, p. 033708, 2014.
[23] J. M. Rafí, M. Zabala, O. Beldarrain, and F. Campabadal, 'Deposition temperature and thermal annealing effects on the electrical characteristics of atomic layer deposited Al_2O_3 films on silicon', J. Electrochem. Soc., vol. 158, no. 5, p. G108, 2011.
[24] Y. Liu, L. Zhu, L. Guo, H. Zhang, and H. Xiao, 'Surface passivation performance of atomic-layer-deposited Al_2O_3 on p-type silicon substrates', J. Mater. Sci. Technol., vol. 30, no. 8, pp. 835–838, 2014.
[25] L. Nyns, 'Atomic layer deposition: nucleation and growth behaviour of HFO_2 dielectrics on semiconductor surfaces.', 2009.
[26] T. D. Lin et al., 'High-performance self-aligned inversion-channel In0.53Ga0.47As metal-oxide-semiconductor field-effect-transistors by in-situ atomic-layer-deposited HfO_2', Appl. Phys. Lett., vol. 103, no. 25, p. 253509, 2013.
[27] J. Wang, S. S. Mottaghian, and M. F. Baroughi, 'Passivation properties of atomic-layer-deposited hafnium and aluminum oxides on Si surfaces', IEEE Trans. Electron Devices, vol. 59, no. 2, pp. 342–348, 2012.
[28] G. Dingemans and W. M. M. Kessels, 'Aluminum oxide and other ALD materials for Si surface passivation', ECS Trans., vol. 41, no. 2, p. 293, 2011.
[29] X. Cheng et al., 'Surface Passivation Properties of HfO_2 Thin Film on n-Type Crystalline Si', IEEE J. Photovolt., vol. 7, no. 2, pp. 479–485, Mar. 2017, doi: 10.1109/JPHOTOV.2016.2645399.
[30] G. Dingemans, N. M. Terlinden, M. A. Verheijen, M. C. M. Van de Sanden, and W. M. M. Kessels, 'Controlling the fixed charge and passivation properties of Si (100)/Al_2O_3 interfaces using ultrathin SiO_2 interlayers synthesized by atomic layer deposition', J. Appl. Phys., vol. 110, no. 9, p. 093715, 2011.
[31] L. Stauffer, 'Fundamentals of semiconductor CV measurements', EE-Eval. Eng., vol. 47, no. 12, pp. 20–24, 2008.
[32] T. Dittrich, S. Fengler, and M. Franke, 'Transient surface photovoltage measurement over 12 orders of magnitude in time', Rev. Sci. Instrum., vol. 88, no. 5, p. 053904, 2017.
[33] V. Aubriet, 'Étude du photo-potentiel de surface pour la caractérisation des interfaces enterrées par microscopie à sonde de Kelvin', PhD Thesis, Université Grenoble Alpes, 2022.
[34] M. Wilson, J. Lagowski, L. Jastrzebski, A. Savtchouk, and V. Faifer, 'COCOS (corona oxide characterization of semiconductor) non-contact metrology for gate dielectrics', in AIP Conference Proceedings, 2001, vol. 550, no. 1, pp. 220–225.

[35] G. Lüpke, 'Characterization of semiconductor interfaces by second-harmonic generation', Surf. Sci. Rep., vol. 35, no. 3–4, pp. 75–161, 1999.
[36] O. A. Aktsipetrov, I. M. Baranova, and K. N. Evtyukhov, Second order non-linear optics of silicon and silicon nanostructures. CRC Press, 2018.
[37] P. A. Franken, A. E. Hill, C. el Peters, and G. Weinreich, 'Generation of optical harmonics', Phys. Rev. Lett., vol. 7, no. 4, p. 118, 1961.
[38] J. J. H. Gielis, P. M. Gevers, I. M. P. Aarts, M. C. M. Van De Sanden, and W. M. M. Kessels, 'Optical second-harmonic generation in thin film systems', J. Vac. Sci. Technol. Vac. Surf. Films, vol. 26, no. 6, pp. 1519–1537, 2008.
[39] R. W. Boyd, Nonlinear optics. Academic press, 2020.
[40] O. A. Aktsipetrov et al., 'dc-electric-field-induced second-harmonic generation in Si (111)-SiO_2-Cr metal-oxide-semiconductor structures', Phys. Rev. B, vol. 54, no. 3, p. 1825, 1996.
[41] C. H. Lee, R. K. Chang, and N. Bloembergen, 'Nonlinear electroreflectance in silicon and silver', Phys. Rev. Lett., vol. 18, no. 5, p. 167, 1967.
[42] B. Jun et al., 'Characterization of multiple Si/SiO_2 interfaces in silicon-on-insulator materials via second-harmonic generation', Appl. Phys. Lett., vol. 85, no. 15, pp. 3095–3097, 2004.

Chapter 2: SHG for the characterization of dielectric- semiconductor interfaces - State of art

Abstract

This chapter shows a brief state of art on how the SHG was exploited for characterization of some electrical parameters in oxide/semiconductor structures. SHG response depends on electrical and optical properties of the materials. We will first focus on the electrical induced SHG phenomena. So, we will show the electric field induced second harmonic (EFISH) contribution and how it can be affected by some factors such as: an external electric field, presence of interlayer films, activation of oxide fixed charges, and existence of surface states. Then, we will discuss the optical phenomena that can occur when measuring the SHG response of a stack of materials. We'll mainly focus on SiO_2/Si and Al_2O_3/Si which correspond to the materials under study during the thesis. We also provide some examples on the investigations of multilayer structures such as silicon on insulator (SOI).

Contents of chapter 2

2.1 Parameters of SHG measurement

Before showing how the SHG was used in the literature for material and interface characterization, we'll explain what are the main parameters of a SHG experiment. These parameters are used later in the thesis for characterization.

In most SHG experiments, a monochromatic laser beam of frequency ω is focused onto the substrate, generating a second harmonic response of the sample. The substrate is placed in air, as shown in Figure 2.1 and the SHG emitted by the sample is detected. The SHG response is influenced by a number of experimental parameters, associated to:

- The laser: laser power, laser wavelength (λ_ω), and the wavelength of SH beam ($\lambda_{2\omega}$).
- The set-up: angle of incidence Θ, input-polarization angle (ψ) of the excitation laser, and output-polarization angle (α) of the SH wave.
- The sample: angle of rotation of the reflecting surface to the surface normal ϕ (azimuthal angle).

The z-axis is the normal to the sample, and the xy plane coincides with the sample surface.

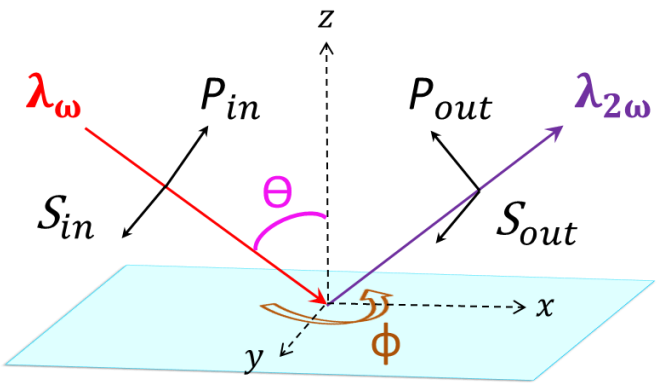

Figure 2.1: *Parameters for SHG experiments. (x, y, z) are the coordinate axes of the set-up.*

The polarization can be controlled for both fundamental (input polarization) and detected SHG (output polarization). The two typical cases are shown in Figure 2.2:

- In polarization P or transverse magnetic (TM) mode, illustrated in Figure 2.2a, the optical electric field $\vec{E}$ is in the plane of incidence of the pump wave (xz). The magnetic field $\vec{B}$ (or magnetic excitation $\vec{H}$) is perpendicular to it, along the y direction.

- In polarization S or transverse electric (TE) mode (the case of Figure 2.2b), $\vec{E}$ is aligned on the y-coordinate. $\vec{B}$ (or $\vec{H}$) is perpendicular to $\vec{E}$ and in the incident plane (xz).

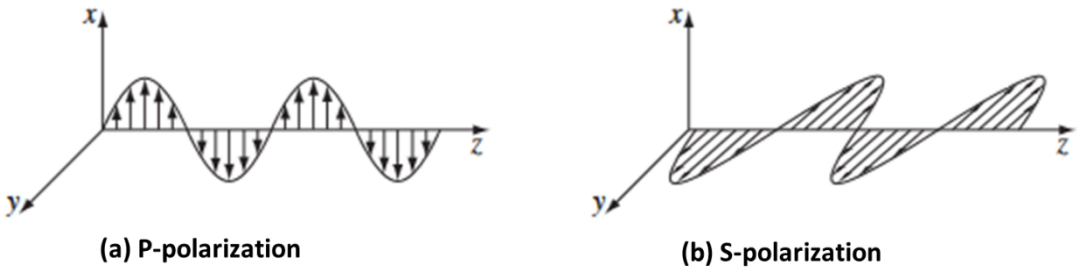

Figure 2.2: *Two independent states of polarization:* ***(a)*** *P-polarization and* ***(b)*** *S-polarization. The (x, y, z) axes mark in this figure is for the beam. Figure taken from [1].*

For general case, one can define a polarization angle along any (x, y, z) direction, which is noted ψ in our definition and is presented in Figure 2.3. The p- and s-polarizations corresponds to ψ=0 and 90°, respectively.

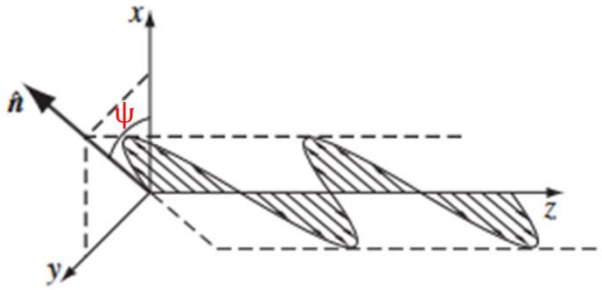

Figure 2.3: *Light electric field oscillating in any direction vector n̂, where ψ is the polarization angle. Figure taken from [1]. The (x, y, z) axes mark in this figure is for the beam.*

These experimental parameters can be varied during the SHG study and can yield to the electrical properties of dielectric/silicon interfaces characterization. A brief overview of the sensitivity of SHG to a variety of material and interface properties will be presented in the following section.

2.2 SHG sensitivity on the properties of dielectric/Si stacks

As discussed in the previous chapter, the materials mostly used in the microelectronic devices and that are studied during the thesis (SiO_2, Al_2O_3, HfO_2 and Si) are centrosymmetric. Thus, there is no second harmonic response coming from the bulk of these materials. Therefore, the SH signal arises typically at the surface/interface. SHG technique demonstrated its effectiveness in providing fundamental insight into interface and material properties such as surface roughness [2], surface hydrogenation [3], surface symmetry [4], etc.

In addition to being non-destructive and interface-related, SHG has a high sensitivity to the interface electric field. This phenomenon is called electric field induced second harmonic (EFISH). It may be resulting from an external bias voltage [5], [6] or an internal electric field [7]. Our research focuses on the EFISH phenomenon produced by the internal electric field that can provide access to the quality of field effect passivation (Q_{ox}) and chemical passivation (D_{it}). Many references in the literature show that the SHG is a powerful technique to probe passivation quality of dielectric/Si interfaces by studying several factors, including density and polarity of built-in charges [8]–[12], density of electron and hole traps [13]–[17] and doping concentration and type [14], [18], [19]. Few studies are performed also on multilayer stacks [20]–[22].

Besides its sensitivity on the electrical parameters, the SHG is a technique based on nonlinear optics. Therefore, both fundamental and SH beam (of intensities I_ω and $I_{2\omega}$), may exhibit optical propagation phenomena (absorption, multiple reflections, interferences) in thin films and stacks.

In this chapter, we will give some literature results that allow positioning our analysis of the passivation quality by SHG. We'll discuss how electrical and optical phenomena in monolayer structures affect the SHG response. We'll also present some examples on the characterization of multilayers.

2.3 Electrical phenomena

Let us remind, the basic relationship between the second harmonic response and the "static" electric field at the dielectric/semiconductor interface due to electric field induced second harmonic (EFISH) phenomenon [23]:

$$I_{2\omega} \sim \left|\epsilon_0 \left[\chi^{(2)} + \chi^{(3)} E_{DC}(t)\right]\right|^2 (I_\omega)^2 \quad (2.1)$$

This phenomenon was first evidenced as a result of an applied external E_{DC}, as will be presented in the next subsection.

2.3.1 Electric field induced second harmonic (EFISH) due to external bias

In the 90s, O. A. Aktsipetrov et al. [6] investigated a planar Cr/SiO_2/Si MOS capacitor using the electric field induced second harmonic (EFISH) phenomenon. As shown in Figure 2.4a, a bias voltage V applied on the capacitor structure induced a quadratic dependence of SHG signals on V, as noticed in Figure 2.4b. Generally, the second harmonic has three source terms: surface electric dipole (P^S), bulk electric quadrupole (P^{BQ}), both occurring in silicon (and not dependent on EFISH) and EFISH (P^{EFISH}) contribution coming from the symmetry breaking due to interface electric field. The total second harmonic polarization source $P^{NL}(2\omega)$ is given by [24]:

$$P^{NL}(2\omega) = P^S(2\omega) + P^{BQ}(2\omega) + P^{EFISH}(2\omega) \quad (2.2)$$

More details on these source terms will be given in chapter 3. Let us focus here on the EFISH contribution only. Figure 2.4b shows the SHG intensity versus the applied voltage (bottom axis) and interface electric field (top axis). With no applied external DC electric field (E_{DC}^{EXT}), the EFISH contribution implies the presence of an intrinsic DC electric field (E_{DC}^{INT}) in the space charge region, close to the SiO_2-Si interface. Thus in presence of external voltage, the EFISH contribution arises from the total of DC electrical field.

$$E_{DC} = E_{DC}^{EXT} + E_{DC}^{INT} \quad (2.3)$$

Therefore, the SHG response is sensitive to all charges present at and near the SiO_2-Si interface and to the SCR width that is also affected by applied electric field. The SHG curves in Figure 2.4b depend on the silicon oxide thickness due to multiple reflections in SiO_2 layer. Furthermore, variations in SiO_2 thickness lead to changes in the interface electric field through the voltage drop across it, or even because of modifications in the oxide charges and/or trapped charges. Decreasing oxide thickness affects the EFISH parabola, as seen in Figure 2.4b, so its minimum becomes sharper and shifts towards lower bias voltages.

When there is no applied voltage, SHG measurements provide access to the intrinsic electric field present at the dielectric-Si interface, confirming the ability of SHG technique to evaluate the interface quality. Indeed, the intrinsic electric field, E_{DC}^{INT}, is induced by fixed oxide charges (Q_{ox}) or/and by charging/discharging mechanisms due to the presence of interface states (D_{it}). The direct effect of each of these two parameters on the SHG signal will be covered in the next two sections, starting with oxide charges impact.

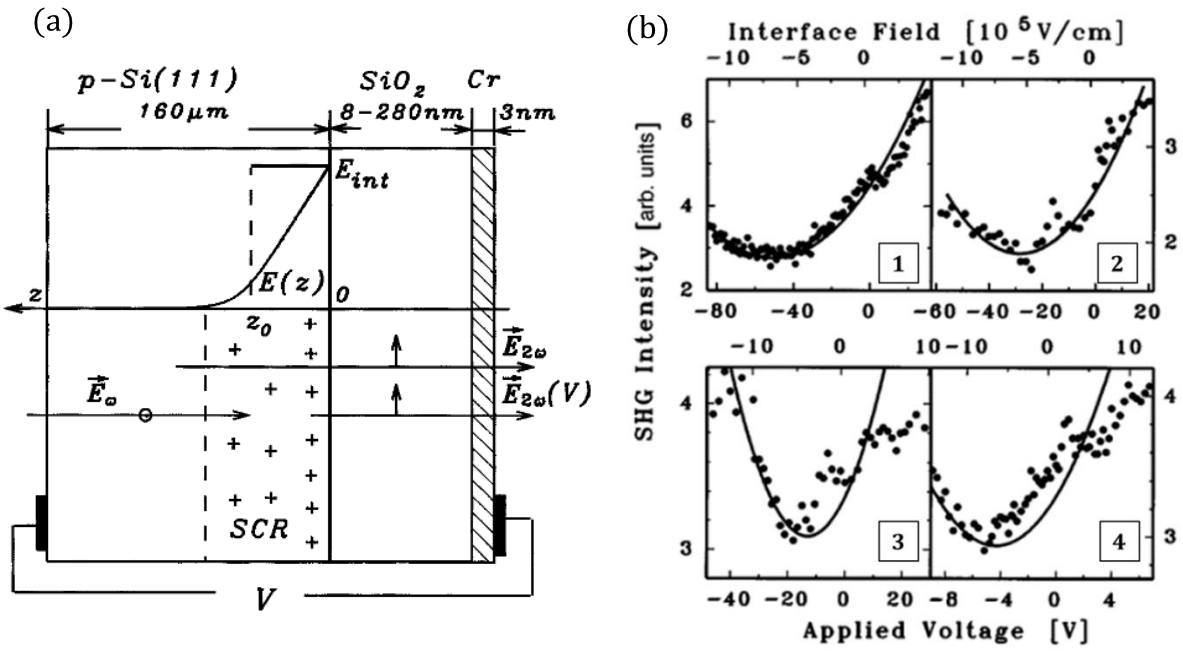

Figure 2.4: (a) *MOS structure band diagram.* ***(b)*** *SHG versus the applied voltage V (bottom axis) and the interface DC electric field (top axis) for MOS structure with different oxide layer thicknesses, including (1) 234 nm, (2) 158 nm, (3) 101 nm and (4) 18 nm. Experimental points are superposed on the model parabolic curves obtained within the interface field approximation, shown as solid lines. Figure taken from [6].*

2.3.2 Fixed charge polarity evaluation

In the high-k dielectric/Si structures, the presence of an interfacial SiO_2 film has a significant role in the modification of surface and interface quality [25]. With Al_2O_3 on Si, the high fixed negative charge density in the alumina provides an important field effect passivation and thus low recombination velocities [26]. Not only the value of the charge is important, but also its polarity. Dingemans et al. [7] show SHG measurements which revealed the influences of interfacial SiO_2 thickness on the polarity of the effective fixed charge density, Q_f, present in the dielectric stacks, and thus, on the field effect passivation. The studied samples in this article are several Al_2O_3/SiO_2/n-type Si(100) stacks annealed in

N_2 ambient with various SiO_2 thickness, between 0.7 and 12.2 nm. The Al_2O_3 film is 30 nm thick. Figure 2.5a illustrates the SHG intensity measured from these stacks as a function of the SHG photon energy. The SHG spectra are dominated by the EFISH contribution at 3.4 eV [27], [11]. The EFISH contribution depends on the SiO_2 thickness (as presented in Figure 2.5b) and is directly related to Q_f. The model proposed by the authors to describe the field effect passivation is explained in the band energy diagrams in Figure 2.5b. The fixed negative and positive charges, called Q_{neg} and Q_{pos}, are located at the Al_2O_3/SiO_2 and at the SiO_2/Si interface, respectively [28], [29]. By increasing the SiO_2 thickness from 0 to 2.3 nm, the positive fixed charge density Q_{pos} in the SiO_2 increases. Hence, the total amount of negative charges in the oxide stack (Q_f) reduces, resulting in a decrease in the interface electric field. Therefore, the EFISH contribution decreases monotonically as shown in Figure 2.5a. For the sample with 4.6 nm SiO_2 thickness, the EFISH intensity disappears, i.e. the significant level of field effect passivation does not exist anymore. For a thicker SiO_2 interlayer (~12.2nm), the role of the positive fixed charge becomes dominant since a thick interlayer screens the negative charge of alumina and the SHG curve increases again.

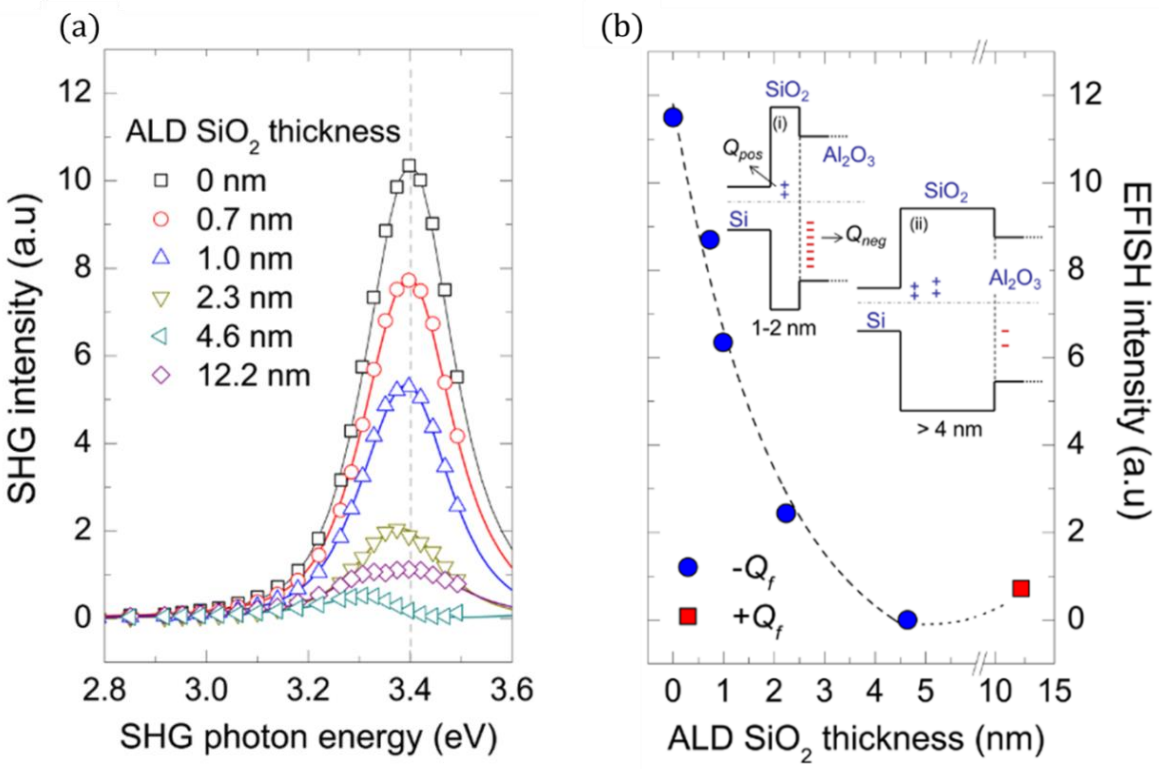

Figure 2.5: (a) *SHG measurements on 30 nm of Al_2O_3/SiO_2/ n-type Si(100) stacks versus incident light energy for several SiO_2 interlayer thicknesses.* ***(b)*** *EFISH contribution versus SiO_2 interlayer thickness. Figure taken from [7].*

This study shows that SHG can measure the total quantity of fixed charges in dielectric stacks on semiconductor. Additionally, the time-dependent measurements can be

performed to identify the sign of the charges. An example of such a study [9] was performed by the same group also on Al_2O_3 (30 nm)/SiO_2 stacks. Figure 2.6a shows the SHG spectra for interlayers with thicknesses between ~1-150 nm, which are similar to those presented in Figure 2.5a. As previously explained, the variation in SHG intensity is caused by a switch from high negative to positive effective charges. To confirm this interpretation, time-dependent second harmonic generation (TD-SHG) measurement was performed for two stacks with thin and thick interlayer. In the case of stack with 0.9 nm SiO_2 thickness (Figure 2.6b), the SH intensity exhibits a monotonic increase with respect to the laser illumination time. The fact that SHG intensity changes with time can be explained the carrier injection caused by the laser irradiation. The inset in Figure 2.6b/c shows the multiphoton carrier injection mechanism proposed by the authors as an explanation of TD-SHG. The signal increase observed in Figure 2.6b implies that the injected charges have the same polarity as the built-in charges of the stack, i.e. the effective charge density is negative. In contrast, for the stack with 18.4 nm SiO_2 (Figure 2.6c), the SH intensity shows an initial decrease until it reaches a minimum value (~t=24 min) before starting to slowly increase again. The SH decrease indicates that the polarity of effective charge density is opposite to charges injected by the laser. This means that the built-in charge density for this particular stack is positive. A balance between the injected electrons and the positive charges present in the stack was considered responsible for the SH minimum.

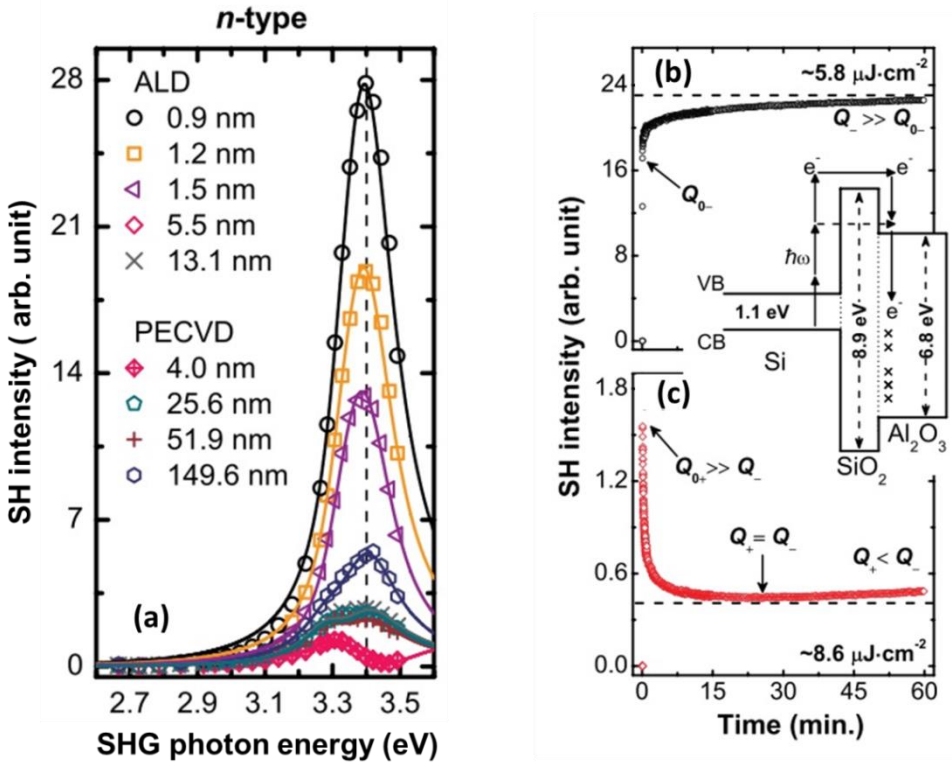

Figure 2.6: (a) *SH spectra of Al_2O_3/SiO_2/n-type Si(100) wafers with varying SiO_2 between ~1 nm and 150 nm. SH intensity versus measurement time of Al_2O_3/SiO_2/n-type Si(100) stacks with SiO_2 thickness :* ***(b)*** *0.9 nm and* ***(c)*** *18.4 nm. Figure taken from [9].*

Another study of field effect passivation modification was performed by Damianos et al. [10]. The study shows the variation of SHG response in different Al_2O_3/Si structures while varying the angle of incidence (Figure 2.7). The Al_2O_3 layers were deposited on silicon substrate by two different processes and parts of samples were annealed in order to improve the interface quality and activate negative charges in the alumina. Each sample was compared before and after annealing.

Figure 2.7 shows experimental and simulation studies. The simulation took into account the constant term of interface electric field which corresponds to the fixed oxide charges. All the electrical and optical phenomena (interferences, absorption) that occur in the structures were included in it. Symbols and solid lines correspond to experimental and simulated curves, respectively. The curves of each sample were normalized by dividing by the maximum value.

The experimental and simulation data are in a good agreement. For the as-deposited sample (black), the $E_{DC}(0)$ integrated in the simulation is supposed to be zero and for the annealed samples (red), $E_{DC}(0) \sim 10^5$ V.cm^{-1}. Consequently, for both samples, higher field effect passivation results (i.e. higher Q_{ox}, so higher E_{DC}) in an increase in the SHG intensity.

These studies, along with existing literature, announce the possibility of calibrated SHG to probe the fixed oxide charges in dielectric/Si structures which is the objective of this thesis.

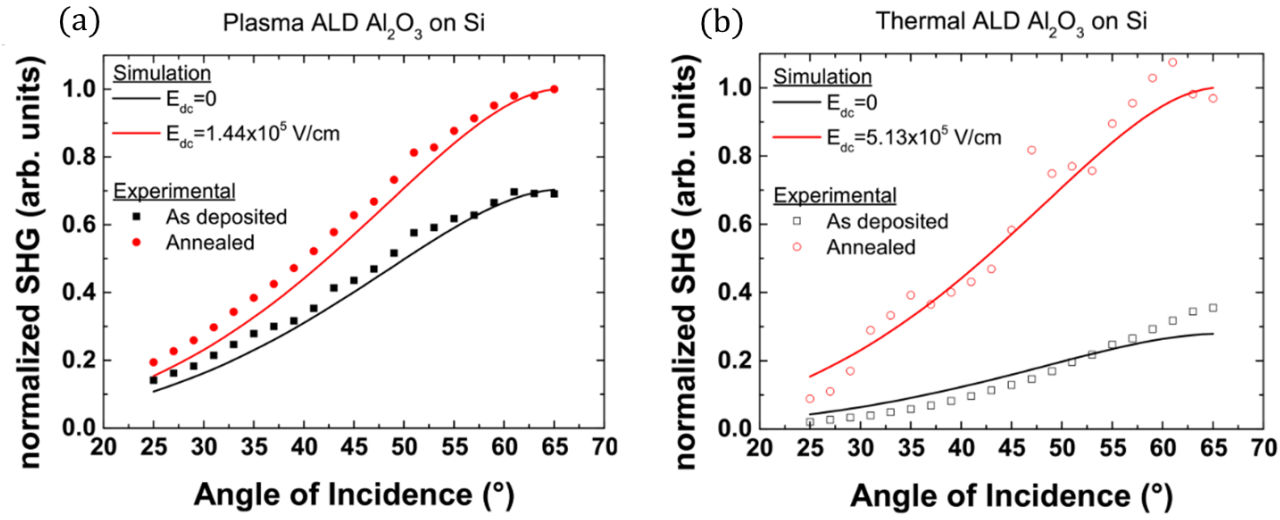

Figure 2.7: *Normalized SHG versus angle of incidence for two Al_2O_3/Si samples fabricated* ***(a)*** *by thermal deposition and* ***(b)*** *by plasma deposition. The black symbols and lines represent the experimental and simulated data for samples as deposited; the red ones for the samples after annealing. Figure taken from [10].*

The SHG measurements were not only used for fixed oxide charges study, but also to monitor the charge injection induced by the multiphoton process, as shown in Figure 2.6b, c. An example explaining the trapping/detrapping mechanisms of the injected charges is given in the next section.

2.3.3 Trapping/detrapping response

Along with the fixed oxide charges, we are interested in measuring the density of interface traps which quantify the interface quality. The time-dependent second harmonic generation (TD-SHG) measurements should be fitted for the study of charging dynamics [14], [15]. The particular example given in this section shows results from SiO_2 layer of 40 Å (Figure 2.8a) and 10 Å (inset of Figure 2.8a) thickness on Si(100) wafer [13]. It focuses on both trapping and detrapping mechanisms. The thickest oxide layer is prepared by thermal growth and the thin one is partially etched with HF solution from the first one. The interface SiO_2/Si should therefore be the same. A laser with a wavelength of 790 nm (1.58 eV) and an average power of 300 mW was utilized for the measurement. At room temperature, the band gap of silicon is 1.1 eV and the one of SiO_2 is 9 eV. The required energy to excite an electron from silicon valence band into the oxide conduction band is 4.1 eV, which corresponds to about three photons with the wavelength used, as illustrated in Figure 2.8b. To create a hole in the oxide valence band, the energy needed is 6.08 eV which requires four photons. The hole injection in the oxide is equivalent to the transfer of an electron from the oxide to the silicon. Despite the possibility of both multiphoton electron and hole transitions, electron excitation is more likely than hole creation since it needs less energy.

Figure 2.8a shows a rapid increase in the TD-SHG signal during the measurement with the fundamental beam with photon energy of 1.58 eV. After few hundreds of seconds, this increase gradually reached a saturation level defined as Δ_1. The authors have suggested that this response is attributed to the multiphoton excitation of electrons into the SiO_2 conduction band and the subsequent electron trapping on the oxide outer surface and also to the creation of holes at the interface (Figure 2.8b). The electron excitation leads to an increase in the quasistatic electric field (E_{DC}) at the SiO_2-Si interface, resulting in an increase in SHG intensity. As seen in Figure 2.8b, when the laser beam is switched off for a while, the holes are expected to quickly move back to the silicon which increases the charge separation. This holes transition under dark was considered responsible for the pronounced increase in the initial TD-SHG signal value (indicated by Δ_2) compared to the previous saturation level. When the beam turned-on again, the holes transfer from the interface into the SiO_2 was suggested to prevail over the electrons movement from the

silicon to the SiO_2. Consequently, these two charge movements combined can reduce the charge separation and therefore the E_{DC} field. Then, the TD-SHG signal decreases until following the same Δ_1 saturation level of the previous beam-on signal. The inset of Figure 2.8a shows the results of the same experiment but from a sample with a thinner oxide of about 10 Å. For thinner oxide films, the dark-related field Δ_2 does not exist because the hole transition effect under dark is less apparent due to the fast electron tunneling back from the oxide to the silicon.

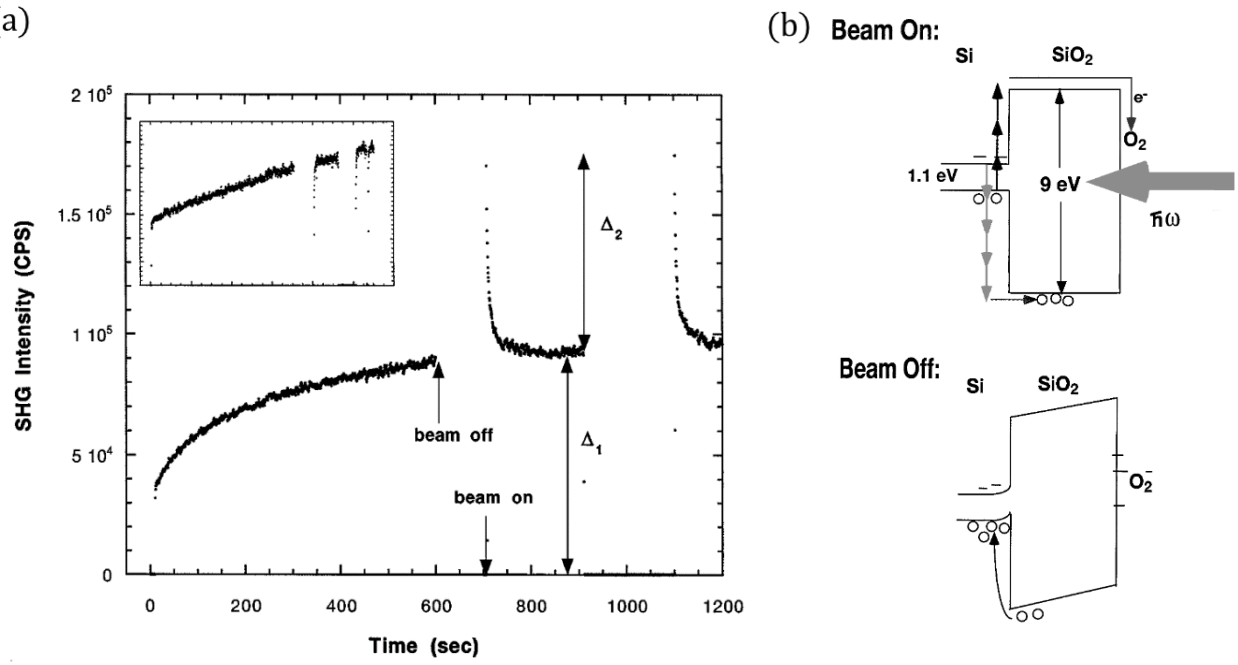

Figure 2.8: (a) *Time-dependent SHG signal from SiO_2-Si(100) structure , Δ_1 is the "beam-on" saturated SHG signal and Δ_2 is the "dark-field" enhanced SHG signal.* ***(b)*** *Schematic band diagrams and charge dynamics during beam on and off sequences. Figure taken from [13].*

This article provides a particular example on how to monitor charging and discharging mechanisms in silicon oxide/Si structures using SHG measurements. Other studies have used exponential fittings to relate the dynamics of TD-SHG curve to the trap densities [10], [14], [30]. However, until now there is no study on how to extract a value of interface trap densities because of the variety of electrical and optical phenomena that can arise in the structure during the laser illumination. The extraction of D_{it} is one of the future objectives of this project.

So far, we have focused on the electrical properties of dielectric/silicon measured by SHG. However, the optical nature of this technique necessitates taking into account the optical phenomena such as interferences and absorption. These phenomena impact the SHG response, as we will see in the next section.

2.4 Optical phenomena: oxide thickness effect

In order to properly study the electrical parameters by SHG (by accessing E_{DC}), we should take into account how optical effects influence the SHG signal. This section presents an example from the literature demonstrating the influence of thickness of the oxide layer on the SHG response. Despite having no effect on nonlinear susceptibility, the oxide has a significant impact on the linear optic phenomena and thus on the SHG signal. Because the oxide is a transparent material with a refractive index between that of air and that of Si, multiple light reflections at both ω and 2ω will play a role in the SHG response.

Hasselt al. [31] performed studies on the effect of oxide thickness on the SHG signal in SiO_2/Si(111) structure, for P_{in}-S_{out} configuration (Figure 2.9). To avoid the multiple reflections at ω, the measurements were taken at 56° angle of incidence. This angle corresponds to Brewster's angle at which there is no reflection for P-polarized light for the air/SiO_2 interface. However, due to multiple reflections of the S-polarized SH waves, measurements and modulation demonstrate strong oscillations of SHG versus oxide thickness (see Figure 2.9). Figure 2.9 also shows the theoretical response calculated by taking into account the linear optics phenomenon of multiple reflections. This shows that the optical response should be considered if we want to predict the SH intensity for a given stack and a given set of experimental parameters.

All the previous studies discuss the case of monolayers. Multiple reflections impact is even more important in multilayers and since such structures are interesting for microelectronic applications, some studies were performed on this type of samples, as we'll show in the next section.

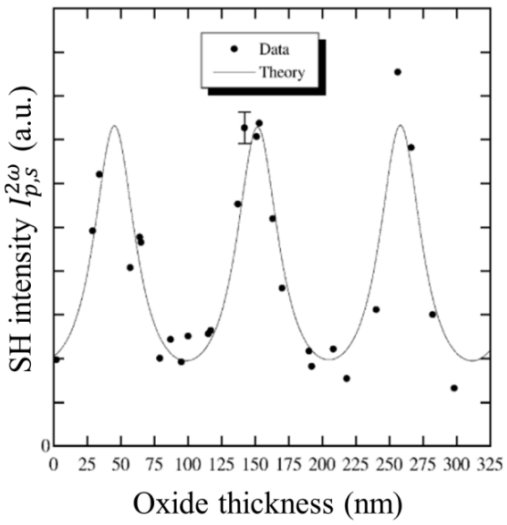

Figure 2.9: *SHG intensity versus oxide thickness at P_{in}-S_{out} configuration and angle of incidence of 56°, from SiO_2/Si structure. Figure taken from [31].*

2.5 SHG for multilayer characterization

Due to the importance of multilayers (in particular silicon on insulator, SOI) for applications in microelectronics, this part presents a couple of investigations of SOI with SHG. Interfaces in SOI structures are typically characterized using invasive electrical characterization of point contact transistors, called pseudo-MOSFET [32]. An optical method to obtain electrical information, such as SHG can be very profitable since it is not destructive. According to Alles et al. [20], TD-SHG measurements can detect both changes in interface properties and metallic contamination of SOI structures. Figure 2.10 shows SHG responses of SOI wafers with different thermal processing during wafer fabrication. In fact, any annealing directly affects the interface quality, which impacts the SHG curves. SHG measurements were also performed on SOI wafers with various Ni contamination concentrations, as illustrated in Figure 2.11a. The sample that was highly contaminated (10^{14} cm^{-2}) produced a stronger SHG compared to the other two samples (reference and 10^{12} cm^{-2} contaminated samples). Moreover, SHG and micro-photoconductance decay (µPCD) measurements were carried out at three locations on a Ni-contaminated wafer. The correlation of both techniques is demonstrated in Figure 2.11b, where the contaminated regions appear as areas of low lifetime and high SHG peak and vice versa.

These studies demonstrate the potential of using the SHG to probe the interface quality and to detect the metal contaminations in SOI multilayer structures. Another study presented below addressed the sensitivity of the SHG to the E_{DC} at each interface of SOI structure, using experimental and simulation approaches.

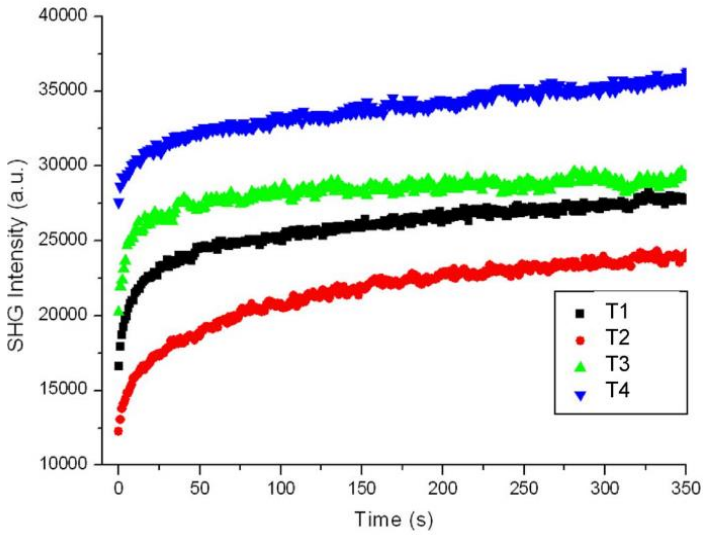

Figure 2.10: *SHG versus time measurements for SOI wafers at different thermal treatments during wafer fabrication. Figure taken from [20].*

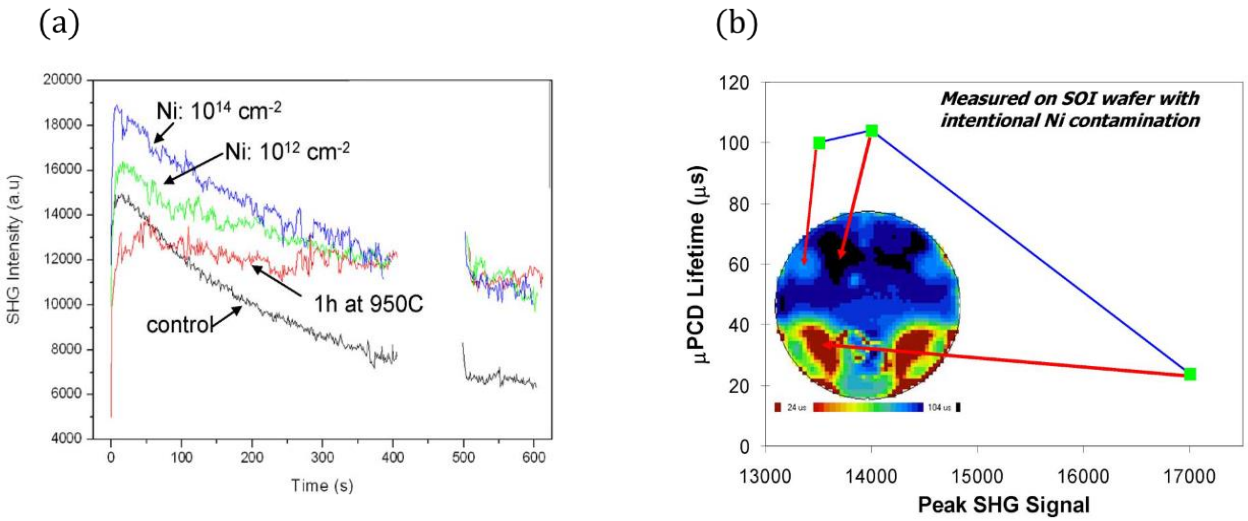

Figure 2.11: (a) *SHG versus time measurements for SOI wafers at different contamination concentrations.* ***(b)*** *Photoconductivity decay (µPCD) lifetime correlation with SHG values for Ni contaminated samples. The µPCD map is presented in the inset, and the locations of the SHG measurements are indicated by the arrows. Figure taken from [20].*

Damianos et al. [22] studied SOI stacks, composed of four layers: native oxide, 12 nm Si film, 145 nm buried oxide (BOX) and Si substrate. Therefore, three interfaces are present, as indicated by the red dots in Figure 2.12a. Due to the unique properties of each interface fabricated differently, the DC electric fields are expected to be different at each interface even if the materials themselves are the same. An experimental SHG investigation was first carried out on the SOI by varying the angle of incidence. To understand how each interface contributes to the global SHG response, simulations were performed by changing one of these E_{DC}, while ignoring the others. Figure 2.12b presents the simulation results when varying the E_1 at the native oxide-Si film interface, while neglecting those of the bottom interfaces ($E_2=E_3=0$). Adjusting E_1 has a noticeable effect on simulated curves and the best match with the experiments is obtained for $E_1 \sim 9.10^4$ V.cm^{-1}. The results of varying the middle field (E_2) at the Si film-BOX interface are shown in Figure 2.12c, with the other fields kept at zero ($E_1=E_3=0$). Although a small modification of the simulated SHG curve is evident, it is not as dramatic as in the previous case. The last case of varying the bottom field (E_3) with $E_1=E_2=0$ is presented in Figure 2.12d. There is almost no variation in the SHG. To summarize, the upper interfacial field has the greatest influence on the simulated SHG response. This is explained by the fact that the SH generated at the bottom interfaces is partially absorbed by the Si film. Moreover, the Si film-BOX interface is of better quality than the native SiO_2-Si film which has a higher electric field due to the presence of more D_{it}.

These encouraging results show a direct dependence between SHG and E_{DC}. An important missing chain would be a calibration curve that will transform these correlation studies based on SHG into a systematic characterization technique using SHG.

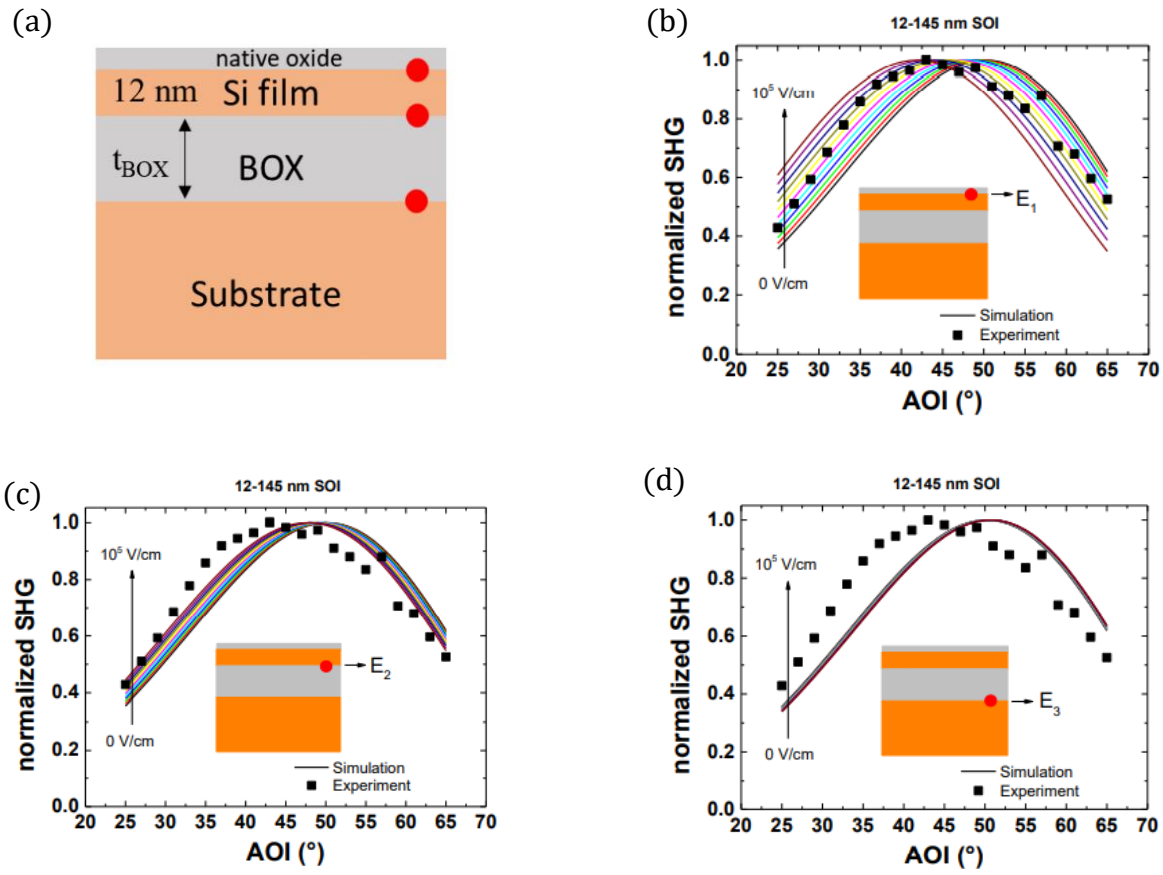

Figure 2.12: ***(a)*** *Silicon on insulator structure with native oxide. Figure taken from [33]. Simulated SHG versus angle of incidence for a 12 nm/145 nm SOI structure with native oxide on the top.* ***(b)*** *E1 variable, E2=E3=0.* ***(c)*** *E2 variable, E1=E3=0.* ***(d)*** *E3 variable, E1=E2=0. Curves taken from [22].*

2.6 Chapter conclusion

The examples presented in this chapter are some of many encouraging and interesting studies that have contributed to the development of the SHG for characterization. The electric field induced second harmonic (EFISH) phenomenon allows to investigate the electrical properties of interfaces of layered structures made of centrosymmetric materials such as SiO_2, Al_2O_3, Si, etc. In particular, we have observed that the material quality influences the interface electric field, which in turn affects the SHG response. Some examples of electrical mechanisms/parameters impacting the SHG signal were shown: variation of fixed oxide charge density and polarity, trapping/detrapping mechanisms for thick and thin oxide layer, and the presence of metallic contaminations on the top of silicon on insulator wafers. Additionally, it has been demonstrated that SHG is also impacted by optical phenomena such as multiple reflections and interferences.

In order to move from these very interesting, but specific studies with SHG, to the SHG as a more systematic characterization tool, calibration of the technique is mandatory. The aim of this thesis is to produce such a calibration of the SHG in order to extract the fixed oxide charges from high-k dielectric passivation layers on silicon structures. However, the presence of optical phenomena may hide information about electrical properties. To distinguish electrical response from the optical one in the measured SHG signal, simulation and modeling are needed. The simulation must take into account all the phenomena of linear and nonlinear optics, as well as the electrical response that occur in the structure under laser beam illumination. All the details on the theoretical phenomenology and the simulation progress will be presented in the following chapter.

2.7 Chapter references

[1] D. J. Griffiths, 'INTRODUCTION TO ELECTRODYNAMICS Fourth Edition', 2021.
[2] J. I. Dadap, B. Doris, Q. Deng, M. C. Downer, J. K. Lowell, and A. C. Diebold, 'Randomly oriented Angstrom-scale microroughness at the Si (100)/SiO_2 interface probed by optical second harmonic generation', Appl. Phys. Lett., vol. 64, no. 16, pp. 2139–2141, 1994.
[3] U. Höfer, 'Nonlinear optical investigations of the dynamics of hydrogen interaction with silicon surfaces', Appl. Phys. A, vol. 63, pp. 533–547, 1996.
[4] H. W. K. Tom, T. F. Heinz, and Y. R. Shen, 'Second-harmonic reflection from silicon surfaces and its relation to structural symmetry', Phys. Rev. Lett., vol. 51, no. 21, 1983.
[5] C. H. Lee, R. K. Chang, and N. Bloembergen, 'Nonlinear electroreflectance in silicon and silver', Phys. Rev. Lett., vol. 18, no. 5, p. 167, 1967.
[6] O. A. Aktsipetrov et al., 'dc-electric-field-induced second-harmonic generation in Si (111)-SiO_2-Cr metal-oxide-semiconductor structures', Phys. Rev. B, vol. 54, no. 3, p. 1825, 1996.
[7] G. Dingemans, N. M. Terlinden, M. A. Verheijen, M. C. M. Van de Sanden, and W. M. M. Kessels, 'Controlling the fixed charge and passivation properties of Si (100)/Al_2O_3 interfaces using ultrathin SiO_2 interlayers synthesized by atomic layer deposition', J. Appl. Phys., vol. 110, no. 9, p. 093715, 2011.
[8] J. J. H. Gielis, B. Hoex, M. C. M. Van De Sanden, and W. M. M. Kessels, 'Negative charge and charging dynamics in Al_2O_3 films on Si characterized by second-harmonic generation', J. Appl. Phys., vol. 104, no. 7, p. 073701, 2008.
[9] N. M. Terlinden, G. Dingemans, V. Vandalon, R. Bosch, and W. M. M. Kessels, 'Influence of the SiO_2 interlayer thickness on the density and polarity of charges in Si/SiO_2/Al_2O_3 stacks as studied by optical second-harmonic generation', J. Appl. Phys., vol. 115, no. 3, p. 033708, 2014.
[10] D. Damianos et al., 'Field-effect passivation of Si by ALD-Al_2O_3: second harmonic generation monitoring and simulation', J. Appl. Phys., vol. 124, no. 12, p. 125309, 2018.
[11] A. Rumpel, B. Manschwetus, G. Lilienkamp, H. Schmidt, and W. Daum, 'Polarity of space charge fields in second-harmonic generation spectra of Si (100)/SiO_2 interfaces', Phys. Rev. B, vol. 74, no. 8, p. 081303, Aug. 2006, doi: 10.1103/PhysRevB.74.081303.
[12] W. Daum, 'Optical studies of Si/SiO_2 interfaces by second-harmonic generation spectroscopy of silicon interband transitions', Appl. Phys. A, vol. 87, pp. 451–460, 2007.
[13] W. Wang et al., 'Coupled electron-hole dynamics at the Si/SiO_2 interface', Phys. Rev. Lett., vol. 81, no. 19, p. 4224, 1998.
[14] H. Park et al., 'Characterization of boron charge traps at the interface of Si/SiO_2 using second harmonic generation', Appl. Phys. Lett., vol. 95, no. 6, p. 062102, 2009.
[15] T. Scheidt, E. G. Rohwer, H. M. Von Bergmann, and H. Stafast, 'Charge-carrier dynamics and trap generation in native Si/SiO_2 interfaces probed by optical second-harmonic generation', Phys. Rev. B, vol. 69, no. 16, p. 165314, 2004.
[16] J. Bloch, J. G. Mihaychuk, and H. M. Van Driel, 'Electron photoinjection from silicon to ultrathin SiO_2 films via ambient oxygen', Phys. Rev. Lett., vol. 77, no. 5, p. 920, 1996.
[17] V. Fomenko, E. P. Gusev, and E. Borguet, 'Optical second harmonic generation studies of ultrathin high-k dielectric stacks', J. Appl. Phys., vol. 97, no. 8, p. 083711, 2005.

[18] T. Scheidt, E. G. Rohwer, P. Neethling, H. M. Von Bergmann, and H. Stafast, 'Ionization and shielding of interface states in native p+-Si/SiO_2 probed by electric field induced second harmonic generation', J. Appl. Phys., vol. 104, no. 8, p. 083712, 2008.
[19] J. L. Fiore, V. V. Fomenko, D. Bodlaki, and E. Borguet, 'Second harmonic generation probing of dopant type and density at the Si/SiO 2 interface', Appl. Phys. Lett., vol. 98, no. 4, p. 041905, 2011.
[20] M. L. Alles et al., 'Second harmonic generation for noninvasive metrology of silicon-on-insulator wafers', IEEE Trans. Semicond. Manuf., vol. 20, no. 2, pp. 107–113, 2007.
[21] M. Lei, J. Price, and M. C. Downer, 'Hot carrier injection from nanometer-thick silicon-on-insulator films measured by optical second-harmonic generation', Appl. Phys. Lett., vol. 96, no. 24, p. 241105, 2010.
[22] D. Damianos et al., 'Second Harmonic Generation characterization of SOI wafers: Impact of layer thickness and interface electric field', Solid-State Electron., vol. 143, pp. 90–96, 2018.
[23] B. Jun et al., 'Characterization of multiple Si/SiO_2 interfaces in silicon-on-insulator materials via second-harmonic generation', Appl. Phys. Lett., vol. 85, no. 15, pp. 3095–3097, 2004.
[24] O. A. Aktsipetrov et al., 'dc-electric-field-induced and low-frequency electromodulation second-harmonic generation spectroscopy of Si (001)- SiO_2 interfaces', Phys. Rev. B, vol. 60, no. 12, p. 8924, 1999.
[25] V. Naumann, M. Otto, R. B. Wehrspohn, M. Werner, and C. Hagendorf, 'Interface and material characterization of thin ALD-Al_2O_3 layers on crystalline silicon', Energy Procedia, vol. 27, pp. 312–318, 2012.
[26] S. P. Muduli and P. Kale, 'State-of-the-art passivation strategies of c-Si for photovoltaic applications: A review', Mater. Sci. Semicond. Process., vol. 154, p. 107202, 2023.
[27] W. Daum, H. J. Krause, U. Reichel, and H. Ibach, 'Nonlinear optical spectroscopy at silicon interfaces', Phys. Scr., vol. 1993, no. T49B, p. 513, 1993.
[28] R. S. Johnson, G. Lucovsky, and I. Baumvol, 'Physical and electrical properties of noncrystalline Al_2O_3 prepared by remote plasma enhanced chemical vapor deposition', J. Vac. Sci. Technol. Vac. Surf. Films, vol. 19, no. 4, pp. 1353–1360, 2001.
[29] J. A. Aboaf, D. R. Kerr, and E. Bassous, 'Charge in SiO_2-Al_2O_3 Double Layers on Silicon', J. Electrochem. Soc., vol. 120, no. 8, p. 1103, 1973.
[30] Z. Marka et al., 'Band offsets measured by internal photoemission-induced second-harmonic generation', Phys. Rev. B, vol. 67, no. 4, p. 045302, 2003.
[31] C. W. van Hasselt et al., 'Oxide-thickness dependence of second harmonic generation from thick thermal oxides on Si (111)', Surf. Sci., vol. 331, pp. 1367–1371, 1995.
[32] S. Cristoloveanu and S. Williams, 'Point-contact pseudo-MOSFET for in-situ characterization of as-grown silicon-on-insulator wafers', IEEE Electron Device Lett., vol. 13, no. 2, pp. 102–104, 1992.
[33] D. Damianos, 'Génération de seconde harmonique (SHG) pour la caractérisation des interfaces entre diélectriques et semiconducteurs', PhD Thesis, Université Grenoble Alpes (ComUE), 2018.

Chapter 3: SHG theory and simulation model in multilayer structures

Abstract

The second harmonic generation theory at dielectric-Si interfaces is based on the interaction theory of electromagnetic radiation with matter, including non-linear optical interaction, and on the physics of semiconductors. This chapter discusses the optical phenomena, both linear and nonlinear, that occur within the layers and across an interface. All optical and electrical phenomena will be entered into a simulation code to create a numerical model for the SHG response of multilayer structures.

Contents of chapter 3

3.1 Modeling of SHG in semiconductors

Over the last several decades, many groups have developed general SHG theories. In the 1960's, Bloembergen laid the fundamentals of nonlinear optics [1]–[3]. In particular, N. Bloembergen and P. S. Pershan described the nonlinear boundary conditions at the interface between linear and nonlinear media, using Maxwell's equations; these conditions have been defined to be compatible with all orientation crystal faces [3]. In 1983, H. Tom et al. revealed that the presence of a boundary gives rise to a surface contribution in the nonlinear polarization, commensurate with the bulk contribution [4]. Since then, the problem of separating surface and bulk contributions has arisen. The first crystal symmetry-dependent SHG in silicon was pointed out by refs. [4]–[6], which showed the dependence of the SHG signals on the rotation angle at various pump and SH wave polarization configurations. References [7] and [8] showed for the first time that the difference of the surface and bulk symmetry properties can solve the problem of the separation of surface and bulk contributions in the nonlinear optical response. A phenomenological SHG response that results from surface and bulk contributions of centrosymmetric crystals was described by J. E. Sipe et al. in [9]. New horizons have opened up in the nonlinear optical study of centrosymmetric semiconductors with Ref. [10] and Ref. [11], where the authors discovered and investigated the dependence of SHG intensity on a DC external electrical field applied to the metal-oxide-semiconductor (MOS) structure. A supplementary dipole contribution associated with this field is added to the nonlinear polarization sources, and thus to the SHG intensity. This is electric field-induced second harmonic (EFISH). This phenomenon is affected by physical parameters such as the charge concentration, the surface charge traps density in the semiconductor, the thickness of dielectric layer on the surface, etc. It allows studying the charge dynamics [12] and the buildup charges [13] in dielectric-semiconductor structures.

Chapter 2 showed an overview of the state of art of the use of the SHG as a characterization tool for monitoring trapping/detrapping phenomena and fixed charge in dielectric layers on the top of semiconductor (in particular Si). On the other hand, SHG is a nonlinear optical technique, which means that in addition to electrical phenomena, optical phenomena (absorption, interferences) can appear in the material during its interaction with the laser. These phenomena can hide some information about the electrical parameters we are interested in, so to distinguish each contribution to the SHG response, we need a model that incorporates all of these phenomena. This is what will be covered in this chapter. Such a model does not exist in the literature so far and we have developed it in a precise way based mainly on refs. [3], [9], [14]. The model gives the repartition of fundamental and second harmonic fields at any point of a multilayer structure, while imposing the boundary conditions for the fields at the interface between 2 media. This approach allows taking into account all optical phenomena such as transmission, reflection,

interference, etc. Figure 3.1 shows an example of simulated SHG dependence on SiO_2 thickness in a SiO_2/Si stack. The curve emphasizes the presence of two interference phenomena inside the materials, one caused by the superposition of fundamental radiations and the other by the superposition of SH radiations. Although this example depicts a simple structure, its study is complicated due to the occurrence of optical and electrical phenomena. Therefore, the difficulty will be increased for multilayers and modeling will be even more critical in that case.

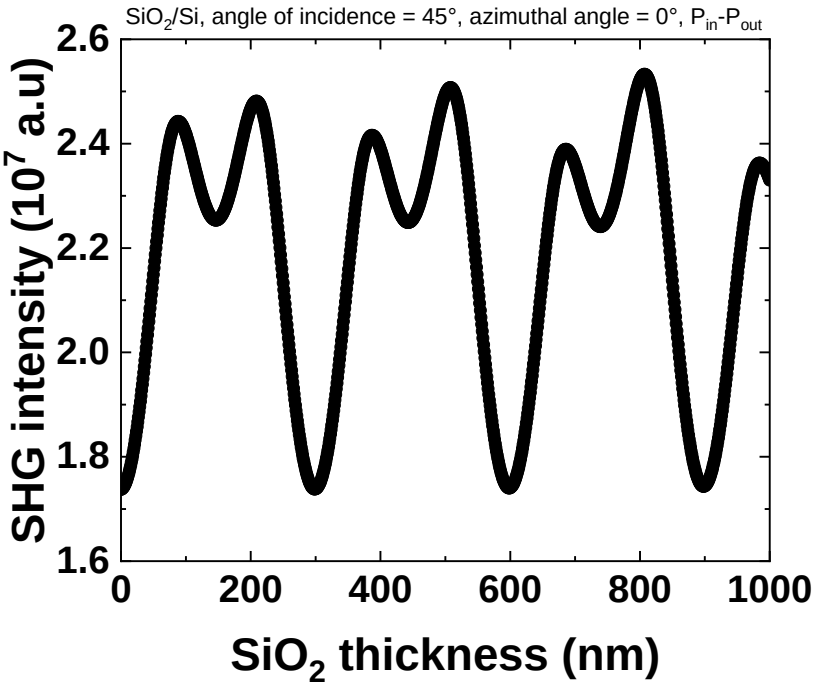

Figure 3.1: *Simulated SHG intensity versus SiO_2 thickness in a SiO_2/Si(100) structure.*

The simplified SHG expression is previously defined as:

$$I_{2\omega} \sim \left| P^{(2)}(2\omega) \right|^2 = \left| \epsilon_0 [\chi^{(2)} + \chi^{(3)} E_{DC}(t)] \right|^2 (I_\omega)^2 \tag{3.1}$$

In reality, the relation between $I_{2\omega}$ and $P^{(2)}(2\omega)$ is not simple, especially in multilayer structures where several NL polarization sources may exist. The intensity of the second harmonic light should thus be calculated using simulation and modeling. The model path is presented in the chapter in order, as following:

1- Firstly, we give the propagation phenomena and notation used during calculation (section 3.2).

2- The fundamental fields repartition inside the structure using linear boundary conditions at the interfaces is given (section 3.3).
3- According to the approach of Sipe et al. [9], we define the second order polarization expressions at each interface involving Si. We treat the case of (100) oriented material with separating bulk and surface contributions (section 3.4.1). We also introduce the electric field induced source terms in the nonlinear polarization (section 3.4.2).
4- The nonlinear boundary conditions adapted for multilayer structures are derived starting from literature results on monolayers as in Bloembergen et al. [3] (section 3.4.3).
5- We validate the correctness of the model by:
- An analytical calculation of the reflected SH fields expressions for a structure already studied by the literature (section 3.5).
- Simulation comparison with the experimental. The simulation processes are first explained in section 3.6 and then the results are presented in section 3.7.

3.2 Propagation of the fundamental and SH waves: notations

This section describes the propagation of reflected and transmitted waves at the fundamental (ω) and second harmonic (2ω) frequencies in a multilayered structure as shown in Figure 3.2a. A coordinate system is chosen with $\hat{z}$ axis oriented upwards, perpendicular to the interfaces. The top interface is located at $z = 0$. The waves propagating in the structure are plane monochromatic. The incidence wave at the fundamental frequency (or pump wave) is defined by its wave vector k_0 and its polarization angle Ψ. The part of the fundamental wave reflected by the multilayer has a wave vector k_1 and the transmitted part for the last layer is k_{last}, as illustrated in Figure 3.1a. When the pump wave interacts with a second order nonlinear material, new waves at a frequency of 2ω will be generated, called second harmonic (SH) waves.

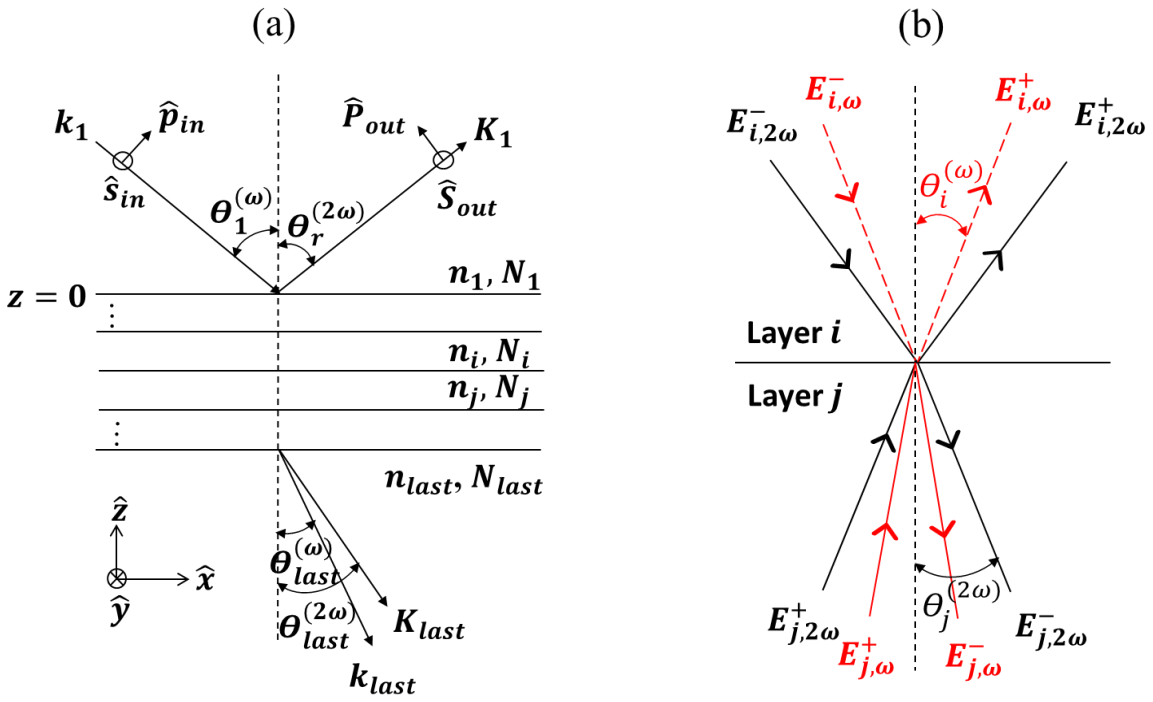

Figure 3.2 : (a) *Definition of the incident, refracted and reflected rays at fundamental and SH waves in a multilayer structure and of the polarization geometry on the input fundamental and output SH waves* ***(b)*** *Zoom on the transition of waves at ω and 2ω at the interface between the layers "i" and "j" in the multilayer structure.*

Inside the multilayer, in a given layer "i", the electric fields of the pump and SH waves will be written in the form [15]:

$$\vec{E}_{i,\omega}^{\pm} = e^{i(-\omega t \pm k_{z,i} z + k_{x,i} x)} (A_{i,s}^{\pm} \hat{s} + B_{i,p}^{\pm} \hat{p}^{\pm}) \tag{3.2}$$

$$\vec{E}_{i,2\omega}^{\pm} = e^{i(-2\omega t \pm K_{z,i} z + K_{x,i} x)} (C_{i,S}^{\pm} \hat{S} + D_{i,P}^{\pm} \hat{P}^{\pm}) \tag{3.3}$$

Where A, B, C and D are the amplitudes of the electric fields at the each frequency and in each polarization state. The + and – sign stand for upward (reflected) and downward (transmitted) waves, respectively, as shown in Figure 3.2b.

$(k_{x,i}, k_{z,i})$ are the components of the fundamental wave vector in the medium "i" along $\hat{x}$ and $\hat{z}$ axes shown in Figure 3.3. (K_x, K_z) are components of the SH wave vector. The expressions for the wavevectors in a given layer i of the structure are:

$$\begin{aligned} k_i &= n_i k_0 \\ k_{x,i} &= k_i \sin\theta_i^{(\omega)} = k_1 \sin\theta_1^{(\omega)} \\ k_{z,i} &= [{k_i}^2 - {k_{x,i}}^2]^{1/2} \end{aligned} \tag{3.4}$$

$K_{x,i}$ and $K_{z,i}$ are the components of the SH wave vector (K_i) in the medium.

$$\begin{aligned} K_i &= N_i K_0 \\ K_{x,i} &= 2k_{x,i} \\ K_{z,i} &= [{K_i}^2 - {K_{x,i}}^2]^{1/2} \end{aligned} \tag{3.5}$$

n_i and N_i correspond to the refractive index of medium i at the fundamental and SH frequency, respectively.

When a light ray propagating into a given medium encounters a new medium with a different refractive index, it will, in the most common case, be refracted as it enters the new medium as shown in Figure 3.3. As the light sources and detectors are generally in air, Snell-Descartes law [16] provides that the angle of refraction inside layer "i" ($\theta_i^{(\omega)}$) and its index n_i to the incidence angle (θ_0) and the refractive index of the air (n_{Air}=1):

$$n_{Air}\sin\theta_1 = \sin\theta_1 = n_2\sin\theta_2^{(\omega)} = n_i\sin\theta_i^{(\omega)} = n_j\sin\theta_j^{(\omega)} = n_{last}\sin\theta_{last}^{(\omega)} \tag{3.6}$$

For an absorbing medium, the refractive index is a complex number and the k coefficient depends on its imaginary part. Therefore, the refraction angle will also be complex number.

Using the Snell's law and the conservation of tangential wave vector, k_x and K_x will be the same everywhere in the multilayer and are fixed by the angle of incidence (θ_0 in Figure 3.3). Using the wavevector in vacuum k_0=ω/c at the pump frequency and K_0=2ω/c at the SH frequency, eq.(3.4) and (3.5) are redefined by:

$$\begin{aligned} k_x &= k_1 \sin\theta_1 \\ k_{z,i} &= k_0[n_i^2 - \sin^2\theta_1]^{1/2} \end{aligned} \tag{3.7}$$

$$\begin{aligned} K_x &= 2k_x \\ K_{z,i} &= K_0[N_i^2 - \sin^2\theta_1]^{1/2} \end{aligned} \tag{3.8}$$

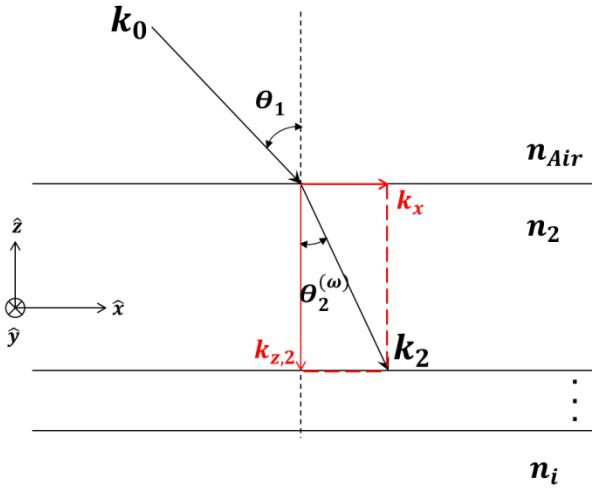

Figure 3.3: *Geometry for the propagating fundamental fields between the air and medium "i", presenting the angle of incidence, the refraction angle and the wavevectors with the projection on x- and z-axis. Note that the refractive index n_i in this schematic is assumed to be real.*

The wavevectors inside the multilayer are linked to angles such as θ_i and θ_j given in Figure 3.2b. In order to be more general and account for total internal reflexion for example, the sinus and cosinus of these angles should be complex numbers. We will thus use the notations introduced by Sipe et al. [9], where f_s and f_c represent the sinus and cosinus of the complex angles at the fundamental frequency and F_s and F_c are the same, at the SH frequency. In a given layer i, we can define these coefficients as:

$$f_{s,i} = \frac{k_x}{n_i k_0}$$
$$f_{c,i} = \frac{k_{z,i}}{n_i k_0} \tag{3.9}$$

$$F_{s,i} = \frac{K_x}{N_i K_0}$$
$$F_{c,i} = \frac{K_{z,i}}{N_i K_0} \tag{3.10}$$

According to eqs.(3.7-3.10), we can deduce the following relations adapted for any layer (i, j...), which will be used for future calculations:

$$F_s^2 = 1 - F_c^2$$
$$f_s^2 = 1 - f_c^2 \tag{3.11}$$

$$NF_s = nf_s$$
$$N^2 - n^2 f_s^2 = N^2 F_c^2 \tag{3.12}$$

$$n^2 f_c^2 - N^2 F_c^2 = n^2 - N^2 \tag{3.13}$$

As shown in chapter 2, the electric fields of light can be seen as the superposition of two rectilinearly polarized waves in independent directions, which are noted $\hat{p}$ and $\hat{s}$ for the pump frequency, and $\hat{P}$ and $\hat{S}$ for the SH frequency. In the case of P-polarized, the electric field $\vec{E}$ is parallel to the incidence plane ($\hat{x}$-$\hat{z}$), and the direction for a downward or upward wave in a given layer can be defined by:

$$\hat{p}^{\pm} = f_s \hat{z} \mp f_c \hat{x}, \text{ for the fundamental wave at } \omega \tag{3.14}$$

$$\hat{P}^{\pm} = F_s \hat{z} \mp F_c \hat{x}, \text{ for SH wave at } 2\omega \tag{3.15}$$

For S-polarization, $\vec{E}$ is parallel to the interface (along the $\hat{y}$ axis).

$$\hat{s} = \hat{y}, \text{ for the fundamental wave at } \omega \tag{3.16}$$

$$\hat{S} = \hat{y}, \text{ for SH wave at } 2\omega \tag{3.17}$$

In order to derive the electric fields on either side of an interface, Maxwell's equations are used to define continuity relations of the total electric and magnetic fields of the fundamental and SH waves. While for the fundamental frequency, the equations are well-known, the second harmonic ones require source terms which depend on nonlinear polarization P^{NL} created by the pump wave in the nonlinear media. The calculation of P^{NL} is detailed in the next sections, separating bulk and surface contributions.

3.3 Linear optical phenomena

This section describes the propagation of electric fields at the fundamental frequency ω in a multilayer structure. If we suppose that the fields at the beginning of layer

i are known, then the calculation of the propagating fields is possible at any z position in the layer:

$$E_{i,\omega}^{\pm}(z) = E_{i,\omega}^{\pm}(z_{initial})e^{-i\omega t \pm ik_{z,i}.(z-z_{initial})} \tag{3.18}$$

In particular, to calculate the fields at the end of the layer as shown in Figure 3.4, it is sufficient to replace $z - z_{initial}$ by the layer thickness t_i.

As shown in Figure 3.4, at the interface between two successive layers of different refractive indices, the electric fields change while passing through it. The boundary conditions at the interface will be discussed next, starting from Maxwell's equations.

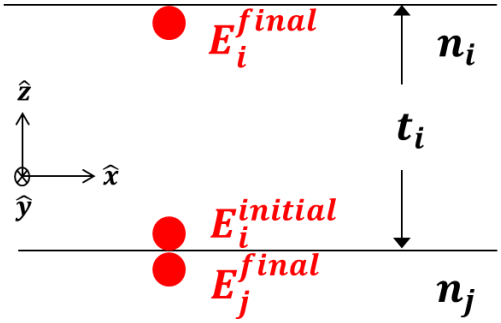

Figure 3.4: *The electric fields propagation between and within the layers of multilayer structure [14].*

3.3.1 Linear boundary conditions

The Maxwell's equations are used to describe the propagation of electromagnetic waves [17]:

$$\begin{aligned} &(1)\ \vec{\nabla}.\vec{D} = \rho \\ &(2)\ \vec{\nabla}.\vec{B} = 0 \\ &(3)\ \vec{\nabla}\mathrm{x}\vec{E} = \frac{-\partial\vec{B}}{\partial t} \\ &(4)\ \vec{\nabla}\mathrm{x}\vec{H} = \frac{\partial\vec{D}}{\partial t} + \vec{J} \end{aligned} \tag{3.19}$$

With D and E, being the electric displacement and field, respectively. ρ and J are the charge and current densities. B and H are the magnetic induction and field.

In the absence of surface charges and for currents of non-magnetic, linear, homogeneous and isotropic media, the electromagnetic fields must be continuous across the interface between two media and must comply with the boundary conditions. The two particular cases of p-polarization and s-polarization will be discussed next.

A. For *p*-polarization

According to eq. (3.19-1) and (3.19-3), the perpendicular displacement ($D^{\perp}$, i. e D_z) components and the tangential electric field components ($E^{/\!/}$, i.e E_x) must be continuous across the interface:

$$\begin{aligned} D_i^{\perp} = D_j^{\perp} \Longrightarrow \varepsilon_i E_i^{\perp} = \varepsilon_j E_j^{\perp} \\ E_i^{/\!/} = E_j^{/\!/} \end{aligned} \tag{3.20}$$

Going back to eqs. (3.2) and (3.4), the spatial distribution of the upward and downward electric fields in the p-polarization seen in Figure 3.5(a) is represented according to its direction ($\hat{x}$-$\hat{z}$):

$$\vec{E}_i^{+} = e^{i(k_{z,i}.z+k_x.x)}(-E_i^{+} f_{ci}\,\hat{x} + E_i^{+} f_{si}\,\hat{z}) \tag{3.21}$$

$$\vec{E}_i^{-} = e^{i(-k_{z,i}.z+k_x.x)}(E_i^{-} f_{ci}\,\hat{x} + E_i^{-} f_{si}\,\hat{z}) \tag{3.22}$$

The total electric field strength depends on the refractive index and is defined by:

$$E_{p,i} = [{f_{c,i}}^2\,(E^{+} - E^{-})^2 + {f_{s,i}}^2\,(E^{+} + E^{-})^2]^{1/2} \tag{3.23}$$

To get the boundary conditions at the interface between two consecutive layers "i" and "j", the equations (3.20) are solved using eq. (3.21) and (3.22).

Linear boundary conditions for p polarization:

$$n_i(E_i^{+} + E_i^{-}) = n_j(E_j^{+} + E_j^{-}) \tag{3.24}$$

$$f_{c,i}(E_i^{+} - E_i^{-}) = f_{c,j}(E_j^{+} - E_j^{-}) \tag{3.25}$$

B. For *s*-polarization

Eq. (3.19-2) and (3.19-4) prove that the total of normal magnetic induction components ($B^{\perp}$, i.e B_z) and the total of tangential magnetic field components ($H^{/\!/}$, i.e H_x) are both continuous over the interface:

$$\begin{aligned} H_i^{\perp} &= H_j^{\perp} \\ H_i^{/\!/} &= H_j^{/\!/} \end{aligned} \tag{3.26}$$

The spatial distribution of the electric fields in s-polarization is represented according to its direction ($\hat{y}$), where:

$$\vec{E}_i^{+} = e^{i(k_{z,i}.z+k_x.x)}(E_i^{+}\hat{y}) \tag{3.27}$$

$$\vec{E}_i^{-} = e^{i(-k_{z,i}.z+k_x.x)}(E_i^{-}\hat{y}) \tag{3.28}$$

And the total electric field strength is:

$$E_{s,i} = E_{s,i}^{+} + E_{s,i}^{-} \tag{3.29}$$

To produce the boundary conditions of s-polarization, eq. (3.26) are solved using the electric field expressions presented above, and taking into account that $\vec{H} = \frac{1}{i\omega\mu_0}(\vec{\nabla}x\vec{E})$.

Linear boundary conditions for *s* polarization:

$$E_i^{+} + E_i^{-} = E_j^{+} + E_j^{-} \tag{3.30}$$

$$n_i f_{c,i}(E_i^{+} - E_i^{-}) = n_j f_{c,j}(E_j^{+} - E_j^{-}) \tag{3.31}$$

For each case of polarization, the linear boundary conditions are used to calculate the unknown electric fields in a given layer (E_j^{+} and E_j^{-} for example) if the fields of the previous layer (E_i^{+} and E_i^{-}) are known. Once the fields at the new layer have been calculated, we use the wave vectors in that layer ($k_{z,j}$) to calculate the fields at the end of that layer, right before the next interface. Then, the new boundary conditions are taken into account to determine the fields inside the next layer from the new known fields (E_j^{+} and E_j^{-}). This scenario is repeated until the electric fields of the last layer are determined.

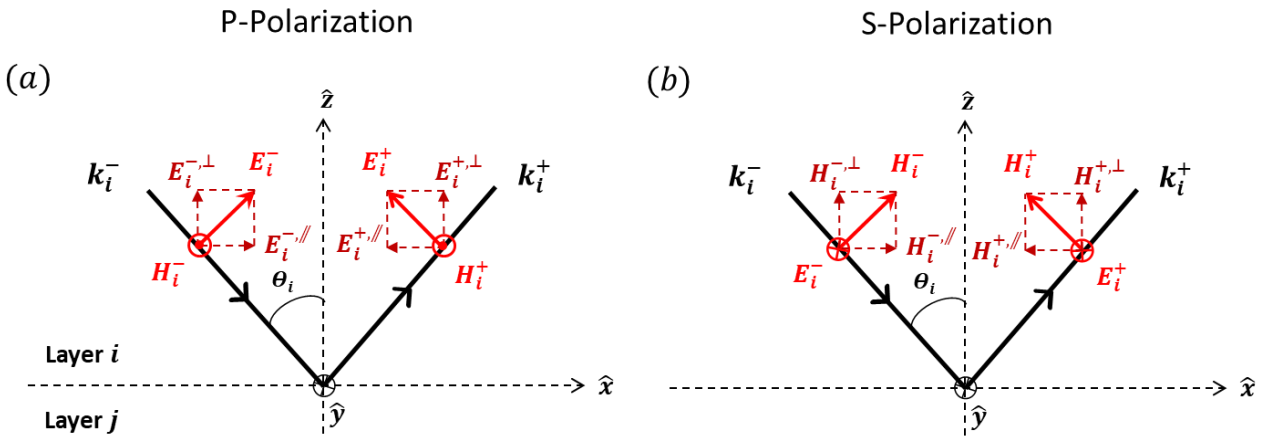

Figure 3.5: *Notations of the electromagnetic fields present inside a given layer "i" of a multilayer for:* ***(a)*** *P-polarization and* ***(b)*** *S-polarization cases [14].*

3.3.2 Fundamental electric field distribution in the structure

As our study deals with multilayered structures, a numerical approach is used to calculate the total electric fields at each position in the structure. To validate this method, we simulated the electric field strength distribution in the z direction in silicon on insulator (SOI) structure, for both s- and p-polarizations, as shown in Figure 3.6. The employed SOI structure's layer thicknesses are defined as follows: 400 nm buried oxide (BOX), 190 nm Si film and 6 nm SiO_2 top layer. The laser wavelength set for the calculation is 780 nm with an average power of 100 mW. The chosen angle of incidence is 45°. As shown in Figure 3.6, the module of the total field amplitude of the electric field is constant in the Si substrate, where we assumed that the incoming field is zero. The electric field in the remaining layers of the structure is sinusoidal because of the superposition of two counter-propagating waves. In the case of p-polarization (Figure 3.6a), we can clearly observe the discontinuity in the field when it passes through the boundary between two layers, as expected from eq. (3.23-3.25). While for s-polarization (Figure 3.6b), the field strength remains continuous all along the structure as expected from eq. (3.29) and (3.30).

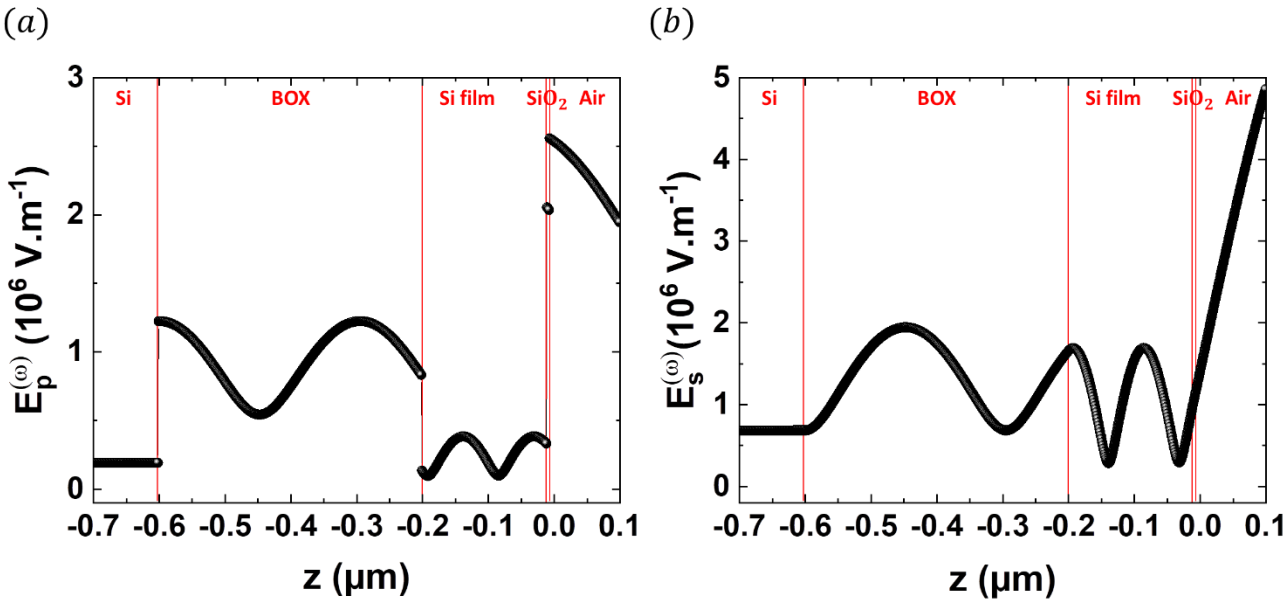

Figure 3.6: *Variation of fundamental electric field in z-axis direction in SOI structure (Si substrate/ 0.4 µm BOX/ 0.19 µm Si film) with native oxide for the case of* ***(a)*** P_{in} *polarization and* ***(b)*** S_{in} *polarization.*

3.4 Second harmonic: source terms and boundary conditions

A nonlinear polarization P^{NL} is created in the material after exposure to the incident electric field $E(\omega)$, which produces SH waves. [18] The SH waves propagate in each layer of the structure and must obey nonlinear boundary conditions at the interface between any two consecutive layers.

To discuss the SHG response in a multilayer structure:

1-we give the P^{NL} expressions in the material that interests us: (100) oriented material, according to Sipe et al. [9].

2-we assume the presence of the "static" electric field at Si interface and describe the EFISH phenomenon.

3-we give the nonlinear boundary conditions, starting from Bloembergen et al. [3].

3.4.1 Nonlinear polarization sources

The nonlinear polarization contains two types of contributions:

- Bulk contributions. Outside of the dipolar approximation (where bulk SHG is zero), electric quadrupole $P^{B}(2\omega)$ and magnetic dipolar $P^{BD}(2\omega)$ terms need to

be considered. For silicon, $P^B > P^{BD}$ [17], so we will consider only this contribution.

- Surface/interface contributions $P^{surf}(2\omega)$, due to symmetry breaking between two medias (structural or chemical discontinuity [19], interface electric field [3]).

Thus, the $P^{NL}(2\omega)$ can be written as [20]:

$$P^{NL}(2\omega) = P^{BD}(2\omega) + P^{surf}(2\omega) + P^{B}(2\omega) \tag{3.32}$$

The expressions of each contribution are given in this section for Si(100).

A. Bulk contribution

Since silicon is a centrosymmetric material, the second harmonic generation in the volume of an infinite nonlinear medium is mainly attributed to the quadratic quadrupole bulk nonlinear polarization P_i^B. This polarization is given by [17]:

$$P_i^B = \epsilon_0 \chi_{ijkl}^{(2)Q} E_j \nabla_k E_l, \quad i,j,k,l = x,y,z \tag{3.33}$$

Where E_j and E_l are the components of the electric field vector of the fundamental wave and ∇_k is the gradient operator applied to the field coordinates. $\chi_{ijkl}^{(2)Q}$ is a fourth rank tensor representing the components of the quadrupole susceptibility. These components depend directly on the symmetry properties of the crystal and some of them will be connected by Kleinman's symmetry rule, while others will simply vanish. For (100) oriented materials which belong to 4mm symmetry, two standard terms of quadrupole susceptibility are taken into account, one isotropic named γ and another anisotropic (ξ) which depends on the rotational angle (ϕ).

Concerning the anisotropic term, we used equation (9) and Table I from the publication of Sipe et al. [9] to solve the matrix for (100) - oriented silicon. The development of this matrix with the following relations: $E_x = f_c E_p$; $E_y = E_s$ and $E_z = f_s E_p$ gives the following anisotropic nonlinear polarization equations:

$$P_x^{B-aniso} = \frac{1}{4} jk_0 n\epsilon_0 \xi \left[f_s\left(E_s^2 + 3f_c^2 E_p^2\right) + 2sin(4\phi) f_s f_c E_s E_p + cos(4\phi) f_s (f_c^2 E_p^2 - E_s^2)\right] \tag{3.34}$$

$$P_y^{B-aniso} = -\frac{1}{4} jk_0 n\epsilon_0 \xi \left[-2f_s f_c E_s E_p - sin(4\phi) f_s (f_c^2 E_p^2 - E_s^2) + 2cos(4\phi) f_s f_c E_s E_p\right] \tag{3.35}$$

$$P_z^{B-aniso} = -jk_0 n\epsilon_0 \xi\, f_c f_s^2 E_p^2 \tag{3.36}$$

For isotropic bulk, the source is identical for all crystal faces and the nonlinear polarization is given by Sipe's equation (21) as follows:

$$P_x^{B-iso} = 2jf_s nk_0\epsilon_0\gamma\left(E_s^2 + E_p^2\right) \tag{3.37}$$

$$P_y^{B-iso} = 0 \tag{3.38}$$

$$P_z^{B-iso} = -2jf_c nk_0\epsilon_0\gamma\left(E_s^2 + E_p^2\right) \tag{3.39}$$

The isotropic and anisotropic bulk nonlinear polarizations are in most cases much lower than the NL polarization due to the surface. Indeed, bulk contribution is of quadrupolar origin, whereas surface contribution is dipolar.

B. Surface contribution

The surface nonlinear polarization expression is defined as in Sipe et al. [9]:

$$P_i^{surf} = \epsilon_0 \chi_{ijk}^{(2)surf} E_j E_k \tag{3.40}$$

With $\chi_{ijk}^{(2)surf}$, the components of electric dipole surface susceptibility tensor. As in the case of bulk tensor $\chi_{ijkl}^{(2)Q}$, the surface one $\chi_{ijk}^{(2)surf}$ is subject to the conditions imposed by Kleinman's rule and the symmetry of the crystal surface.

For a surface from 4mm symmetry class for a (100) face, eq.(3.40) can be rewritten:

$$\begin{pmatrix} P_x^{surf} \\ P_y^{surf} \\ P_z^{surf} \end{pmatrix} = \epsilon_0 \begin{bmatrix} 0 & 0 & 0 & 0 & \chi_{xxz} & 0 \\ 0 & 0 & 0 & \chi_{yyz} & 0 & 0 \\ \chi_{zxx} & \chi_{zyy} & \chi_{zzz} & 0 & 0 & 0 \end{bmatrix} \begin{pmatrix} E_x^2 \\ E_y^2 \\ E_z^2 \\ 2E_yE_z \\ 2E_xE_z \\ 2E_xE_y \end{pmatrix} \tag{3.41}$$

With $\chi_{xxz} = \chi_{xzx} = \chi_{yyz} = \chi_{yzy}$, $\chi_{zxx} = \chi_{zyy}$.

This equation is deduced from equations (23) and (25) of Sipe and from the Table III which describes the elements Δ_{ijk}. It allows calculating the components of the nonlinear polarization at the interface, along the (x, y, z) axes.

$$P_x^{surf} = 2\epsilon_0 \chi_{xxz} f_s f_c E_p^2 \tag{3.42}$$

$$P_y^{surf} = 2\epsilon_0 \chi_{xxz} f_s E_s E_p \tag{3.43}$$

$$P_z^{surf} = \epsilon_0 \chi_{zxx} E_s^2 + \epsilon_0 (\chi_{zxx} f_c^2 + \chi_{zzz} f_s^2) E_p^2 \tag{3.44}$$

As seen in the literature in Chapter 2, the main response term to characterize high-k dielectric layers passivation on silicon by SHG, is the one that describes the EFISH phenomenon. Therefore, it will be explained and added to the dipole polarization equations in the next section.

3.4.2 EFISH source inclusion

In semiconductor materials, a surface electric field, E_{DC}, exists in the space charge region, caused by the charge separation, and directed along the z-axis. E_{DC} gives rise to a new term in the dipole polarization expressions that depends on a fourth rank tensor, $\chi^{(3)}$ [17], [21]. $\chi^{(3)}$ has 81 components in total. In Si(100), 18 of them are non-vanishing and three are independent [22]. Due to mirror symmetry near the dielectric-silicon interface, where E_{DC} is induced, the second-order polarization is expressed as follows [22], [23]:

$$P_x^{surf} = 2\epsilon_0 (\chi_{xxz} + \chi_{xxzz}^{(3)} E_{DC}) f_s f_c E_p^2 \tag{3.45}$$

$$P_y^{surf} = 2\epsilon_0 (\chi_{xxz} + \chi_{xxzz}^{(3)} E_{DC}) f_s E_s E_p \tag{3.46}$$

$$P_z^{surf} = \epsilon_0 (\chi_{zxx} + \chi_{zxxz}^{(3)} E_{DC}) E_s^2 + \epsilon_0 [(\chi_{zxx} + \chi_{zxxz}^{(3)} E_{DC}) f_c^2 + (\chi_{zzz} + \chi_{zzzz}^{(3)} E_{DC}) f_s^2] E_p^2 \tag{3.47}$$

The independent components are :

$$\chi_{xxzz}^{(3)} = \chi_{xzxz}^{(3)} = \chi_{yyzz}^{(3)} = \chi_{yzyz}^{(3)} = \chi_{xxyy}^{(3)} = \chi_{xyxy}^{(3)} = \chi_{yyxx}^{(3)} = \chi_{yxyx}^{(3)} = \chi_{xyyx}^{(3)} \tag{3.48}$$

$$\chi^{(3)}_{zxxz} = \chi^{(3)}_{xzzx} = \chi^{(3)}_{yzzy} = \chi^{(3)}_{zyyz} = \chi^{(3)}_{yxxy} = \chi^{(3)}_{xyyz}$$
$$\chi^{(3)}_{zzzz} = \chi^{(3)}_{xxxx} = \chi^{(3)}_{yyyy}$$

In general, $\chi^{(3)}$ ($\sim 10^{-22}$ m^3.V^{-2} [17]) values are lower than $\chi^{(2)}$($\sim 10^{-18} - 10^{-19}$ m^2.V^{-1} [24]). However, when the E_{DC} is strong, as in the case of high-k dielectric-semiconductor interfaces ($\sim 10^5$ V.cm^{-1} [25]–[27]), the EFISH contribution becomes dominant. Whereas when studying silicon substrates even if E_{DC} is "weak" ($\sim 10^3$ V.cm^{-1} [28]), the EFISH term is simply comparable with the second order susceptibility terms. Moreover, E_{DC} can be time-dependent (TD), so for a TD-SHG curve, the response versus time comes explicitly from E_{DC}. To study the light polarization effect in such a curve, the total nonlinear polarizations, including bulk, surface and EFISH contributions, of the four main sources are shown below, with the rotation angle considered null. For a P-polarized fundamental beam $E_s = 0$ and for S-polarized fundamental beam $E_p = 0$.

$$P^{total}_{P_{in}-P_{out}} = -jk_0 n\epsilon_0[\xi\,(F_s f_c f_s^2 + F_c f_s f_c^2) + 2\gamma(F_s f_c + F_c f_s)] + \epsilon_0 F_s\left[\left(\chi_{zxx} + \chi^{(3)}_{zxxz}E_{DC}(t)\right)f_c^2 + \left(\chi_{zzz} + \chi^{(3)}_{zzzz}E_{DC}(t)\right)f_s^2\right] - 2\epsilon_0 F_c(\chi_{xxz} + \chi^{(3)}_{xxzz}E_{DC}(t))f_s f_c \quad (3.49)$$

$$P^{total}_{S_{in}-P_{out}} = -2jnk_0\epsilon_0\gamma(F_s f_c + F_c f_s) + \epsilon_0 F_s(\chi_{zxx} + \chi^{(3)}_{zxxz}E_{DC}(t)) \quad (3.50)$$

$$P^{total}_{P_{in}-S_{out}} = 0 \quad (3.51)$$

$$P^{total}_{S_{in}-S_{out}} = 0 \quad (3.52)$$

In the equations, P_{in}/S_{in} refer to the polarization state of the pump laser (at the fundamental frequency) and P_{out}/S_{out} correspond to the polarization state of the SH signal which is monitored. These equations show a strong time dependency for the P-polarized second harmonic beam, for both cases of P- and S-polarized fundamental beam. This behavior is confirmed by the experimental study (black and red signals) shown in Figure 3.7. In this experiment, a Si (100) wafer with native oxide has been used. Conversely, for S-polarized SH beam, the equations announce no response for the two configurations P_{in}-S_{out} and S_{in}-S_{out}, which is observed experimentally on the green and blue signals.

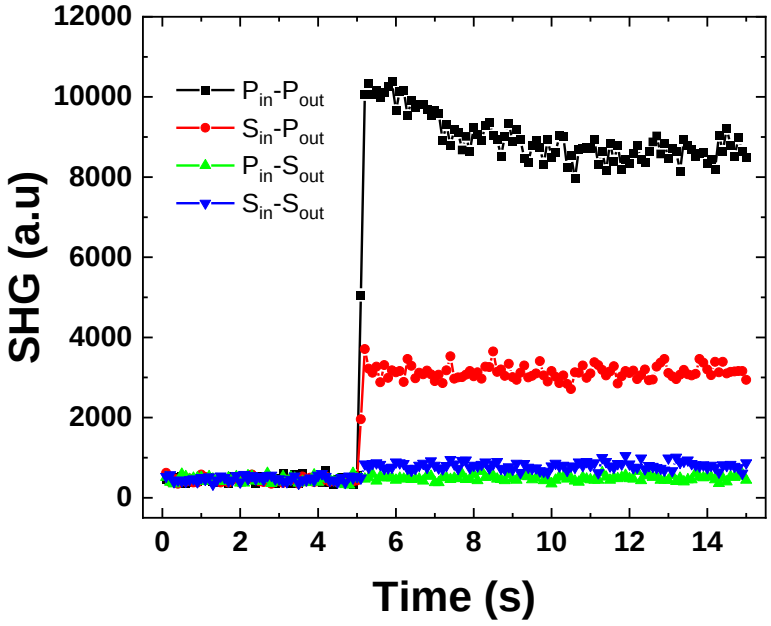

Figure 3.7 : *Time-dependent SHG experimental results in the four main polarization configurations from a Si(100) substrate. During the first 5 s, the laser was blocked. The experimental parameters used are: laser with a wavelength* λ*= 780 nm and a power of 100 mW, 45° angle of incidence and 0° rotation angle.*

To complete our model for the calculation of the SHG intensity, we must compute how the SH signal generated by these NL polarization sources propagate inside the multilayer structure. This requires the study of nonlinear boundary conditions.

3.4.3 Nonlinear boundary conditions

The $P^{NL}(2\omega)$ created inside the material is a source term added to the nonlinear boundary conditions, as shown by Bloembergen and Pershan [3]. So, the boundary conditions between two successive media will take into account the total nonlinear source terms (bulk and surface related).

Similarly to linear optics, we assume that the media are non-magnetic and the electric charge density is zero. The boundary conditions are different whether the outgoing wave is P or S polarized.

i. Bulk contribution in the boundary conditions

The equations in this section are derived from publication [3]. However, they could not be directly taken from the article and a long calculation of several pages was performed to find each equation within our notations and the nonlinear polarization components described earlier, for both P_{out} and S_{out}. Moreover, the equations here are developed to adapt multilayer structures. After determining our equations, we converted them from centimetre–gram–second system of units (CGS) to international system of units (SI) using reference [29]; this necessitated additional calculation work. In the next sections, we'll only give the final equations.

A. For P_{out}-polarization

We start from Bloembergen equations resulting boundary conditions involving the amplitudes of electric fields at 2ω (E_i^+, E_i^-, E_j^+, E_j^- in Figure 3.2b, $D^{\pm}$ in eq. (3.3), transformed into SI units are:

$$N_i(E_i^+ + E_i^-) + n_i \frac{f_{ci}P_{xi}^B + f_{si}P_{zi}^B}{\epsilon_0(n_i^2 - N_i^2)} = N_j(E_j^+ + E_j^-) + n_j \frac{f_{cj}P_{xj}^B + f_{sj}P_{zj}^B}{\epsilon_0(n_j^2 - N_j^2)} \quad (3.53)$$

$$F_{ci}(E_i^+ - E_i^-) - \frac{P_{xi}^B N_i^2 F_{ci}^2 + P_{zi}^B f_{ci} f_{si} n_i^2}{\epsilon_0 N_i^2 (n_i^2 - N_i^2)} = F_{cj}(E_j^+ - E_j^-) - \frac{P_{xj}^B N_j^2 F_{cj}^2 + P_{zj}^B f_{cj} f_{sj} n_j^2}{\epsilon_0 N_j^2 (n_j^2 - N_j^2)} \quad (3.54)$$

The terms P^B correspond to the nonlinear polarization source term due to the bulk contribution, which is the sum $P^{B-aniso} + P^{B-iso}$. Unlike the original publication, where the nonlinear medium was explicitly located below a linear medium, we have written the previous equations so that the nonlinear medium can be either i or j. If i or j are linear, the corresponding bulk polarization term P_i^B or P_j^B is set to zero.

Note that for SH waves at boundaries, where $P^{NL} \neq 0$, the tangential electric field is no longer continuous, because of the source terms associated to P^{NL}.

B. For S_{out} polarization

Similarly, for S-polarized SH waves, the relations between amplitudes of electric fields at the interface between media i and j are:

$$(E_i^+ + E_i^-) + \frac{P_{yi}^B}{\epsilon_0(n_i^2 - N_i^2)} = (E_j^+ + E_j^-) + \frac{P_{yj}^B}{\epsilon_0(n_j^2 - N_j^2)} \quad (3.55)$$

$$N_i F_{ci}(E_i^+ - E_i^-) - \frac{n_i f_{ci} P_{yi}^B}{\epsilon_0(n_i^2 - N_i^2)} = N_j F_{cj}(E_j^+ - E_j^-) - \frac{n_j f_{cj} P_{yj}^B}{\epsilon_0(n_j^2 - N_j^2)} \quad (3.56)$$

In these equations, the quantities E_i^+, E_i^-, E_j^+, E_j^- are the amplitudes of the electric fields of the SH waves in media i and j and they correspond to the $C^{\pm}$ amplitudes in eq. (3.3).

ii. Surface electric dipoles contribution in boundary conditions

The main source of SHG is the dipolar contribution at the interface, where the inversion symmetry is broken. Since other contributions of the interface may also exist, we follow Sipe et al. [9] to account for the various physical phenomena giving rise to SHG at the interface, using an effective surface dipole polarization density P^{Surf}.

To study the nonlinear surface contribution on the SH field, the model proposed by Bloembergen and Pershan [3] was used. This model considers the surface as a thin transition layer of thickness d between two media i and j.

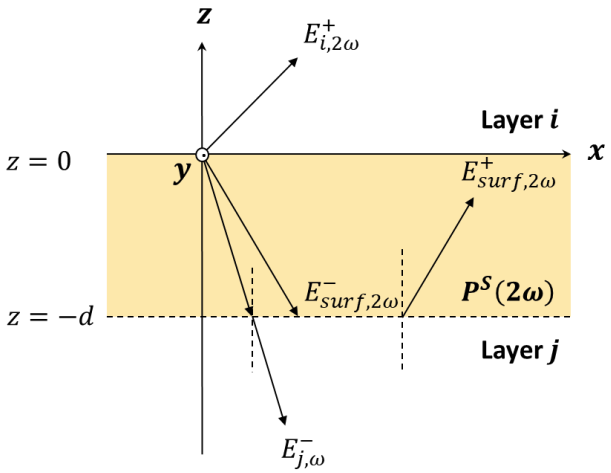

Figure 3.8 : *The interaction of waves within a thin layer that models a surface effect.*

Outside the thin layer, no nonlinear source is considered. When $-d < z < 0$, the NL polarization source term is identical to the one described in section 3.4.1. This NL

polarization $P^S(2\omega)$ creates inhomogeneous waves at the SH frequency. We can then use the boundary conditions and the propagation equations in order to determine the radiations transmitted in media i and j. More explicitly, Bloembergen's [3] equations define the continuity of electric and magnetic fields at each interface at both $z = 0$ (i.e. between air and thin layer) and at $z = -d$ (i.e. between material and thin layer). These equations, with the phase shifts of the inhomogeneous and homogeneous waves can be used to deduce the boundary conditions applied between two layers i and j for any media, under the condition $d << \lambda$. In the expressions of the boundary conditions, a surface polarization term noted P^{surf} appears:

$$P^{surf} = d.P^S(2\omega). \tag{3.57}$$

Where $P^S(2\omega)$ is the nonlinear polarization induced by the incident wave inside the medium, based on the dipolar interaction with the lattice.

Following this method and Bloembergen equations, we obtained for P_{out} polarization:

$$N_i(E_i^+ + E_i^-) = N_j(E_j^+ + E_j^-) - \frac{jK_0}{\epsilon_0}(P_{xi}^{Surf} + P_{xj}^{Surf}) \tag{3.58}$$

$$F_{ci}(E_i^+ - E_i^-) = F_{cj}(E_j^+ - E_j^-) + \frac{jK_0}{\epsilon_0}\left(\frac{f_{si}n_iP_{zj}^{Surf}}{N_i^2} + \frac{f_{sj}n_jP_{zi}^{Surf}}{N_j^2}\right) \tag{3.59}$$

Similarly for S_{out} polarization, the boundary conditions between layers i and j are:

$$(E_i^+ + E_i^-) = (E_j^+ + E_j^-) \tag{3.60}$$

$$N_iF_{ci}(E_i^+ - E_i^-) = N_jF_{cj}(E_j^+ - E_j^-) + jK_0\frac{P_{yi}^{Surf}}{\epsilon_0} + jK_0\frac{P_{yj}^{Surf}}{\epsilon_0} \tag{3.61}$$

iii. Final nonlinear boundary conditions

The final equations of the boundary conditions that take into account the total nonlinear source terms (bulk and surface related), for two layers "i" and "j" in the multilayer can be given:

A. For P_{out} polarization

For an outgoing P-polarization, equations (3.53) and (3.54), which contain the volume source term, combined with equations (3.58) and (3.59), which contain the surface source term, give access to the general boundary conditions of any interface between two layers in a multilayer structure:

$$N_i(E_i^+ + E_i^-) + n_i \frac{f_{ci}P_{xi}^B + f_{si}P_{zi}^B}{\epsilon_0(n_i^2 - N_i^2)} = N_j(E_j^+ + E_j^-) + n_j \frac{f_{cj}P_{xj}^B + f_{sj}P_{zj}^B}{\epsilon_0(n_j^2 - N_j^2)} - jK_0 \frac{P_{xi}^{Surf} + P_{xj}^{Surf}}{\epsilon_0} \quad (3.62)$$

$$F_{ci}(E_i^+ - E_i^-) - \frac{P_{xi}^B N_i^2 F_{ci}^2 + P_{zi}^B f_{ci} f_{si} n_i^2}{\epsilon_0 N_i^2 (n_i^2 - N_i^2)} = F_{cj}(E_j^+ - E_j^-) - \frac{P_{xj}^B N_j^2 F_{cj}^2 + P_{zj}^B f_{cj} f_{sj} n_j^2}{\epsilon_0 N_j^2 (n_j^2 - N_j^2)} + jK_0 \left(\frac{f_{si} n_i P_{zj}^{Surf}}{\epsilon_0 N_i^2} + \frac{f_{sj} n_j P_{zi}^{Surf}}{\epsilon_0 N_j^2} \right) \quad (3.63)$$

B. For S_{out}-polarization

For a polarization S_{out}, the boundary conditions with the volume terms (equations (3.55) and (3.56)) and surface ones (equations (3.60) and (3.61)) are:

$$(E_i^+ + E_i^-) + \frac{P_{yi}^B}{\epsilon_0(n_i^2 - N_i^2)} = (E_j^+ + E_j^-) + \frac{P_{yj}^B}{\epsilon_0(n_j^2 - N_j^2)} \quad (3.64)$$

$$N_i F_{ci}(E_i^+ - E_i^-) - \frac{n_i f_{ci} P_{yi}^B}{\epsilon_0(n_i^2 - N_i^2)} = N_j F_{cj}(E_j^+ - E_j^-) - \frac{n_j f_{cj} P_{yj}^B}{\epsilon_0(n_j^2 - N_j^2)} + jK_0 \frac{P_{yi}^{Surf} + P_{yj}^{Surf}}{\epsilon_0} \quad (3.65)$$

In the case where the nonlinear material is layer "i", the properties of the nonlinearity used are those of the medium "i" and the terms of the nonlinear polarization of the medium "j" is zero, and vice versa.

iv. Example of a second harmonic electric field distribution in a multilayer

Using the nonlinear boundary conditions, we study the SH electric field distribution in the same SOI structure used in section 3.3.2, for both P_{out} and S_{out} polarizations, with the input polarization angle set to 45°. We choose this angle because in the case of 0° (P_{in}) and 90° (S_{in}), there is no second harmonic response for S_{out}-polarization according to equations (3.51) and (3.52). The other parameters for the simulation are: SH wavelength of 390 nm and angle of incidence of 45°. No EFISH contribution is taken into account to obtain these curves. For both cases in Figure 3.9, the field oscillates in a periodic sinusoidal way due to the interferences between upward and downward waves. In Si layers, the amplitude of the oscillations is not constant due to the absorption. The difference in refractive indices and the source term cause the discontinuity seen in the case of P_{out} during the transition between two different layers. In the case of S_{out}, we can explain the continuity by eq. (3.64), where the bulk nonlinear polarization is very weak, almost negligible in comparison to the total field.

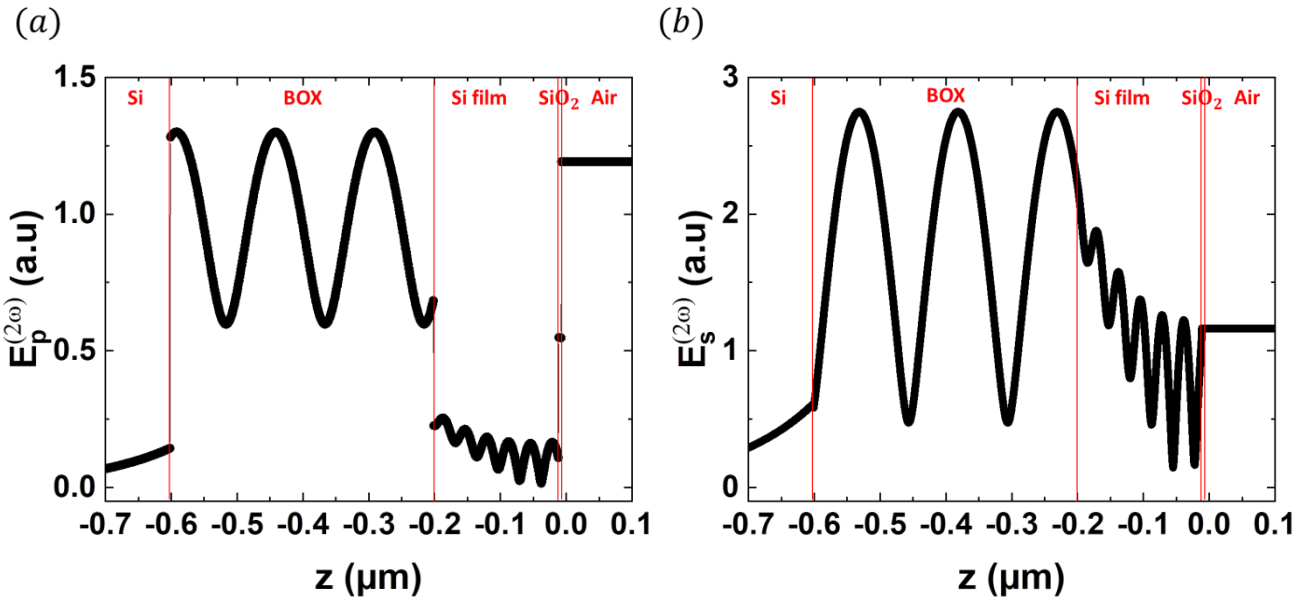

Figure 3.9: *SH electric field distribution in SOI structure for* ***(a)*** *45°-P_{out} configuration and* ***(b)*** *45°-S_{out} configuration.*

3.5 Analytical validation of SH equations

Before incorporating the above-mentioned equations into a simulation model, we will validate them by performing an analytical calculation of SH electric fields in a simple structure of Si(100) that was previously studied by Sipe et al. [9]. To calculate the surface polarization and the reflected SH wave, two interface geometries can be considered:

- The first follows Sipe's approach (Figure 3.10a) and supposes that the dipole sheet is placed in the air at z = 0^+, just above the interface which is in z = 0. The optical properties are those of the nearby substrate, i.e. Si.

- The second approach follows Bloembergen and Pershan [3] and assumes that the generated nonlinear polarization is placed in the substrate, at the nonlinear interface between two linear materials as shown in Figure 3.10b.

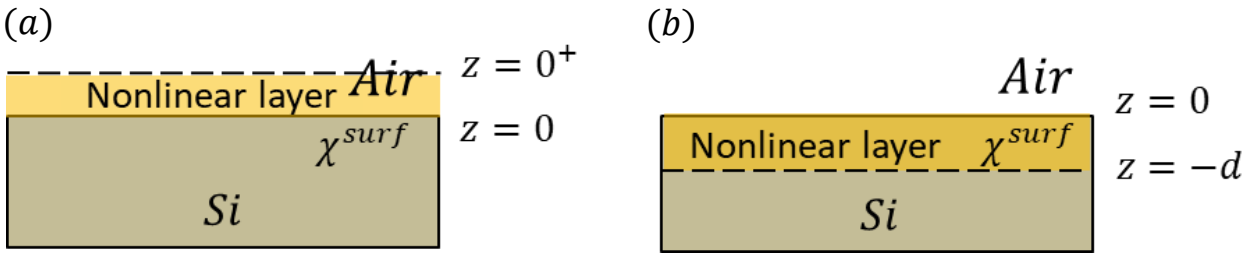

Figure 3.10: *Two configurations of the interface geometry* ***(a)*** *The nonlinear region is located above the nonlinear material.* ***(b)*** *The nonlinear region is located at the silicon surface while the other layer is linear.*

Sipe's approach of Figure 3.10a provides directly the reflected fields expressions, while Bloembergen (Figure 3.10b) deals with the boundary conditions. We based our multilayer calculations on the boundary conditions as given by Bloembergen et al. These conditions will be used to calculate the reflected SH fields and verify that they agree with Sipe's expressions.

The reflected SH fields, which come from the bulk and the air-Si interface sources are calculated, for both P_{out} and S_{out} cases. Considering a semi-infinite substrate, the physical boundary conditions are: no SH wave incident in $z = 0$ on the substrate ($E^{-}_{air,2\omega} = 0$) and no SH wave reflected from the bottom of the thick substrate $E^{+}_{Si,2\omega} = 0$.

Solving the bulk source boundary conditions (3.51) with (3.54), and (3.55) with (3.56) gives access to the reflected generated SH fields in the air for the P_{out} and S_{out} polarizations, respectively:

For P_{out} polarization: $$E^{+}_{air,bulk} = \frac{-1}{\epsilon_0(F_{Ci}N_j + F_{Cj})(n_j f_{Cj} + N_j F_{Cj})}[P_{zj}F_{sj} - P_{xj}F_{Cj}] \quad (3.66)$$

For S_{out} polarization: $$E^{+}_{air,bulk} = \frac{-1}{\epsilon_0(F_{Ci} + F_{Cj}N_j)(n_j f_{Cj} + N_j F_{Cj})}P_{yj} \quad (3.67)$$

The equations (3.66) and (3.67) in SI units are identical to those of Sipe in CGS system [29].

Likewise, to determine the equations of SH reflected in the air coming from the surface source, the boundary conditions (3.58) with (3.59), and (3.60) with (3.61) give the following equations for the P_{out} and S_{out} polarizations, respectively:

For P_{out} polarization:
$$E^{+}_{air,surface} = \frac{1}{\epsilon_0(F_{Ci}N_j + F_{Cj})}(iK_0\, N_j^2 F_{sj} P^{Surf}_{zj} - iK_0\, F_{cj} P^{Surf}_{xj}) \quad (3.68)$$

For S_{out} polarization:
$$E^{+}_{air,surface} = \frac{1}{\epsilon_0\left(F_{Ci} + F_{Cj}N_j\right)}(iK_0\, P^{Surf}_{yj}) \quad (3.69)$$

Again, these equations are also identical to Sipe's equations. So, this demonstrates analytically that our equations for a simple structure of Si are equivalent to previous results in the literature. These equations are used to build a simulation code adapted for multilayer structures; its flow will be discussed in the following section.

3.6 Numerical procedure

Before my thesis, the team had developed a numerical code implemented in Matlab [20]. This code was the starting point of this work. Since we have created a coherent model, we modified the simulation accordingly. We briefly give the modifications made in Table 3.1.

Table 3.1: *Modeling and simulation modification during the thesis.*

	Previous model and simulation	Our modification
Layer number	3 or 5	From 2 to n
Input polarization angle selection	0° or 90°	From 0° to 90°
Nonlinear polarization Source terms	Global expressions for P_{out} and S_{out}: $P_{P_{out}}$ $P_{S_{out}}$	Separating bulk and surface contributions and recompose them along x, y and z, for both P_{out} and S_{out}: $P_x^{bulk\ aniso}$, $P_y^{bulk\ aniso}$, $P_z^{bulk\ aniso}$ $P_x^{bulk\ iso}$, $P_y^{bulk\ iso}$, $P_z^{bulk\ iso}$ P_x^{surf}, P_y^{surf}, P_z^{surf}
	Only the source term ($\chi^{(3)}_{zzzz} E_{DC}(t)$) was taken into account in the EFISH	The EFISH source term is added to all surface components (as shown in section 3.4.2)
	The nonlinear sources were calculated using the light electric fields located at the end of each layer near the interface.	The nonlinear sources are calculated using the light electric fields located at the beginning or the end of the layers depending on where is the nonlinear layer as we will see later.
Nonlinear boundary conditions	Given in [14] and adapted to the global expression for P_{out} and S_{out}	Given in section 3.4.3 and adapted to our nonlinear source expressions
Time-dependence SHG	–	Introduced in the simulation (shown in the perspectives section of thesis) It may be used and developed for future study of interface states

The program flow is described in Figure 3.11a: the red blocks represent the calculation steps of the electric fields at the fundamental wavelength (in our case, $\boldsymbol{\lambda}$=780 nm). The orange block represents the SHG source terms calculation. The purple blocks are the steps for determining the SH beams generated at 390 nm. The iteration steps of the main function which calculates the propagation of optical electric fields in the multilayer are depicted in Figure 3.11b. This calculation algorithm is employed for both the fundamental and SH beams.

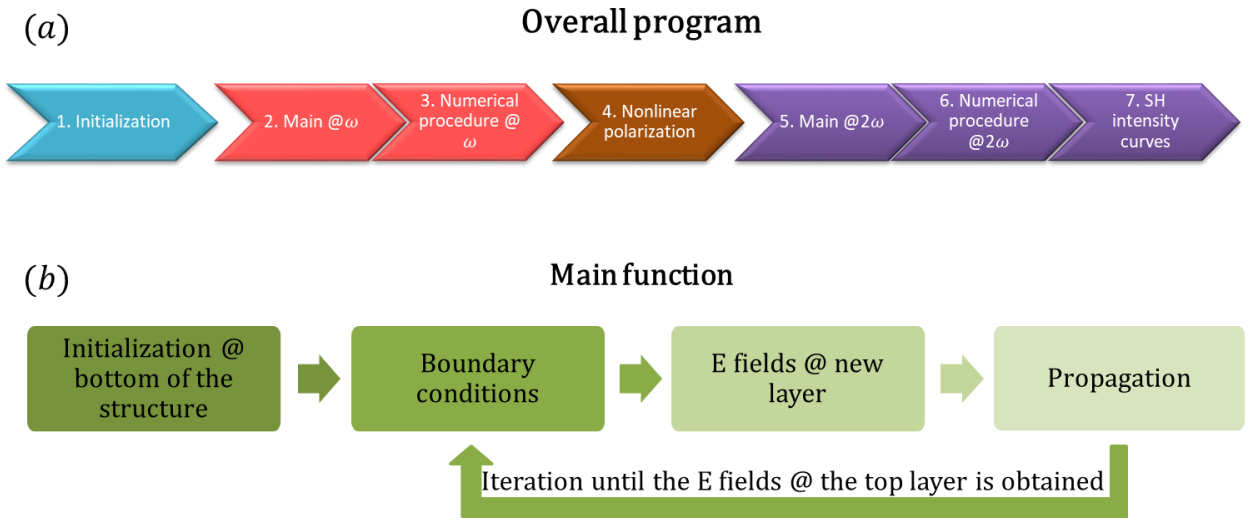

Figure 3.11: *Simulation execution for:* ***(a)*** *overall program and* ***(b)*** *main functions [14].*

The program flow steps are given as follows:

1- Initialization

We define all the numerical parameters such as:

- Incident laser beam parameters: wavelength, power, repetition rate, pulse duration, beam radius and focal length.
- Setup parameters: angle of incidence θ_0, input- and output- light polarization angles.
- Materials parameters and properties such as: azimuthal angle ϕ, refractive indices, second and third order susceptibility tensors, layer thicknesses, interface "static" electric fields.

We choose the number of layers and start numbering from the bottom, as shown in Figure 3.12, because it is easier to set any desired number of layers.

Calculation of fundamental electric fields

2- Main function execution at ω

The main function in Figure 3.11b runs to calculate the reflected and transmitted electric fields at fundamental frequency at each position in the structure.

i. The electric fields values are initialized from the bottom of the structure (substrate), E_1^+, E_1^- in Figure 3.12.
ii. These fields cross the interface by respecting the linear boundary conditions, which allows to obtain those at the beginning of the next layer.
iii. The electric fields propagate up until they reach the end of the layer.
iv. This algorhythm is repeated until calculating the electric fields of the top layer (air).

3- Numerical procedure at ω

It should be noted that from the practical point of view, the known field is that of the incident laser ($E_m^- = E_0$) and no fields enter from the substrate ($E_1^+ = 0$). Therefore, from these physical boundary conditions, a numerical method is used to determine the value of the transmitted field at E_1^- from which we begin the calculation. We treat the problem using the matrix formalism [14], [30]:

$$\begin{pmatrix} E_m^+ \\ E_m^- \end{pmatrix} = \begin{pmatrix} A & B \\ C & D \end{pmatrix} \begin{pmatrix} E_1^+ \\ E_1^- \end{pmatrix} \tag{3.70}$$

ABCD matrix contains all the propagation phenomena such as reflection and transmission inside each layer, as well as the linear boundary conditions at each interface.

With $E_1^+ = 0$, we have:

$$\begin{aligned} E_m^+ &= BE_1^- \\ E_m^- &= DE_1^- \end{aligned} \tag{3.71}$$

Based on the relationship between the fields at the bottom and top of the structure, the main function should run twice, as shown in Figure 3.12:

1- We start with $(E_1^-)_1 = 1$, to calculate the incident electric field $(E_m^-)_1$, which will be used to find the real value for the second execution.
2- We enter the correct initial value $(E_1^-)_2 = E_0/(E_m^-)_1$ to calculate the fundamental electric fields for the rest of structure.

This method is performed for the two cases of P_{out}- and S_{out}-polarization, using the compatible boundary conditions which are given in eqs. (3.24)-(3.25) and (3.30)-(3.31), respectively. Thus, the total electric field strength, E_p and E_s, are both

calculated at each position in the structure in order to determine the nonlinear sources that depend on them.

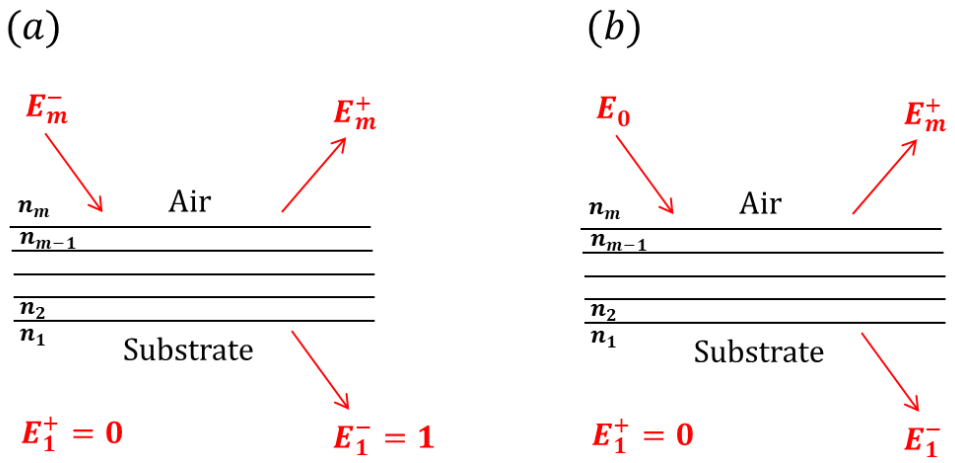

Figure 3.12: *Fundamental wavelength physical boundary conditions for* ***(a)*** *the first execution with an arbitrary starting value* for E_1^-. ***(b)*** *The second execution with* E_m^- *value corresponding to the realistic incident fie*ld E_0.

4- Nonlinear polarization

In multilayer structures, there can be both nonlinear and linear media. As a result, as illustrated in Figure 3.13, the nonlinear polarization is calculated on both sides of the interface based on the electric fields located there and the nonlinear polarization considered is the one located in the nonlinear medium.

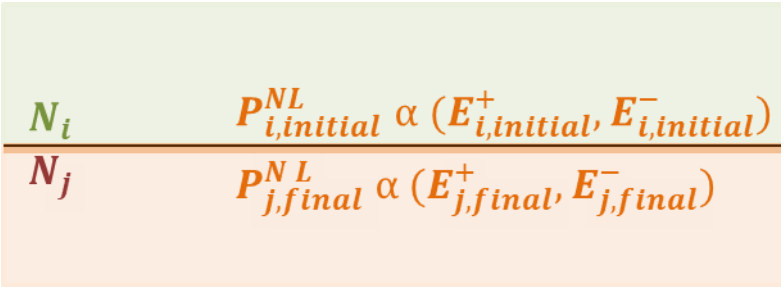

Figure 3.13: *Source of the nonlinear polarization at the interface.*

Calculation of second harmonic electric fields

5- Main function execution at 2ω

The procedure for running the main function at the SH frequency works like that at the fundamental frequency, which was described previously in the second part and in Figure 3.11b.

6- Numerical procedure at 2ω

The numerical procedure for calculating SH fields is explained by the following matrix:

$$\begin{pmatrix} E_m^+ \\ E_m^- \end{pmatrix} = \begin{pmatrix} \mathrm{U} \\ \mathrm{V} \end{pmatrix} + \begin{pmatrix} A & B \\ C & D \end{pmatrix} \begin{pmatrix} E_1^+ \\ E_1^- \end{pmatrix} \tag{3.72}$$

This equation differs from eq.(3.70) by the additional vectors (U, V) which describe the nonlinear polarization source terms calculated in the previous step. The physical boundary conditions for SH light are: no light at 2ω entering the structure from outside, either from bottom or from top, i.e. $E_1^+ = 0$ and $E_m^- = 0$. For the first case with $E_1^+ = 0$, eq.(3.72) becomes:

$$\begin{aligned} E_m^+ &= \mathrm{U} + BE_1^- \\ E_m^- &= \mathrm{V} + DE_1^- \end{aligned} \tag{3.73}$$

Based on these equations, the main function must be run three times, as shown in Figure 3.14, in order to calculate the SH electric fields in the structure:

1- With assuming $(E_1^-)_1 = 0$ (see Figure 3.14a), we find U and V values.

2- Entering an arbitrary value for E_1^- ($(\mathrm{E}_1^-)_2 = 1$ for example in Figure 3.14b), gives B and D values.

3- By imposing the second condition $E_m^- = 0$, we find the correct initial value of E_1^- inferred from the two previous executions: $E_1^- = \frac{(E_m^-)_1}{(E_m^-)_1 - (E_m^-)_2}$. In this execution, it is possible to calculate the SH electric fields at each position inside the structure.

This method is used for the P- and S-polarization cases, using the nonlinear polarizations and boundary conditions corresponding to each case.

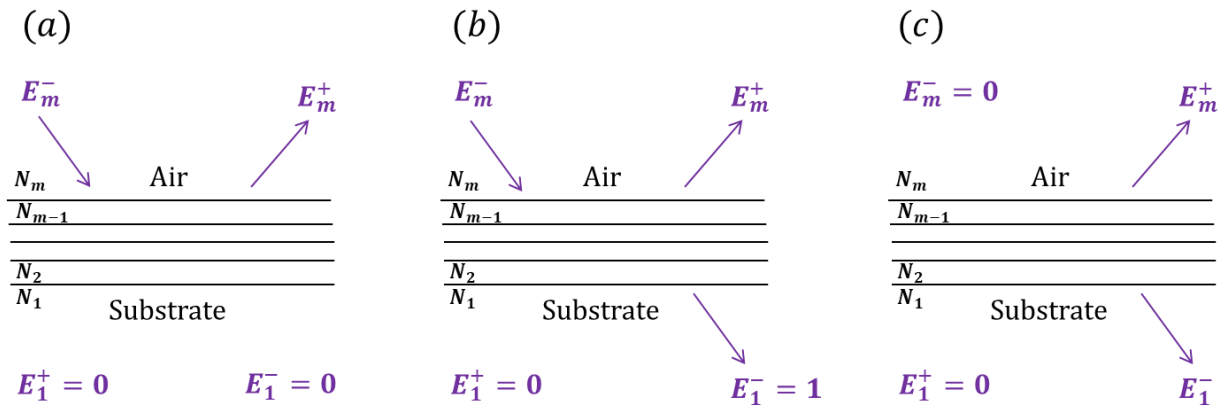

Figure 3.14: *SH physical boundary conditions for* ***(a)*** *the first execution with* $E_1^- = 0$, ***(b)*** *the second execution with arbitrary starting value for* $E_1^- = 1$ *and* ***(c)*** *the third execution with* E_m^- *value corresponding to the realistic incident field equal to zero.*

7- SH intensity curves

The last step is to plot the SHG light intensity versus any desired parameter or structural property.

In the following section, we will compare some simulated curves with the experimental ones for bilayer and multilayer structures to ensure that our simulation model is correct and can be applied to the multilayers.

3.7 Modeling validation thanks to simulation versus experiments

To validate the ability of our numerical method to reproduce the experimental results, we study two structures: a simple Si(100) and a multilayer SOI. The simulation respects all the experimental parameters and the properties of the studied materials. The experimental SHG measurements were carried out with a pulsed femtosecond laser (~90 fs) of fundamental wavelength λ= 780 nm and an average laser power of 100 mW. The experimental results were performed on the Harmonic F1X tool from Femtometrix [31], which will be shown in detail in the following chapter. The refractive indices of Si and SiO_2 are extracted at 780 nm and 390 nm, which correspond to the experimental pump and SH wavelength, respectively. The values of electric dipole surface and quadrupole bulk susceptibility depend on sample fabrication method and various values can be found in the literature (see Table 3.2). However, the order of magnitude is similar as we will see in Table 3.2 for values extracted by two references [24] and [32].

Table 3.2: *values for the materials properties used in the simulation.*

	Material property	Values extracted from the literature
SiO_2	n_ω	1.4695 [33]
	$N_{2\omega}$	1.4851 [33]
Si	n_ω	3.696+0.006i [34]
	$N_{2\omega}$	6.039+0.445i [34]
	$\chi^{(2)}_{zzz}$	$5.8\text{x}10^{-18}$ m/V [32] $6.5\text{x}10^{-18}$[24]
	$\chi^{(2)}_{xxz}$	$1.2\text{x}10^{-18}$ m/V [32] $0.35\text{x}10^{-18}$[24]
	$\chi^{(2)}_{zxx}+\gamma$	$0.043\text{x}10^{-18}$ m/V [32] $0.13\text{x}10^{-18}$[24]
	ξ	$4.4\text{x}10^{-18}$ m/V [32] $0.23\text{x}10^{-18}$[24]
	$\chi^{(3)}$	$\sim 10^{-22}$ m^2/V^2 [17]

3.7.1 Native SiO_2 on Si(100)

The first studied structure is a simple Si(100) substrate with 2 nm thick native oxide. The nonlinear polarization equations have several parameters that can be varied as shown in section 3.4.1. Here, we chose to investigate SHG versus the input-polarization angle and the angle of incidence, in both experiments and simulations.

Figure 3.15 represents the normalized SHG versus input-polarization angle. Normalization (necessary for comparisons) is done by dividing the experimental and simulation curves by their own maximum. The investigation was carried out for P-output and S-output SH polarization, with the laser focused at 45° incidence angle on the sample surface at 0° azimuthal angle. The EFISH contribution is taken into account in the simulation with a low E_{DC} value of 10^3 $V.cm^{-1}$, making it comparable to the interface second-order contribution. The experimental and simulated curves agree very well, as shown in both cases of Figure 3.15. In the case of P_{out} configuration, the SHG intensity shows a global maximum for input p-polarization (Ψ=0°), a minimum at 55° input-polarization, and a local maximum at the input s-polarization (Ψ=90°). This polarization dependency is associated with the presence of the second order nonlinear surface susceptibility $\chi^{(2)surf}$ components and the $\chi^{(3)}$ components of EFISH contribution. For S_{out} configuration, we see that the maximum of SHG intensity is at Ψ=45°, and that there is no

signal at Ψ=0° and Ψ=90°, which is theoretically expected according to the S_{out} nonlinear polarization equations (3.51) and (3.52).

The normalized SHG intensity as a function of the angle of incidence is illustrated in Figure 3.16, for both P_{in}-P_{out} and S_{in}-P_{out} configurations, with the azimuthal angle set to 0°. Both experimental and simulated curves show an agreement in shape for both configurations.

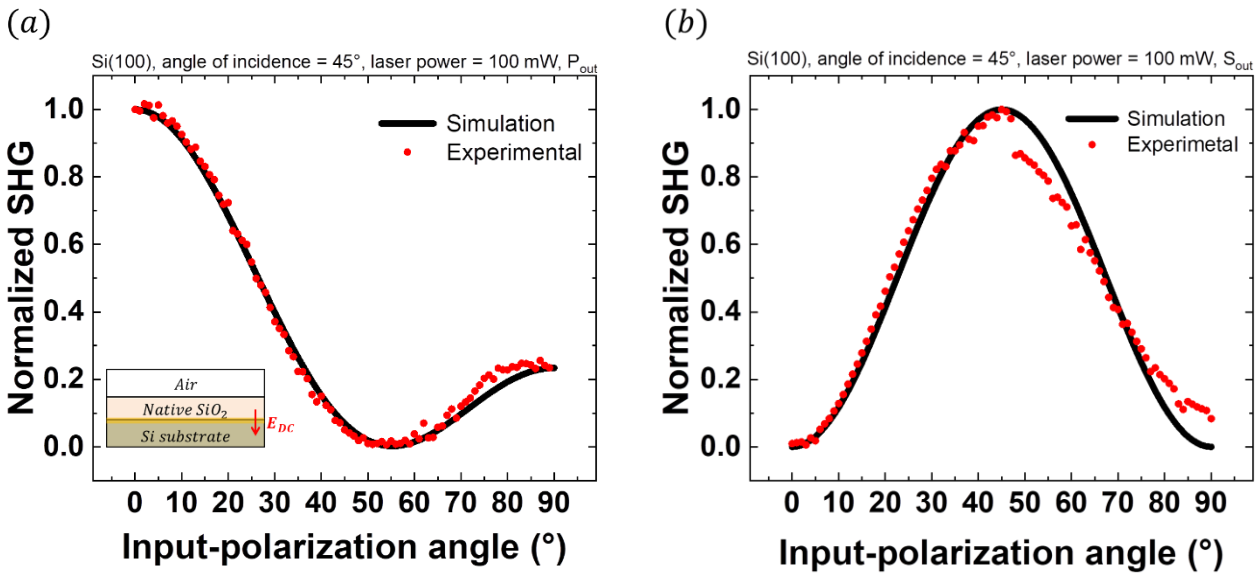

Figure 3.15: *Simulated and experimental normalized SHG intensity versus input polarization angle (Ψ) from Si(100) substrate for* ***(a)*** P_{out} *and* ***(b)*** S_{out}.

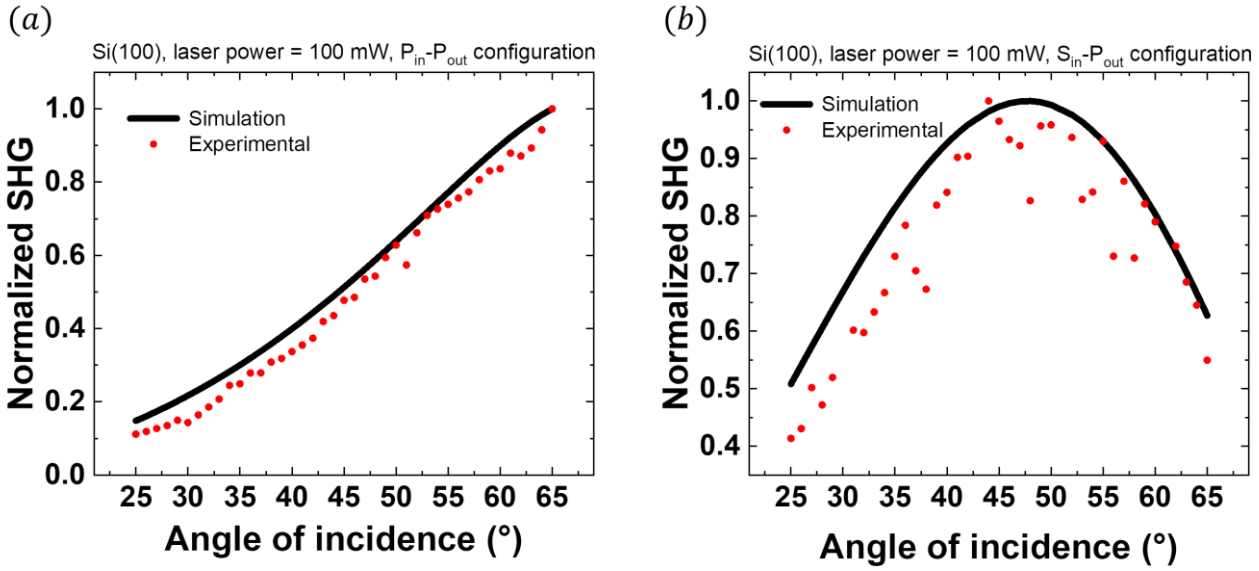

Figure 3.16: *Simulated and experimental normalized SHG intensity versus angle of incidence (θ) from Si(100) substrate for* ***(a)*** P_{in}-P_{out} *configuration and* ***(b)*** S_{in}-P_{out} *configuration.*

3.7.2 SOI structure with top oxide

In the previous study, we confirmed that our numerical model works successfully in a bilayer structure. We'll now apply it to investigate silicon on insulator (SOI) multilayer with 4.5 nm thick top oxide and 26.5 nm thick silicon film on a 190 nm buried oxide (BOX). The SOI stack structure is represented in the inset of Figure 3.17a. A strong EFISH contribution is introduced in the simulation code, with $E_{DC}(1)= 10^3$ V.cm^{-1}, $E_{DC}(2)= 10^4$ V.cm^{-1} and $E_{DC}(3)= 5x10^4$ V.cm^{-1}. The experimental and simulated SHG curves versus input-polarization angle (Figure 3.17) are consistent, as are the SHG curves as a function of the angle of incidence (Figure 3.18). The input-polarization angle dependent SHG in the case of P_{out} only shows a maximum for input p-polarization (Ψ=0°), then the intensity decreases until reaching the minimum for s-polarization (Ψ=90°) unlike for the SiO_2/Si case. Once more, the simulated curves are in excellent agreement with the experimental ones.

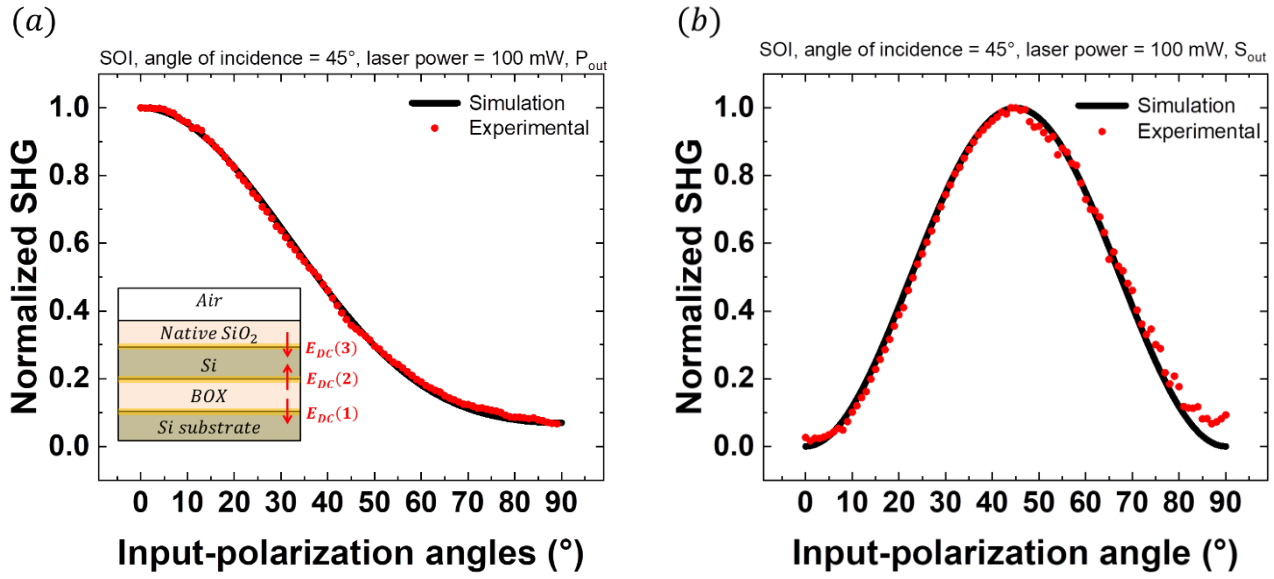

Figure 3.17: *Simulated and experimental normalized SHG intensity versus Ψ from SOI stack for* ***(a)*** P_{out} *and* ***(b)*** S_{out}.

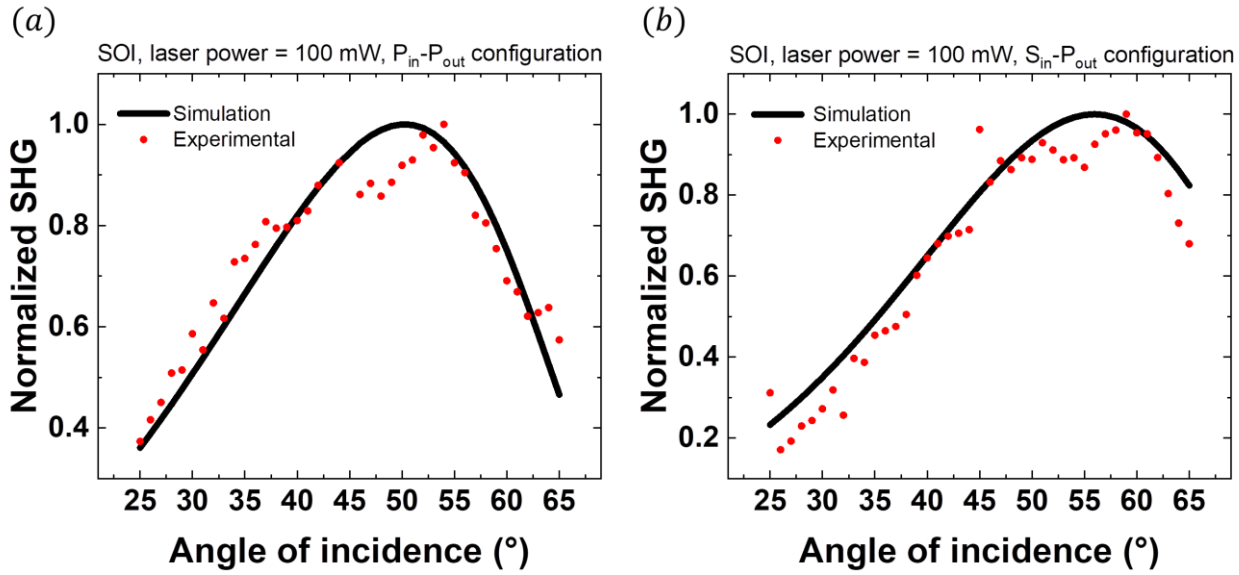

Figure 3.18: *Simulated and experimental normalized SHG intensity versus θ from SOI stack for* ***(a)*** P_{in}-P_{out} *configuration and* ***(b)*** S_{in}-P_{out} *configuration.*

The difference in the shape of the curves between the two structures, Si(100) substrate and SOI stack (see for example Figure 3.15a versus Figure 3.17a), comes from the sensitivity of SHG response to interference phenomena in the silicon layer. To confirm the origin of this difference, a simulation study of the SHG response for different silicon film thicknesses in a SOI structure has been performed. The SH signal for 4 different Si film thicknesses is reported on Figure 3.19a, where the thicknesses used are t=26.5, 185, 190 and 900 nm. The signal at t=26.5 nm was used for the normalization, since it is the same value as in the structure used for experiments and reported on Figure 3.17a. In the case of a very thick Si layer (t=900 nm, red curve in Figure 3.19a), the silicon absorbs light and the SHG response resembles that of the Si(100) substrate as shown in zoomed in in Figure 3.19b. The penetration depths of Si at 390, 780 nm wavelengths are equal to 133 nm, 23 µm, respectively. For the two curves of thickness 185 nm (green) and 190 nm (blue), the large changes are due to the sensitivity of the SHG response to interference phenomena in the silicon layer. These interferences modify the repartition of both exciting light at 780 nm and SH light and are thus difficult to anticipate without the simulation tool.

Figure 3.20 illustrates the comparison of SH electric field distribution between SOI structures with Si film thickness of 26.5 nm (a) and 190 nm (b) at 0°-P$_{out}$ polarizations. Although the BOX thickness is same in both structures, the amplitude of the electric field oscillation in the BOX varies because of a difference in the interferences between the up and

down waves. The oscillations in the Si layers also differ due to the difference in absorption and interference phenomena. The electric field in the air corresponds to the reflected SH beam shown in Figure 3.19. For example, at 0°-P_{out} (Figure 3.20), the output response in curve of 190 nm Si film is higher than that of 26.5 nm Si, confirming the Figure 3.19 with respect to $I_{2\omega} = {E_p}^2$.

Another example is given in Figure 3.21 for the SH electric field distribution at 45°-P_{out}. The curves shows that the sample with 190 nm Si film has very weak SH reflection signal and the sample with 26.5 nm Si has a response lower than the case of at 0°-P_{out} which can be observed in Figure 3.19.

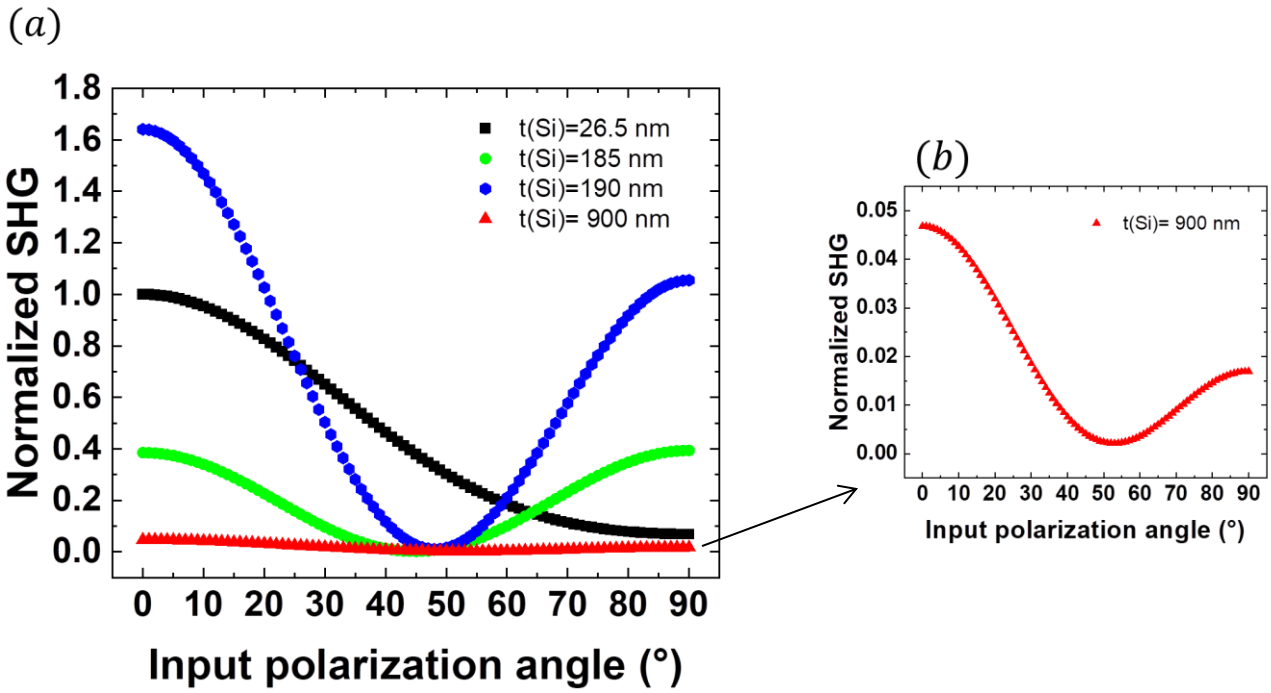

Figure 3.19: (a) *Simulated SHG P_{out} response versus input polarization angle for several silicon film thicknesses in the SOI structure.* ***(b)*** *Zoom in the curve simulated with 900 nm Si film. The angle of incidence used is 45°.*

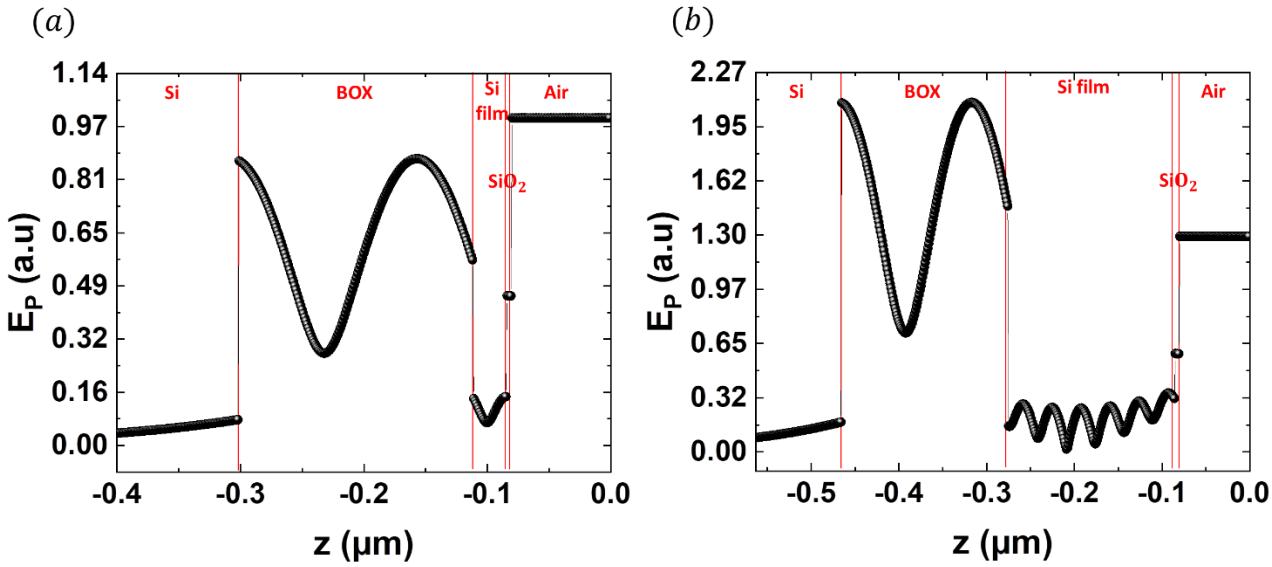

Figure 3.20: *Comparison of SH electric field distribution in SOI structure at 0°-P_{out} configuration for samples of* ***(a)*** *26.5 nm and* ***(b)*** *190 nm Si film thicknesses.*

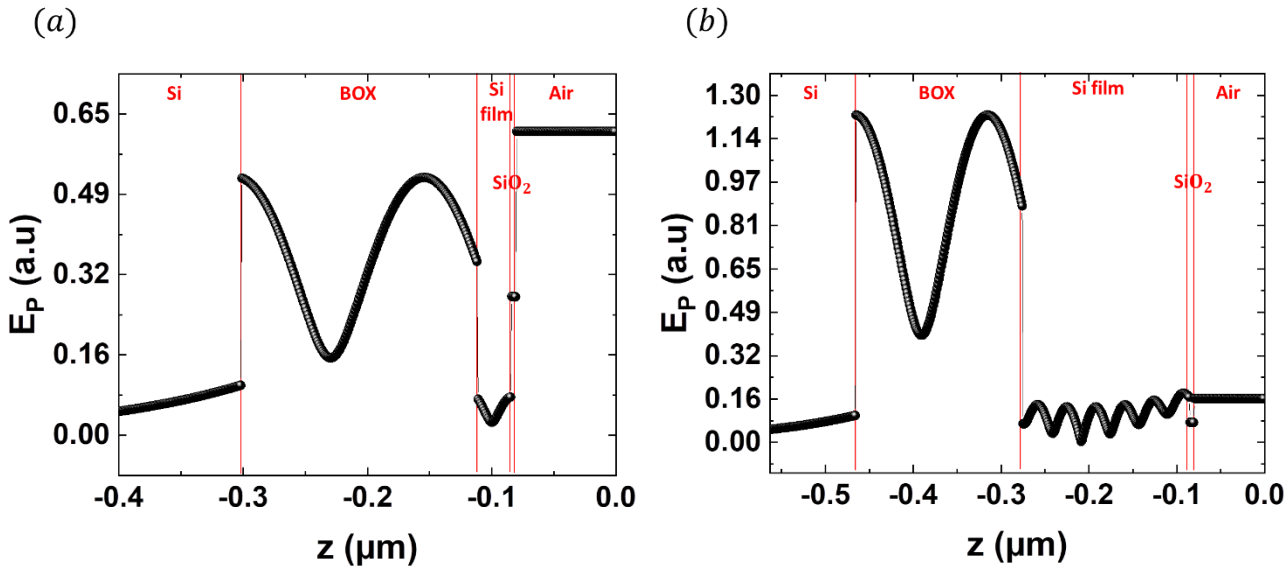

Figure 3.21: *Comparison of SH electric field distribution in SOI structure at 45°-P_{out} configuration for samples of* ***(a)*** *26.5 nm and* ***(b)*** *190 nm Si film thicknesses.*

3.8 Chapter conclusion

This chapter has established the theoretical foundations of the developed model, explaining the linear and the nonlinear optical phenomena that occur in the structure. Additionally, it covered the simulation progress that was implemented and validated. Our study was carried out in the following sequence:

1- The development of a model to calculate the SHG response of a multilayer structure containing linear and nonlinear media. The model is explained in the order:

a- Propagation of fundamental fields by:
- Defining the propagation equations and notations
- Extracting the linear boundary conditions for the fundamental light using Maxwell equations. These conditions allow calculating the transmitted and reflected fundamental electric fields at the interfaces.

b- Calculate of the nonlinear response by:
- The extraction of nonlinear polarization equations for a (100) oriented material. The nonlinear sources were separated by bulk and surface terms and decomposed along x, y, z.
- Adding the additional contribution EFISH term to the nonlinear surface sources.
- Extraction of the nonlinear boundary conditions imposed on the interface based on the literature [3]. These conditions were developed to be adapted with multilayer structures.

2- The model is integrated in a simulation code. The numerical procedure of this code has been discussed.

3- Validation of the model by:
- Analytical calculation of the SHG reflected wave in air from a single silicon substrate previously studied in the literature.
- Comparison between simulations and measurements of SHG as a function of input polarization and incidence angle. It was shown that the simulations reproduce very well the experimental results for the Si and SOI samples. We have seen also that the shape of the SHG curve varies depending on the structure used. Therefore, we demonstrate the ability of our model to successfully determine the SHG response from complex structures.

Finally, the SHG simulations of SOI structures with different Si film thicknesses have shown how different the response could be, because of the variation in interference

phenomena. These results confirm that the optical phenomena play an important role in the SHG response, which has a particularly high impact on multilayers, where even a small variation of thickness can induce a strong variation of global SHG response. Thus, the modeling is necessary to distinguish the electrical phenomena from the optical ones, before extending the use of the SHG as a characterization tool for multilayers.

The simulation will be used later in the thesis to calibrate the experimental measurements and evaluate the silicon passivation quality with high-k dielectrics. Before discussing the measurement results, the experimental methodologies are given in the next chapter.

3.9 Chapter references

[1] N. Bloembergen, R. K. Chang, and C. H. Lee, 'Second-harmonic generation of light in reflection from media with inversion symmetry', Phys. Rev. Lett., vol. 16, no. 22, p. 986, 1966.
[2] N. Bloembergen, R. K. Chang, S. S. Jha, and C. H. Lee, 'Optical second-harmonic generation in reflection from media with inversion symmetry', Phys. Rev., vol. 174, no. 3, p. 813, 1968.
[3] N. Bloembergen and P. S. Pershan, 'Light waves at the boundary of nonlinear media', Phys. Rev., vol. 128, no. 2, p. 606, 1962.
[4] H. W. K. Tom, T. F. Heinz, and Y. R. Shen, 'Second-harmonic reflection from silicon surfaces and its relation to structural symmetry', Phys. Rev. Lett., vol. 51, no. 21, 1983.
[5] D. Guidotti, T. A. Driscoll, and H. J. Gerritsen, 'Second harmonic generation in centro-symmetric semiconductors', Solid State Commun., vol. 46, no. 4, pp. 337–340, 1983.
[6] T. A. Driscoll and D. Guidotti, 'Symmetry analysis of second-harmonic generation in silicon', Phys. Rev. B, vol. 28, no. 2, p. 1171, 1983.
[7] T. F. Heinz, M. M. Loy, and W. A. Thompson, 'Study of Si (111) surfaces by optical second-harmonic generation: reconstruction and surface phase transformation', Phys. Rev. Lett., vol. 54, no. 1, p. 63, 1985.
[8] O. A. Aktsipetrov, I. M. Baranova, and Y. A. Il'inskii, 'Surface contribution to the generation of reflected second harmonic light for centrosymmetric semiconductors', Zh Eksp Teor Fiz, vol. 91, pp. 287–297, 1986.
[9] J. E. Sipe, D. J. Moss, and H. M. Van Driel, 'Phenomenological theory of optical second- and third-harmonic generation from cubic centrosymmetric crystals', Phys. Rev. B, vol. 35, no. 3, p. 1129, 1987.
[10] C. H. Lee, R. K. Chang, and N. Bloembergen, 'Nonlinear electroreflectance in silicon and silver', Phys. Rev. Lett., vol. 18, no. 5, p. 167, 1967.
[11] O. A. Aktsipetrov et al., 'dc-electric-field-induced second-harmonic generation in Si (111)-SiO_2-Cr metal-oxide-semiconductor structures', Phys. Rev. B, vol. 54, no. 3, p. 1825, 1996.
[12] H. Park et al., 'Boron induced charge traps near the interface of Si/SiO_2 probed by second harmonic generation', Phys. Status Solidi B, vol. 247, no. 8, pp. 1997–2001, 2010.
[13] N. M. Terlinden, G. Dingemans, V. Vandalon, R. Bosch, and W. M. M. Kessels, 'Influence of the SiO_2 interlayer thickness on the density and polarity of charges in Si/SiO_2/Al_2O_3 stacks as studied by optical second-harmonic generation', J. Appl. Phys., vol. 115, no. 3, p. 033708, 2014.
[14] D. Damianos, 'Second harmonic generation (SHG) for contactless characterization of dielectric-semiconductor interfaces', PhD Thesis, Université Grenoble Alpes, 2018.
[15] Y. R. Shen, 'The Principles of Nonlinear Optics (Wiley, New York, 1984).', Google Sch. W Lee Smith Opt Eng, vol. 17, p. 489, 1978.
[16] E. Hecht, 'Optics, 4th editio ed', Addison-Wesley San Franc., vol. 2, p. 3, 2002.
[17] O. A. Aktsipetrov, I. M. Baranova, and K. N. Evtyukhov, Second order non-linear optics of silicon and silicon nanostructures. CRC Press, 2018.
[18] R. W. Boyd, Nonlinear optics. Academic press, 2020.

[19] T. F. Heinz, 'Nonlinear surface electromagnetic phenomena', H-E Ponath GI Stegeman Elsevier Sci. Publ. BV Amst. 1991 P, vol. 353, 1991.
[20] D. Damianos et al., 'Field-effect passivation of Si by ALD-Al_2O_3: second harmonic generation monitoring and simulation', J. Appl. Phys., vol. 124, no. 12, p. 125309, 2018.
[21] G. Lüpke, 'Characterization of semiconductor interfaces by second-harmonic generation', Surf. Sci. Rep., vol. 35, no. 3–4, pp. 75–161, 1999.
[22] H. Park, J. Qi, Y. Xu, G. Lüpke, and N. Tolk, 'Polarization-dependent temporal behaviour of second harmonic generation in Si/SiO_2 systems', J. Opt., vol. 13, no. 5, p. 055202, 2011.
[23] V. Fomenko, E. P. Gusev, and E. Borguet, 'Optical second harmonic generation studies of ultrathin high-k dielectric stacks', J. Appl. Phys., vol. 97, no. 8, p. 083711, 2005.
[24] M. Falasconi, L. C. Andreani, A. M. Malvezzi, M. Patrini, V. Mulloni, and L. Pavesi, 'Bulk and surface contributions to second-order susceptibility in crystalline and porous silicon by second-harmonic generation', Surf. Sci., vol. 481, no. 1–3, pp. 105–112, 2001.
[25] G. Dingemans, N. M. Terlinden, D. Pierreux, H. B. Profijt, M. C. M. Van de Sanden, and W. M. M. Kessels, 'Influence of the oxidant on the chemical and field-effect passivation of Si by ALD Al_2O_3', Electrochem. Solid-State Lett., vol. 14, no. 1, p. H1, 2010.
[26] G. von Gastrow, S. Li, M. Putkonen, M. Laitinen, T. Sajavaara, and H. Savin, 'Effect of ozone concentration on silicon surface passivation by atomic layer deposited Al_2O_3', Appl. Surf. Sci., vol. 357, pp. 2402–2407, 2015.
[27] G. von Gastrow, S. Li, P. Repo, Y. Bao, M. Putkonen, and H. Savin, 'Ozone-based batch atomic layer deposited Al_2O_3 for effective surface passivation', Energy Procedia, vol. 38, pp. 890–894, 2013.
[28] P. J. Jorgensen, 'Effect of an electric field on silicon oxidation', J. Chem. Phys., vol. 37, no. 4, pp. 874–877, 1962.
[29] T. Cvitas and N. Kallay, 'Equations of electromagnetism from CGS to SI', J. Chem. Educ., vol. 54, no. 9, p. 530, 1977.
[30] O. S. Heavens, Optical properties of thin solid films. Courier Corporation, 1991.
[31] 'Femtometrix®'. https://femtometrix.com/ (accessed Mar. 04, 2022).
[32] Y. Q. An, R. Carriles, and M. C. Downer, 'Absolute phase and amplitude of second-order nonlinear optical susceptibility components at Si (001) interfaces', Phys. Rev. B, vol. 75, no. 24, p. 241307, 2007.
[33] L. Gao, F. Lemarchand, and M. Lequime, 'Refractive index determination of SiO_2 layer in the UV/Vis/NIR range: spectrophotometric reverse engineering on single and bi-layer designs', J. Eur. Opt. Soc.-Rapid Publ., vol. 8, 2013.
[34] M. A. Green, 'Self-consistent optical parameters of intrinsic silicon at 300K including temperature coefficients', Sol. Energy Mater. Sol. Cells, vol. 92, no. 11, pp. 1305–1310, Nov. 2008, doi: 10.1016/j.solmat.2008.06.009.

Chapter 4: Experimental methodologies

Abstract

In this chapter, we explain the fabrication process used to create the passivated samples. Generally, the electrical properties related to the passivation interface vary depending on the method and conditions of oxide deposition. To evaluate these properties, we use second harmonic generation and capacitance-voltage techniques. Consequently, this chapter also covers the SHG experimental setup and the C-V samples, fabrication, measurements and extraction techniques for fixed oxide charge densities (Q_{ox}) and interface state densities (D_{it}). All these methods will be exploited afterwards in the next chapter for the characterization of our samples.

Contents of chapter 4

4.1 Comprehensive thesis methodology

As seen in chapter 1, the performances of microelectronic devices heavily depend on the quality of the passivation layer deposited on silicon. In this thesis, we have mostly studied alumina on silicon structures fabricated at STMicroelectronics for image sensor applications. The main characterization technique used in the thesis is second harmonic generation. The SHG study involves two approaches: modeling/simulation and experimental. The simulation was explained in the previous chapter and its goal was to distinguish between electrical and optical phenomena in the SHG response in order to properly relate the experimental SHG intensity to Q_{ox} or/and D_{it} and not to the optical phenomena. The two approaches were performed simultaneously on samples of various electrical properties in order to establish the foundations of a calibration process. Since modeling and simulation approaches have already been shown in chapter 3, in this chapter, we will focus on measurement strategy.

Figure 4.1 depicts the fabrication and characterization sequences for the samples. First, thermal ALD deposition was used to passivate several p-type Si(100) samples with high-k oxide layers. A SiO_2 thin layer is formed by chemical oxidation between the high-k dielectric and the silicon. Half of the samples were annealed to increase the passivation quality. COCOS measurements were exploited to determine interface parameters and fixed oxide charges. These steps were performed at STMicroelectronics, before we received the samples. This work will be discussed in section 4.2.

After receiving the substrates at the laboratory, they were cut into several pieces, to study the qualities of the materials by different characterization techniques. SHG technique was mainly used. The experimental setup and measurement methodology will be presented in section 4.3. Electrical C-V measurements were also utilized as a complement to SHG technique. C-V curves allow extracting precise values of Q_{ox} and D_{it} and then calculate the interface electric field E_{dc}. The methodology will be shown in section 4.4. The results from these techniques will be exploited later in the chapter 5 to produce a SHG calibration curve.

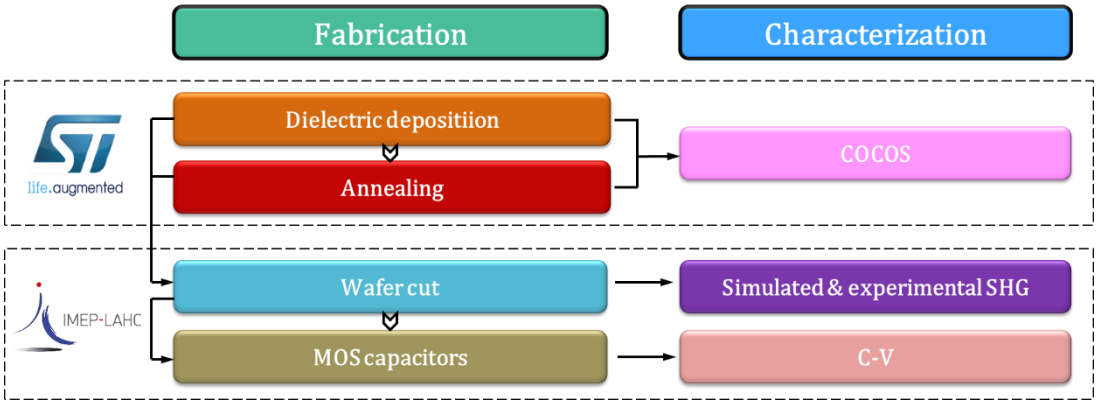

Figure 4.1: *Sample fabrication and characterization steps.*

4.2 Sample fabrication

The samples were fabricated at STMicroelectronics as explained in [1]. They are p-type Si(100) wafers on which oxide films were deposited using atomic layer deposition (ALD), a method producing extremely homogeneous films with precise thickness control [2]. ALD thermal processes were used to grow 13 nm of alumina (Al_2O_3) and hafnium oxide (HfO_2) layers, either in an ozone (O_3) ambient environment at 325° or under water (H_2O) at 325°C or 100°C. The precursor used to deposit Al_2O_3 and HfO_2 films are $Al(CH_3)_3$-TriMethylAluminium (TMA) and $HfCl_4$, respectively. Figure 4.2 explains the chemical reactions that occur during thermal deposition of ALD by H_2O on an oxidized silicon wafer (Figure 4.2a). When the first TMA pulse is introduced, the aluminum atoms react with the oxygen and hydrogen atoms at the silicon surface (Figure 4.2b). The reaction products (methane CH_4 and excess TMA) are then purged with inert gas, nitrogen for example (Figure 4.2c). To form the first layer of Al_2O_3, a pulse of oxidant precursor H_2O replaces the CH_3 at the surface (Figure 4.2d). Finally, the remaining hydrogens are purged (Figure 4.2e) and the cycle is repeated until the required thickness is reached (Figure 4.2f).

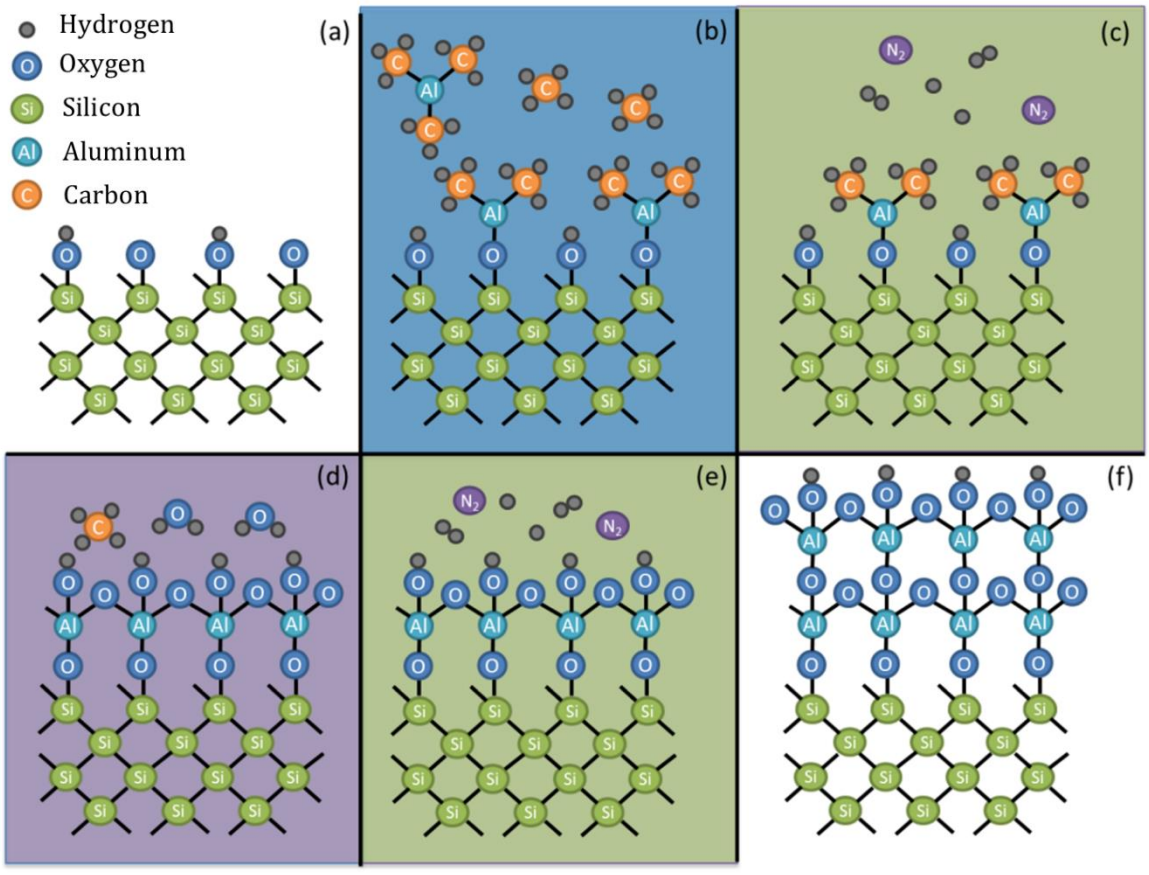

Figure 4.2: *Principle of growth of Al_2O_3 with the thermal-ALD process. Figure taken from [3].*

To create a smooth Si-oxide interface of high quality with low recombination velocities, the samples were annealed for 120 min at a temperature of 400°C in a N_2 atmosphere. This temperature range has been established for optimal Si passivation with Al_2O_3 thin films by ALD [1].

These samples will be investigated using SHG and C-V techniques. The methodologies for these measurements are described in more detail below, and the precise results obtained on the samples will be explained in the following chapter.

4.3 SHG characterization methodology

The experimental SHG characterization of the oxide-semiconductor interfaces goes through several stages:

1- Expose the sample to the fundamental laser beam in the experimental setup.
2- Detect the SHG response over time SHG(t).
3- Extract the value of interest from the SHG(t) measured curve.
4- Plot the SHG as a function of the experimental parameter under study (e.g. incident angle).

At the beginning of the thesis, we had to install a new laser in the tool, so an optical alignment was needed. The details of this work will be discussed in the next sections. We will also describe the treatment of the raw SHG data as a function of time in order to obtain a curve SHG that depends on the experimental parameters under study.

4.3.1 SHG experimental setup

Figure 4.3 depicts the harmonic F1X tool from FemtoMetrix [4] used in this thesis for characterization, from the inside (a) and the outside (b). The pump laser is located on the left side and is a pulsed femtosecond laser with 780 nm wavelength, 90 fs pulse duration, 125 mW average power and 80 MHz repetition rate. The angle of incidence (θ) of the laser beam can be adjusted between 25° and 65° with respect to the normal to the sample surface. To select the polarization angle of the incident light (ψ), a rotating half wave plate (HWP) with a range of rotation from 0° (p-polarized, parallel to the incident plane) to 90° (s-polarized, perpendicular to the incident plane) is implanted. The studied sample is placed on a metallic chuck that can accommodate wafers up to 300 mm diameter. The chuck can be moved in the xy plane by the software. Φ shown in Figure 4.3a is the azimuthal angle. The reflected fundamental beam and the generated second harmonic beam from the sample pass through a collimator and a rotating polarizer to adjust the

polarization angle of the second harmonic light (α). Before the beams reach the detector, single pass and band pass filters are placed in the system to separate the two wavelengths. The collimated and filtered SH beam is detected and measured by a photomultiplier tube (PMT) coupled with a gated photon counter. The experimental parameters that are controlled by the software are the in and out polarization angles, the incident angle, the x,y position.

At the beginning of this thesis, we installed a new laser in the equipment and optimized the SHG signal thanks to an optical alignment, as described in the next section.

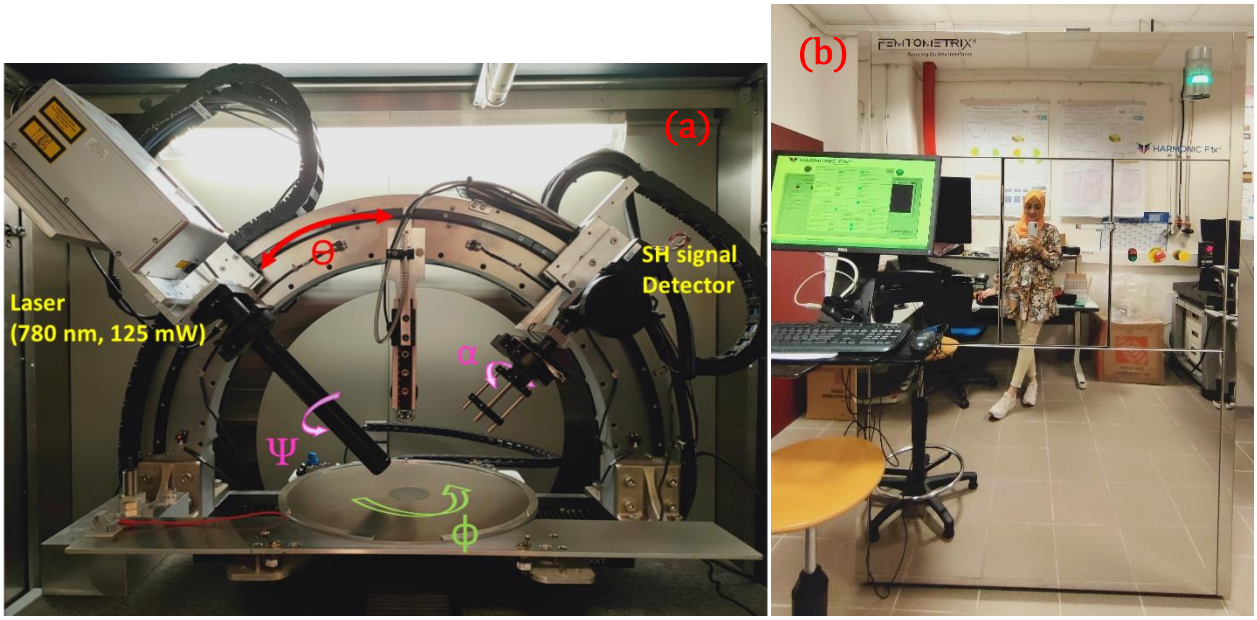

Figure 4.3: (a) *Picture inside the SHG equipment installed by FemtoMetrix at IMEP-LAHC.* ***(b)*** *External view of the SHG tool.*

4.3.2 Laser installation and optical alignment

During this thesis we installed a new laser 780 nm femtosecond laser from TOPTICA PHOTONICS, with a power range from 40 to 125 mW.

Originally, the equipment had CALMAR femtosecond laser (780 nm, 360 mW) [5]. The previous optical scheme is illustrated in Figure 4.4a. The laser beam was focused on the sample surface using a converging lens (L1) with a focal length of 150 mm. The minimum spot size was of about 50 µm for an angle of incidence of 45°. Figure 4.4b depicts the SHG response from this setup; the measurement time is of 100 seconds, with a step every 0.1

second. The tested sample was a Si(100) substrate, and the generated SHG intensity appeared strong due to the high laser power and the proper optical alignment.

After changing the laser without modifying the optical setup (Figure 4.4c), the SHG signal measured from the same sample was very weak, with a very low signal-to-noise ratio (Figure 4.4d). The measurement was carried out with 100 mW power for 15 seconds each 1 second. Theoretically, the SHG intensity is proportional to the square of the laser power. From the calculated the laser power ratio, $(350/100)^2$ we expect SHG ratio of 12.25. On the other hand the measured SHG ratio is about $40/2=20$. The mismatch is due to the beam that is not well-centered after the laser replacement.

In order to increase the SHG intensity, we decided to increase the optical power density on the sample by producing a smaller spot. L1 lens was thus changed by one with a focal length of 50 mm, which leads to a spot diameter smaller by a factor 9 when compared to the original setup. However, this lead to an increase of the angle of the cone of light arriving on the sample, and thus a more diverging beam exiting the sample. The beam arriving on the detector was thus larger than the detector size, leading to a decrease in the measured power. In order to fix this, a new L2 lens of 100 mm focal length was installed to maintain the power of the SH beam on the detector side (Figure 4.4e). After the optical alignment, measurements were performed for 100 seconds, with a step every 0.1 second. A noticeable increase in the SHG signal/noise was observed (see Figure 4.4d).

After setting up the new laser into the experimental equipment, the first tests to validate the alignment were the measurements of the reflection coefficients of the fundamental beam on Silicon and their comparison with the theoretical data, as will be shown in the next section.

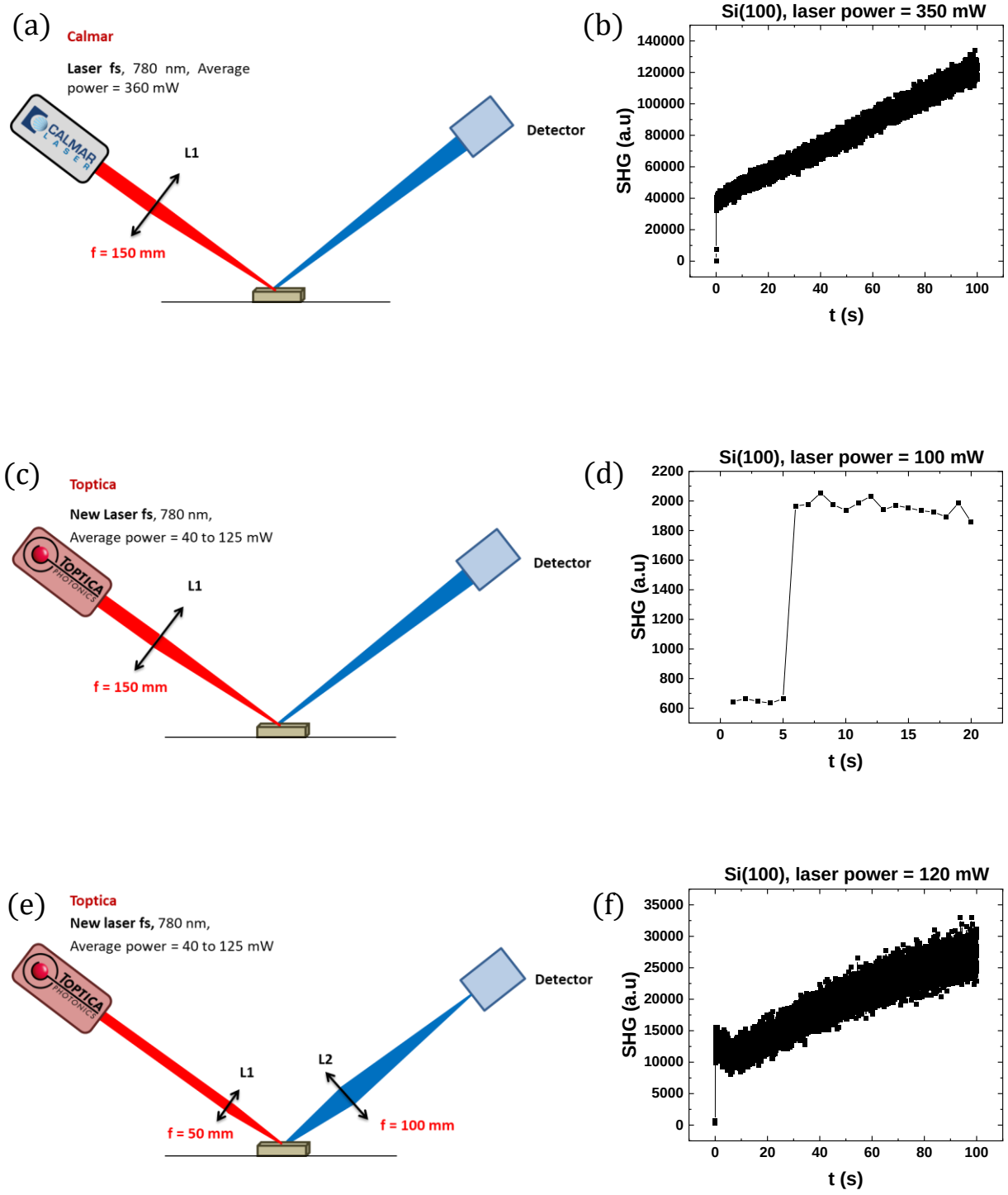

Figure 4.4: *Schematic of the SHG measurement configuration with the* ***(a)*** *old experimental setup and laser,* ***(c)*** *old experimental setup and new laser and* ***(e)*** *new experimental setup and laser. The TD-SHG curve* ***(b, d and f)*** *for each configuration is displayed next to it. All the SHG signals were done at 45° angle of incidence and P_{in}-P_{out} configuration. The laser diameter is 40 µm.*

4.3.3 Validation of the optical alignment

We validated the optical alignment thanks to measurement of reflection coefficients for s- and p- polarizations on a Si(100) sample. The comparison with the theoretical values will confirm the good setup. The linear optical properties of the interface can be represented by the complex Fresnel transmission and reflection coefficients obtained from the Maxwell's continuity relations. Theoretically, the reflectivity R depends on the properties of the two isotropic media constituting the interface, the angle of incidence and the beam polarization angle [6]. For s- and p- polarizations:

$$R_s = \left| \frac{n_i \cos\theta_i - n_j \sqrt{1 - (\frac{n_i}{n_j}\sin\theta_i)^2}}{n_i \cos\theta_i + n_j \sqrt{1 - (\frac{n_i}{n_j}\sin\theta_i)^2}} \right|^2$$

$$R_p = \left| \frac{n_j \cos\theta_i - n_i \sqrt{1 - (\frac{n_i}{n_j}\sin\theta_i)^2}}{n_j \cos\theta_i + n_i \sqrt{1 - (\frac{n_i}{n_j}\sin\theta_i)^2}} \right|^2 \quad (4.1)$$

This reflectivity can also be calculated for an arbitrary multilayer device using our simulation code by dividing the reflected wave amplitude at the fundamental frequency by the incident wave amplitude:

$$R_{s,p} = \left| \frac{E^+_{s,p}}{E^-_{s,p}} \right|^2 \quad (4.2)$$

Figure 4.5a shows the reflectivity of both P_{in}-P_{out} and S_{in}-S_{out} configurations as a function of the angle of incidence from air/silicon structure plotted theoretically using eq. (4.1) and replacing n_i by n_{Air} and n_j by n_{Si}= 3.696+0.006i for λ=780 nm [7]; and by using eq. (4.2) in our simulator which takes into account the propagation of the reflected wave in the structure and also the boundary conditions. Both approaches give the theoretical curves which are used as a reference to test the reflection of the experimental fundamental light (Figure 4.5b), to confirm the correctness of the optical alignment on this side.

The experimental results are extracted with the two schemes of Figure 4.4c (2nd setup) and Figure 4.4e (3rd setup). In order to measure the reflectivity at ω, a beamsplitters that separates the beams of frequencies at ω and at 2ω has been added to the setup. The fundamental field was then measured by a detector, while the intensity of the SHG was measured by another detector. After having multiplied the experimental curves by 1.6,

Figure 4.5b demonstrates that the reflectivity detected from setup 3 fits well with the theory contrary to the measurements with setup 2 where we see no reflection on the different angles of incidence. The multiplication factor 1.6 is needed to superpose experimental points to the theoretical curves. It can be caused by losses on the various elements on the optical path (lenses, waveplates, and separator cube). So, this measurement confirms a good alignment at the different angles of incidence between 25° and 65°. In order to evaluate the detector alignment with the SH beam, a dependence of the SHG intensity with the laser power is shown in the following section.

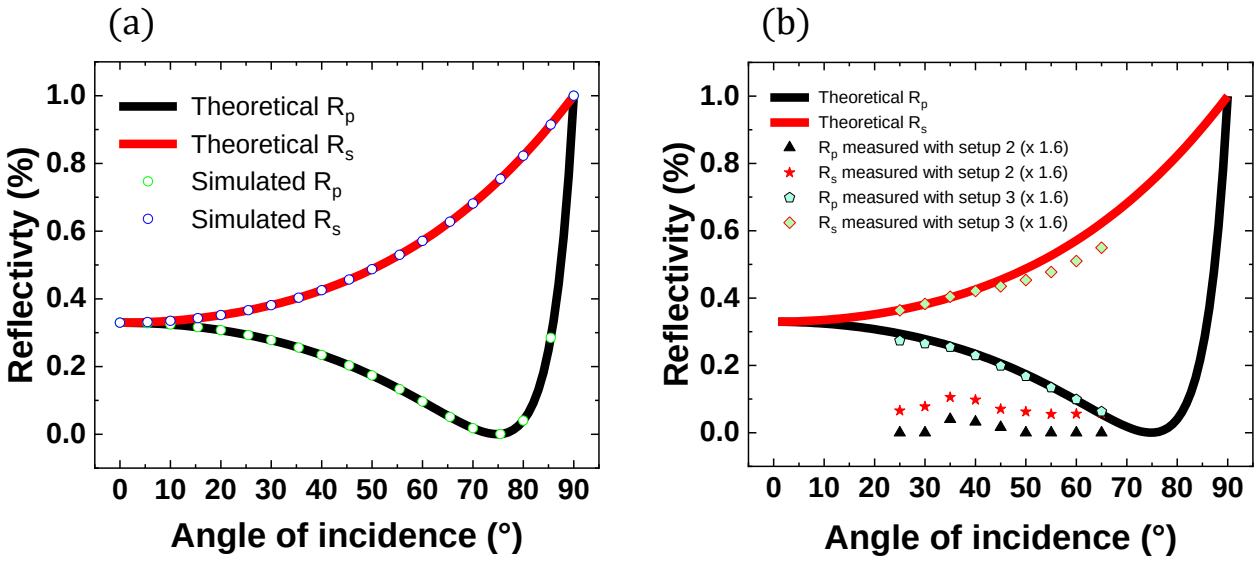

Figure 4.5: *Reflectivity of silicon substrate calculated* ***(a)*** *theoretically and by simulation and* ***(b)*** *comparison with the measured results in the case of Pin-Pout (R_p) and Sin-Sout (R_s) polarizations.*

4.3.4 SHG response to the laser power

Following the optimization of the fundamental reflection, the SHG response should also be validated. A laser power dependent SHG measurement was used to achieve this. The SHG intensity is proportional to the square of the fundamental beam intensity (laser power). As a result, the SHG measurement should have a quadratic dependence on the intensity of incident beam. Figure 4.6 shows the test results on a silicon substrate. The SHG response from this sample comes from the surface. The experimental parameters used are P_{in}-P_{out} polarizations, 45° angle of incidence and 0° azimuthal angle. A quadratic equation of fundamental beam power fits the SHG intensity well and a square root of SHG depends linearly on the laser power (Figure 4.6). These results demonstrate accurate measurements and thus a good alignment of the detector side. Therefore, we validated the SHG experimental configuration. It should be noted that this kind of curve cannot be extracted

directly by the tool and it must be calculated, since the equipment only measures the SHG intensity versus time. The treatment of the raw data to achieve this is described in the following section.

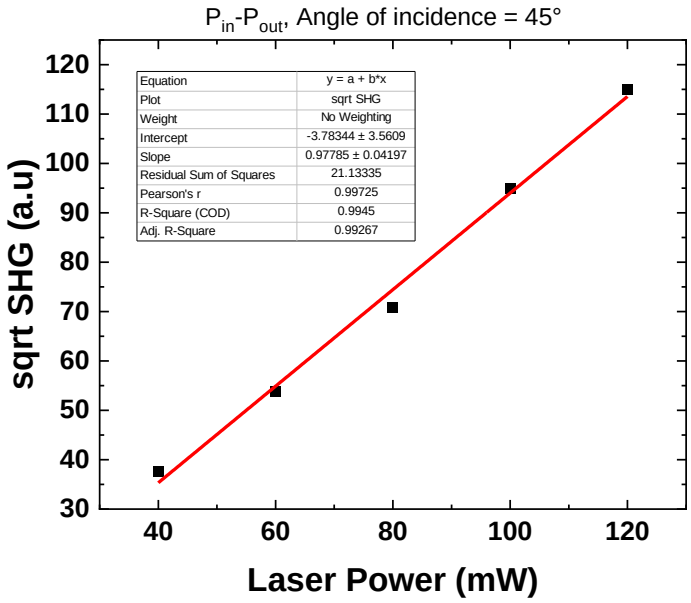

Figure 4.6: *Sqrt of SHG intensities from Si(100) wafer with respect to fundamental beam power. Approximate linear dependence is shown by the fit line.*

4.3.5 Treatment of SHG raw data

The measurement tool is automated with respect to many parameters (AOI, ψ, position of the laser spot on the sample) and it is very easy to obtain a lot of data. However, the detector collects SHG radiation in counts per second (cps) over time (time-dependent SHG). Therefore, the SHG intensities versus experimental parameters such as laser power, angle of incidence (θ), input polarization angle (ψ), etc. need to be extracted because they are the ones providing information on the interface field, E_{DC}. The protocol for plotting such a curve is given in Figure 4.7a on an example SHG versus the input-polarization angle ψ, at fixed AOI and position on the sample. ψ is varied from 0 to 90°, while the TD-SHG is measured for each ψ. The average of the TD-SHG intensities is calculated from each curve by using only the points after the SHG intensity is stabilized. The detector electrical noise is obtained from the SHG measured at the time the shutter was closed (first 3 seconds on the curves in Figure 4.7a). This electrical noise is subtracted from the average SHG intensity and leads to the final value of SHG intensity. The resulting curve of SHG versus ψ using many individual SHG versus time measurement is shown in Figure 4.7b. This protocol can be applied to all the other parameters and is implemented by a Python code that we created

using pandas library. The code treats and organizes the data, removes measurement noise and plots SHG intensity against several experimental parameters.

The curves SHG versus experimental parameters (AOI, ψ, etc.) will be used in the next chapter to access E_{DC}, and thus to provide information about Q_{ox}/D_{it}. In order to obtain a calibration curve afterwards, electrical (C-V) measurements will be used as a reference, and the methodology associated to them is described next.

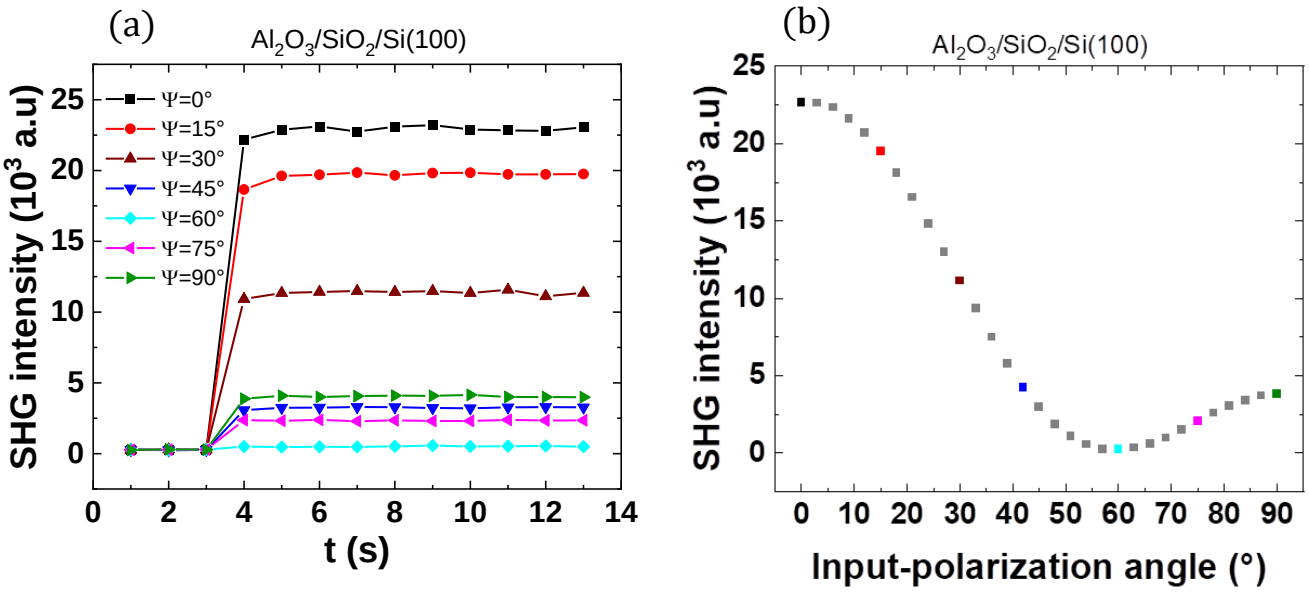

Figure 4.7: *SHG response from $Al_2O_3/SiO_2/Si$ sample* ***(a)*** *over time for various input-polarization angles (ψ). Only some of the values of ψ are shown.* ***(b)*** *SHG versus ψ after data treatement. The parameters are: P_{out}, angle of incidence = 47°, azimuthal angle = 0°, laser power = 60 mW.*

4.4 C-V measurement methodology

To determine fixed charges Q_{ox} and interface traps D_{it} of the dielectric on semiconductor stacks, C-V characterization is performed on MOS (Metal Oxide Semiconductor) capacitors. This characterization technique thus requires to fabricate a structure on top of the device we want to characterize. The manufacturing steps for these structures, as well as the method for extracting Q_{ox} and D_{it} from C-V curve, are shown in the subsections below.

4.4.1 MOS capacitor fabrication

A MOS capacitor is necessary to perform C-V measurements. Since we want to characterize dielectric/silicon interfaces, a metallic layer needs to be added to produce a MOS structure. In order to produce a large number of metallic contact patterns for the MOS capacitors in each sample, a mask has been produced. The mask design was made using the editing program "KLayout". This program allows drawing variety of geometric shapes of very small dimensions in an iterative and fast way. The created mask is composed of square and rectangular patterns with various sizes. The fabrication of MOS structures requires a low roughness and clean surface to avoid studying the electronic quality of polluted samples. Therefore, before proceeding with the fabrication, the samples were cleaned with deionized water. Then, the fabrication steps were performed in the clean room and are shown in Figure 4.8, as follows:

a) Annealing of the oxide/Si(100) samples in the vacuum deposition chamber at a temperature of 200° C for 30 min. Then, 450 nm of aluminum was deposited by sputtering in vacuum.

b) Deposition of 1.8 µm of photoresist (AZ1518) by spin coating followed by soft bake at 100°C for 90 seconds.

c) UV Hg lamp exposure through the mask.

d) Development of resist by AZ developer (50% developer + 50% DI water) followed by hard bake at a temperature of 115°C for 5 min.

e) Aluminum etching with the Al etching solution (Phosphoric/nitric and acetic acid) at 50°C for 1 min.

f) Removing the resist with the "Remover SVC 14" solution at 40°C for 4 min.

This process flow also has also been performed without the pre-deposition annealing step a), since it might modify the properties of dielectrics under study.

As will be shown later in the next chapter the samples produced through this method were not fully appropriate for our study, so a second fabrication process based on lift-off was tested in order to improve the manufacturing quality. However, it has not been successful, either since resist removal after lift-off was not working. More details about this flow are given in Appendix.

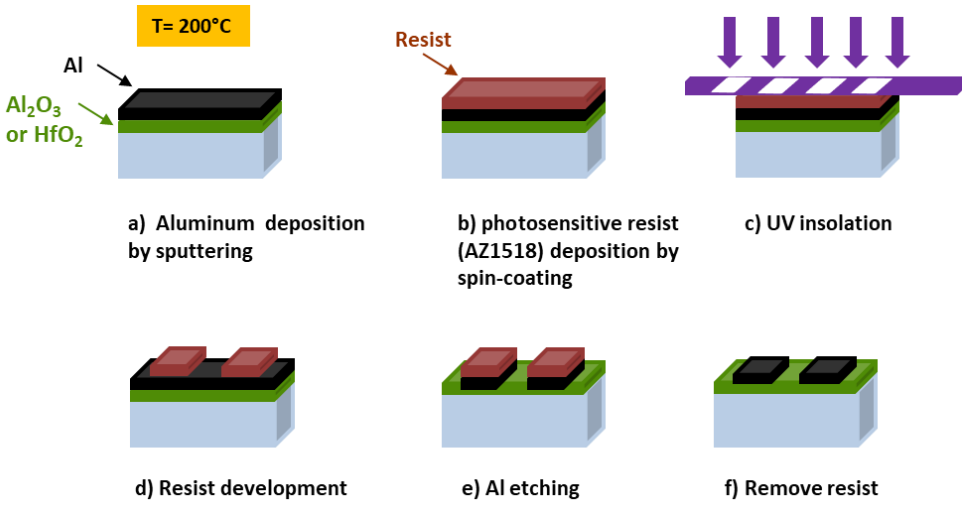

Figure 4.8: *Fabrication steps of MOS capacitors in the clean room by deposition, lithography and etching.*

Figure 4.9 shows an image obtained with an optical microscope of the aluminum metal contacts that were fabricated with the process flow previously described. The deposited thickness of Al is about 450 nm. The contacts sizes are from 50 up to 2000 µm.

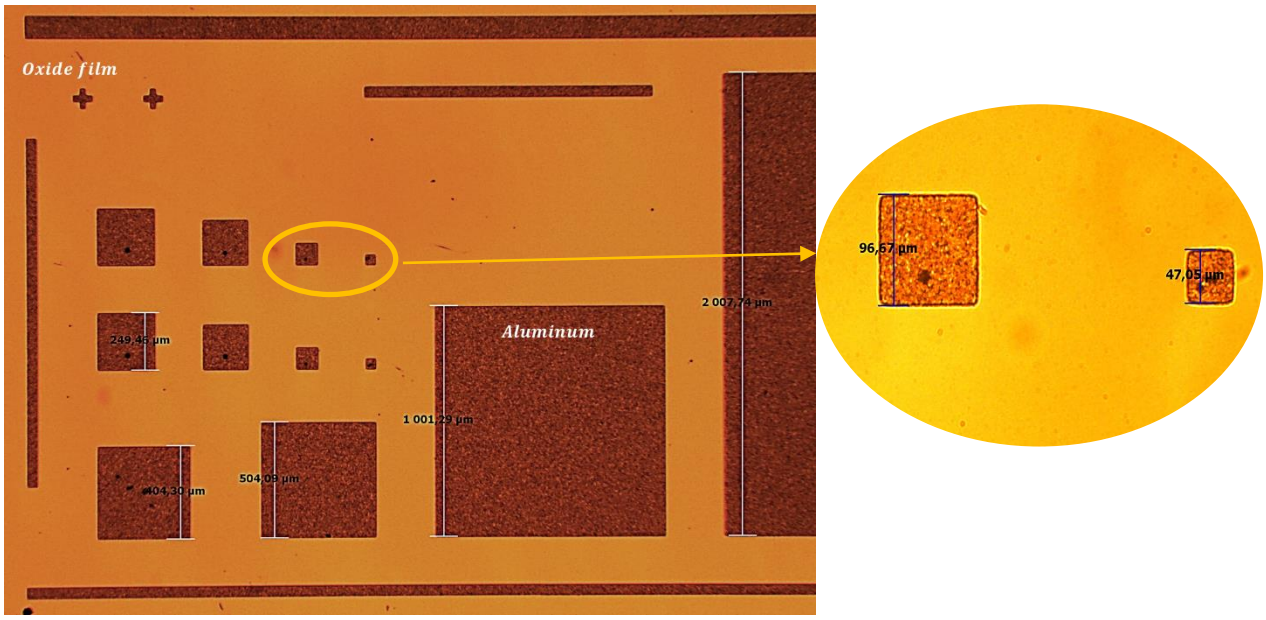

Figure 4.9: *Optical microscopy image of MOS capacitors after full fabrication with zoom on the smallest patterns.*

4.4.2 C-V measurement

Once the MOS structure has been produced, the C-V curves are obtained using a probe station to contact the devices and Keysight (Agilent) 4284A semiconductor characterization system for the C-V measurements.

The tool used is the parallel capacitance-conductance model C_p-G_p in order to obtain the measured capacitance versus the gate voltage V_g [8]. The studied samples are dielectric layers on p-type Si(100) substrate. In order to obtain C-V measurements, the gate bias voltage was swept from negative to positive values (from accumulation to inversion) with a step of 100 mV. A small ac signal is set at 30 mV. The application of an electric field forces the charges to migrate from the silicon and from the gate contact to the interface.

Figure 4.10 shows two examples of C-V curves measured at high (500kHz) and low (1kHz) ac frequencies. The measurements are performed on a square gate MOS capacitor with a size of 10^{-4} cm^2. The three regimes (accumulation, depletion and inversion) shown in Figure 4.10 were explained in details in chapter 1. Let us just remind them here:

- **Accumulation regime:** for $V_g<0$, the total capacitance is essentially constant and corresponds to the oxide capacitance C_{ox}.
- **Depletion regime:** for $V_g>0$, the surface of semiconductor is depleted of holes (majority carriers). Thus, the measured capacitance is a series association of the oxide capacitance and the depletion layer capacitance, resulting in a decrease in the total measured capacitance. The transition from accumulation to depletion region occurs at the flat band voltage V_{FB}. Additionally, the width of the depletion region widens with V_g, so the total capacitance decreases when V_g increases.
- **Inversion regime:** for $V_g >>0$, electrons (minority carriers) are attracted towards the substrate-oxide interface, forming an inversion layer. Therefore, the depletion region reaches its maximum depth. In this region, the total capacitance is built of the series association between the oxide and the semiconductor ones and it depends on the measurement frequency. Figure 4.10 shows a significant difference in the C-V response at low and high frequencies. At high frequency (500 kHz), the inversion layer does not have the time to respond to the small ac signal on V_g and the silicon capacitance is given by the maximum width of the depletion region. At low frequency (1kHz), the inversion layer follows the V_g signal, its capacitance is very high so the total capacitance is mainly given by the oxide one.

The exploitation of this type of curves allows extracting the fixed oxide charge density and the interface defects density of each structure [9]. The 'bump' observed at the low-frequency curve is a sign of the presence of such interface traps. The methodologies of the D_{it} calculation is shown later.

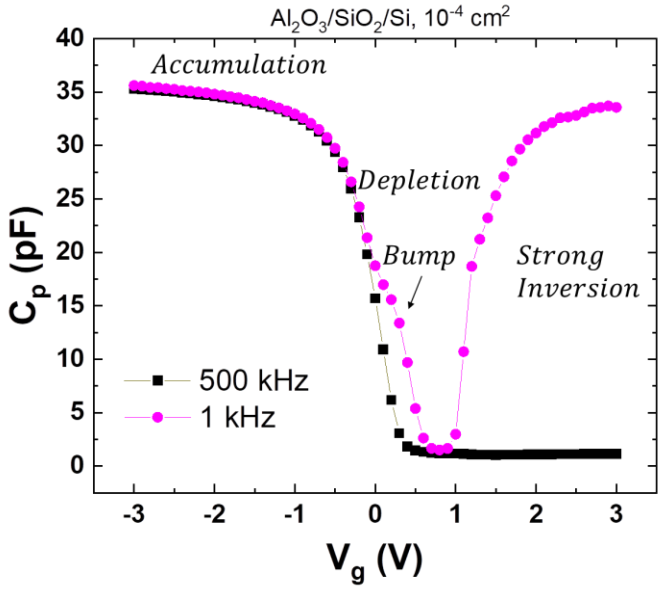

Figure 4.10: *C-V curves measured from Al_2O_3/SiO_2/p-type Si sample at low and high frequencies.*

In order to find the best measurement conditions, we carried out measurements on patterns of different dimensions. The measured C_{ox} should be constant in the accumulation region. Theoretically, oxide capacitance is expressed as [9]:

$$C_{ox} = \frac{\varepsilon_{ox}}{t_{ox}} S \tag{4.3}$$

With ε_{ox} and t_{ox} are the dielectric permittivity and thickness, respectively. S represents the surface area of the MOS capacitor.

Theoretical and measured oxide capacitance (C_{ox}) versus the surface area curves are presented in Figure 4.11 for Al_2O_3/SiO_2 stack as-deposited and annealed. The measurements were performed with ac signal of low (1kHz) and high (1MHz) frequencies. For both cases, the C_{ox} measured on small MOS areas such as 0.0025 mm^2 (50 x 50 μm^2) and 0.01 mm^2 (100 x 100 μm^2) fit the theory better than the larger area capacitors. This may be due to the fact that larger areas are more prone to defects that can affect CV results. As a result, the majority of measurements will be carried out on the smallest patterns.

Let us start with Q_{ox} extraction, method described in the next section.

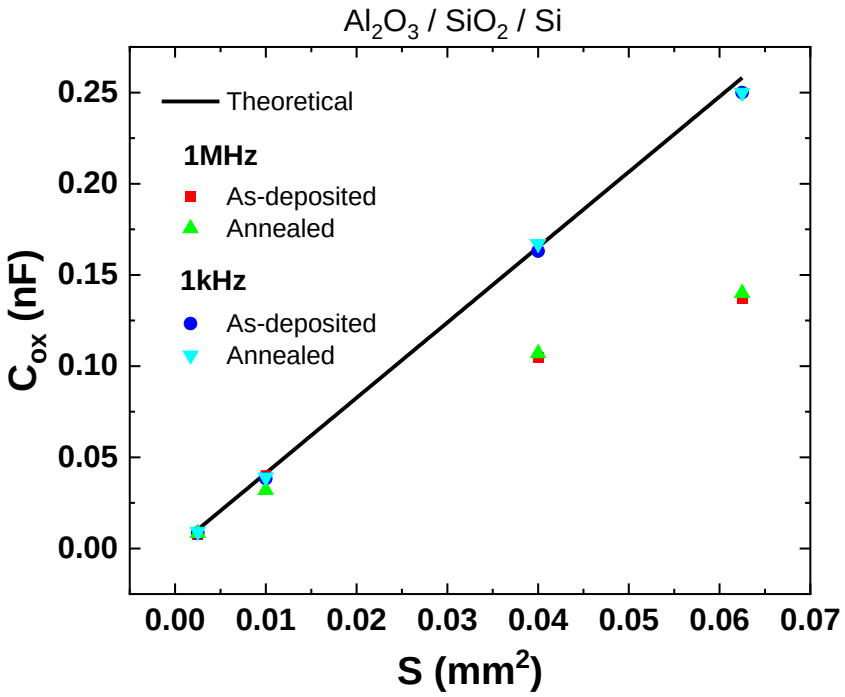

Figure 4.11: *Capacitance versus MOS surface area for $Al_2O_3/SiO_2/Si$ sample.*

4.4.3 Q_{ox} extraction

The C-V curves are shifted by the presence of Q_{ox}. Figure 4.12 depicts schematically this effect. The black curve is the theoretical normalized C-V curve at $Q_{ox} = 0$. When $Q_{ox} \neq 0$, the curve shift and the relation between Q_{ox} and the value of the flat band voltage V_{FB} is [9]:

$$Q_{ox} = \frac{(\varphi_{ms} - V_{FB})C_{ox}}{qS} \text{ in cm}^{-2} \qquad (4.4)$$

φ_{ms} is the difference in work functions between the metal gate and the semiconductor. φ_{ms} can be obtained by theoretical calculation or by measuring the work function of each material. In our case, φ_{ms} between Al gate and Si substrate is equal to -0.71 V. The calculation was done with band gap of silicon ~ 1.12 eV, intrinsic carrier concentration of silicon at room temperature ~ 10^{10} cm^{-3} and a p-doped Si with 10^{15} cm^{-3} dopant concentration [10]. C_{ox} is the oxide capacitance that can be either calculated theoretically using eq. (4.3) from the geometry of the MOS structure, or using the measured accumulation capacitance, which corresponds to the oxide capacitance.

According to eq. (4.4), in the case of negative oxide charges in the oxide, the value of V_{FB} increases and thus the C-V curve shifts to the right with respect to the ideal curve.

Reciprocally, in the case of positive oxide charges, V_{FB} is negative and the shift goes to the left.

To determine the value of V_{FB} for C-V curves, the method consists of calculating the square of the inverse of the measured parallel capacitance, $(1/C_p^2)$. The curve used in this calculation is the one measured at high frequency (500kHz) because the response of interface traps is minimum. $1/C_p^2$ in the depletion zone follows V_g by the linear relationship [9]:

$$\frac{1}{C_p^2} = \frac{1}{C_{ox}^2} + \frac{2}{S^2 N_A q \varepsilon_{Si}} (V_g - V_{FB}) \tag{4.5}$$

Where N_A is the acceptor doping level, q is the elementary charge and ε_{Si} is the dielectric permittivity of silicon, $\varepsilon_{Si}=11.7\varepsilon_0$ [11].

The curve $1/C_p^2$ (V_g) obtained shows a linear zone (see Figure 4.13). The straight line passing through this linear zone gives the value of the V_{FB} at its intersection with the $1/C_{ox}^2$. Subsequently, Q_{ox} is calculated using eq. (4.4).

The Q_{ox} values used in the next chapter to build calibration curves are extracted using this procedure. C-V curves are also used to extract the interface trap density and the method used in this thesis is presented the next section.

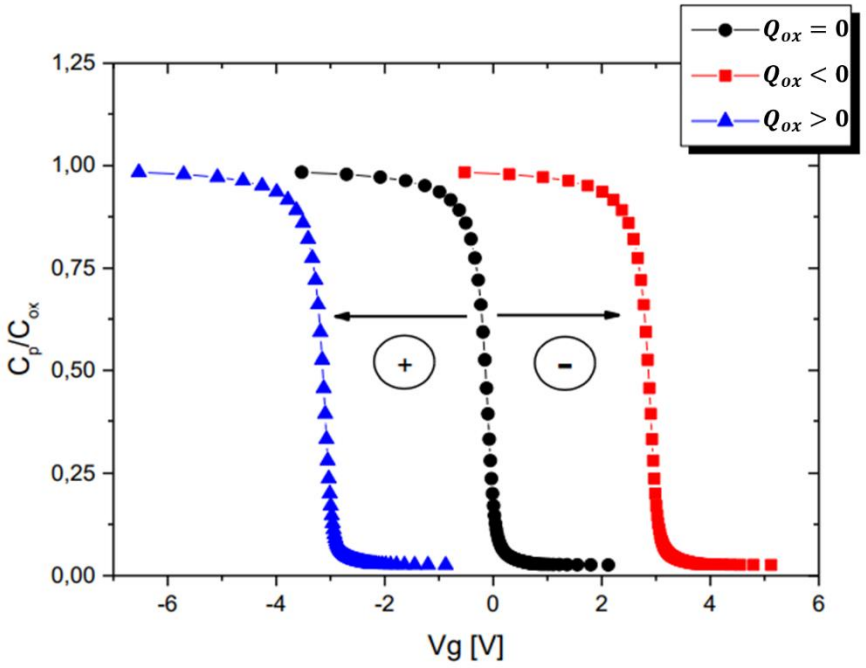

Figure 4.12: *Effect of presence of oxide fixed charges on the C-V curves for p-type semiconductor. Figure taken from [3].*

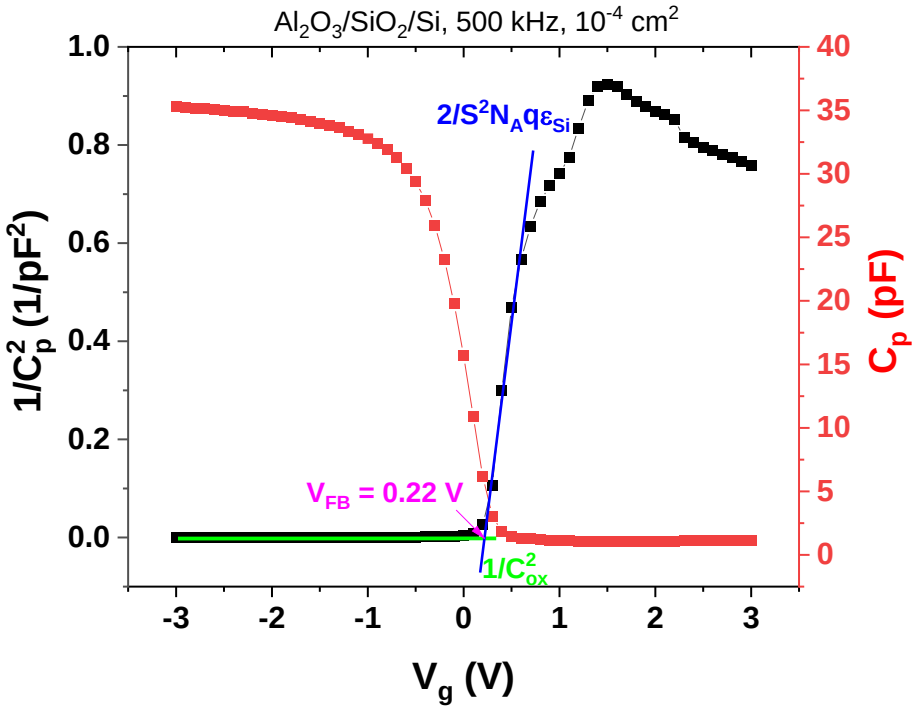

Figure 4.13: *Illustration of the determination of V_{FB} by the $1/C_p^2$ method.*

4.4.4 D_{it} extraction

The HF-LF (high frequency-low frequency) method proposed by Castagné and Vapaille [12] is used to calculate the value of interface defect density at each V_g. It is based on the difference between the curves measured at high frequency (HF) and at low frequency (LF). Indeed, for each structure, several tests are performed at various frequencies ranging from 1 kHz to 1 MHz, as shown in Figure 4.14a. As previously said, if the frequency is high, the defects do not have the time to respond during the capacitance measurement. On the other hand, if the frequency is sufficiently low (<100 kHz), defects can respond and will influence the measurement. This effect is observed in Figure 4.14a. The dispersion in the accumulation region shown in Figure 4.14a is probably caused by the series resistance in the silicon substrate [13]. Note that the results on similar samples from the literature [13], [14] (Figure 4.14b) showed a much stronger effect of the series resistances, that necessitated corrections of the data. This effect is not significant in our case.

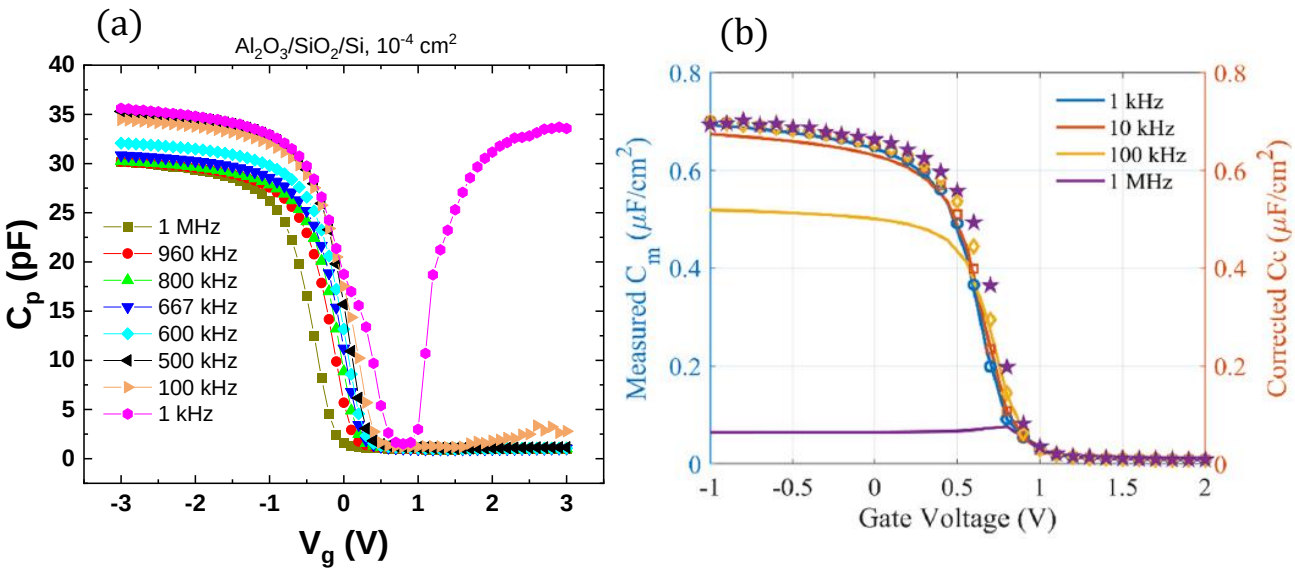

Figure 4.14: (a) *Our C-V curves measured from Al_2O_3/SiO_2/p-type Si sample at various frequencies between 1kHz and 1MHz.* ***(b)*** *Literature curves taken from [13].*

The equivalent capacitance measured at HF (C_{HF}) corresponds to the oxide and the semiconductor capacitance in series as shown in Figure 4.15a [9]:

$$\frac{1}{C_{HF}} = \frac{1}{C_{ox}} + \frac{1}{C_{Si}} \tag{4.6}$$

The equivalent circuit at low frequencies is illustrated in Figure 4.15b, where the semiconductor and interface trap capacitances are in parallel and their sum is in series with the oxide capacitance. Therefore, the equivalent capacitance C_{LF} is given as [9]:

$$\frac{1}{C_{LF}} = \frac{1}{C_{ox}} + \frac{1}{C_{Si} + C_{it}} \tag{4.7}$$

By normalizing eqs. (4.6) and (4.7) with the oxide capacitance, the equations can be written as:

$$\frac{C_{HF}}{C_{ox}} = \frac{C_{Si}}{C_{ox} + C_{Si}} \tag{4.8}$$

$$\frac{C_{LF}}{C_{ox}} = \frac{C_{Si} + C_{it}}{C_{ox} + C_{Si} + C_{it}} \tag{4.9}$$

Using eqs. (4.8) and (4.9), the interface trap capacitance is given as follows [9]:

$$\frac{C_{it}}{C_{ox}} = \frac{C_{LF}}{C_{ox} - C_{LF}} - \frac{C_{HF}}{C_{ox} - C_{HF}} \tag{4.10}$$

C_{it} is related to the interface trap density D_{it} by:

$$D_{it} = \frac{C_{it}}{qS} \tag{4.11}$$

This formula yields a curve D_{it} as a function of V_g using the capacitances measured at high and low frequencies.

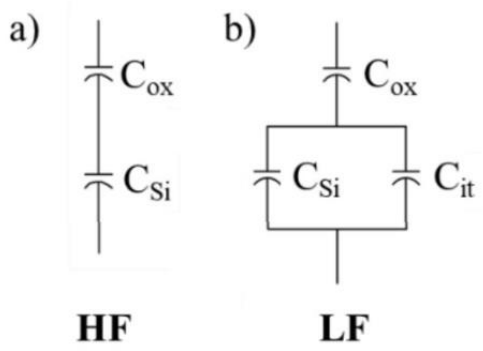

Figure 4.15: *Equivalent circuit capacitance for* ***(a)*** *high frequency, and* ***(b)*** *low frequency for C-V measurements. Figure taken from [9].*

An example of D_{it} curve versus V_g is given in Figure 4.16. The curve was determined using two different frequencies (HF at 500 kHz and LF at 1 kHz). The interface trap value was taken at the flat band voltage V_{FB} (0.22V), so we plotted the curve between -0.8 and 0.8 V to identify the D_{it} value at this point. V_{FB} was calculated at HF using the method mentioned in the previous section. This method will be used in the next chapter to extract the D_{it} at the interface between dielectric and silicon.

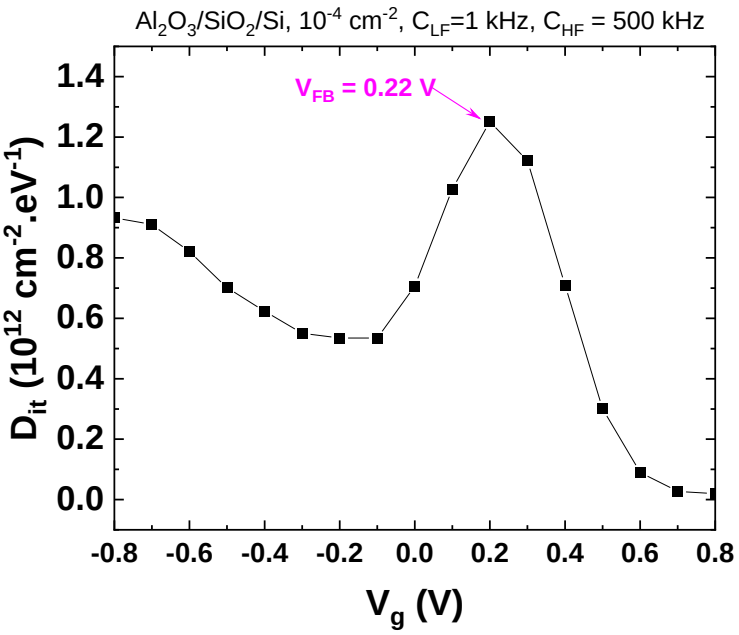

Figure 4.16: *D_{it} versus V_g curve calculated from eq. (4.10) and (4.11), using data shown in Figure 4.10.*

4.5 Chapter conclusion

This chapter provided the methodology employed for sample fabrication, for SHG and for C-V measurements. The samples are several oxide layers on silicon wafers prepared by ALD under different conditions, as we'll show in the next chapter.

The second harmonic generation tool needed the replacement of the laser. After installing the laser, we performed an optical alignment to properly center the beam and to increase the optical power density on the sample in order to obtain SHG curves with a correct signal-to-noise ratio. The optical alignment was then validated on the laser and detector sides by measuring the reflectivity as a function of angle of incidence and the SHG intensity versus laser power. The tool gives the SHG response over time for a wide variety of parameters that can be easily modified, so the quantity of raw data that can be obtained is large. We explained how to extract SHG response versus experimental parameters such as angle of incidence, laser power, input-angle polarization, and so on from the raw data. This procedure will be used in the next chapter for the study of the passivation layers.

We then presented the structures and fabrication process of the MOS capacitors used for conventional electrical C-V characterization (that will carried out alongside the SHG to plot a calibration curve). So we presented the methodology of C-V measurements and the extraction of Q_{ox} from the V_{FB} shift and of D_{it} using HF-LF (high frequency - low frequency) method.

All these methods will be exploited to measure samples with various passivation schemes, as presented in the next chapter, the final aim being to show the possibility of calibration of the SHG for characterization of the passivation layers on silicon.

4.6 Chapter references

[1] V. Aubriet, 'Étude du photo-potentiel de surface pour la caractérisation des interfaces enterrées par microscopie à sonde de Kelvin', PhD Thesis, Université Grenoble Alpes, 2022.

[2] S. M. George, 'Atomic layer deposition: an overview', Chemical reviews, vol. 110, no. 1, pp. 111–131, 2010.

[3] M. Pawlik, 'Etude de la passivation de surface du silicium cristallin type P par dépôt de couches atomiques d'alumine pour application aux cellules solaires à haut rendement', PhD Thesis, Ecole centrale de Lille, 2015.

[4] 'Femtometrix®'. https://femtometrix.com/ (accessed Dec. 24, 2022).

[5] D. Damianos et al., 'Second Harmonic Generation characterization of SOI wafers: Impact of layer thickness and interface electric field', Solid-State Electronics, vol. 143, pp. 90–96, 2018.

[6] A. Marten and P. Misme, 'Réflexion d'ondes électromagnétiques par des surfaces irrégulières et optique géométrique', in Annales des Télécommunications, 1971, vol. 26, pp. 31–36.

[7] M. Falasconi, L. C. Andreani, A. M. Malvezzi, M. Patrini, V. Mulloni, and L. Pavesi, 'Bulk and surface contributions to second-order susceptibility in crystalline and porous silicon by second-harmonic generation', Surface science, vol. 481, no. 1–3, pp. 105–112, 2001.

[8] E. H. Nicollian and J. R. Brews, MOS (metal oxide semiconductor) physics and technology. John Wiley & Sons, 2002.

[9] D. K. Schroder, Semiconductor material and device characterization. John Wiley & Sons, 2015.

[10] W. M. Werner, 'The work function difference of the MOS-system with aluminium field plates and polycrystalline silicon field plates', Solid-State Electronics, vol. 17, no. 8, pp. 769–775, 1974.

[11] G. Parker, 'Encyclopedia of materials: science and technology', 2001.

[12] R. Castagne and A. Vapaille, 'Description of the SiO_2-Si interface properties by means of very low frequency MOS capacitance measurements', Surface Science, vol. 28, no. 1, pp. 157–193, 1971.

[13] Y. Yan et al., 'Characterization of thin Al_2O_3/SiO_2 dielectric stack for CMOS transistors', Microelectronic Engineering, vol. 254, p. 111708, 2022.

[14] Y. Yan, V. Kilchytska, D. Flandre, and J.-P. Raskin, 'Investigation and optimization of traps properties in Al_2O_3/SiO_2 dielectric stacks using conductance method', Solid-State Electronics, vol. 194, p. 108347, 2022.

Chapter 5: SHG calibration to probe dielectric stacks/Si(100) interfaces

Abstract

This chapter presents the SHG results to evaluate the quality of silicon passivation with high-k dielectric layers. We start by showing the studied samples along with Q_{tot} and D_{it} values measured with corona oxide characterization of semiconductors (COCOS) method. In order to identify the highest SHG signal/noise ratio, we perform tests using a variety of experimental parameters (including polarization configurations and laser power). Metal-oxide-semiconductor capacitors are also fabricated and studied by C-V to extract the fixed oxide charges (Q_{ox}) and the defects densities. The electrical parameters extracted from COCOS and C-V will be first correlated with SHG response to compare various passivation layers. In a second time, experimental and simulated calibrated curves SHG versus E_{DC} are discussed. At the end, some SHG results of silicon on insulator substrates will reveal the difficulties encountered to analyze the SHG response from multilayer structures.

Contents of chapter 5

5.1 Passivated samples used

The studied samples are 13 nm high-k dielectric (Al_2O_3 or HfO_2)/2 nm SiO_2 stacks deposited on 300 mm p-type Si(100) wafer. As described in the previous chapter, the deposition method is thermal ALD. Preliminary investigation of these samples was performed at STMicroelectronics using corona charges (COCOS) measurements [1]. Table 5.1 shows the interface properties (Q_{tot} and D_{it}) extracted by COCOS for the samples, as-deposited and after annealing. All the Q_{tot} and D_{it} minimum, maximum and mean values are depicted in Figure 5.1a and b, respectively. These properties depend on the oxidant precursor and temperature used during the deposition. Indeed, several elements can create negative charges such as the ionized oxygen form O_2^{2-}, the $AlO_{4/2}^-$ anions [2], or even the interstitial hydrogens H^-. The results show that Al_2O_3 layer fabricated with O_3 as an oxidant source stores more negative charges than those fabricated with H_2O. These results can be influenced by an excess of oxygen concentration. Additionally, as-deposited H_2O based layers exhibit lower trap densities compared to O_3-based ALD layers as already demonstrated in the literature [3]. Furthermore, the decrease in the deposition temperature of Al_2O_3 (H_2O) can induce a decrease in the growth rate, resulting in a higher density of vacancies or interstitial atoms that can trap charges, which explains the increase in the D_{it} values for samples fabricated at 100°C. This can also be caused by electron trapping by extrinsic elements like carbon contamination from the chamber or even the precursor TMA [1]. Moreover, it has been shown that the post-deposition annealing modifies the interface quality [4], [5]. For example, most of the alumina samples exhibit a reduction in defect density and an activation of fixed negative charges. Naturally another oxide material exhibit differences in the interface quality. For example, among these samples, HfO_2 has the lowest level of field effect passivation because of the lowest negative charges density and the best chemical passivation (lowest D_{it}). These COCOS results will be used later to interpret the SHG response of the materials.

Table 5.1: *Comparison of D_{it} and Q_{tot} in high-k dielectric/Si structures prepared by thermal ALD with H_2O and O_3, as-deposited and after annealing* [1].

Material and method		D_{it} ($eV^{-1}.cm^{-2}$)	Q_{tot} (cm^{-2})
Al_2O_3 O_3 at 325°C-ALD	As-deposited	9.8×10^{12}	-2.9×10^{12}
	Annealed	6.2×10^{11}	-2.1×10^{12}
Al_2O_3 H_2O at 325°C-ALD	As-deposited	4.8×10^{11}	-1.1×10^{12}
	Annealed	4.3×10^{11}	-1.2×10^{12}
Al_2O_3 H_2O at 100°C-ALD	As-deposited	7.8×10^{11}	8.5×10^{10}
	Annealed	8.4×10^{11}	-3.5×10^{12}
HfO_2 H_2O at 325°C-ALD	As-deposited	2.3×10^{11}	-2.3×10^{11}
	Annealed	1.7×10^{11}	-7×10^{10}

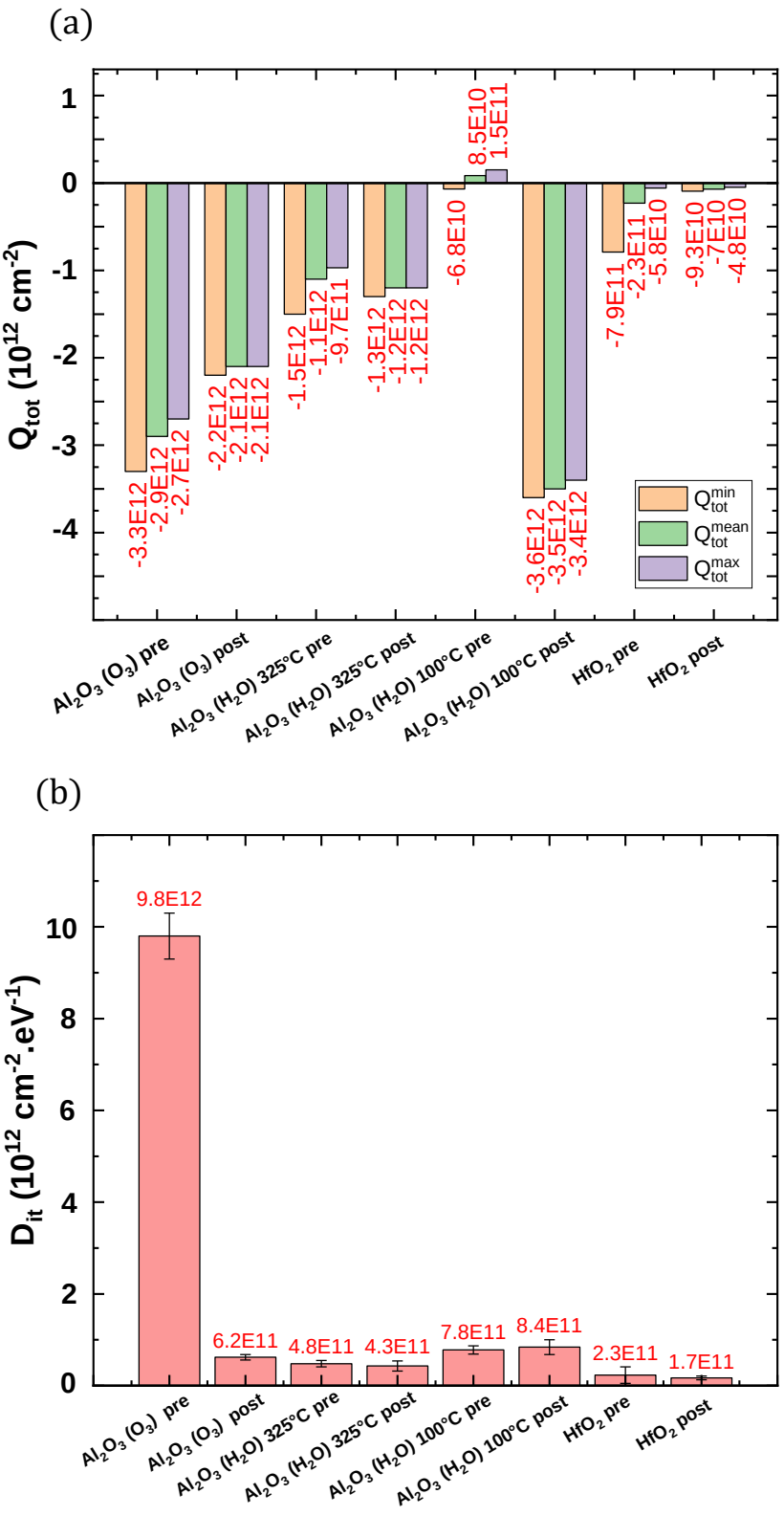

Figure 5.1: *COCOS results for the studied samples pre and post annealed:* ***(a)*** Q_{tot} *and* ***(b)*** D_{it} *[1].*

5.2 Typical experimental SHG parameters

In order to find the appropriate experimental parameters for our study of passivation quality of Al_2O_3 samples, this section explains the effect of several parameters on the measured SHG. Figure 5.2 shows an example of SHG versus time from as-deposited Al_2O_3 (H_2O) 100°C on Si sample. These first measurements were performed with 120 mW laser power, at 47° incident angle, on the sample at 0° azimuthal angle and varying the input and output polarizations. Further discussions in section 5.4.2 will cover how the laser power influences the results and how to modify it to focus on Q_{ox}.

Figure 5.2 shows the time-dependent SHG (TD-SHG) intensity of the sample for four configurations P_{in}/P_{out}, S_{in}/P_{out}, P_{in}/S_{out} and S_{in}/S_{out}. Each measurement is performed for 35 seconds. During the first 5 seconds, the incident laser beam is blocked and the cache is opened for the next 30 seconds of measurement. A visible time dependency can be observed when the reflected second harmonic (SH) beam is P-polarized (black and red lines in Figure 5.2) for P- and S-polarized fundamental beams (P_{in}/P_{out} and S_{in}/P_{out}, respectively). Conversely, for S-polarized SH beam, the signal-to-noise ratio (SNR) for the both configurations (P_{in}/S_{out} and S_{in}/S_{out}) is very low (green and blue lines). The SHG intensity of P_{in}/P_{out} configuration is higher than that of S_{in}/P_{out}, which is theoretically expected, as shown in eqs. (3.49) and (3.50) in chapter 3 [6]. Therefore, the next TD-SHG studies will be performed with P_{in}/P_{out} configuration, where the SNR is high.

Figure 5.3 depicts the normalized SHG intensity versus the angle of incidence (AOI) for the P_{in}/P_{out} (a) and S_{in}/P_{out} (b) configurations, obtained experimentally and by simulation. The normalization is performed by dividing each curve by its maximum. The simulation takes into account all experimental parameters and material properties. According to Figure 5.3, the maximum SHG response for P_{in}/P_{out} configuration is found at an AOI of 65° and for the S_{in}/P_{out} at around 45° AOI. In order to obtain an SHG response for the two polarization cases, the next experiments will be perform at angles of incidence around 45°.

Before trying to evaluate the passivation quality using SHG, the reproducibility of the SHG measurements is discussed in the next section.

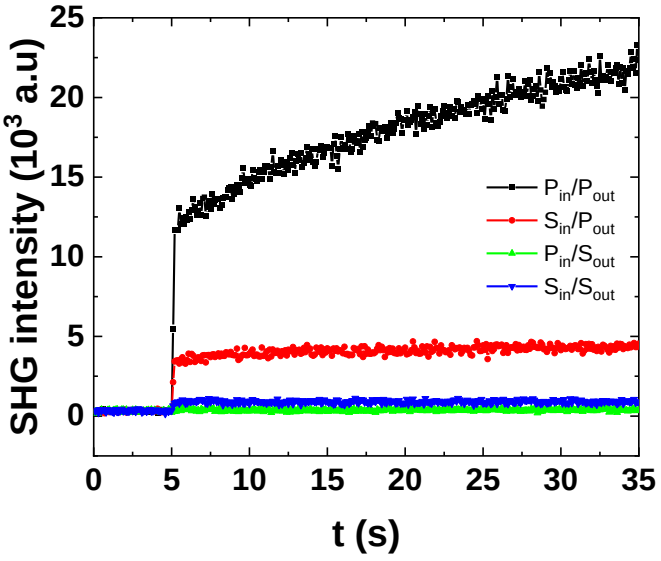

Figure 5.2: *TD-SHG experimental signals in four different polarization configurations from a sample of Al_2O_3 (H_2O) 100°C as-deposited.*

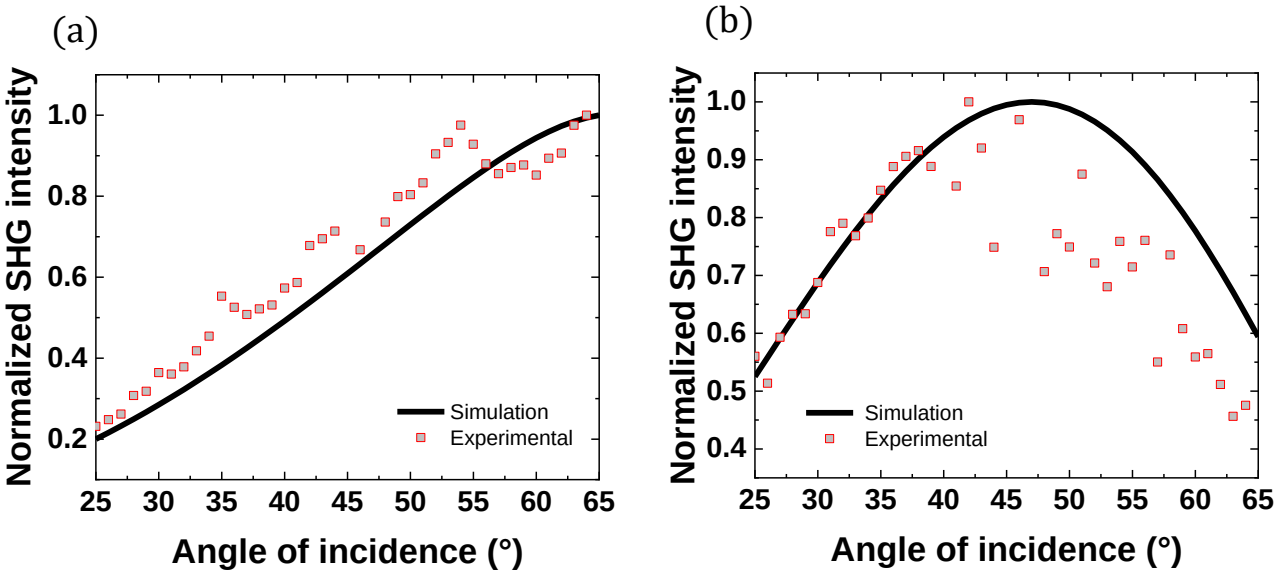

Figure 5.3: *Experimental and simulated SHG as a function of the angle of incidence for* ***(a)*** *P_{in}/P_{out} and* ***(b)*** *S_{in}/P_{out} polarizations, from Al_2O_3 (H_2O) 100°C as-deposited sample.*

5.3 Reproducibility

Evaluating the reproducibility of the SHG response is an important step before any attempt to perform a correlation or calibration. The reproducibility is assessed by measuring SHG at different locations on each wafer. Figure 5.4 shows the TD-SHG signals measured on five points on a specific region near the center for two materials (Al_2O_3 H_2O (100°C) and HfO_2) before (b and d) and after (c and e) annealing, respectively. Figure 5.4a illustrates the schematic of the wafer; the red dots show the rough position for each SHG measurement. For each sample in Figure 5.4, the SHG curves measured at different positions are very close, which validates a good reproducibility of the SHG measurements. However, the Al_2O_3 as-deposited films in Figure 5.4a show more variations compared to the other samples. To understand the reason of this difference, SHG measurements were also taken in several dispersed regions on the wafer.

Figure 5.5b, c, d and e illustrate TD-SHG signals measured at the center and on two sides of the wafer, as shown in Figure 5.5a. The SHG responses in Figure 5.5 especially of the as-deposited Al_2O_3 (b) and HfO_2 (d) samples vary a lot depending on the measurement locations. These samples were already subjected to pump-probe Kelvin Probe Force Microscopy (pp-KPFM) measurements in Aubriet's thesis [1]. The pp-KPFM results revealed higher surface photovoltage SPV_{trap} at the wafer borders, which was explained by an inhomogeneity of the passivation layer for these samples. The SHG results are in agreement with pp-KPFM where the higher SHG intensities obtained at the borders can be explained by the existence of more trap densities. This issue is less noticeable for the annealed samples in Figure 5.5c and e, since they have better passivation quality.

All the other wafers were also tested and demonstrated a very good repeatability (not shown in the thesis). Consequently, the variation in SHG signals from various locations on the wafers is not caused by a limited accuracy of the technique but is related to the spatial variations of the passivation layer quality. Given the sensitivity of SHG measurements to this inhomogeneity, we will perform further studies only on the central region of wafers.

Figure 5.5b and d also reveal a variation of the dynamics towards saturation of measured curve on regions that exhibit high and low defect densities. This variation can be also attributed to the D_{it} charges as we will explain in the next section.

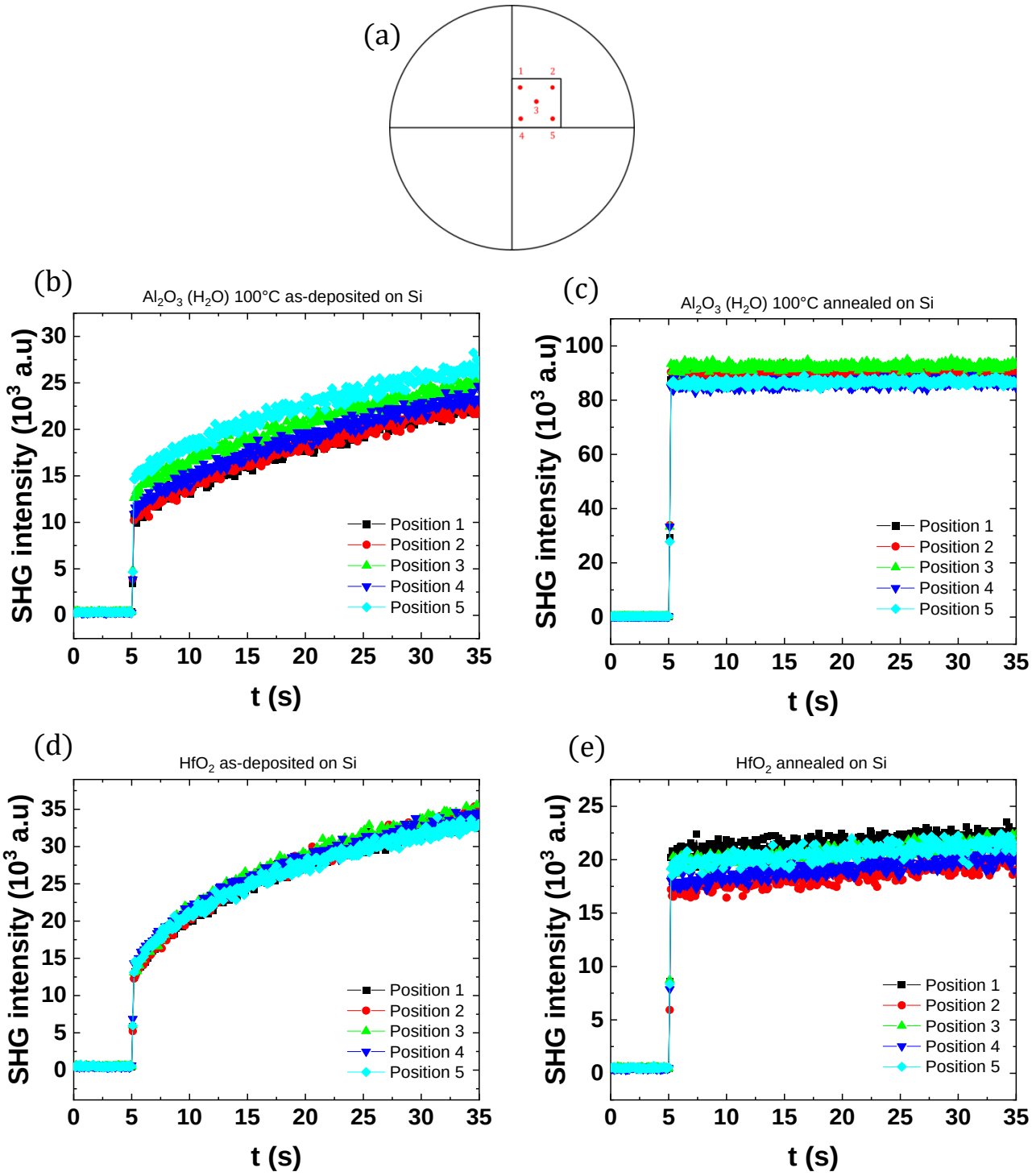

Figure 5.4: (a) *The different locations of measurements performed on cuts coming from the wafer center. TD-SHG signals at various locations on* ***(b)*** *Al_2O_3 H_2O (100°C) as-deposited,* ***(c)*** *Al_2O_3 H_2O (100°C) annealed,* ***(d)*** *HfO_2 as-deposited,* ***(e)*** *HfO_2 annealed samples. The position variation differences are in the order of cm. The experimental parameters used are 45° incident angle, 120 mW laser power, 0° azimuthal angle and P_{in}/P_{out} polarization configuration.*

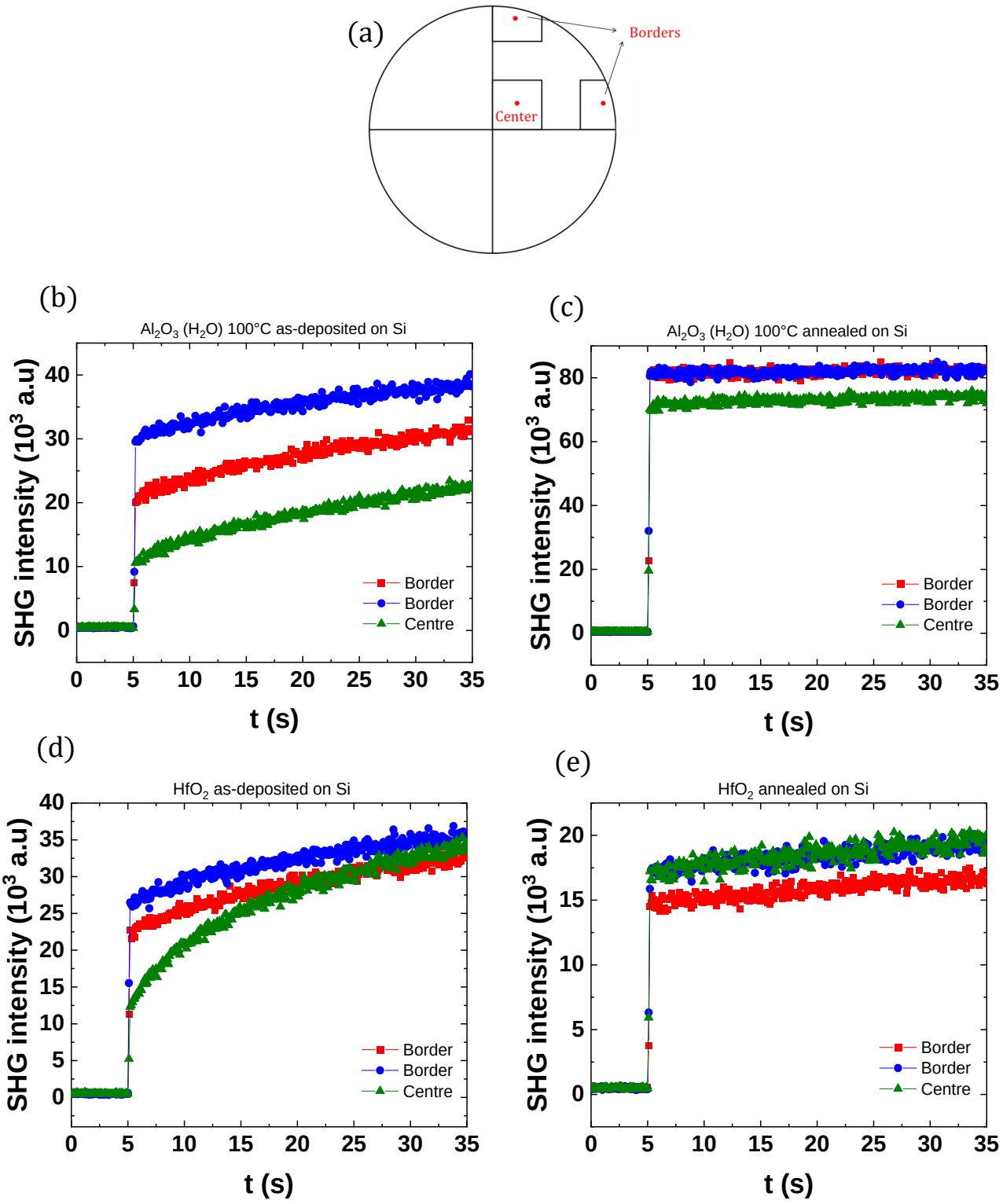

Figure 5.5: (a) *Wafer schematic with the location of measurements. TD-SHG measurements at the borders and at the center of* ***(b)*** *Al_2O_3 H_2O (100°C) as-deposited,* ***(c)*** *Al_2O_3 H_2O (100°C) annealed,* ***(d)*** *HfO_2 as-deposited,* ***(e)*** *HfO_2 annealed wafers. The measurements are made at 45° incident angle, 120 mW laser power, 0° azimuthal angle and P_{in}/P_{out} polarization configuration.*

5.4 TD-SHG response and chemical passivation

In the previous sections where we discussed the choice of SHG experimental parameters and reproducibility, we could notice that saturation level of the TD-SHG signal and the dynamics towards saturation varied for each sample. Let us remind that TD-SHG signal can be described in a simple view by:

$$I_{2\omega}(t) \sim \left|\epsilon_0 \left[\chi^{(2)} + \chi^{(3)} \left(\boldsymbol{E_{DC}(0)} + E_{DC}(t)\right)\right]\right|^2 (I_\omega)^2 \quad (5.1)$$

Consequently, $I_{2\omega}$ time variation is related to $E_{DC}(t)$, while the saturation SHG contains both $E_{DC}(0)$ and $E_{DC}(t)$. The aim of this section is to describe the mechanisms that can modify the TD-SHG and correlate them to D_{it} (section 5.4.1). Then, we will show how to reduce the D_{it} effects on the measured SHG signal by adjusting the laser power in order to focus on Q_{ox} (section 5.4.2).

5.4.1 D_{it} charges effect on the TD-SHG

The quality of passivation of Si by Al_2O_3 films varies according to the ALD deposition conditions [3], as previously shown. In this section, we will focus on using the alumina H_2O-based film deposited at 100°C before and after annealing. The electrical parameters of this sample before annealing are measured by COCOS with a total charge density Q_{tot} ~8.5×10^{10} cm^{-2} and defect density D_{it} of 7.8×10^{11} $eV^{-1}.cm^{-2}$. Figure 5.6a shows five consecutive TD-SHG measurements from this sample with laser blocking moments (dark) of 5 seconds between each. At each measurement, the laser beam at 120 mW is shined for 30 seconds. Because the SHG is sensitive to the interface electric field, the signals exhibit behavior that can be related to charging and discharging of traps as already explained in literature [8]. Specifically, the strong monotonous increase in the EFISH intensity during the illumination time can be induced by two mechanisms depicted in Figure 5.7:

1- Generation of electron-hole pairs in silicon caused by the excitation with photon energy (~1.59 eV) larger than the gap energy of silicon (~1.1 eV) [9].
2- Photon-induced charge injection into the Al_2O_3. During the measurement, the electrons from the silicon valence band can be injected towards the dielectric conduction band via multiphoton absorption processes and eventually become trapped by the states present at the Al_2O_3-SiO_2 interface for thick oxides, as in our case. Note that for thinner oxides (~1-2 nm), the electrons can be injected on the oxide outer surface. Generally, the charge separation can be seen through the time evolution of SHG signal [10], [11].

The charge transfers may be favored by a relatively high density of interface traps between the alumina and the silicon [12].

In Figure 5.6a, the SHG intensity continues to increase for two consecutive measurements without returning to the first initial value, indicating that the 5 seconds dark time between the two measurements was insufficient for the electrons to discharge. After 145 s, the initial SHG value increased four times over the initial value. This means that the injected electrons have filled some of the traps.

COCOS results showed an increase in the field effect passivation ($Q_{tot} \sim -3.5\times10^{12}$ cm^{-2}) after annealing this sample, while maintaining the same low order of chemical passivation ($D_{it} \sim 8.4\times10^{11}$ $eV^{-1}.cm^{-2}$). Figure 5.6b depicts the SHG variation over time from this annealed sample. The intensity level of the five consecutive SHG measurements obtained here appears to be stable. The presence of high negative charges can be the responsible for this quick saturation because it can mask any time variation due to D_{it}. Thereby, the SHG results from samples with different Q_{tot} and D_{it} should be carefully interpreted.

Although field effect passivation plays the most important role in the SHG initial value, our results underline that multiphoton process can affect the SHG level especially of samples with low density of fixed charges. As a result, if we want to focus on fixed oxide charges correlation with the SHG, the D_{it} effect should be eliminated or at least minimized. Generally, the multiphoton phenomenon arises when the laser beam is sufficiently intense [13]. So, a laser power decrease could be a solution and will be discussed in the next section.

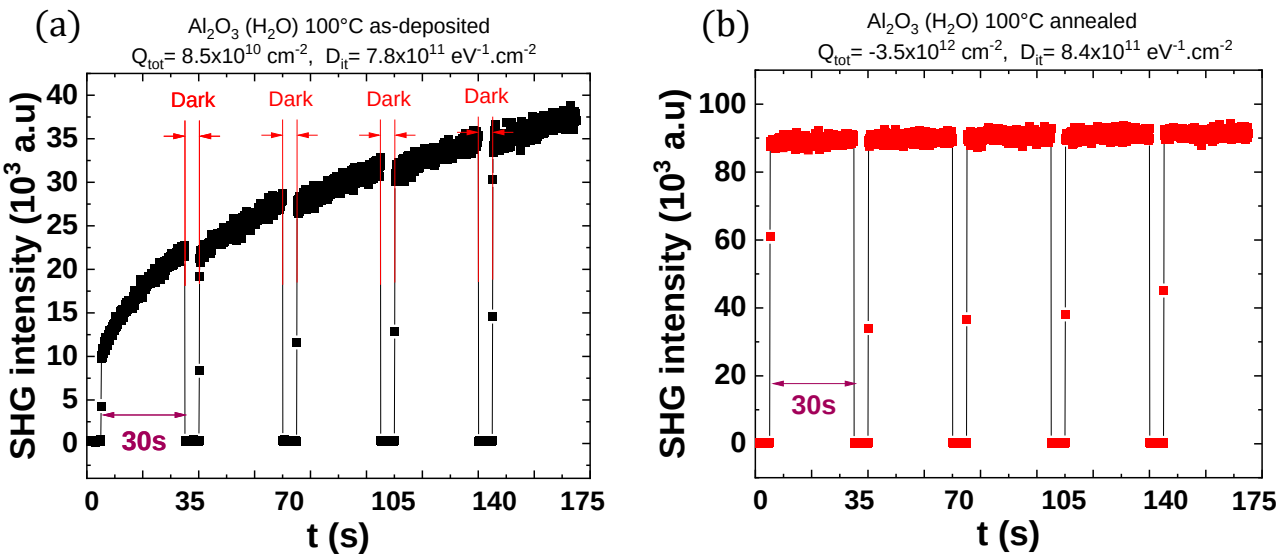

Figure 5.6: *Five consecutive TD-SHG measurements at the same spot on the sample Al_2O_3 (H_2O) 100°C on Si,* ***(a)*** *before and* ***(b)*** *after annealing the wafer.*

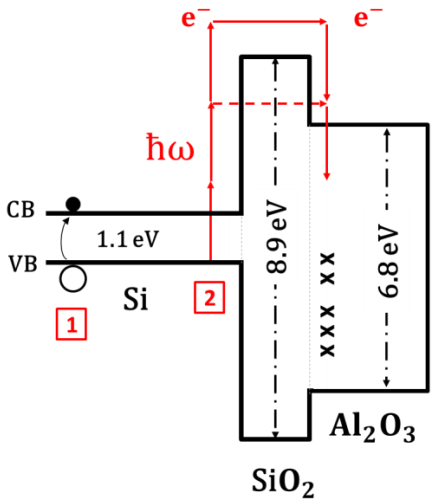

Figure 5.7: *Band diagram and charge dynamics for a $Al_2O_3/SiO_2/Si$ structure during laser beam exposure [8].*

5.4.2 Dynamics of TD-SHG curve against the laser power

Figure 5.8 shows the TD-SHG measurements carried out for two laser powers, 120 mW and 60 mW. At higher laser power (120 mW), the continuous increase in SHG intensity during the illumination time seems to be more significant than that obtained with 60 mW. In fact, the offset between the valence band of silicon and the conduction band of the oxide is 4.1 eV and the laser energy used is 1.59 eV. Therefore, the absorption of three photons is necessary to give sufficient energy to excite an electron from the valence band of the silicon and inject it into the dielectric, as shown in Figure 5.7 [10]. Therefore, the multiphoton process probability roughly depends on the cube of the laser power and is thus reduced rapidly when using a lower laser power. Indeed on Figure 5.8, it can be seen that the slope of the curve is reduced by a factor ~8 when the laser power is reduced by a factor 2 (from 120mW to 60 mW), which is in-line with cube dependency expected from a three-photon absorption phenomenon.

Additionally, the ratio of initial SHG values of the two curves in Figure 5.8a and b is equal to 4 (2^2). This was expected because the intensity of second harmonic wave is proportional to the square of the incident light intensity and thus of the laser power [14]. This proves that our measurement is indeed sensitive to a second order non-linear phenomenon and not to a thermal phenomenon for example, which would not be quadratic.

The aim of the next studies is to identify the signature of the fixed charges on the SHG intensity. In order to have a SHG response with a minimum effect of D_{it}, we seek to have stable signals as the one shown in Figure 5.8b. So a lower laser power must be used.

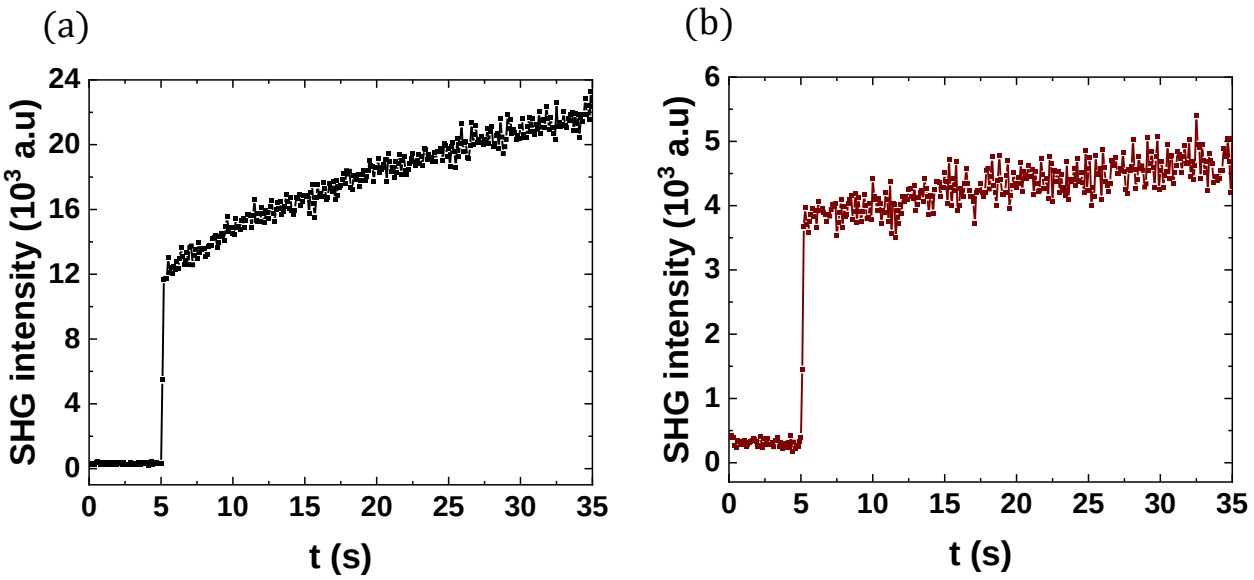

Figure 5.8: *TD-SHG signal from Al_2O_3 (H_2O) 100° as-deposited for an incident laser power of* ***(a)*** *120 mW and* ***(b)*** *60 mW.*

5.5 Field effect passivation and calibration of the SHG response

As previously stated, while $E_{DC}(t)$ is a result of trapping/detrapping mechanisms, the initial value in the TD-SHG curve corresponds to $\chi^{(2)}$ and $\chi^{(3)}E_{DC}(0)$. Fixed oxide charges, which are responsible for field effect passivation induce the pre-existing field $E_{DC}(0)$. Correlations and calibrations of SHG for fixed charge evaluation should therefore be performed using the initial SHG value that is less impacted by D_{it}. In the first subsection, we will discuss the correlation of the initial SHG and Q_{tot}. Then, we will use the electrical parameters extracted from COCOS (Q_{tot}) and C-V (Q_{ox}) to reach a quantitative analysis and a calibration of the SHG.

In order to advance the calibration process, appropriate measurement conditions are used in this section: i) P_{in}/P_{out} polarization to have the highest SNR; and ii) laser power = 60 mW to minimize the occurrence of the trapping mechanisms.

5.5.1 Correlation between SHG and COCOS (Q_{tot})

In this first study, Q_{tot} measured by COCOS will be used as a guide to explore the SHG dependency on fixed charges.

i. SHG versus time: SHG evolution with Q_{tot}

We started by relating the SHG response to the oxide charge values from the passivation stacks of Al_2O_3/SiO_2. Comparative studies, using TD-SHG measurements, were performed to evaluate the influence of the post-deposition annealing for each sample presented in Table 5.1. Figure 5.9 shows the time-dependent SHG intensity measured under 60 mW incident laser power, for P_{in}/P_{out} configuration, 47° angle of incidence and 0° azimuthal angle. The black and red signals correspond to as-deposited and annealed substrates, respectively.

As displayed in Table 5.1, a low total oxide charge density of $Q_{tot} \sim 8.5 \times 10^{10}$ cm^{-2} was extracted by COCOS measurement for as deposited Al_2O_3 (H_2O) sample prepared at low temperature (100°C). After annealing, there was a large increase in Q_{tot} of about -3.5×10^{12} cm^{-2} and a slight increase in D_{it} which remained at around 8×10^{11} $eV^{-1}.cm^{-2}$. Since the oxide negative charges are activated during annealing, the DC electric field at the interface of SiO_2/Si increases, resulting in an increase in the SHG intensity signal, as shown in Figure 5.9a.

For the Al_2O_3 (H_2O) sample deposited at 325°C (Figure 5.9b), similar SHG values were measured for the material before and after the annealing. Based on the COCOS data in Table 5.1, the Q_{tot} obtained after annealing is close to that before annealing. Thus, a good qualitative agreement between SHG and Q_{tot} from COCOS is obtained for the H_2O based samples prepared at low and high temperature.

Figure 5.9c shows the SHG signals of as-deposited and annealed O_3-based ALD films. Before annealing, the Q_{tot} value was slightly higher. As a consequence of the higher negative fixed charges, the expected response was to find the SHG of the as-deposited sample higher than that of the annealed one. Experimentally, this was not the case, as SHG level for the samples before and after annealing is very close. This mismatch might be due to the significant defect density (9.8×10^{12} $eV^{-1}.cm^{-2}$) for the sample before annealing, which was reduced by annealing to 6.2×10^{11} $eV^{-1}.cm^{-2}$. So, the question is whether the D_{it} has also an effect on the SHG level? To go for a global comparison between the six alumina layers with various Q_{tot} and D_{it} values, a SHG calibration curve versus the E_{DC} is plotted in the following section.

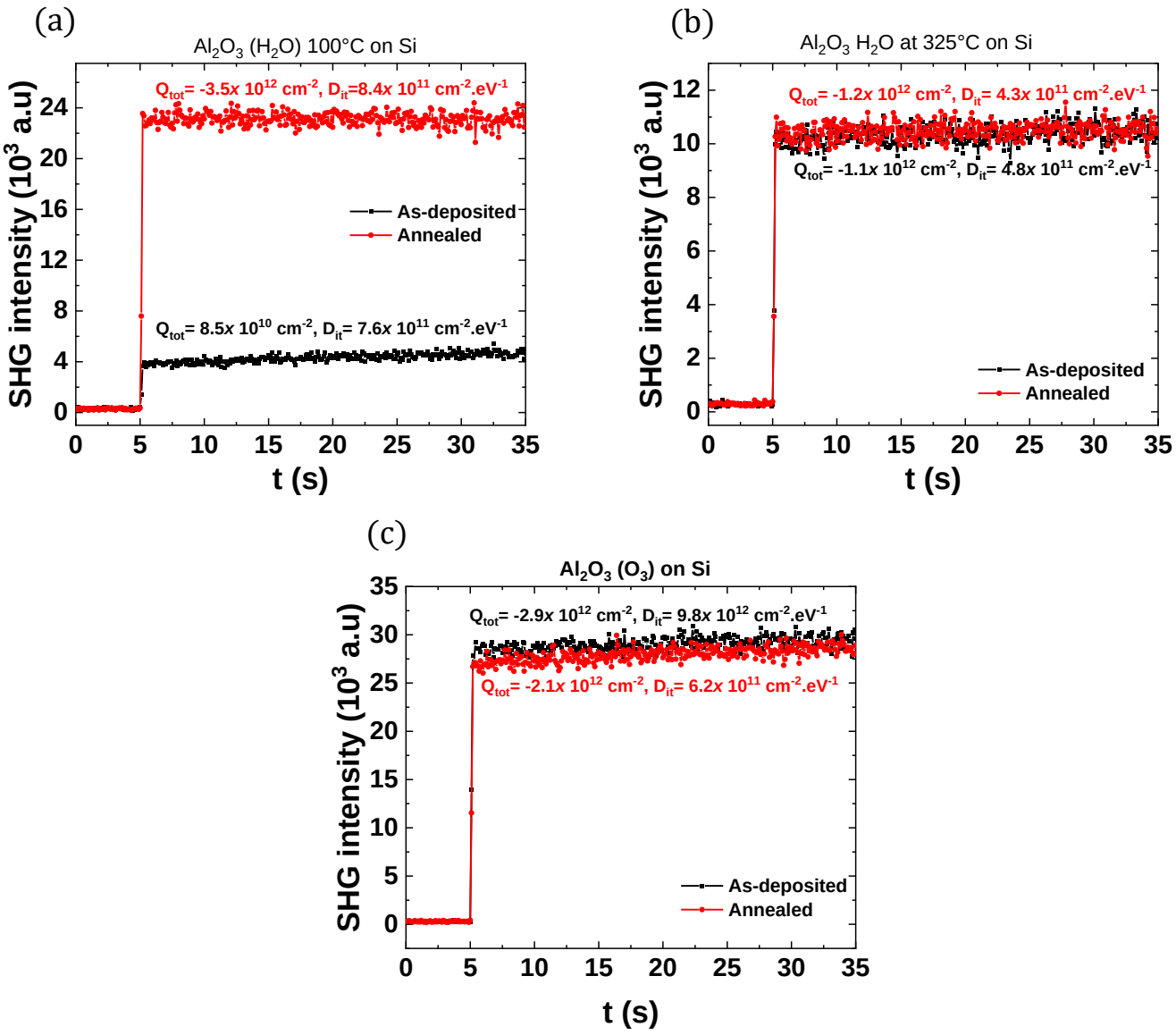

Figure 5.9: *TD-SHG signals from Al_2O_3 on Si(100) before and after annealing from* ***(a)*** *H_2O 100°C,* ***(b)*** *H_2O at 325°C, and* ***(c)*** *O_3 based ALD processes. The experimental parameters used are P_{in}/P_{out} configuration, 47° angle of incidence and 60 mW laser power.*

ii. Tentative of SHG calibration using Q_{tot}

A calibration of the SHG with respect to electrical parameters of the samples would make the technique a really powerful characterization method. Our first tentative described here focuses on the initial response point of SHG which is associated with the initial electric field $E_{DC}(0)$, attributed to fixed charges.

To better visualize the influence of E_{DC}, the square-root of SHG intensity versus initial E_{DC} value was preferred since eq. (5.1) leads us to expect a linear relationship in this case. Figure 5.10 shows the normalized experimental SHG intensity versus the E_{DC}, for all $Al_2O_3/SiO_2/Si(100)$ samples superposed with a simulated curve. The normalization aims to compare the experimental results with the simulated ones. The simulated curve, obtained by our tool, was plotted taking into account all the terms of eq. (5.1) and all optical phenomena (i.e absorption, multiple reflection, etc.) in the $Al_2O_3/SiO_2/Si$ structure as described in chapter 3. The SHG conditions (given in section i) and material properties are introduced in the simulation code. The Al_2O_3 refractive indices implanted into the simulator at the fundamental and SH wavelengths are 1.76 and 1.79, respectively [15].

It is worth reminding that the SHG intensity contains the two tensors: the interfacial second-order and third order optical susceptibilities ($\chi^{(2)}$ and $\chi^{(3)}$). The SHG intensity for $E_{DC} = 0$ is very low in the simulation as shown in Figure 5.10 (the solid line) because $\chi^{(2)}$ components terms are supposed very small compared to the EFISH terms as explained in chapter 3.

The experimental SHG data of samples are represented in Figure 5.10 with different colored shapes. They correspond to the initial value from the TD-SHG curves, extracted from data in Figure 5.9.

Both experimental and simulated curves are normalized by the SHG intensity of the annealed Al_2O_3 (H_2O) 100° sample, since it has the higher Q_{tot}. That's why a perfect superposition is observed for the initial value in Figure 5.10. Both experimental and simulated exhibit a linear response of the square root of SHG with the electric field, though a shift between them is visible. Some of the possible reasons for not obtaining a perfect superposition between simulations and experiments are:

1- The response that comes from the $\chi^{(2)}$ terms might not be negligible experimentally, and it could have a comparable value with the $\chi^{(3)}E_{DC}(t)$ terms. It is indeed very difficult to have precise values for these parameters in the literature, as shown in chapter 3 [16], [17].

2- The electric field introduced in the simulator is the variable for the simulation.

$$E_{DC}^{simulation} = E_{DC}(0) \tag{5.2}$$

For the experimental points $E_{DC}(0)$ were determined from Q_{tot} using Gauss equation:

$$E_{DC}^{experimental} = \frac{qQ_{tot}}{\varepsilon_{Si}} \tag{5.3}$$

Indeed, Q_{tot} from COCOS is not Q_{ox}. Q_{tot} represents the total charges introduced into and onto the dielectric and it contains not only the fixed charges Q_{ox}, but also the interface trapped charge at flat bands (Q_{it}) and the oxide trapped charges (Q_{ot}) [18]:

$$Q_{tot} = Q_{ox} + Q_{it} + Q_{ot} \tag{5.4}$$

Therefore, the $E_{DC}^{experimental}$ obtained does not correspond to Q_{ox} only.

3- Our procedure only uses one measurement point of a full SHG versus time curve for each sample. Could this be responsible for the mismatch?

The 3rd point can actually be avoided by working for example with families of curves SHG versus input polarization for various E_{DC}, as will be explained in the next section.

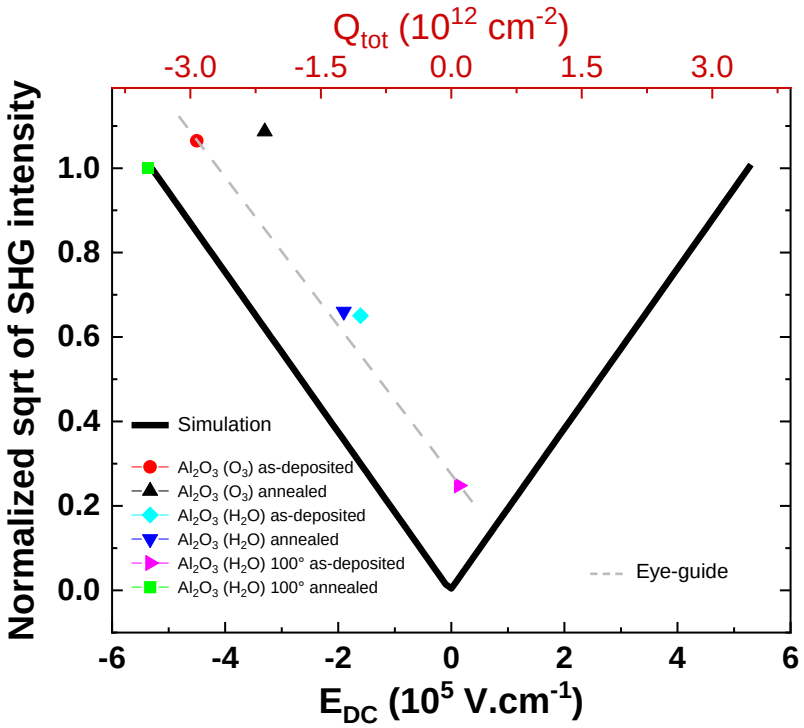

Figure 5.10: *Simulated and experimental SHG signals versus E_{DC} (bottom axis) and Q_{tot} (top axis) from $Al_2O_3/SiO_2/Si(100)$ samples. The E_{DC} for the experimental points is calculated based on the Q_{tot} results obtained from COCOS in Table 5.1.*

iii. SHG versus input polarization angle: Q_{tot} impact

One of the measurements that could give access to E_{DC} of the samples is the SHG measurement versus input-polarization angle. The advantage is that instead of using only one SHG measurement point for each sample (i.e the initial SHG value of the TD-SHG curve), we'll exploit a range of SHG values obtained for various input polarization angles.

The analysis will be done for the two output polarizations, P-out and S-out. Note that from the theoretical point of view, the expressions of SHG intensity for P-output $I_{2\omega}^{P_{out}}$ and S-output $I_{2\omega}^{S_{out}}$ are directly related with the interface electric field [6]:

$$I_{2\omega}^{P_{out}}(t) = | a + [b\chi_{xxzz}^{(3)} E_{DC}(t) + c\chi_{zxxz}^{(3)} E_{DC}(t) + d\chi_{zzzz}^{(3)} E_{DC}(t)] \cos^2\psi + e\chi_{zxxz}^{(3)} E_{DC}(t) \sin^2\psi|^2 \ |I_\omega|^2 \quad (5.5)$$

$$I_{2\omega}^{S_{out}}(t) = | f + g\, \chi_{xxzz}^{(3)} E_{DC}(t) \sin\psi \cos\psi|^2 \ |I_\omega|^2 \quad (5.6)$$

In these expressions, a and f are the time-independent terms that contain the different components of the material second-order susceptibility. b, c, d, e and g depend to the incident angle. In our case, the angle of incidence is fixed to 47°, thus they are constants. ψ is the input polarization angle that will be the variation parameter.

Figure 5.11 and Figure 5.12 represent the experimental and simulated SHG intensity of the samples before and after annealing versus input polarization angle for the two cases P- and S-output polarization, respectively. Figure 5.11a and Figure 5.12a display fully measured curves that that have identical shapes to the simulated curves (Figure 5.11b and Figure 5.12b). However, the experimental and simulations do not have the same order. This confirms that the disagreement in Figure 5.10 is not due to a simple possible error on the initial point. Experimentally, the curves which have the higher intensities are those of Al_2O_3 (O_3) sample. The negative charges measured by COCOS from this sample (before and after annealing) are lower than that of annealed Al_2O_3 (H_2O) 100° sample. The E_{DC} values introduced in the simulator are calculated using Gauss equation based on Q_{tot}. This confirms that the difference between simulation and experiment values is more likely related to the material properties ($\chi^{(2)}, \chi^{(3)}$) and/or E_{DC} values we introduced in the simulation.

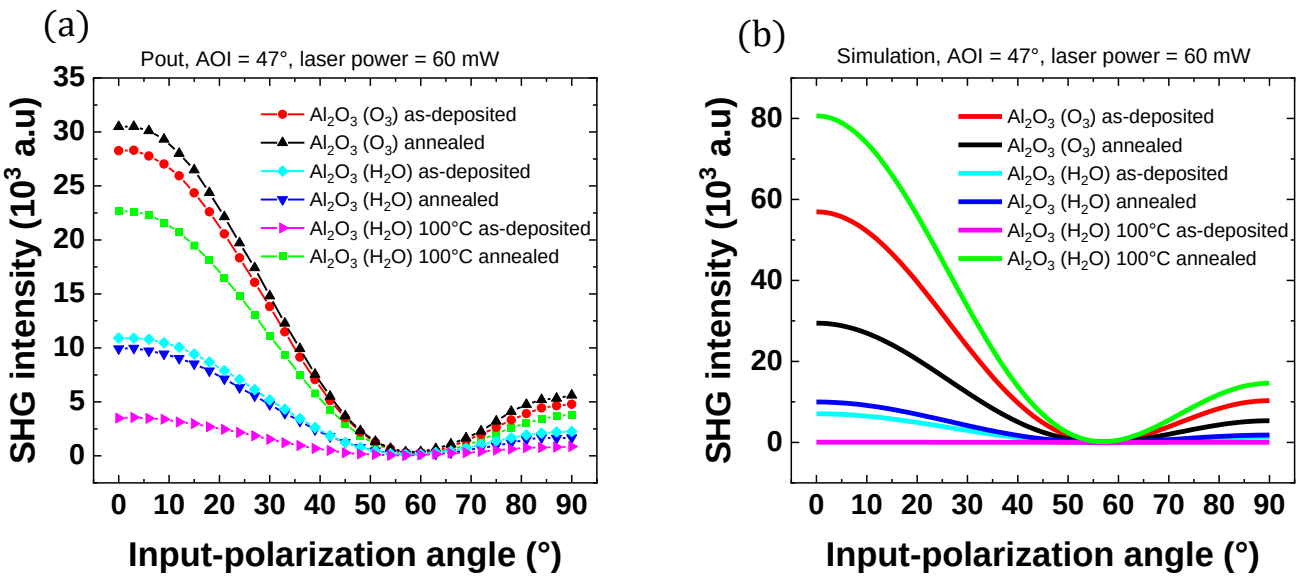

Figure 5.11: *Experimental **(a)** and simulated **(b)** SHG intensity versus input polarization angle for P-output SH polarization from $Al_2O_3/SiO_2/Si(100)$ samples. The simulated curves are plotted using the same code color and with E_{dc} calculated from Q_{tot}.*

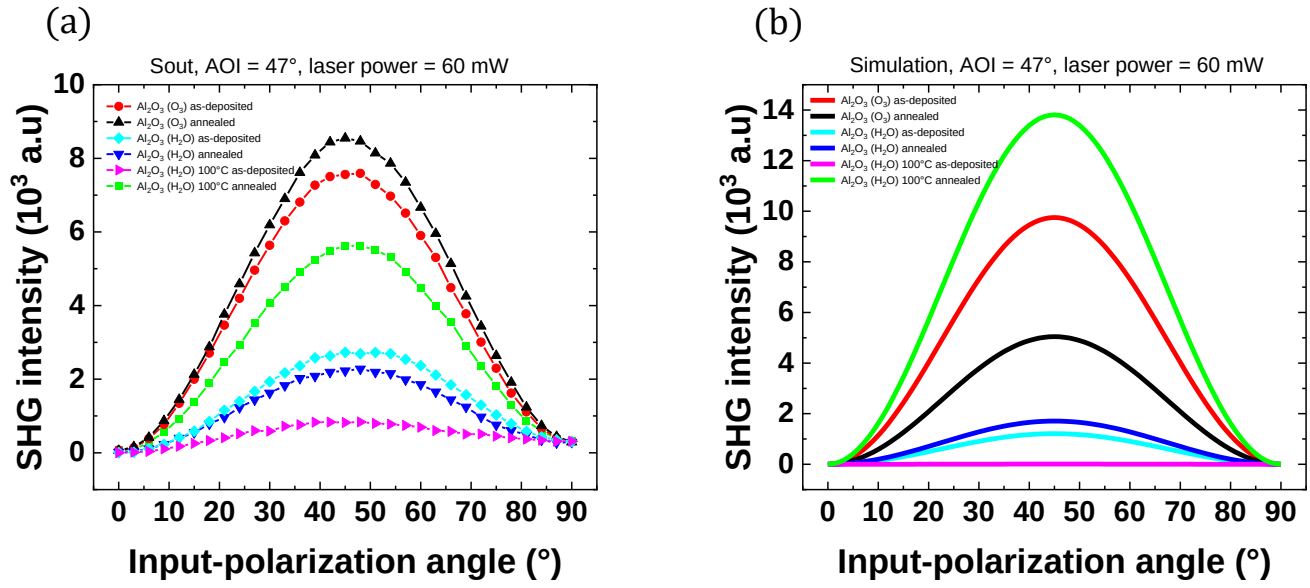

Figure 5.12: *Experimental **(a)** and simulated **(b)** SHG intensity versus input polarization for the S-output SH polarization from $Al_2O_3/SiO_2/Si(100)$ samples. The simulated curves are plotted using the same code color and with E_{dc} calculated from Q_{tot}.*

In order to further exploit the results presented above, based on the theoretical expressions (5.5) and (5.6), we define SHG intensity ratios from the experimental curves. Annealed Al_2O_3 (O_3) sample is chosen as a reference sample ("REF") for calculating the

ratios with the other samples, because it has the highest experimental SHG intensity. Based on the theoretical eq. (5.5) of $I_{2\omega}^{P_{out}}$, the E_{DC}-dependent SHG ratios at an input-polarization angle ψ of 0° (P_{in}) and at 90° (S_{in}) are given by:

$$\left.\frac{\sqrt{I_{2\omega}^{P_{out}}}}{\sqrt{I_{2\omega}^{P_{out}}("REF")}}\right|_{\psi=0°} = \left|\frac{a+[b\chi_{xxzz}^{(3)}E_{DC}+c\chi_{zxxz}^{(3)}E_{DC}+d\chi_{zzzz}^{(3)}E_{DC}]}{a+[b\chi_{xxzz}^{(3)}E_{DC}("REF")+c\chi_{zxxz}^{(3)}E_{DC}("REF")+d\chi_{zzzz}^{(3)}E_{DC}("REF")]}\right| \quad (5.7)$$

$$\left.\frac{\sqrt{I_{2\omega}^{P_{out}}}}{\sqrt{I_{2\omega}^{P_{out}}("REF")}}\right|_{\psi=90°} = \left|\frac{a'+e\chi_{zxxz}^{(3)}E_{DC}]}{a'+[e\chi_{zxxz}^{(3)}E_{DC}("REF")]}\right| \quad (5.8)$$

a and a' include the bulk anisotropic (ξ), the isotropic γ and the surface ($\chi_{zxx}^{(2)}$, $\chi_{xxz}^{(2)}$, $\chi_{zzz}^{(2)}$) second order susceptibility of the material (see chapter 3). Depending on the choice of the input-polarization angle, the contribution of some of the components can be canceled. a and a' correspond to the case of P_{in} and S_{in}, respectively.

In the case of S_{out}, the E_{DC}-dependent SHG ratio is calculated at an input-polarization angle of 45° where the maximum is obtained, as shown in Figure 5.12:

$$\left.\frac{\sqrt{I_{2\omega}^{S_{out}}}}{\sqrt{I_{2\omega}^{S_{out}}("REF")}}\right|_{\psi=45°} = \left|\frac{f+g\,\chi_{xxzz}^{(3)}E_{DC}}{f+g\,\chi_{xxzz}^{(3)}E_{DC}("REF")}\right| \quad (5.9)$$

The aim here will be to calculate the experimental ratios based on the measured curves and try to evaluate if the dominant parts are related to a, a', f or to the terms including E_{DC}.

The corresponding E_{DC} used in the simulation was calculated using Gauss law based on Q_{tot} charges extracted by COCOS and the ratio:

$$|\,\text{COCOS ratio}\,| = \left|\frac{E_{DC}}{E_{DC}("REF")}\right| = \left|\frac{Q_{tot}}{Q_{tot}("REF")}\right| \quad (5.10)$$

Table 5.2: *SHG ratios between "Annealed $Al_2O_3(O_3)$ on Si(100)" sample (used as reference) and the other samples, calculated from the experimental curves and from COCOS results included in the simulation.*

Sample		Experimental SHG			Simulation
		$\lvert ratio \rvert_{P_{in}P_{out}}$	$\lvert ratio \rvert_{S_{in}P_{out}}$	$\lvert ratio \rvert_{45°-S_{out}}$	$\lvert$COCOS ratio$\rvert$
Al_2O_3 O_3 at 325°-ALD	As-deposited	0.96	0.92	0.94	1.38
	Annealed ("REF")	–	–	–	–
Al_2O_3 H_2O at 325°-ALD	As-deposited	0.6	0.63	0.57	0.52
	Annealed	0.57	0.55	0.5	0.57
Al_2O_3 H_2O at 100°-ALD	As-deposited	0.33	0.38	0.32	0.04
	Annealed	0.86	0.82	0.8	1.67

As demonstrated in Table 5.2, the values of different ratios calculated from the experimental SHG curves at the three polarization configurations are close. This implies that a, a' and f values in equations (5.7-5.9) which correspond to the second order susceptibility terms have a low role in the SHG response compared to the term that corresponds to E_{DC}. This conclusion is consistent with what is described in the literature [19]. Consequently, the variation of E_{DC} at the interface of the different samples is the responsible for the variation in SHG ratio.

It should be noted that the highest experimental SHG level is obtained from Al_2O_3 (O_3) samples, which indicates that it has the highest interface electric field caused mainly by highest fixed oxide charges. Based on the literature [3], [20]–[23], even before annealing, O_3-based processes are more capable to store negative charges than those using H_2O as an oxidant source. This is due to an excess oxygen concentration. In articles [3], [20], [21] for example, O_3 samples show fixed oxide charges between 5×10^{12} and 8×10^{12} while the value is lower when H_2O is used (1.3×10^{11} - 4×10^{12}). The higher D_{it} value obtained for the O_3 process is also in agreement with other studies [3], [20]. It may be caused by the higher interface carbon density and lower interface hydrogen density [20]. Generally, the fixed oxide charges and D_{it} properties depend to several deposition factors such as the deposited ozone concentration [21] and the deposition temperature [24]. So, even though the literature shows that deposition with O_3 produces better surface field effect passivation quality which is in agreement with our SHG results, it cannot be generalized to include our case because the electrical parameters depend on the fabrication conditions.

Thereby, the question is whether the high SHG initial values obtained from the Al_2O_3 (O_3) samples were caused by the high D_{it} density measured by COCOS or by a high value of Q_{ox} that was masked by the D_{it} in the Q_{tot} combination. In order to study this issue, we used capacitance-voltage (C-V) measurements which allow extracting the actual Q_{ox} (instead of the Q_{tot} from COCOS) of each sample as presented in the next section.

5.5.2 SHG calibration relying on C-V data

In this section, C-V measurements are used to extract the fixed oxide charges and interface state densities for the various samples and will allow to plot a new SHG calibration curve using more precise values for the initial electric field $E_{DC}(0)$.

i. C-V results

To perform C-V measurements, MOS capacitors were fabricated on the samples as described in the previous chapter. Figure 5.13 illustrates an example of C-V curves obtained on capacitors with Al_2O_3 (H_2O) 100°C as-deposited and annealed dielectrics. The measurements are performed with a small ac signal at frequency of 500 kHz on a MOS capacitor of area 10^{-4} cm^2. The relative permittivity of Al_2O_3 used to calculate the theoretical C_{ox} (shown in the figure) equals to 7 [25], [26].

Figure 5.13 shows that the flat-band voltage of the as-deposited sample is shifted towards a positive applied gate voltage. This indicates that the as-deposited sample contains more negative oxide charges than the annealed one; this is in contradiction to the COCOS results shown in Table 5.1. In order to investigate this difference, new SHG measurements were done on the fabricated samples and will be presented in the next section.

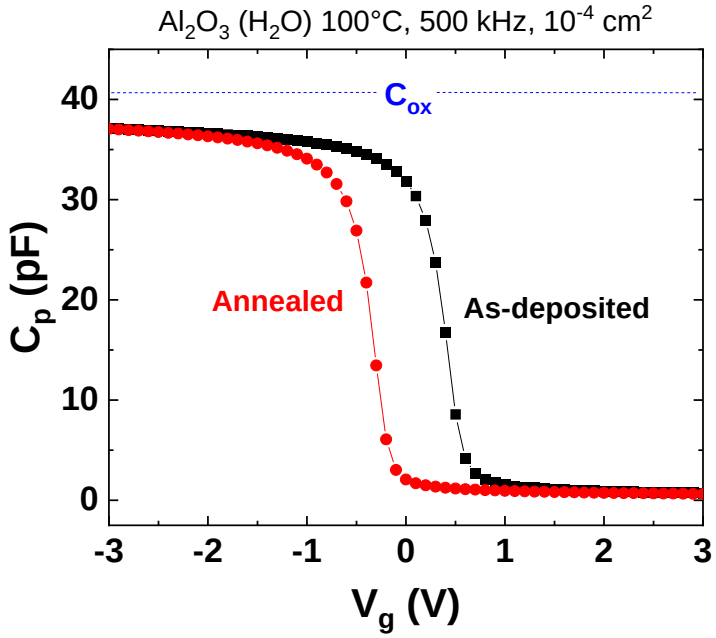

Figure 5.13: *Measured capacitance versus gate voltage on capacitors with Al_2O_3 (H_2O) 100°C as-deposited and annealed dielectrics.*

ii. MOS capacitor fabrication issues revealed by SHG response

To explore the disagreement in sign of the fixed oxide charges between C-V and COCOS techniques, we will compare the SHG signals of samples before and after MOS fabrication. SHG measurements were made on the oxide between MOS capacitors of fabricated samples. The SHG results of the samples before and after MOS fabrication process are shown in Figure 5.14a and b, respectively.

As stated previously, according to the EFISH phenomenon, high charge oxide density results in a high SHG intensity. Figure 5.14a recalls the results from Al_2O_3 (H_2O) 100°C before MOS fabrication, showing a higher signal for the annealed sample.

After MOS fabrication, the SHG intensity of as-deposited substrate (black curve in Figure 5.14b) becomes higher than that of annealed substrate (red curve). This means that the amount of oxide charges becomes more important in as-deposited sample than in the annealed sample, after MOS fabrication. The C-V curves from the previous section show indeed that the sample before annealing stores more negative charges than the annealed sample. Consequently, SHG and C-V measurements on samples after MOS fabrication are in agreement. These results indicate that the MOS fabrication has modified the properties of the dielectric materials.

A second fabrication procedure has been set-up in order to avoid modifying the electrical properties of the samples, and will be presented in the following section.

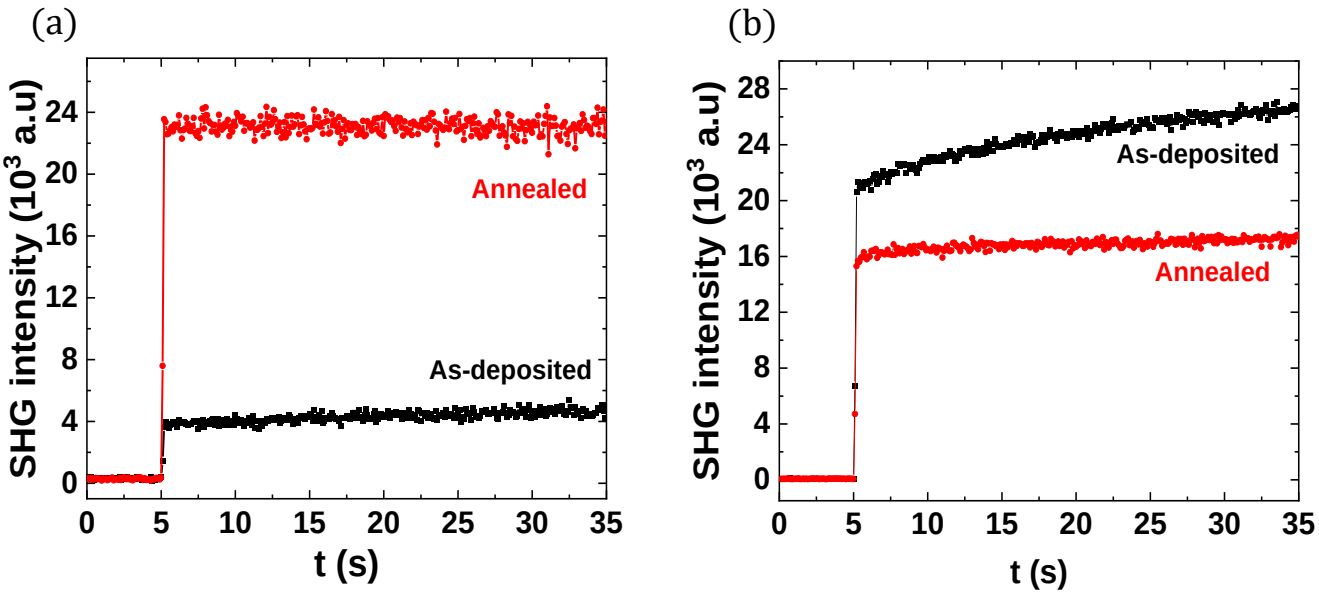

Figure 5.14: *TD-SHG curves from Al_2O_3 (H_2O) 100°C as-deposited and annealed samples* ***(a)*** *before and* ***(b)*** *after MOS fabrication. SHG measurements of samples which contain MOS capacitors were carried out on the oxide surface, between the capacitors.*

iii. Electrical parameters of two batches measured by C-V

As explained in the previous chapter, before depositing aluminum layer to create the metal gate of MOS capacitors, the samples were annealed in the vacuum deposition chamber for 30 min at a temperature of 200°C. After fabrication of the first batch, we found that the electrical parameters had been modified. We hypothesized that the pre-deposition annealing step was the reason for this change in the dielectric stacks. Therefore, the second batch of capacitors was fabricated without pre-deposition annealing. The MOS capacitor fabrication process used is described in chapter 4.

Figure 5.15 displays C-V curves from Al_2O_3 (H_2O) as-deposited sample measured after MOS capacitors fabrication with the first (a) and the second (b) process. The ac frequencies used during measurements are 500, 100, 10 and 1 kHz.

The comparison of Figure 5.15a and b shows that the two fabricated batches give different electrical properties. For example, C-V curve measured at high frequency (500 kHz) of the sample fabricated with pre-deposition annealing (Figure 5.15a) is shifted

towards more positive voltages compared to sample fabricated without annealing (Figure 5.15b). This means that the negative charge density of batch 1 sample is higher than that of batch 2. Additionally, for the sample fabricated in batch 2, strong bumps appear at low frequency, which indicates the presence of a high defect density, in contrast to sample fabricated in batch 1, which does not.

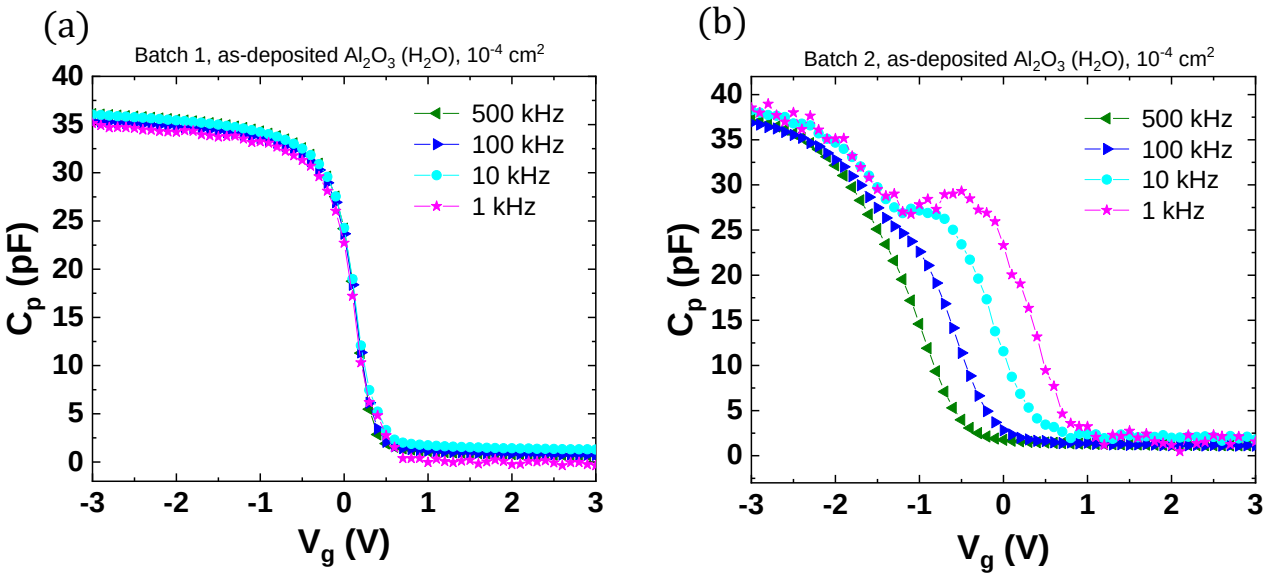

Figure 5.15: *Measured C-V curves at 500 KHz, 100 kHz, 10 kHz and 1kHz for Al_2O_3 (H_2O) as-deposited sample. The measurements were taken with samples fabricated in batch 1 and batch 2 issued from the same wafer* ***(a)*** *batch 1: with pre- deposition annealing and* ***(b)*** *batch 2: without annealing before Al deposition.*

Fixed oxide charges and D_{it} values are determined from the C-V measurements for both batches. Their values are shown in Table 5.3 with batch 1/batch 2 samples represented in black/red color. As shown in Table 5.3, samples from batch 1 contain high Q_{ox} densities (in the range of 10^{12} cm^{-2}) and very low interface states densities (10^{10}—10^{11} $eV^{-1}.cm^{-2}$). In contrast, the defects of samples from batch 2 are high compared to the fixed charges. Thus, for batch 1, the negative charges were activated and the D_{it} values have been reduced by the annealing before the metal layer deposition. Whereas for batch 2, the MOS fabrication process increased the defect density in the samples. Therefore, the dielectric stacks were modified by our MOS capacitor fabrication processes and any comparison with COCOS data (Table 5.1) is not relevant.

None of the batches realized preserved the initial state of materials, i.e. the COCOS data differed from the C-V results every time. Thus, the problem is not only the annealing

process. The observed electrical modifications may also be due to the use of chemical solution that etches the aluminum and that might affect the alumina layer.

We did not have time to develop a third fabrication process, which could also potentially fail to produce MOS capacitors while leaving the electrical parameters of the dielectric stack unmodified. We thus decided to work on the samples after the fabrication of MOS capacitors. We knew the electrical parameters from these samples were different than after the dielectric layer fabrication at STMicroelectronics, so we could not use COCOS measurements. However, we could use the C-V results to measure Q_{ox} on these samples and use those Q_{ox} values to produce a new calibration curve. The experimental SHG measurements on this curve were obtained on the oxide regions between the MOS capacitors.

Table 5.3: *Electrical parameters extracted by C-V measurements and E_{DC} calculated with Gauss law. Batch 1 and 2 corresponds to the MOS capacitor fabrications with and without pre-deposition annealing, respectively.*

	Material		D_{it} ($eV^{-1}.cm^{-2}$)	Q_{ox} (cm^{-2})	E_{DC} ($V.cm^{-1}$)
Batch 1	Al_2O_3 O_3 at 325°-ALD	● As-deposited	1.14×10^{11}	-1.88×10^{12}	-2.9×10^{5}
		▲ Annealed	8.7×10^{11}	-2.2×10^{12}	-3.4×10^{5}
	Al_2O_3 H_2O at 325°-ALD	◆ As-deposited	4.7×10^{10}	-2.3×10^{12}	-3.6×10^{5}
		▼ Annealed	2.3×10^{10}	-2.6×10^{12}	-4.03×10^{5}
	Al_2O_3 H_2O at 100°-ALD	▶ As-deposited	2.3×10^{10}	-2.9×10^{12}	-4.8×10^{5}
		■ Annealed	2.1×10^{10}	-2.1×10^{12}	-3.3×10^{5}
Batch 2	Al_2O_3 O_3 at 325°-ALD	★ As-deposited	1.6×10^{11}	-1×10^{12}	-1.5×10^{5}
		⊲ Annealed	5.9×10^{12}	-8×10^{11}	-1.2×10^{5}
	Al_2O_3 H_2O at 325°-ALD	◓ As-deposited	6.2×10^{12}	-2.8×10^{11}	-5×10^{4}
		✳ Annealed	2.9×10^{12}	-5.4×10^{11}	-8.3×10^{4}
	Al_2O_3 H_2O at 100°-ALD	⊞ As-deposited	1.7×10^{12}	8.2×10^{11}	1.3×10^{5}
		⊕ Annealed	3.9×10^{12}	1.9×10^{12}	3×10^{5}

iv. SHG calibration using Q_{ox} from C-V measurements

Figure 5.16 illustrates the new calibration curve, i.e. the normalized SHG intensity versus the electric field E_{DC} (bottom axis) and the fixed oxide charges Q_{ox} (top axis). E_{DC} values are calculated with Gauss law using Q_{ox} obtained from C-V measurements. The experimental SHG points correspond to the initial values from TD-SHG curves. To measure the SHG on samples containing MOS capacitors, the laser was focused on the oxide surface, between capacitor patterns. The experimental SHG configuration is: 60 mW laser power, P_{in}-P_{out} polarizations and 47° angle of incidence. As mentioned previously, the simulations were done with the same SHG parameters and material properties as in experiments. The SHG measured from Al_2O_3 (H_2O) 100°C as-deposited sample from batch 1 has the highest intensity, hence this value is used to normalize the experimental results of all the other samples. The normalization of simulated curves is made using the same point.

The majority of experimental points measured from batche 1 match the simulation. However, samples of batch 2 in particular those that exhibit high defect densities (indicated by the red arrows) show higher experimental intensity compared to the simulation. According to Table 5.3, although Q_{ox} of these samples are quite low, their D_{it} values are high (in the order of 10^{12} $eV^{-1}.cm^{-2}$). Therefore, the first SHG intensity measurement point in the TD-SHG used for the calibration can be affected by the strong D_{it} values. Indeed for those samples, since the D_{it} is high, some of them will trap carriers rapidly when the laser is shined on the surface and their charge will add to the fixed Q_{ox}. Indeed in these cases, it can be difficult to separate Q_{ox} and D_{it} effect in the SHG response.

For samples containing lower amounts of interface traps D_{it}, the calibration curve presented on Figure 5.16 can thus be used to measure the Q_{ox} charge as a function of the measured SHG intensity on our setup, using the same parameters (angle of incidence, polarizations, etc.). The only thing we cannot know from the SHG measurement is the sign of the oxide charge, since opposite charges produce the same SHG intensity.

These results confirm the efficiency of SHG technique to extract Q_{ox} density for Al_2O_3/SiO_2 stacks thanks to the possibility to calibrate the SHG response. In the next section, we will explore SHG characterization on another dielectric material (HfO_2).

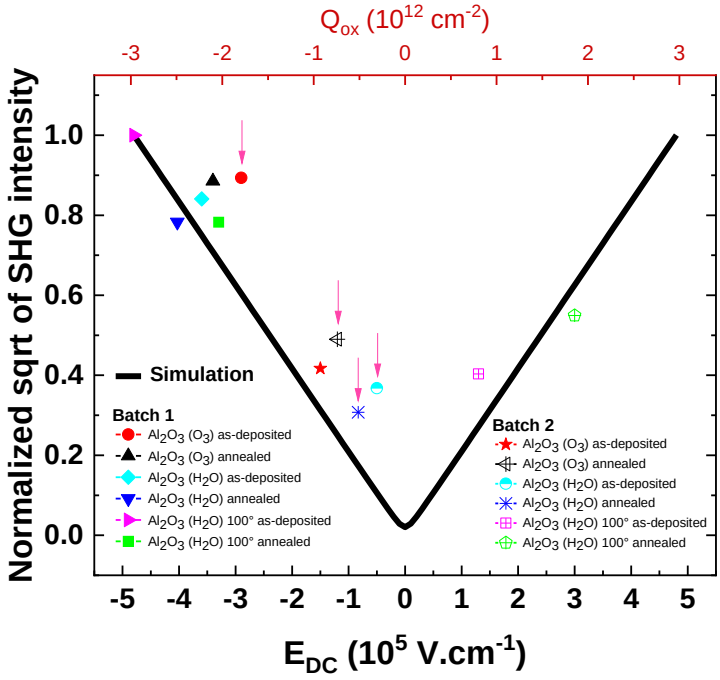

Figure 5.16: *Simulated and experimental SHG versus E_{DC} (bottom axis) and Q_{ox} (top axis) from all the Al_2O_3 samples. The experimental E_{DC} values were calculated using C-V results presented in Table 5.3.*

5.5.3 Preliminary tests on HfO_2

This section presents measured SHG response from $HfO_2/SiO_2/Si$ stacks versus time (Figure 5.17a) and versus input-polarization angle (Figure 5.17b). Before sample annealing, COCOS gave Q_{tot} of -2.3×10^{11} cm^{-2} and D_{it} of 2.3×10^{11} $eV^{-1}.cm^{-2}$. After annealing, D_{it} value is slightly reduced to 1.7×10^{11} $eV^{-1}.cm^{-2}$ and Q_{tot} is also reduced (-7×10^{10} cm^{-2}). Generally, the annealing at temperature 400-450° enhances both the chemical and field effect passivation [27]–[30]. However, we observed a decrease in the negative charges. After annealing, the interface between HfO_2 and Si can be reorganized. This rearrangement could induce an increase in the interfacial layer between the oxide and the Si substrate. The interfacial formation may contain either SiO_2 interlayer or a compositional mixture of Hf-Si-O [31]. As a result, the positive charges in the dielectric stack may increase, decreasing the total negative charges.

Both SHG curves in Figure 5.17a and b are in agreement with COCOS data, as the higher SHG signal is found for the as-deposited sample (black curve) and the lower is for the annealed one (red curve). These preliminary encouraging data should be completed in order to obtain a calibration curve adapted for this material.

All the studies that we presented until now involved only one nonlinear interface. Given the importance of multilayers in microelectronics, the use of SHG characterization for multilayers (for example, silicon on insulator) can also be interesting and will be discussed in the next section.

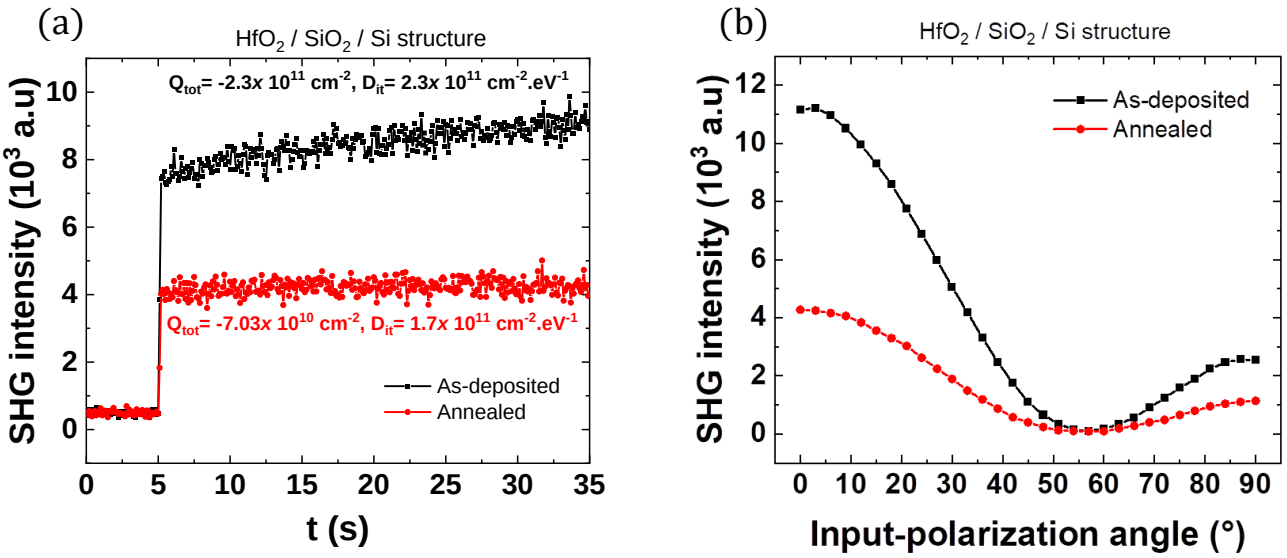

Figure 5.17: *SHG intensities from as-deposited and annealed $HfO_2/SiO_2/Si$ stacks versus* ***(a)*** *time and* ***(b)*** *input-polarization angle.*

5.6 Challenges for characterization of multilayers by SHG: a preliminary study

Silicon-on-insulator (SOI) substrates are composed of three main layers, a thin top film of silicon and a bulk silicon that are electrically isolated by the buried oxide layer BOX (SiO_2). Additionally, a "stand-alone" SOI is covered by native oxide. These substrates are used in microelectronics to reduce bulk related parasitical effects in transistors and to improve device performance [32].

Several charges, including oxide fixed charges Q_{ox} and interface states D_{it}, may exist in this structure and can affect the electrical behavior of the future devices. The presence of interface D_{it} decreases the carrier mobility. As a result, these parameters limit device performance. Hence, the evaluation of the interface properties requires appropriate characterization technique. For example, the pseudo-MOS transistor (Ψ-MOSFET) technique is specified to characterization of SOI [33]. However, this technique consisting in placing two metallic probes on the Si film, is destructive, particularly for ultrathin SOI and cannot be applied at wafer level [34], [35]. Therefore, a non-invasive characterization

method such as SHG could be very promising for extracting the electrical interface properties. Indeed the charges present induce a "static" electric field at each individual interface which can be measurable with SHG. The SHG technique was already used to study the charge generation, transport and recombination processes in ref. [36], as well as to detect the roughness, charge states and the presence of metallic contamination in ref. [37] in the SOI structures.

The previous PhD on the SHG at the laboratory already studied on various SOI structures of different Si film and BOX thicknesses. Particularly, measurements and simulations of SHG intensity versus the angle of incidence were performed on 88 nm Si film on a 145 nm BOX and a native oxide [9]. Simulations were done with varying the value of the electric field at each individual interface while keeping the rest at zero. Due to the strong absorption phenomena in the "thick" Si film, the SHG intensity showed a significant impact on the electric field presented at the upper interface and no effect on those at the bottom interfaces.

It should be noted that the fundamental and SH beams have different absorption coefficients. The penetration depth in Si is of 23 μm for the fundamental and of 133 nm for the SH [38]. This means that the SH generated at the bottom interface (film-BOX) can pass through a Si film up to 133 nm and be detected, but if the Si film thickness is "big" the impact is going to be attenuated.

In order to detect the SHG response at all interfaces in the SOI multilayer, we chose to investigate two different wafers with 12 nm Si film on 20 nm BOX and with a native oxide covering the surface of Si film. Figure 5.18a illustrates the experimental SHG curves from these samples. Although the two wafers have in principle the same geometrical parameters, the SHG responses are different. This variation may be caused by the different electrical properties of the two SOI wafers in particular their evolution in time, since both are more than 5 years old, or because the wafers were not made at the same time, so the fabrication processes may be different. Using optical simulation, we will adjust various parameters to explore which ones have the greatest influence on the SHG response and could reproduce the measured effect.

Our study deals with thin SOI. Since the Si film thickness used here is much lower than 133 nm, E_{DC} at the three interfaces is expected to contribute to the SHG response. Let us remind that the oxide is transparent to both $\boldsymbol{\lambda}$ and $\boldsymbol{\lambda}/2$. A variation of E_{DC} could be responsible for the difference on the SHG response. To investigate the effect of each E_{DC}, we carried out simulations with a variable amount of E_{DC} at a given interface, while holding the others constant.

The first test was made for $E_{DC}(3)$ at the native oxide/Si film interface. The simulated SHG curves in Figure 5.18b show a strong influence even if the electric field was increased

slowly from 10^5 V.cm^{-1} to 2×10^5 V.cm^{-1} with a step of 0.2×10^5 V.cm^{-1}. More precisely, the SHG response decreases with $E_{DC}(3)$ at 0° input-polarization angle, while it increases at 90°.

Additionally, the simulated SHG curves in Figure 5.18c show also a significant impact due to the $E_{DC}(2)$ at the Si film/BOX interface, but this time the SHG response increases for all input-polarization angles.

At the bottom interface, i.e. BOX/Si substrate interface, $E_{DC}(1)$ was also adjusted from 10^5 V.cm^{-1} to 2×10^5 V.cm^{-1}. Since a part of the SH generated at the bottom is absorbed by the Si film, the SHG modification is less important in this case (Figure 5.18d).

As a result, the top and intermediary interfacial fields play the most significant roles for our SOI structure, and the bottom one has the least impact. So far, it is still difficult to identify the difference in the two experimental curves in Figure 5.18a just by changing E_{DC}. Even if the geometry of the two samples is supposed to be the same, small variations of the thickness can be present and might influence the SHG responses.

Figure 5.18e demonstrates the decrease of SHG signal as the Si layer thickness increases. Moreover, from 0° to 45° input-polarization angle, the SHG response in Figure 5.18f increases with the BOX thickness and nearly stabilizes from 45° to 90°.

In conclusion, to reproduce the experimental results of sample 1 and 2, there are two possible configurations:

1- Sample 1 has a lower $E_{DC}(3)$ and a slightly thicker Si film, compared to the second one.
2- Sample 1 has a BOX that is slightly thinner than sample 2.

The sensitivity of the SHG on each of these parameters is promising for the use of the technique in multilayer characterization. However, the influence of the silicon thicknesses or the BOX makes the characterization of thin SOI structure more complex because it can mask information about the interfacial fields. Therefore, calibration of SHG for multilayers will be a challenging subject due to the important number of free parameters that need to be adjusted (3 interfacial electric fields + 2 thicknesses). However, this also means that SHG is a very sensitive tool that can detect both geometrical and electrical modifications of a structure. This technique could thus be very interesting to study the deviation of fabrication processes of complex stacks. Future studies could explore this challenge further and compare the results of electrical techniques that give access to interface field values with those of experimental/simulated SHG, using a procedure similar to the one that we used for alumina.

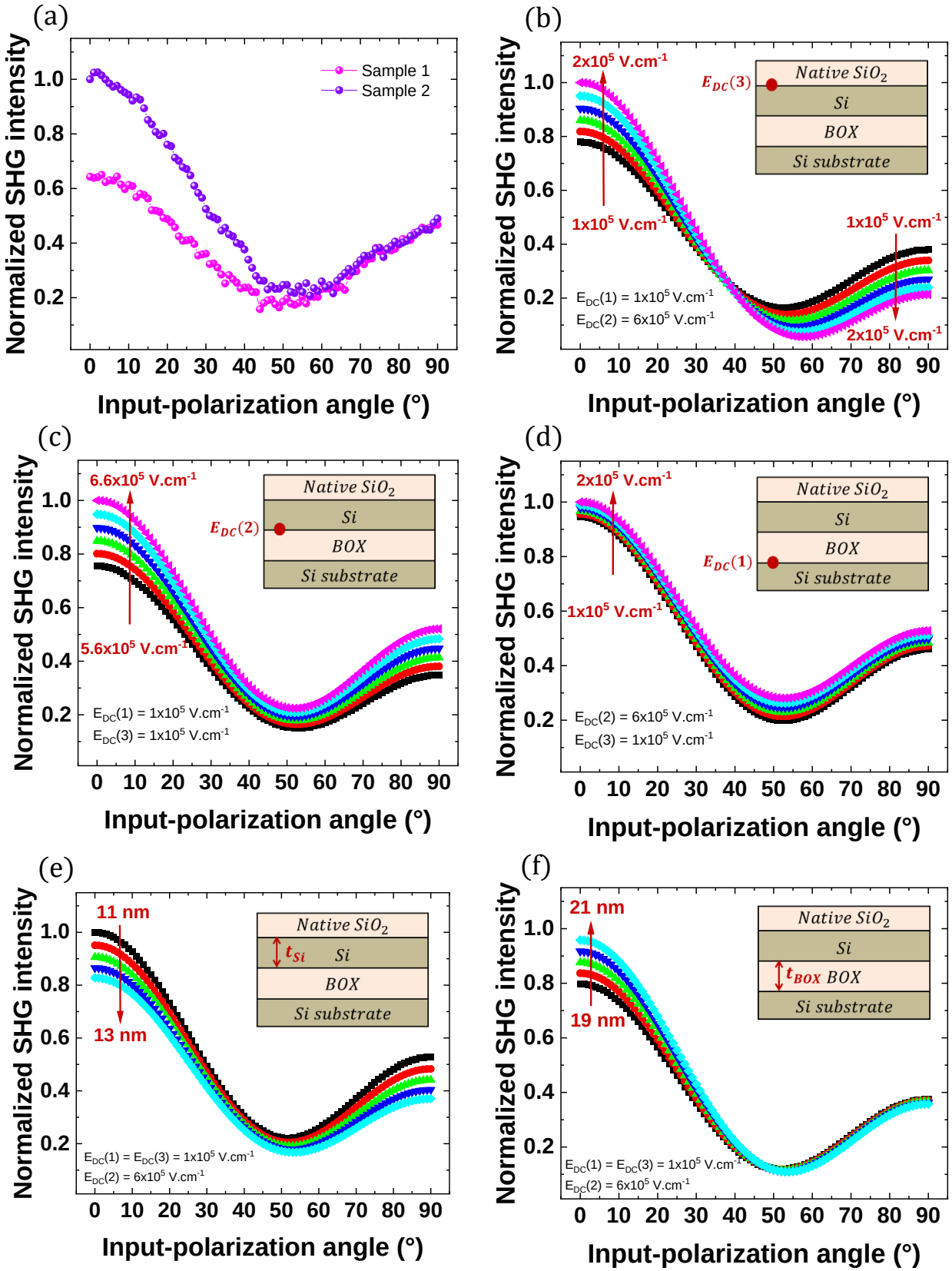

Figure 5.18: (a) *SHG measurements versus input-polarization angle from two SOI wafer with 12 nm Si film/20 nm BOX. Simulated SHG curves with varying* ***(b)*** $E_{DC}(3)$, ***(c)*** $E_{DC}(2)$ *and* ***(d)*** $E_{DC}(1)$, ***(e)*** *Si film thickness,* ***(f)*** *BOX thickness.*

5.7 Chapter conclusion

The thesis goal was to use the SHG to characterize high-k dielectrics/silicon interfaces used for passivation. Theoretically, the SHG response can be induced by the interface electric field associated with the oxide fixed charges Q_{ox} and the interface states D_{it}.

This chapter presented our main experimental results of the investigation of passivation interfaces. The wafers used are different Al_2O_3/SiO_2/p-type Si(100). The alumina films were deposited using various oxidant precursors and the preliminary characterization performed by COCOS gave access to the total oxide charge Q_{tot} and the interface traps D_{it} density for each sample.

The first task involved determining the appropriate experimental parameters that produce a high signal to noise ratio SHG. P_{in}-P_{out} configuration, angle of incidence around the 45° and azimuthal angle of 0° were found to offer the best measurements. Additionally we were able to validate the SHG repeatability by doing SHG measurements at different positions on the wafer (border and center).

Time-dependent SHG (TD-SHG) measurements were performed first using a 120 mW laser power and the signature of trapping/detrapping mechanisms was clearly observed in particular on samples with high defect densities and low fixed oxide charges. These effects might have an impact on the initial SHG value even though this value should mainly correspond to the fixed oxide charge. In order to minimize D_{it} effects and focus on Q_{ox}, a reduced laser power was preferred for the calibration for Q_{ox}.

The TD-SHG curves of each sample before and after annealing allowed to correlate the field effect passivation with SHG intensity (i.e. samples with higher Q_{tot} show stronger SHG).

A quantitative analysis consisted in obtaining a simulated and experimental calibration curve of SHG intensity versus the interface field E_{DC}. The experimental E_{DC} in the curve were calculated using Gauss equation based on Q_{tot} from COCOS. The experimental curves versus input-polarization angle had the same shape as the simulated ones. However, the order of the levels of SHG did not match between experimental and simulation data, which was also observed in the calibration curve. The discrepancy seems to be due to the E_{DC} values that were calculated with the total oxide charge from COCOS, which contains not only Q_{ox} but also some D_{it} and oxide trapped charges that respond to COCOS. So, capacitance versus voltage experiments were used to extract only Q_{ox}. Metal-Oxide-Semiconductor MOS capacitors had to be fabricated in order to perform these measurements. The comparison of electrical parameters extracted by C-V and COCOS revealed that the MOS capacitor fabrication process had modified the interface qualities. However, the SHG responses

obtained for samples after fabrication of the MOS structures had also evolved with respect to first results and SHG after MOS fabrication was consistent with Q_{ox} extractions from C-V. Therefore, we were able to plot a new calibration curve based on C-V data. The new calibration curve showed a good agreement with the simulation which confirms the ability of SHG to determine the electric field associated to fixed charges.

Finally, we tested two samples of $HfO_2/SiO_2/Si$ to show that the technique can extended to other dielectric materials. In addition, some preliminary SHG results on SOI multilayers (silicon on insulator) with three ”nonlinear” interfaces have been shown and they give a view on the complexity of extraction of fields at interfaces for these type of structures because the SHG response can be affected by a large number of parameters.

5.8 Chapter references

[1] V. Aubriet, 'Étude du photo-potentiel de surface pour la caractérisation des interfaces enterrées par microscopie à sonde de Kelvin', PhD Thesis, Université Grenoble Alpes, 2022.
[2] G. Lucovsky, 'A chemical bonding model for the native oxides of the III–V compound semiconductors', Journal of Vacuum Science and Technology, vol. 19, no. 3, pp. 456–462, 1981.
[3] G. Dingemans, N. M. Terlinden, D. Pierreux, H. B. Profijt, M. C. M. Van de Sanden, and W. M. M. Kessels, 'Influence of the oxidant on the chemical and field-effect passivation of Si by ALD Al_2O_3', Electrochemical and Solid-State Letters, vol. 14, no. 1, p. H1, 2010.
[4] B. Hoex, S. B. S. Heil, E. Langereis, M. C. M. Van de Sanden, and W. M. M. Kessels, 'Ultralow surface recombination of c-Si substrates passivated by plasma-assisted atomic layer deposited Al_2O_3', Applied physics letters, vol. 89, no. 4, p. 042112, 2006.
[5] F. Werner et al., 'Electronic and chemical properties of the c-Si/Al_2O_3 interface', Journal of Applied Physics, vol. 109, no. 11, p. 113701, 2011.
[6] H. Park, J. Qi, Y. Xu, G. Lüpke, and N. Tolk, 'Polarization-dependent temporal behaviour of second harmonic generation in Si/SiO_2 systems', Journal of Optics, vol. 13, no. 5, p. 055202, 2011.
[7] J. Bloch, J. G. Mihaychuk, and H. M. Van Driel, 'Electron photoinjection from silicon to ultrathin SiO_2 films via ambient oxygen', Physical Review Letters, vol. 77, no. 5, p. 920, 1996.
[8] N. M. Terlinden, G. Dingemans, V. Vandalon, R. Bosch, and W. M. M. Kessels, 'Influence of the SiO2 interlayer thickness on the density and polarity of charges in Si/SiO_2/Al_2O_3 stacks as studied by optical second-harmonic generation', Journal of Applied Physics, vol. 115, no. 3, p. 033708, 2014.
[9] D. Damianos et al., 'Second harmonic generation for contactless non-destructive characterization of silicon on insulator wafers', Solid-State Electronics, vol. 115, pp. 237–243, 2016.
[10] J. Bloch, J. G. Mihaychuk, and H. M. Van Driel, 'Electron photoinjection from silicon to ultrathin SiO_2 films via ambient oxygen', Physical review letters, vol. 77, no. 5, p. 920, 1996.
[11] W. Wang et al., 'Coupled electron-hole dynamics at the Si/SiO_2 interface', Physical review letters, vol. 81, no. 19, p. 4224, 1998.
[12] D. Damianos et al., 'Field-effect passivation of Si by ALD-Al_2O_3: second harmonic generation monitoring and simulation', Journal of Applied Physics, vol. 124, no. 12, p. 125309, 2018.
[13] H. Park et al., 'Characterization of boron charge traps at the interface of Si/SiO_2 using second harmonic generation', Applied Physics Letters, vol. 95, no. 6, p. 062102, 2009.
[14] R. W. Boyd, Nonlinear optics. Academic press, 2020.
[15] I. H. Malitson and M. J. Dodge, 'Refractive-index and birefringence of synthetic sapphire', in Journal of the Optical Society of America, 1972, pp. 1405–1405.
[16] M. Falasconi, L. C. Andreani, A. M. Malvezzi, M. Patrini, V. Mulloni, and L. Pavesi, 'Bulk and surface contributions to second-order susceptibility in crystalline and porous

silicon by second-harmonic generation', Surface science, vol. 481, no. 1–3, pp. 105–112, 2001.
[17] Y. Q. An, R. Carriles, and M. C. Downer, 'Absolute phase and amplitude of second-order nonlinear optical susceptibility components at Si (001) interfaces', Physical Review B, vol. 75, no. 24, p. 241307, 2007.
[18] M. Wilson, J. Lagowski, L. Jastrzebski, A. Savtchouk, and V. Faifer, 'COCOS (corona oxide characterization of semiconductor) non-contact metrology for gate dielectrics', in AIP Conference Proceedings, American Institute of Physics, 2001, pp. 220–225.
[19] T. Scheidt, E. G. Rohwer, P. Neethling, H. M. Von Bergmann, and H. Stafast, 'Ionization and shielding of interface states in native p+-Si/SiO_2 probed by electric field induced second harmonic generation', Journal of Applied Physics, vol. 104, no. 8, p. 083712, 2008.
[20] G. von Gastrow, S. Li, M. Putkonen, M. Laitinen, T. Sajavaara, and H. Savin, 'Effect of ozone concentration on silicon surface passivation by atomic layer deposited Al_2O_3', Applied surface science, vol. 357, pp. 2402–2407, 2015.
[21] G. von Gastrow, S. Li, P. Repo, Y. Bao, M. Putkonen, and H. Savin, 'Ozone-based batch atomic layer deposited Al_2O_3 for effective surface passivation', Energy Procedia, vol. 38, pp. 890–894, 2013.
[22] P. Repo and H. Savin, 'Effect of different ALD Al_2O_3 oxidants on the surface passivation of black silicon', Energy Procedia, vol. 92, pp. 381–385, 2016.
[23] M. B. González, J. M. Rafí, O. Beldarrain, M. Zabala, and F. Campabadal, 'Charge trapping analysis of Al2O3 films deposited by atomic layer deposition using H_2O or O_3 as oxidant', Journal of Vacuum Science & Technology B, Nanotechnology and Microelectronics: Materials, Processing, Measurement, and Phenomena, vol. 31, no. 1, p. 01A101, 2013.
[24] J. B. Kim, D. R. Kwon, K. Chakrabarti, C. Lee, K. Y. Oh, and J. H. Lee, 'Improvement in Al_2O_3 dielectric behavior by using ozone as an oxidant for the atomic layer deposition technique', Journal of applied physics, vol. 92, no. 11, pp. 6739–6742, 2002.
[25] M. D. Groner, F. H. Fabreguette, J. W. Elam, and S. M. George, 'Low-temperature Al_2O_3 atomic layer deposition', Chemistry of materials, vol. 16, no. 4, pp. 639–645, 2004.
[26] D. K. Simon, P. M. Jordan, T. Mikolajick, and I. Dirnstorfer, 'On the control of the fixed charge densities in Al_2O_3-based silicon surface passivation schemes', ACS applied materials & interfaces, vol. 7, no. 51, pp. 28215–28222, 2015.
[27] A. B. Gougam, B. Rajab, and A. B. Afif, 'Investigation of c-Si surface passivation using thermal ALD deposited HfO_2 films', Materials Science in Semiconductor Processing, vol. 95, pp. 42–47, 2019.
[28] J. Gope et al., 'Silicon surface passivation using thin HfO2 films by atomic layer deposition', Applied Surface Science, vol. 357, pp. 635–642, 2015.
[29] S. L. Pain et al., 'Electronic Characteristics of Ultra-Thin Passivation Layers for Silicon Photovoltaics', Advanced Materials Interfaces, vol. 9, no. 28, p. 2201339, 2022.
[30] X. Cheng et al., 'Surface Passivation Properties of HfO_2 Thin Film on n-Type Crystalline Si', IEEE journal of photovoltaics, vol. 7, no. 2, pp. 479–485, 2017.
[31] B. Aguirre et al., 'Growth, microstructure and electrical properties of sputter-deposited hafnium oxide (HfO_2) thin films grown using a HfO2 ceramic target', Applied Surface Science, vol. 257, no. 6, pp. 2197–2202, 2011.
[32] S. Cristoloveanu, 'Silicon on insulator technologies and devices: from present to future', Solid-State Electronics, vol. 45, no. 8, pp. 1403–1411, 2001.

[33] S. Cristoloveanu and S. Li, Electrical characterization of silicon-on-insulator materials and devices, vol. 305. Springer Science & Business Media, 1995.
[34] L. Pirro, 'Caractérisation et modélisation électrique de substrats SOI avancés', PhD Thesis, Université Grenoble Alpes (ComUE), 2015.
[35] D. Damianos, 'Second harmonic generation (SHG) for contactless characterization of dielectric-semiconductor interfaces', PhD Thesis, Université Grenoble Alpes, 2018.
[36] B. Jun et al., 'Characterization of multiple Si/SiO_2 interfaces in silicon-on-insulator materials via second-harmonic generation', Applied Physics Letters, vol. 85, no. 15, pp. 3095–3097, 2004.
[37] M. L. Alles et al., 'Second harmonic generation for noninvasive metrology of silicon-on-insulator wafers', IEEE transactions on semiconductor manufacturing, vol. 20, no. 2, pp. 107–113, 2007.
[38] H. Zimmermann, 'Basics of optical emission and absorption', Integrated silicon optoelectronics, pp. 1–10, 2000.

Chapter 6: General conclusions and perspectives

Contents of chapter 6

6.1 General conclusions

Silicon passivation with high-k dielectrics is essential for microelectronic and optoelectronic devices such as MOSFETs, image sensors, and solar cells. The two passivation mechanisms that reduce the carrier recombination at the surface/interface are:

1- Field effect passivation, induced by the activation of fixed oxide charge Q_{ox} which modifies the free carrier concentration present at the surface.
2- Chemical passivation, which reduces interface trap density D_{it} thanks to the atoms of the high-k dielectric.

The thesis focuses on the characterization of Q_{ox} and D_{it} in order to evaluate the passivation quality using a nonlinear optics technique: the second harmonic generation (SHG). This method is interesting for characterization purposes thanks to its high sensitivity to the surface and interface for centrosymmetric materials such as silicon, SiO_2, Al_2O_3, HfO_2, etc. Moreover, the SHG is also induced by the interface electric field (EFISH). In a simplified approach, the full SHG intensity $I_{2\omega}(t)$ can be written as:

$$I_{2\omega}(t) \sim \left| \chi^{(2)} + \chi^{(3)} \left[E_{DC}(0) + E_{DC}(t) \right] \right|^2 (I_\omega)^2 \tag{6.1}$$

$\chi^{(2)}$ and $\chi^{(3)}$ are the second and third order susceptibilities of the material, I_ω is the incident laser beam intensity. The term $E_{DC}(0)$ refers to the preexistent field at the interface between two materials which mainly depends on Q_{ox}. The time-dependent term, $E_{DC}(t)$, appears as a result of the charging/discharging phenomena, that can be associated with D_{it}.

The materials studied in the thesis are high-k dielectric stacks (mostly alumina) on Si(100) with different interface quality, fabricated at STMicroelectronics. The aim of the thesis was to calibrate the SHG response related to fixed oxide charges in order to provide a measurement technique that could potentially replace or complement the ones typically used inline (e.g. COCOS, photoconductance decay).

Given that SHG is an optical technique, optical phenomena (e.g. multiple reflections, absorption and interferences) can arise in the stack and influence the response. In order to properly extract the electrical parameters (i.e. Q_{ox} and D_{it}) from SHG, the optical phenomena had to be understood and taken into account properly. This was achieved by modeling and simulation, as described in chapter 3 of the thesis. The developed model considers the propagation of both fundamental (ω) and SH (2ω) radiation and is adapted for multilayer structures. The linear boundary conditions were established using Maxwell equations in order to calculate the fundamental electric field at the interface between materials. Using the literature, the nonlinear polarization source terms were introduced, separating bulk, surface and EFISH contributions. The nonlinear boundary conditions, that depend on the nonlinear sources, were determined starting from founding papers. We adapted the various expressions in the literature to obtain general terms separated in x, y, z components. Our equations and simulation program is adapted to any multilayer. The electric fields at the

interface were evaluated using the nonlinear boundary conditions. All these steps, as well as the calculation processes, were integrated into our simulation tool. Since the primary goal of our work is the extraction of Q_{ox}, the only EFISH term introduced in the simulation is the constant one, $E_{DC}(0)$. The validation of the equations derived from the literature and introduced in the simulation tool was done by two complementary methods:

1- Analytically, by calculating with our equations the SH reflected electric fields for a structure previously studied by the literature. Our equations yield the ones from the literature.
2- By simulating SHG curves versus various experimental parameters and comparing the results to the measurements, for both monolayers of dielectrics (e.g. native oxide on Si substrate) and multilayer (e.g. silicon on insulator) structures.

Chapter 4 gave the different experimental methodology elements exploited in the thesis with a focus on SHG and the complementary capacitance versus voltage measurements. Before beginning the experimental characterization, we installed a new laser in the SHG tool and worked on optical alignment for several months. The laser integration and the measurement methodology were discussed in chapter 4. Measurements of reflectivity versus angle of incidence and of SHG intensity versus laser power were used to validate the optical alignment. To extract SHG curves versus various experimental parameters (i.e. polarization angles, angle of incidence, etc.) from raw time-dependent SHG experiments, we developed data treatment procedures, also explained in this chapter. The methods used to extract Q_{ox} and D_{it} from C-V measurements are presented also.

Chapter 5 showed the results obtained from SHG, COCOS and C-V techniques in order to characterize the interface between the dielectric stacks and the silicon. Before investigating the passivation quality, SHG repeatability was examined on the borders and the center of each wafer. The majority of samples showed good repeatability. For the few samples that do not exhibit same results at different locations on wafer, the explanation was an inhomogeneity in terms of passivation that had been previously observed in the literature on the same wafers with other measurement technique.

In order to properly characterize Q_{ox}, the optimal SHG experimental configuration was found at P_{in}-P_{out} polarizations and angle of incidence around the 45°. In addition, the time-dependence SHG (TD-SHG) curves showed that the high laser power of 120 mW favors the trapping/detrapping mechanisms associated to D_{it}. In order to focus just on the Q_{ox} response, measurements with a laser power of 60 mW were the best compromise to have a signal to noise ratio large enough and a low influence of D_{it}.

Conventional electrical techniques were utilized alongside the SHG to extract the electrical parameters that are useful in interpreting the second harmonic signals and that were introduced in the calibration curves. Preliminary measurements performed by corona

oxide characterization of semiconductor (COCOS) technique at STMicroelectronics gave access to the total oxide charges Q_{tot} and the interface traps density D_{it}.

TD-SHG curves of each sample before and after annealing were analyzed using COCOS results in chapter 5. The results showed that a high SHG intensity correlates to a high Q_{tot}. To proceed with a quantitative analysis, we traced a simulated and experimental calibration curve of SHG intensity versus the interface field E_{DC}. The E_{DC} values of the experimental curve were first calculated with Q_{tot} from COCOS measurements, using Gauss law. This tentative of calibration was not conclusive since the experimental data did not exactly match the simulation, probably due to the E_{DC} calculation from the total oxide charges, which not only include Q_{ox}, but also some D_{it} and oxide trapped charges. As previously stated, the initial value of SHG used to plot the calibration curve depends mainly on the fixed oxide charges. Therefore, capacitance-voltage (C-V) technique was utilized in order to extract the Q_{ox}. To perform C-V measurements, we fabricated Metal-Oxide-Semiconductor (MOS) capacitors on the samples. The C-V results reveal a modification in the quality of interfaces and materials due to the fabrication process of the capacitors. Interestingly, the SHG response of samples was also modified after MOS fabrication. A new calibration curve based on C-V data and SHG after MOS fabrication was thus plotted and showed good agreement with the corresponding simulation.

Same tests were performed to break new ground in using the SHG to probe the silicon passivation with HfO_2 and to investigate multilayer structures such as silicon on insulator (SOI). The results of HfO_2 showed a good correlation between SHG and the charges measured by COCOS. On the other side, the investigation of multilayers was more challenging because the optical phenomena (i.e. interferences, absorption) have a significant influence on the SHG signal and are influenced by the thickness of each layer, for example; this can mask the information about the electrical parameters.

During the thesis, we were able to confirm the efficiency of SHG for field effect passivation characterization by calibrating the SHG curve versus fixed oxide charges. Additionally, we found that chemical passivation had an effect on the dynamics of TD-SHG curve and also on the initial value, announcing opportunities for future SHG calibration for D_{it} estimation. Some other perspectives will be presented in the following section.

6.2 Perspectives

This section addresses some opened perspectives, partially supported by simulated curves.

6.2.1 Solve the fabrication issues

Using a calibration, we were able to demonstrate the efficiency of SHG for Q_{ox} extraction. The consistency between simulation and experimental SHG was successfully shown with the experimental E_{DC} calculated from C-V measurements and the SHG performed on the samples containing the MOS capacitors. However, the fabrication processes used to create the MOS capacitors have changed the materials and the interface properties, as the demonstrated by the SHG before/after capacitor processing. Therefore, correlation based on three characterization methods (SHG, C-V and COCOS) was not possible during the thesis. For a more complete study, a fabrication method for MOS structures that preserves the interface quality should be used.

We have so far attempted a variety of processes to create aluminum patterns.

1- Metal deposition with pre-deposition annealing step of the samples followed by lithography and etching processes.
2- Same as the first one but without pre-deposition annealing the samples
3- Lift-off process with positive mask and reversible resist
4- Lift-off process with negative mask and positive resist

None of these processes yielded the expected results since all the samples were modified after MOS fabrication. So, it is necessary to adjust the MOS fabrication steps (e.g. modify metal gate, etching solution, etc.). As Aluminum etching solution used in the MOS fabrication is probably damaging the alumina layer, changing the metal deposited as gate and subsequently the solution that etches may be one of the choices. Indium tin oxide (ITO), a transparent metal for gate, could also be an interesting option not only for C-V measurements, but also for SHG studies under external voltage.

6.2.2 SHG with external voltage

One of the methods that can be useful in extracting the intrinsic electric field present at the oxide/Si interface is the measurements of SHG against an applied external voltage. To perform this measurement, it is necessary to fabricate metal-oxide-semiconductor structures with a metal transparent to both fundamental laser and SH wavelengths. Figure 6.1a

illustrates this concept on an example of simulated normalized square root of SHG intensity versus applied E_{DC} to a sample having intrinsic E_{DC} equal to $2x10^5$ V.cm^{-1}. Indeed, the bulk and surface contributions are weak compared to the EFISH, so the minimum of SHG is reached when $E_{DC}^{EXT} = -E_{DC}^{INT}$. This type of analysis used along with the calibration curve can help determining the quantity and the polarity of the fixed oxide charge.

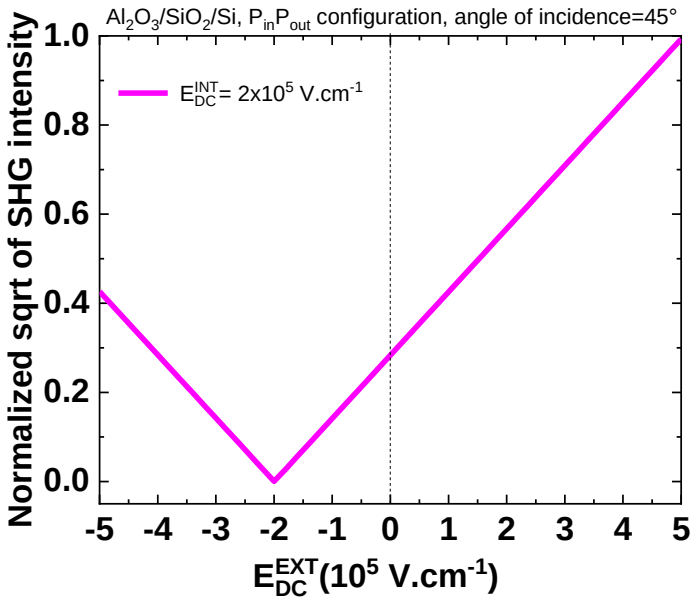

Figure 6.1 : *Simulated square root of intensity versus applied electric field (voltage) for a sample with an intrinsic E_{DC} equal to $2x10^5$ V.cm^{-1}.*

6.2.3 Identification of fixed charge polarity using SHG

Another method that can be performed to identify the charge polarity in the oxide is the measurement of SHG intensity versus azimuthal angle. Figure 6.2 shows simulated SHG versus azimuthal angle for $Al_2O_3/SiO_2/Si$ stacks with negative and positive E_{DC}^{INT} of $1x10^5$ V.cm^{-1}. The configuration selected is P_{in}-P_{out} polarization and 45° angle of incidence. The variation of SHG signal in Figure 6.2 is related to anisotropic bulk contribution from the silicon. For both curves, the four-fold symmetry of Si(100) can be seen but they are shifted by 45° from each other. This shift is due to a flip in the direction of the space charge field as stated in [1], [2]. The observed effect is due to phase differences between the interface and bulk contributions.

So far, the focus was on Q_{ox} and field effect passivation but the technique can be also extend to characterize the chemical passivation (D_{it}), as described in the next section.

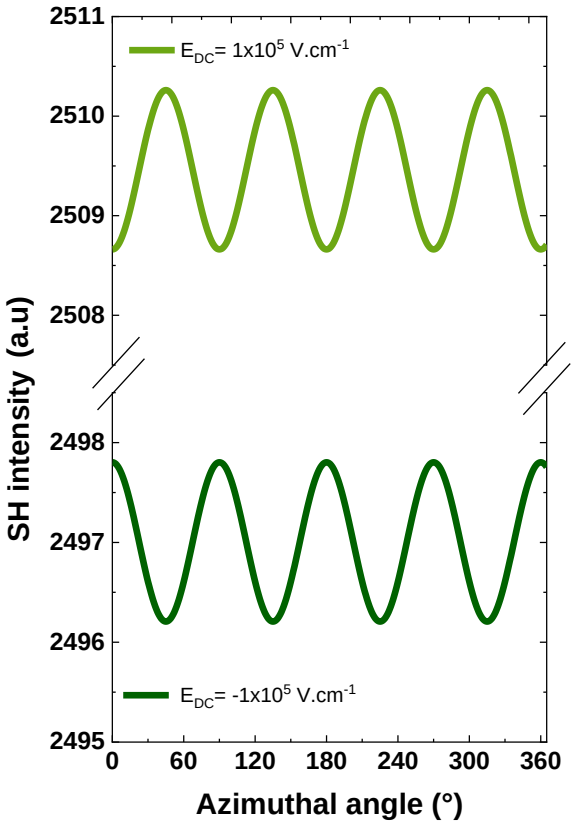

Figure 6.2 : *Simulated SHG versus azimuthal angle with negative E_{DC} (upper curve) and positive E_{DC} (lower curve).*

6.2.4 Time-dependent SHG and trapping mechanisms

The TD-SHG signal is due to the time variations of the interface electric field created by the carrier injection processes and subsequently surface/interface trapped charges. During the thesis, we incorporated a time dependency of E_{DC} in the simulation tool. Simulations can be done using different trap filling rates ($1/\tau$), which are related to the trap densities (D_{it}). Figure 6.3 depicts examples of some simulated SHG intensity versus time curves, with $E_{DC}(t)$ expression extracted from literature [3], as:

$$E_{DC}(t) = E_{DC}(0) + A\,[1-e^{-t/\tau}] \tag{6.2}$$

$E_{DC}(0)$ and A values correspond to the initial and saturation SHG intensities. This equation takes into account one filling rate that can be associated to one type of traps. In reality, there are many sources of traps at the dielectric-semiconductor interfaces, each having its own

response time. For example, let us consider two types of traps, by defining $E_{DC}(t)_1$ and $E_{DC}(t)_2$, for τ_1=2s and τ_2=8s. Depending if the traps are both filling or if one is filling, while the other is releasing carriers, the combination of these fields can be done as follows:

$$E_{DC}(t)_3 = E_{DC}(0) + A\,[1 - e^{-t/\tau_1} - e^{-t/\tau_2}] \quad (6.3)$$

$$E_{DC}(t)_4 = E_{DC}(0) + A\,[1 - e^{-t/\tau_1} + e^{-t/\tau_2}] \quad (6.4)$$

Figure 6.3 shows simulated TD-SHG curve when only one type of traps exists, so we introduced $E_{DC}(t)$ in the nonlinear polarization for the traps two filling rates: τ_1=2s and τ_2=8s. Figure 6.3 also illustrates the SHG response when the electrons are trapped with two different traps during the laser illumination, expressed by $E_{DC}(t)_3$ (Figure 6.3a), and when they are trapped with one type of traps and detrapped with the other, i.e. $E_{DC}(t)_4$ (Figure 6.3b). Therefore, the simulation shows the different dynamic of TD-SHG curve depending on trapping/detrapping mechanisms present at the interface. In real experiments, the situation will be probably even more complex, since many types of traps can be present.

These simulation results suggest that future SHG studies on various high-k dielectrics/Si(100) samples with Q_{ox} and very different D_{it} could be of interest to evaluate D_{it} and eventually calibrate the SHG for this purpose.

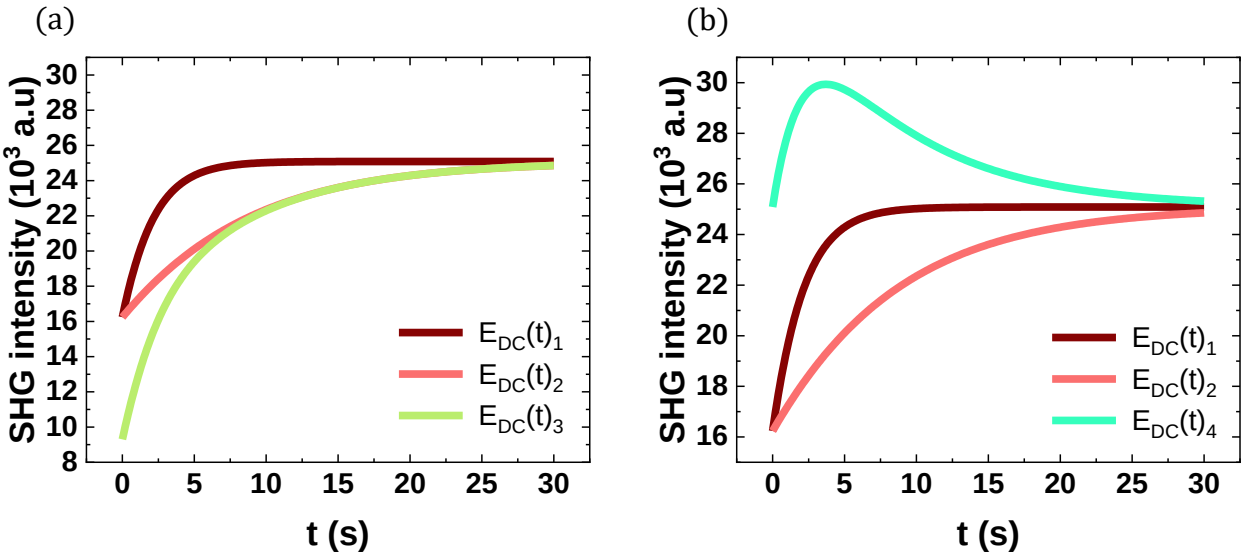

Figure 6.3 : *Simulated SHG versus time using exponential functions for $Al_2O_3/SiO_2/Si$ structure.*

6.2.5 Challenge of SHG calibration for multilayer structures

During the thesis, we performed some measurements of SHG versus input polarization angle on thin and thick silicon on insulator (SOI) structures and the curves showed different responses partially because the optical phenomena, such as absorption and interferences are thickness-dependent. A future SHG calibration in order to characterize the interfaces of such multilayer structures will be more challenging. Consequently, various SOI structures with different interface qualities and with same layer thicknesses should be studied in order to envision a calibration of the SHG for multilayers. Simulations could serve to take into account the electrical and optical phenomena. In addition, the use of complementary electrical techniques will be necessary to interpret the SHG signals (in particular to deconvolute geometry and optics from electrical properties) and to complete SHG calibration curve for this type of samples.

The results obtained in this thesis along with these perspectives show the bright future of using the SHG to directly characterize the interfaces between dielectrics and semiconductors... Lots of challenges and targets are thrown into the playground for future PhD students...

6.3 Chapter references

[1] J. I. Dadap, X. F. Hu, M. H. Anderson, M. C. Downer, J. K. Lowell, and O. A. Aktsipetrov, 'Optical second-harmonic electroreflectance spectroscopy of a Si (001) metal-oxide-semiconductor structure', Physical Review B, vol. 53, no. 12, p. R7607, 1996.
[2] T. Scheidt, E. G. Rohwer, P. Neethling, H. M. Von Bergmann, and H. Stafast, 'Ionization and shielding of interface states in native p+-Si/SiO_2 probed by electric field induced second harmonic generation', Journal of Applied Physics, vol. 104, no. 8, p. 083712, 2008.
[3] Z. Marka et al., 'Band offsets measured by internal photoemission-induced second-harmonic generation', Physical Review B, vol. 67, no. 4, p. 045302, 2003.

Appendix

This appendix shows the second fabrication flow for the MOS capacitors, carried out in clean room and based on a lift-off process. The first step is cleaning of the samples with deionized water as in the flow presented in chapter 4. Then, the fabrication steps are shown in Figure 1 as follows:

a) Using spin coating to deposit Hexamethyldisilazane (HMDS) primer to adhere the resist and then to deposit 1.27 µm of reversible resist (AZ-5214E). These steps are followed by a soft bake on a hot check at 110°C for 50 seconds.
b) UV Hg lamp exposure through the mask, followed by reverse annealing at 120°C for 2 minutes and UV insolation without mask.
c) Development of resist using AZ developer (50% developer + 50% DI water) during 100 seconds at room temperature.
d) Deposition of 400 nm of aluminum by sputtering.
e) Lift-off process with acetone using ultrasonic bath.

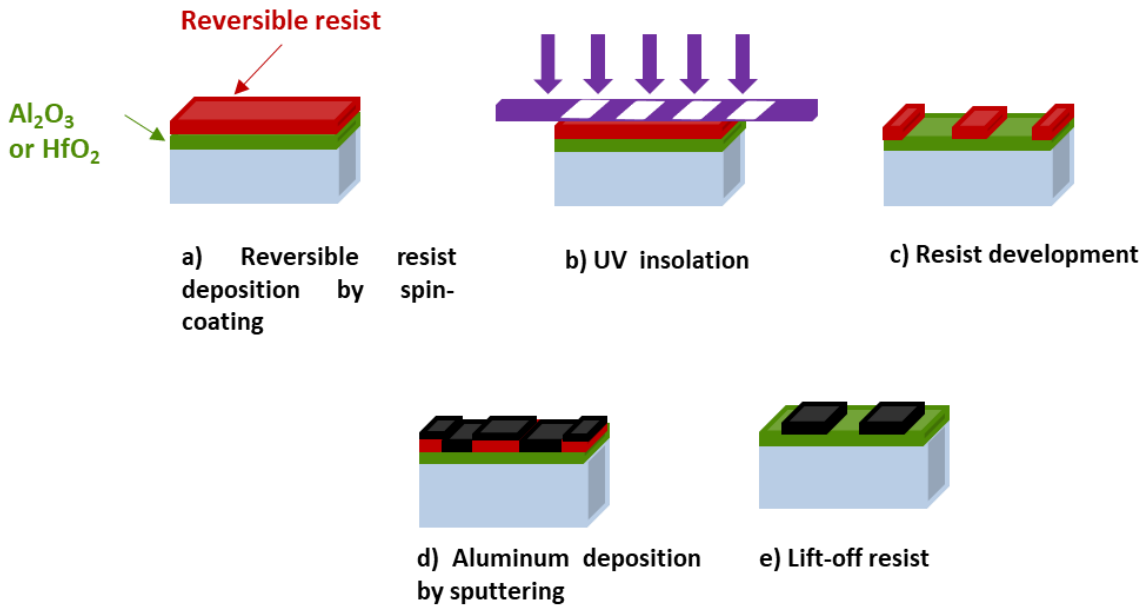

Figure 1 : *Fabrications of MOS capacitors by lift-off using reversible resist.*

The removal of the resist averred by the aluminum layer during the last stage of lift-off was difficult and time-consuming. After about ten of minutes in acetone, large blotches of Al still remained on the surface of samples, not just on the gate of MOS capacitor. Figure 2a

and b show an example of such samples, where we can see the residual Al on the surface of the sample. This problem can be due either to the strong adhesion of the resist used or to the extremely smooth surface of our samples, which makes the lift-off more difficult. Figure 3 shows C-V curves measured from some samples of this fabrication. Although the difficulty of fabrication, the voltage shifts of curves are in agreement with what was expected from the COCOS results. However, it was impossible to make SHG measurements on these samples because of the presence of residual Al all over the surface.

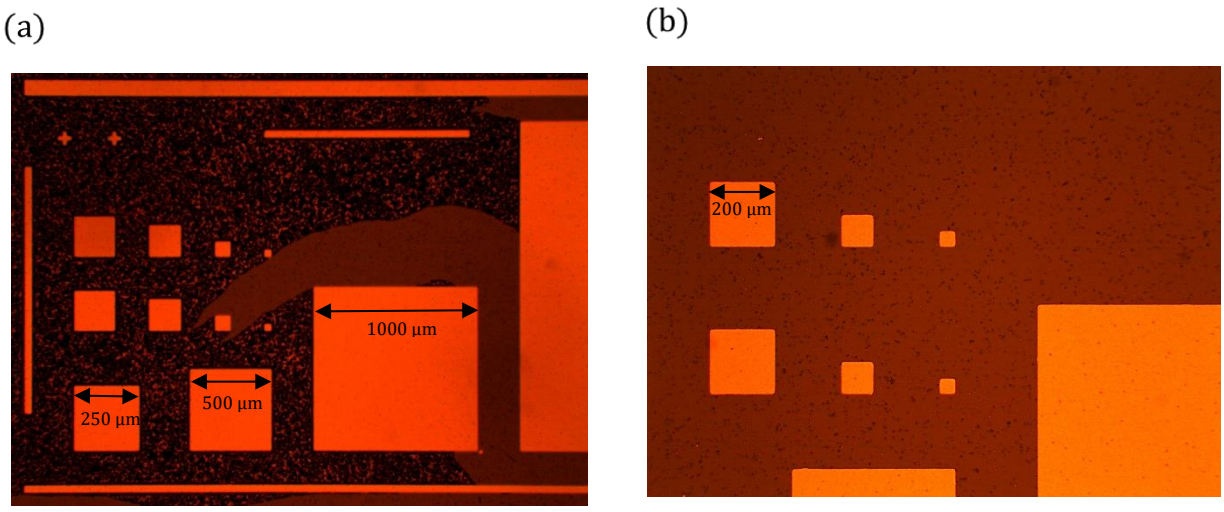

Figure 2 : (a) *Image taken with optical microscope for one of the samples with lift-off failure.* ***(b)*** *Zoom showing the small residual Al all over the surface.*

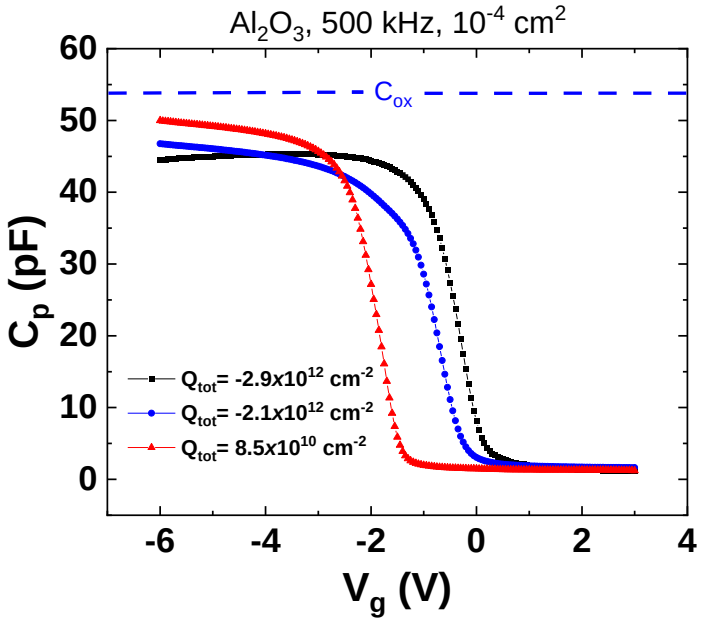

Figure 3 : *C-V measurements on the fabricated samples.*

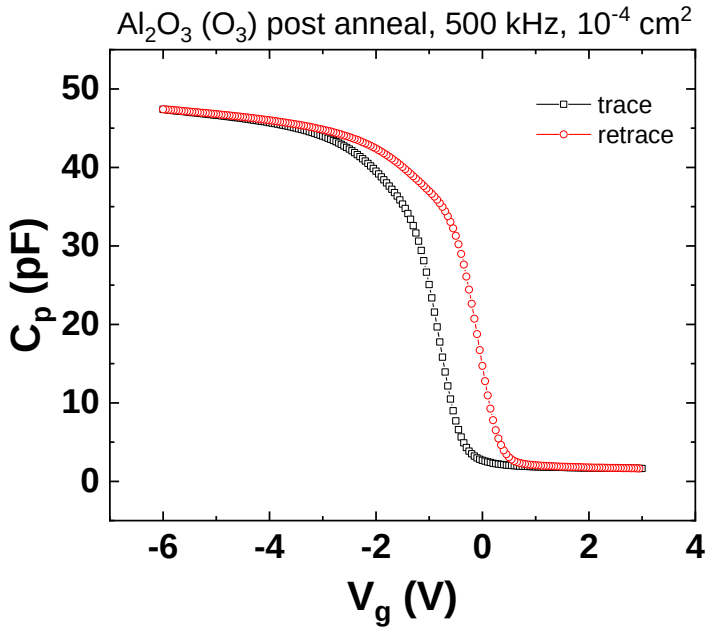

Figure 4 : *C-V measured at 500 kHz on the Al/13 nm Al_2O_3/SiO_2/Si (100) capacitor with 10 µm size. The D_{it} calculated from this sample by C-V is 6.8×10^{12} $cm^{-2}.eV^{-1}$.*

Résumé en français

Table des matières

1- Contexte

Les diélectriques à haute permittivité (high-k) sur silicium constituent un empilement essentiel pour les dispositifs microélectroniques et optoélectroniques tels que les MOSFET, les capteurs d'image et les cellules solaires. Ces diélectriques peuvent servir comme une couche de passivation pour les dispositifs optoélectroniques. Les deux mécanismes de passivation qui permettent de diminuer la recombinaison des porteurs à la surface/interface sont :

1- La passivation par effet de champ, induite par la présence d'une charge fixe d'oxyde Q_{ox} qui modifie la concentration en porteurs libres présents à la surface du silicium.
2- La passivation chimique qui permet de réduire la densité des pièges d'interface D_{it} grâce aux liaisons avec les atomes constituant le diélectrique.

Les méthodes électriques typiquement utilisées pour caractériser la qualité de passivation sont les mesures de capacités-tension (C-V) [1], la décroissance de la photoconductance (PCD) [2], les mesures par charges corona (COCOS) [3]. La thèse porte sur la caractérisation de Q_{ox} et D_{it} afin d'évaluer la qualité des interfaces en utilisant une technique alternative basée sur l'optique non linéaire : la génération de seconde harmonique (SHG). Le Tableau 1 présente une analyse comparative de la SHG par rapport aux autres méthodes comme C-V et COCOS, en soulignant certains de ses avantages et ses difficultés.

Tableau 1 : *Comparaison entre les techniques de caractérisation de passivation : avantages (+) et difficultés (-).*

	C-V	COCOS	SHG
Structure de test spécifique	–	+	+
Non-destructif	–	+	+
Mesure au niveau du wafer	–	+	+
Extraction de Q_{ox}	**Direct**	**Indirect**	**A calibrer (l'objectif de la thèse)**
Extraction de D_{it}	**Direct**	**Direct**	**A calibrer**

Le C-V est une technique très connue et efficace qui permet de déterminer les paramètres électriques d'interface (c.à.d. Q_{ox} et D_{it}). Cependant, elle ne peut être appliquée qu'à des capacités MOS. Par conséquent, elle ne sonde pas l'ensemble du wafer et des étapes de fabrication de structures de test spécifiques sont nécessaires.

La mesure COCOS est non destructive et peut être appliquée au niveau du wafer, mais elle ne fournit pas les charges fixes de l'oxyde mais plutôt une charge totale qui englobe plusieurs éléments et peut être plus compliquée à traiter. De plus, elle peut charger la surface.

Dans ce contexte, nous proposons la SHG, une technique alternative et complémentaire aux techniques existantes. Dans cette méthode, un faisceau laser monochromatique de fréquence ω est focalisé sur le substrat, générant une lumière à la fréquence double (2ω), que l'on appelle seconde harmonique. L'avantage de cette technique est qu'elle est non-destructive, rapide et sensible aux surfaces et aux interfaces des matériaux centrosymétriques (tels que le silicium, SiO_2, Al_2O_3, HfO_2, etc.) et non pas à leur volume [4]. De plus, la SHG peut être également induite par un champ électrique présent aux interfaces (EFISH). L'intensité SHG, $I_{2\omega}$ (t), peut être décrite par [5]:

$$I_{2\omega}(t) \sim \left| \chi^{(2)} + \chi^{(3)} \left[E_{DC}(0) + E_{DC}(t)\right] \right|^2 (I_\omega)^2 \quad (1)$$

$\chi^{(2)}$ et $\chi^{(3)}$ sont les susceptibilités de second et troisième ordre du matériau, I_ω est l'intensité du faisceau laser incident. Le terme $E_{DC}(0)$ représente le champ électrique initial préexistant à l'interface entre deux matériaux qui dépend principalement de Q_{ox} [6]–[10]. Le terme dépendant du temps, $E_{DC}(t)$, se produit à cause des phénomènes de chargement/déchargement pendant l'illumination laser, qui peuvent être associés à D_{it} [11]–[15].

Ainsi, la SHG donne accès aux propriétés électriques des interfaces. En outre, la réponse SHG dépend de la géométrie de l'empilement étudié et des phénomènes optiques qui peuvent s'y produire. Alors, l'implémentation de cette technique comme caractérisation de routine (éventuellement en industrie) n'est pas évidente. L'objectif de cette thèse est de calibrer cette technique afin de caractériser la passivation par effet de champ (Q_{ox}, c.à.d. E_{DC} (0)), en utilisant des approches modalisation/simulation et expérimentales. En effet, la modélisation permet de distinguer l'effet des phénomènes électriques de ceux optiques comme décrit dans la section suivante.

2- Modalisation et simulation de SHG pour les empilements multicouches

Bien évidemment, la nature optique de la SHG rend sa réponse sensible aux phénomènes optiques (par exemple, réflexions multiples, absorption et interférences) qui peuvent se produire dans la structure. Afin d'extraire correctement la densité de charge fixe (Q_{ox}) par SHG, il est nécessaire de décorréler les effets associés aux champs électriques d'interface des phénomènes optiques. Le modèle développé part d'un faisceau laser incident qui traverse une structure multicouche et induit la génération de seconde harmonique. Nous avons considéré la structure multicouche comme une série de couches avec des propriétés optiques et diélectriques différentes.

Les étapes implémentées dans Matlab pour le calcul de la réponse non linéaire (illustrées à la Figure 1) sont :

1- Définitions des paramètres correspondant à l'expérience considérée (e.g. angle d'incidence, angle de polarisation incidente, etc.) et de structure (e.g. indices de réfraction, épaisseurs, etc.) .
2- Calcul des champs électriques réfléchis et transmis de la lumière fondamentale (ω) en tout point de la structure. A l'interface entre deux matériaux, ces champs sont soumis à des conditions aux limites linéaires établies à l'aide des équations de Maxwell.
3- En utilisant l'approche de Sipe et al. [16], les termes sources de polarisation non linéaire sont calculés, en séparant les contributions de volume, de surface et EFISH.
4- Les conditions aux limites non linéaires sont utilisées pour calculer les champs de la lumière SH (2ω). Elles ont été déterminées en se basant à l'article de Bloembergen et al. [17] et développées afin d'obtenir des expressions générales, permettant de simuler n'importe quel multicouche.
5- L'intensité de SHG peut finalement être tracée en fonction de différents paramètres "expérimentaux" (e.g. angle d'incidence, angle de polarisation, puissance laser, etc.).

Les expressions utilisées aux étapes 3 et 4 n'ont pas été prises simplement telles quelles dans la littérature, elles ont dû être développées et généralisées pour pouvoir être utilisées dans une structure multicouches quelconque. Elles sont présentées dans le chapitre 3 de la thèse.

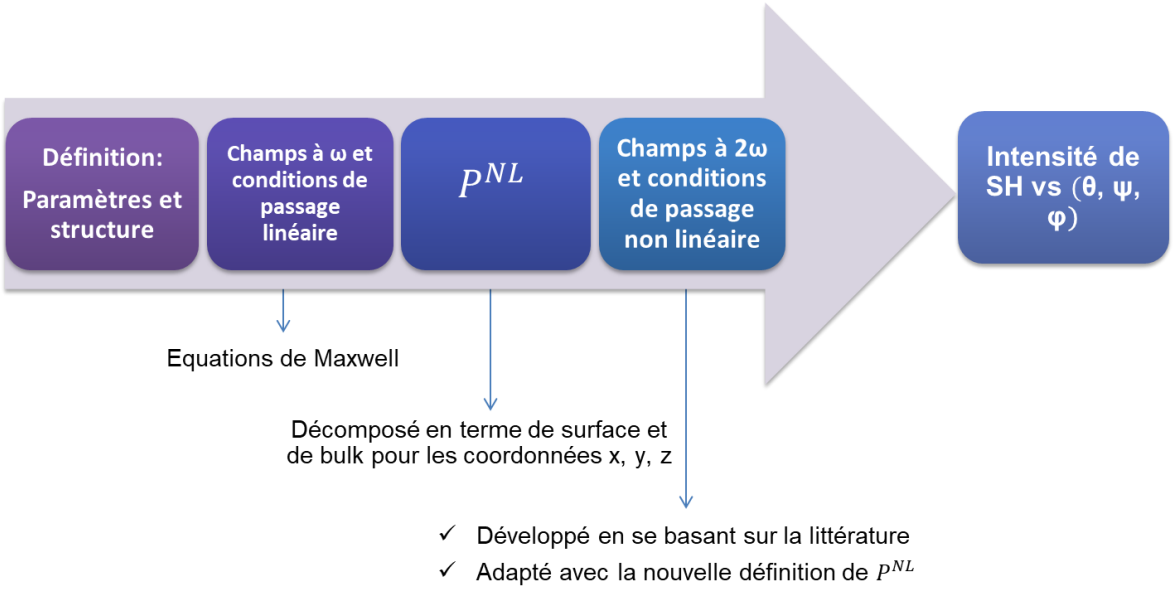

Figure 1 : *Processus de calcul de la réponse SHG selon le modèle développé pendant la thèse.*

Ces étapes ont été intégrées dans un code de simulation Matlab avec des processus de calcul. La validité de notre modèle s'est faite en deux façons :

1- Analytiquement, nous avons calculé les champs électriques de seconde harmonique réfléchis pour une structure simple précédemment étudiée par la littérature (Si oxydé). Nos équations plus générales, se réduisent à celles trouvées dans la littérature pour ce cas particulier.
2- Par simulation : nous avons tracé et comparé la réponse SHG simulée et mesurée pour plusieurs structures. Des tests simples ont été effectués sur un substrat Si(100) avec de l'oxyde natif (illustrés à la Figure 2) en faisant varier l'angle de polarisation de la lumière fondamentale (a) et l'angle d'incidence (b). Il est clair que la simulation a pu reproduire les résultats expérimentaux, en incluant une valeur faible de $E_{DC}(0) \sim 10^3$ $V.cm^{-1}$ pour le terme d'EFISH.
   Nous avons également étendu notre modèle à des structures multicouches plus complexes composées de 3 couches (ex. high-k diélectrique/SiO_2/Si) et de 4 couches comme les substrats de silicium sur isolant (SOI) avec oxyde natif, en considérant chaque fois la présence d'interfaces et de couches de diélectrique avec des propriétés optiques différentes. Tous ces résultats sont présentés dans le chapitre 3 de la thèse.

Cette modélisation/simulation de SHG a été utilisée en conjonction avec les mesures pour calibrer la méthode afin qu'elle puisse évaluer la qualité de passivation des structures high-k diélectriques/silicium comme nous le montrons dans la prochaine section.

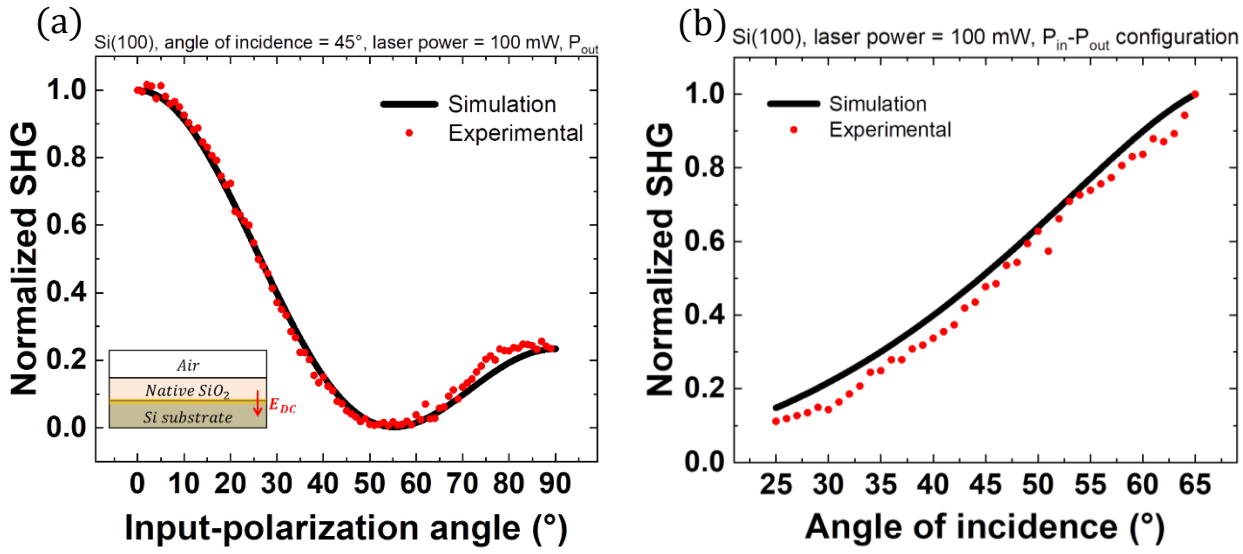

Figure 2 : *Intensité de la lumière SHG normalisée simulée et expérimentale du substrat Si (100) en fonction de* ***(a)*** *l'angle de polarisation,* ***(b)*** *angle d'incidence.*

3- Calibration de SHG pour sonder les interfaces des monocouches de high-k diélectriques/Si(100)

Les matériaux principalement étudiés durant la thèse sont des empilements de diélectrique high-k sur Si(100) avec différentes qualités d'interface. L'objectif de la thèse était de calibrer la réponse SHG liée aux charges d'oxyde fixes afin de développer une technique de mesure qui pourrait potentiellement remplacer ou compléter celles généralement utilisées (e.g. C-V, COCOS, décroissance de photoconductivité). Pour compléter les courbes de d'étalonnage, les échantillons sont également caractérisés par des techniques telles que C-V et COCOS.

La Figure 3 représente les deux courbes de calibration de la racine carrée de l'intensité SHG en fonction de E_{DC}. Ce choix d'axes devrait conduire à une dépendance linéaire, comme suggéré par l'équation (1). La ligne continue correspond à la courbe simulée et les différents symboles colorés représentent les résultats expérimentaux des différents échantillons. Les courbes ont été normalisées pour comparer les résultats expérimentaux avec ceux simulés. La normalisation se fait en divisant l'intensité SHG de chaque substrat par celle de l'échantillon qui possède la valeur E_{DC} maximale. C'est pourquoi une superposition parfaite est observée pour la première valeur de la Figure 3.

La courbe simulée a été tracée en prenant en compte tous les termes de l'équation (1) et tous les phénomènes optiques (c.à.d. l'absorption, la réflexion multiple, etc.) que se

produisent dans la structure $Al_2O_3/SiO_2/Si$. Les paramètres de mesure et les propriétés des matériaux sont introduits dans le code de simulation décrit précédemment. Puisque l'objectif principal de notre travail est l'extraction de Q_{ox}, le seul terme EFISH introduit dans la simulation est celui correspondant à $E_{DC}(0)$. L'intensité SHG pour $E_{DC} = 0$ est très faible en simulation car les termes des composantes $\chi^{(2)}$ sont très petits par rapport aux termes EFISH [18].

Les données SHG expérimentales des échantillons correspondent aux points initiaux des courbes SHG dépendant du temps (TD-SHG) et qui correspondent aux valeurs Q_{ox} avant le chargement des échantillons pendant la mesure. Le challenge est comment d'obtenir le champ E_{DC} pour la courbe d'étalonnage.

La première tentative de calibration est illustrée à la Figure 3a et est tracée à l'aide des données COCOS. En fait, les E_{DC} expérimentaux sont calculés à l'aide de l'équation de Gauss basée sur la charge totale d'oxyde (Q_{tot}) mesurée par la méthode COCOS comme montré ci-dessous :

$$E_{DC}^{experimental} = \frac{qQ_{tot}}{\varepsilon_{Si}} \tag{2}$$

Où q est la charge de l'électron et ε_{Si} est la permittivité diélectrique du silicium.

Chacun des résultats expérimentaux et simulés à la Figure 3a présentent une réponse linéaire de la racine carrée de SHG par rapport au champ électrique, cependant, un décalage entre eux est observé. Nous avons fait l'hypothèse que ce décalage provient du calcul $E_{DC}^{experimental}$ par la charge totale qui contient non seulement les charges d'oxyde fixes Q_{ox}, mais aussi les pièges d'interface et d'oxyde (D_{it} et Q_{ot}).

Par conséquent, nous avons fait appel à une 2ème méthode de mesure complémentaire, la capacité-tension obtenue sur une capacité MOS (métal-oxide-semiconducteur). La fabrication des motifs métalliques s'est déroulée en salle blanche, d'abord par dépôt d'aluminium par pulvérisation cathodique (PVD), puis par dépôt, insolation et développement d'une résine photosensible, et enfin l'aluminium a été gravé et la résine retirée. Une seconde courbe de calibration a été tracée en calculant cette fois le $E_{DC}^{experimental}$ à l'aide des Q_{ox} extraient des mesures C-V, comme montre la Figure 3b. Pour mesurer la SHG sur des échantillons contenant des capacités MOS, le laser a été focalisé sur la surface d'oxyde, entre les structures MOS.

La majorité des résultats expérimentaux de la Figure 3b est en accord avec la simulation. Cependant, quelques échantillons présentant des densités de défauts élevées et Q_{ox} relativement faibles (indiquées par les flèches rouges) montrent une intensité

expérimentale plus élevée par rapport à la simulation. Il est possible que le premier point de mesure d'intensité SHG dans la courbe TD-SHG utilisé pour la calibration soit affecté par des fortes valeurs de D_{it}. En effet, pour ces échantillons, puisque le D_{it} est élevé, des pièges peuvent être chargés rapidement par les porteurs lorsqu'on envoie le laser sur la surface et leur charge s'ajoutera à Q_{ox} et sera visible dans la valeur initiale de TD-SHG. Dans ces cas, il peut être difficile de séparer les effets Q_{ox} et D_{it} dans la réponse SHG.

Ces résultats confirment l'efficacité de la technique SHG pour extraire la densité Q_{ox} pour des structures de monocouches de diélectrique/Si grâce à une calibration de la réponse SHG.

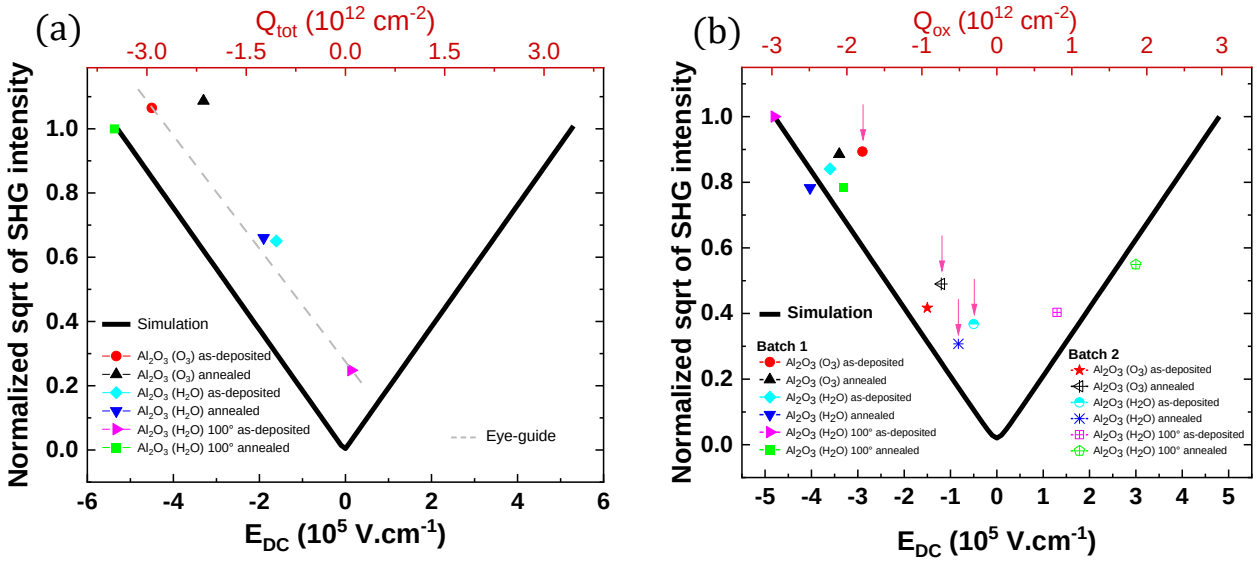

Figure 3 : *Courbes de calibration simulées et expérimentales de SHG en fonction de E_{DC} sur des structures $Al_2O_3/SiO_2/Si$. L'E_{DC} a été calculé à l'aide de l'équation de Gauss en utilisant* ***(a)*** *Q_{tot} (axe en haut) de COCOS,* ***(b)*** *Q_{ox} (axe en haut) de C-V. Les mesures sont effectuées à un angle d'incidence de 47°, une puissance laser de 60 mW et une configuration de polarisation Pin/Pout.*

4- Conclusions & perspectives

La génération de seconde harmonique s'est révélée être une technique prometteuse pour évaluer la qualité des interfaces des structures diélectrique/Si dans la chaîne de fabrication. Les informations pouvant être détectées par SHG sont liées aux charges fixes (Q_{ox}) et aux pièges d'interface (D_{it}). Pour étudier ces paramètres correctement, une modélisation/simulation a été nécessaire afin de distinguer les effets électriques et optiques

qui peuvent se produire dans des empilements de couches silicium/diélectriques. Un calcul a été fait pour déterminer les équations de la polarisation non linéaire et les conditions aux limites non linéaires, en se basant sur la littérature. Le modèle a été validé par une comparaison des intensités SHG en fonction de divers paramètres, et cela pour plusieurs structures de 2, 3 et 4 couches.

Des calibrations de SHG ont été effectuées pour démontrer l'efficacité de SHG dans l'extraction de Q_{ox} de différentes structures de Al_2O_3/Si avec une couche intermédiaire de SiO_2, en comparant la simulation et les mesures de SHG, de COCOS et de C-V. Un bon accord entre la SHG et la C-V a été observé, particulièrement pour les échantillons pour lesquels la valeur de D_{it} est faible par rapport aux charges fixes.

Ce travail a donc permis de calibrer les courbes de SHG de manière à extraire la densité de charge présente sur les interfaces diélectrique/silicium. Cependant, plusieurs perspectives peuvent être envisagées à ces travaux. Pour compléter l'étude des interfaces des multicouches contenant plusieurs interfaces silicium/diélectrique, il serait intéressant d'utiliser une technique électrique en conjonction avec SHG afin d'analyser correctement les paramètres électriques sur chaque interface de la structure.

Une seconde perspective consiste en l'étude de la SHG avec une tension externe appliquée à la structure. Une telle méthode pourrait en effet être utile pour extraire le champ électrique statique de l'interface. La calibration de SHG pour estimer la densité de pièges d'interface D_{it} pourra également faire partie des objectifs d'un futur projet sur cette thématique.

5- Références

[1] D. K. Schroder, Semiconductor material and device characterization. John Wiley & Sons, 2015.
[2] A. B. Sproul, M. A. Green, and A. W. Stephens, 'Accurate determination of minority carrier- and lattice scattering-mobility in silicon from photoconductance decay', Journal of Applied Physics, vol. 72, no. 9, pp. 4161–4171, 1992.
[3] M. Wilson, J. Lagowski, L. Jastrzebski, A. Savtchouk, and V. Faifer, 'COCOS (corona oxide characterization of semiconductor) non-contact metrology for gate dielectrics', in AIP Conference Proceedings, American Institute of Physics, 2001, pp. 220–225.
[4] G. Lüpke, 'Characterization of semiconductor interfaces by second-harmonic generation', Surface Science Reports, vol. 35, no. 3–4, pp. 75–161, 1999.
[5] B. Jun et al., 'Characterization of multiple Si/ Si O 2 interfaces in silicon-on-insulator materials via second-harmonic generation', Applied Physics Letters, vol. 85, no. 15, pp. 3095–3097, 2004.
[6] J. J. H. Gielis, B. Hoex, M. C. M. Van De Sanden, and W. M. M. Kessels, 'Negative charge and charging dynamics in Al 2 O 3 films on Si characterized by second-harmonic generation', Journal of Applied Physics, vol. 104, no. 7, p. 073701, 2008.
[7] N. M. Terlinden, G. Dingemans, V. Vandalon, R. Bosch, and W. M. M. Kessels, 'Influence of the SiO2 interlayer thickness on the density and polarity of charges in Si/SiO2/Al2O3 stacks as studied by optical second-harmonic generation', Journal of Applied Physics, vol. 115, no. 3, p. 033708, 2014.
[8] D. Damianos et al., 'Field-effect passivation of Si by ALD-Al2O3: second harmonic generation monitoring and simulation', Journal of Applied Physics, vol. 124, no. 12, p. 125309, 2018.
[9] A. Rumpel, B. Manschwetus, G. Lilienkamp, H. Schmidt, and W. Daum, 'Polarity of space charge fields in second-harmonic generation spectra of Si (100) / Si O 2 interfaces', Phys. Rev. B, vol. 74, no. 8, p. 081303, 2006.
[10] W. Daum, 'Optical studies of Si/SiO 2 interfaces by second-harmonic generation spectroscopy of silicon interband transitions', Applied Physics A, vol. 87, pp. 451–460, 2007.
[11] W. Wang et al., 'Coupled electron-hole dynamics at the Si/SiO 2 interface', Physical Review Letters, vol. 81, no. 19, p. 4224, 1998.
[12] H. Park et al., 'Characterization of boron charge traps at the interface of Si/SiO 2 using second harmonic generation', Applied Physics Letters, vol. 95, no. 6, p. 062102, 2009.
[13] T. Scheidt, E. G. Rohwer, H. M. Von Bergmann, and H. Stafast, 'Charge-carrier dynamics and trap generation in native S i/S i O 2 interfaces probed by optical second-harmonic generation', Physical Review B, vol. 69, no. 16, p. 165314, 2004.
[14] J. Bloch, J. G. Mihaychuk, and H. M. Van Driel, 'Electron photoinjection from silicon to ultrathin Si O 2 films via ambient oxygen', Physical Review Letters, vol. 77, no. 5, p. 920, 1996.
[15] V. Fomenko, E. P. Gusev, and E. Borguet, 'Optical second harmonic generation studies of ultrathin high-k dielectric stacks', Journal of Applied Physics, vol. 97, no. 8, p. 083711, 2005.

[16] J. E. Sipe, D. J. Moss, and H. M. Van Driel, 'Phenomenological theory of optical second- and third-harmonic generation from cubic centrosymmetric crystals', Physical Review B, vol. 35, no. 3, p. 1129, 1987.
[17] N. Bloembergen and P. S. Pershan, 'Light waves at the boundary of nonlinear media', Physical review, vol. 128, no. 2, p. 606, 1962.
[18] T. Scheidt, E. G. Rohwer, P. Neethling, H. M. Von Bergmann, and H. Stafast, 'Ionization and shielding of interface states in native p+-Si/SiO 2 probed by electric field induced second harmonic generation', Journal of Applied Physics, vol. 104, no. 8, p. 083712, 2008.